Clustering and settling dynamics of inertial particles under turbulence

Daniel Mora-Paiba

To cite this version:

Daniel Mora-Paiba. Clustering and settling dynamics of inertial particles under turbulence. Fluid mechanics [physics.class-ph]. Université Grenoble Alpes [2020-..], 2020. English. NNT : 2020GRALI044 . tel-03363092

HAL Id: tel-03363092
https://theses.hal.science/tel-03363092

Submitted on 3 Oct 2021

Thèse

pour obtenir le grade de

DOCTEUR DE L'UNIVERSITE GRENOBLE ALPES

Spécialité : **Mécanique des fluides, Energétique, Procédés**

Arrêté ministériel : 7 août 2006

Présentée par

Daniel Andrés Odens MORA-PAIBA

Thèse dirigée par **Alain CARTELLIER** et
codirigée par **Alberto ALISEDA** et **Martín OBLIGADO**

préparée au sein du **Laboratoire des Écoulements Géophysiques et Industriels**
dans **l'École doctorale IMEP-2**

Clustering and settling dynamics of inertial particles under turbulence

Thèse soutenue publiquement le **19 octobre 2020**,
devant le jury composé de:

Léonie CANET
PU, UGA, Présidente du jury
Romain MONCHAUX
MCF, HDR, ENSTA-Paris Tech, Rapporteur
Romain VOLK
MCF, HDR, ENS-Lyon, Rapporteur
Alain CARTELLIER
Directeur de recherche au CNRS, Directeur de thèse
Martín OBLIGADO
MCF, UGA , Co-directeur de thèse
Alberto ALISEDA
Professeur Étranger, University of Washington , Co-directeur de thèse

UNIVERSITÉ DE GRENOBLE ALPES
ÉCOLE DOCTORALE I-MEP2
Ingénierie - Matériaux, Mécanique, Environnement, Energétique, Procédés, Production.

THÈSE

pour obtenir le titre de

Docteur en sciences

de l'Université Grenoble Alpes
Mention : Mécanique des fluides, Energétique, Procédés

Présentée et soutenue par

Daniel Andrés Odens MORA-PAIBA

Clustering and settling dynamics of inertial particles under turbulence

Thèse dirigée par Alain CARTELLIER et
codirigée par Alberto ALISEDA et Martín OBLIGADO

préparée au Laboratoire des Écoulements Géophysiques et Industriels

soutenue le 19 octobre 2020

Jury :

Rapporteurs :	Romain MONCHAUX	-	ENSTA-Paris Tech
	Romain VOLK	-	ENS-Lyon
Présidente :	Léonie CANET	-	UGA
Directeur :	Alain CARTELLIER	-	Directeur de recherche au CNRS
Co-directeurs de thèse :	Martín OBLIGADO	-	UGA
	Alberto ALISEDA	-	University of Washington

Acknowledgements

I would like to express my gratitude to the following people:

- Alain Cartellier for the opportunity to work in this very challenging project, and for the fruitful discussions we had regarding the different topics involved in the project. Thanks Alain for your advice regarding how to properly deliver the information, and make concise, and direct points.
- Martin Obligado for his faith in my skills, his patience and his enthusiasm in the topic helped me to cope with the different stages of this research project; frustration, joy, and boredom (writing up). I also thank you Martin for the genuine interest you put into developing my scientific career.
- Alberto Aliseda for his friendship and support during my stay in his lab at the University of Washington in Seattle. More importantly, for his guidance, which helped me immensely during each phase of the project there, and gave me a broader perspective about what involves to build an experiment from almost the very scratch.

My personal experience was also enriched by the different people I met in my PhD in both labs: I thank Yann Mezui for sharing pizzas and beers with me after all those long days at work, and for helping me to improve my French during my time in Grenoble. I also acknowledge the help of the LEGI staff: Laure, Muriel, and Sebastien, which improved the quality of the experiments conducted.

During my stay in Seattle, I would like to thank Chris, Fanette, Laurel, Sari, Ting Ting (Maria), Nate, Rodrigo, and Pete for their advise and friendship, you all allowed my stay in Seattle to be much more comfortable.

Finally, I thank my family and my friends back in Colombia for always supporting me, and encouraging me to follow my dreams throughout the years.

Résumé

Les écoulements chargés de particules turbulentes sont répandus dans les applications industrielles et les phénomènes naturels. Au cours des dernières décennies, deux observations: la concentration préférentielle et la modification de la vitesse de sédimentation des particules se sont révélées être les conséquences les plus pertinentes de ces interactions particules - turbulence. Compte tenu de la complexité du problème, ce travail est composé de quatre lots de travaux.

Le premier paquet implique une analyse des pièges de la méthode de pavage Vorono ï, qui est largement utilisée pour quantifier la concentration préférentielle. Nous avons trouvé quelques pièges qui compromettent les résultats de l'analyse en utilisant des enregistrements unidimensionnels. En outre, nous proposons une nouvelle méthode pour démêler les amas induits par la turbulence des fluctuations spatiales aléatoires, un problème commun signalé par d'autres chercheurs.

Le deuxième paquet comprend l'analyse de la turbulence de la phase porteuse dans notre soufflerie. À cet égard, nous conjecturons que les différents générateurs de turbulence (réseaux actifs, ouverts et passifs) modifient la cascade de turbulence, et par conséquent, ils pourraient avoir un impact sur la concentration préférentielle des particules et le comportement de décantation. À cette fin, nous avons analysé les flux générés par une grille active et avons constaté qu'une grille active laissée ouverte (avec un blocage minimum) présente des échelles similaires à celles trouvées dans les grilles fractales. De plus, l'échelle de longueur intégrale n'a pas pu être facilement calculée pour les flux générés par la grille active en utilisant des protocoles triples aléatoires en raison du comportement de la fonction d'autocorrélation dans de tels flux, qui ne passe pas par zéro. Nous proposons une nouvelle méthode pour aborder ce problème qui pourrait être facilement appliquée dans une myriade de situations.

Le troisième package consiste à estimer le taux de dissipation turbulente sur la phase porteuse du fait de la présence de particules. Au moyen d'une extension du théorème de Rice, qui relie l'échelle de longueur de Taylor à la distance moyenne entre les passages à zéro d'un signal de vitesse, nous avons proposé une méthode pour estimer la turbulence de phase porteuse en présence de particules. Cette méthode utilise des ensembles de données de particules enregistrés par interférométrie doppler de phase. Nos résultats sont cohérents avec les expériences précédentes et les simulations numériques.

Le quatrième paquet se réfère à la modification de sédimentation des particules. Nous avons trouvé que le nombre de Taylor Reynolds Re_λ est le principal contributeur à la modification de la sédimentation des particules: à des valeurs croissantes de Re_λ, la vitesse de sédimentation des particules est réduite. De plus, à des valeurs croissantes de Re_λ, les frontières entre la modification positive et négative de la sédimentation se déplacent vers des valeurs plus petites du nombre de Rouse $Ro = V_T/u$.

Summary

Turbulent particle laden flows are widespread in industrial applications, and natural phenomena. Over the last decades, two observations: preferential concentration, and particle settling velocity modification have stood out as the most relevant consequences of such particle - turbulence interactions. Given the complexity of the problem, this work is composed of four work packages.

The first package involves a pitfall analysis of the Voronoï tessellation method, which is widely used to quantify preferential concentration. We found some pitfalls that compromise the results of the analysis using uni-dimensional records. In addition, we propose a new method to disentangle turbulence driven clusters from random spatial fluctuations, a common problem reported by other researchers.

The second package involves the analysis of the carrier phase turbulence in our wind tunnel facility. In this regard, we conjecture that the different turbulence generators (active, open, and passive grids) do change the turbulence cascade, and thereby, they could impact the particles preferential concentration and settling behavior. To this aim, we have analysed active grid generated flows, and found that an active grid left open (with minimum blockage) exhibits scalings similar to those found in fractal grids. Moreover, The integral length scale could not be easily computed for active grid generated flows using triple random protocols due to the behavior of the autocorrelation function in such flows, which does not cross zero. We propose a new method to tackle this problem which could be easily applied in a myriad of situations.

The third package consists of estimating the turbulent dissipation rate on the carrier phase due to the particle presence. By means of an extension of the Rice theorem, which relates the Taylor length scale with the average distance between zero crossings of a velocity signal, we have proposed a method to estimate the carrier phase turbulence in the presence of particles. This method uses particle datasets recorded by phase doppler interferometry. Our results are consistent with previous experiments, and numerical simulations.

The fourth package refers to the particle settling modification. We found that the Taylor Reynolds number Re_λ is the leading order contributor the particles settling modification: at increasing values of Re_λ the settling velocity of the particles is reduced. Also, at increasing values of Re_λ the boundaries between positive, and negative particle settling modification shifts to smaller values of the Rouse number $Ro = V_T/u$.

Contents

List of Figures

List of Tables

CHAPTER 1

Introduction

1.1 Motivation and context

Particle laden flows seeded with inertial particles have been extensively researched (by numerical simulations and experimental realizations) for the last four decades [1]. However, their underlying physics have not been completely understood, hindering the possibility of accurate simulations, and modelling of particle laden phenomena present in industrial applications, or environmental flows.

These gaps in our knowledge are not minor, as consequences of the interactions between the particles (the disperse phase), and the carrier fluid (continuous phase) have deep implications in rain formation, pollutant dispersion, marine snow, or sprays [2]. These latter phenomena have direct connection with challenges our civilization currently faces: extended droughts, and a need for emissions reduction to curb global warming. Thus, our ability to understand, model and control these particle laden flows is essential to solve these important conundrums, for instance, it has been found that marine snow is responsible of 'cooling' the planet by sequestrating CO_2.

Given the complexity and importance of this subject, progress could not be achieved without a multi-disciplinary approach combining numerical simulations, theoretical methods, and experimental campaign. Hence, such effort can only crystallize by an International Strategic Partnership (ISP), launched by the UGA, between several institutions. Our work dealing with the experimental studies is part of the ISP; *Clustering and settling dynamics of inertial particles under turbulence* involving the Imperial College London, the ENS-Lyon, the University of Washington and the Université Grenoble Alpes, and we kindly acknowledge the financial support from the Tec21 (`https://www.tec21.fr/`) (Investissements d'Avenir - Grant Agreement # ANR-15-IDEX-02).

1.2 Scope

This work addresses open questions of two observations found in turbulent particle laden flows subjected to a body force (e.g., gravity): preferential concentration and particle settling velocity modification. Considering that the physical phenomena involved are very complex, and therefore, a comprehensive analysis cannot be conducted, this study was restricted to following conditions (aimed at reducing the problem complexity while retaining the most of the dominant physics):

1. The particle laden flows studied are those composed of two phases: one continuous phase called the 'carrier', and one discrete phase composed of 'spherical' particles [2].
2. The carrier phase is under homogeneous, and isotropic turbulent conditions (**HIT**) [3].
3. The particles diameter D_p is smaller than the smallest turbulent scale η, i.e., the Kolmogorov length scale, i.e., $D_p < \eta$ with $\eta = (\nu^3/\varepsilon)^{1/4}$, being ν the kinematic viscosity of the carrier phase, and ε the turbulent kinetic energy dissipation rate [3].
4. The particle concentration, which is the ratio between the discrete and carrier phases in a volumetric sense, is low and in a dilute regime, i.e., $\phi_v = O(10^{-5})$.
5. The particles are 'heavy' in the sense that the particles density ρ_p is larger than the carrier phase density ρ_f; $\rho_p \gg \rho_f$.

Under the previous conditions, several numerical and experimental studies [1, 2, 4–15], have shown that: first, the particles tend (subjected or not to a body force) to spatially agglomerate, and form clusters; second, some of these studies report that the particle's terminal speed (in the direction of the body force) V_y changes depending on the carrier phase turbulent characteristics, and thus, this speed is in general different than its value attained under the stagnant flow conditions (terminal velocity V_T), i.e., $|\Delta V| = |V_y - V_T| \neq 0$. Recent investigations have also reported these two observations are intertwined, for instance, some research suggests that the velocity enhancement is a direct consequence of the increased local concentration induced by particles local agglomeration [6, 13, 16, 17].

1.3 Open questions

Despite the new insight brought by previous studies, some fundamental questions (under the conditions aforementioned) are still unanswered:

1. What is/are the fundamental driving mechanism/s of preferential concentration?
    - What are the leading order characteristics of the structures formed via this phenomenon?
    - Does the sweep-stick [7] mechanism explain the experimental observations?
2. What are the physical scalings that control the particle settling velocity?
3. Does the turbulence of the carrier phase changes due to the presence of particles? If so to what extent?
4. Does the turbulence of the carrier phase changes due to the particle size distribution? If so to what extent?
5. Does the experimental facility play a role on the particles clustering or settling characteristics? If so to what extent?
6. What are the mechanisms linking preferential concentration to the modification of particle settling velocity, i.e., hindering or enhancement?
7. When is the onset of the collective effects?

Although answers to these questions are sorely needed, the technology available hinders the progress in that direction in either numerical or experimental studies. In the former case, most of numerical studies have neglected the mechanical coupling ('1-way' coupling simulations to reduce computational resources) between the carrier, and the particle phases [1, 5, 15], and when this coupling is included ('2-way' coupling simulations) the values of the Taylor-based Reynolds number are rather small $\mathrm{Re}_\lambda \approx 40$ [16, 18–20]; there seems that no-consensus can be extracted from these numerical studies regarding the consequences of this mechanical coupling (particle back reaction) between the phases on the particles settling, preferential concentration. The origin of these discrepancies can be diverse, for instance, different forcing schemes yield different settling velocities [21]. Considering that some studies [7, 12, 22] have used the '1-way' coupling approximation to validate their respective theoretical approaches, it is still unknown how '2-way' coupling effects affect these proposed mechanisms to explain clustering, and particle settling modification.

On the other hand, it is not straight forward to experimentally measure the mechanical coupling between the discrete and carrier phases with the current technology [1]. Hence, most experimental studies [6, 9, 10, 17, 23] have focused on measuring the particle properties, and relate their results to the unladen turbulence characteristics. However, besides a few studies [24, 25], the available experimental data barely verifies (if at all) the '1-way' coupling point particle approximation.

Given that answering some of the open questions entails measuring the characteristics of the turbulent carrier phase, it seems reasonable to develop new methods to estimate some of the turbulent parameters when the particles are present, and thereby, survey the underlying physics of the phenomenon more accurately. By the same token, some of these answers are sensitive to the post-processing techniques employed to treat the data. For instance, Voronoï tessellations have become very popular to assess the existence of preferential concentration. Despite its widespread use, some research has found that the results from these analyses could mislead [8, 13, 26] if care is not taken.

1.4 Work overview

In order to cater for the previous issues, we have:

- Developed a method to estimate the energy dissipation rate in the presence of particles.
- Devised a new method to compute the integral length scale in a turbulent flow. This method could also extended to particle records under certain conditions.
- Analyzed the extension of the classical 2D Voronoï tessellation cluster analysis [8] to 1D particle records, and found some pitfalls that compromise the results of this analysis in 1D.
- Found that Voronoï analysis applied to 1D projections of 2D, and 3D datasets also exhibit a peak at a scale close to the average cluster size $\langle L_C \rangle$ in agreement with different methods, and previous studies.
- Envisioned a to complement the algorithm to detect turbulence driven clustering by Voronoï tessellations in any dimension.

With the aid of these results, we further scrutinized the data of two experiments conducted in two different experimental facilities (wind tunnels). Our data provide strong evidence suggesting that the mechanical coupling between the carrier and particle phase has to be considered in the scalings dominating the particle settling velocity (question 2). Furthermore, our data suggest that the largest scales and the turbulence cascade of the carrier phase have an important effect on the results measured (questions 3-5 in section 1.3).

The analytical reasoning behind these developed methods, and their respective experimental validation are provided in the different chapters composing this work. Hence, the remaining chapters are organized as follows:

- Chapter 2: Reviews the most pertinent bibliography available on preferential concentration, and particle settling velocity modification in turbulent flows, and introduces the articulation between the different chapters ('articles' published).
- Chapter 3: Illustrates the experimental setup, and reviews the post-processing tools employed.
- Chapter 4: Examines the conference proceeding:
  'Pitfalls Measuring 1D Inertial Particle Clustering.' (Progress in Turbulence VIII 2018) by **D.O. Mora**, A. Aliseda, A. Cartellier, and M. Obligado.
- Chapter 5: Examines the paper:
  'Characterising 1D particle clustering' (to be submitted) by **D.O. Mora**, A. Aliseda, A. Cartellier, and M. Obligado.
- Chapter 6: Examines the paper:
  'Experimental estimation of turbulence modification by inertial particles at moderate Re_λ' (PRF 4 074309 2019) by **D.O. Mora**, A.Cartellier, and Martin Obligado.
- Chapter 7: Examines the paper:
  'Energy cascades in active-grid-generated turbulent flows' (PRF 4, 104601 2019) by **D.O. Mora**, E. Muniz Pladellorens, P. Riera Turro, M. Lagauzere, and M. Obligado.
- Chapter 8: Examines the paper:
  'Estimating the integral length scale from the variance of distance between successive zero crossings of a turbulent signal' (Experiments in Fluids (2020) 61:199) by **D.O. Mora** and M.Obligado.
- Chapter 9: Examines the paper:
  'The effect of Re_λ and Rouse Ro numbers on the settling of inertial particles in homogeneous isotropic turbulence' (to be submitted) by **D.O. Mora**, M.Obligado, A.Aliseda , and A.Cartellier.
- Chapter 10: Illustrates the work conducted in Aliseda's lab in Seattle.
- Chapter 11: Discusses the different articles contribution in the framework of turbulent particle laden flows.
- Chapter 12: Concluding remarks and perspectives.

A graphical outline that describes the links between the chapters can be found in section 2.6 (see figure 2.9).

This work is organized as collection of 'article' chapters, following the guidelines of the document *Thèse sur articles* drafted by the *École Doctoral I-MEP2*, and that can be found on the url: `https://www.adum.fr/as/ed/page.pl?site=edimep2&page=soutenance`; and are reproduced below (in French).

ED I-MEP^2 – COMUE UGA

▪ Thèse sur articles

Recommandations élaborées et validées par le conseil de l'ED du 14 février 2019.

À côté de la thèse classique existe la thèse par articles qui permet d'intégrer des articles publiés ou prêts à être publiés dans des revues à comité de lecture reconnues dans le domaine disciplinaire de la thèse (en général trois articles au minimum).

Une thèse par articles n'est pas interdite en France ; toutefois, elle nécessite un certain nombre de précautions au niveau du travail de rédaction du doctorant et au niveau de l'évaluation par les rapporteurs désignés pour examiner les travaux de thèse.

Le doctorant doit être l'auteur principal des articles, respecter les droits des co-auteurs et vérifier les droits de diffusion conformément au contrat établi avec l'éditeur de la revue.

La thèse par articles n'est pas une simple juxtaposition des articles, mais doit mettre en évidence les liens entre ces articles et la démarche qui a été menée au cours du doctorat pour atteindre les objectifs fixés.

Même si les principaux résultats sont présentés sous forme d'articles publiés ou prêts à être publiés, le mémoire de thèse doit satisfaire aux exigences de l'exercice attendu dans le cadre d'un travail académique de niveau doctorat, à savoir constituer un ensemble cohérent et original et permettre d'apprécier la valeur individuelle du doctorant (part du travail personnel par rapport au travail collectif).

Le mémoire doit être structuré avec une introduction générale comprenant un positionnement de la contribution dans l'espace bibliographique, une présentation de chacun des articles qui doivent être conçus dans le but d'être un chapitre ou une partie de chapitre de la thèse, une partie analyse globale des résultats, une discussion générale et une conclusion.

Chaque article doit être présenté tel que soumis à la revue. Hors les articles le cas échéant, la thèse doit être rédigée en français sauf si une dérogation de rédiger en langue anglaise a été accordée (selon règlement de scolarité en cours).

Il appartient aux rapporteurs de juger si le manuscrit de thèse respecte les exigences de qualité attendues d'un travail de thèse (valeur scientifique et contribution personnelle).

Les rapporteurs ne doivent pas être co-auteurs des articles intégrés dans le mémoire de thèse ni avoir déjà publié avec le doctorant.

Au moment du dépôt du mémoire de thèse sur l'ADUM, une période d'embargo (jusqu'à 12 mois) devra être demandée afin que les articles non

encore publiés puissent l'être avant que la thèse soit mise en ligne sur le site theses.fr

Règles additionnelles :

- En plus des articles, le texte rédigé doit représenter au moins 40 à 60 pages
- Les articles doivent être au nombre de 3 minimum
- Au moins 2 articles doivent être soumis dans des journaux int. de rang A
- Le doctorant doit être premier auteur sur au moins 2 articles
- Statut du 3e article ; plusieurs possibilités :
  - article écrit non encore soumis
  - article de Conf. Int. reconnue, expertisé par des pairs et accepté.
    Cet article doit être équivalent (dans son contenu) à un article publié dans une revue scientifique reconnue.
  - chapitre de livre

Structure typique du mémoire de thèse sur article :

1- Pages liminaires

2- Résumé

3- Présentation générale de l'étude (ex. recension des écrits, problématique, question de recherche, cadre théorique et méthodologique, etc.). Cette présentation générale devrait inclure une discussion de l'articulation des liens entre les articles de la thèse.

4- Chapitre « Material and methods » : présentation détaillée des outils mis en œuvre par le doctorant.

5- Chapitres

  - Présentation des articles
  - Présentation de la participation de l'étudiant dans le travail présenté, et dans le cas d'articles réalisés en collaboration, démonstration que l'étudiant en a été l'auteur principal.

6- Discussion autour de l'avancement des connaissances apportées par les articles.

7- Conclusion/Perspectives

8- Annexes :

  - L'accord écrit des coauteurs pour la soumission des articles à la revue ainsi que le pourcentage de participation de tous les coauteurs.

  - En cas d'acceptation d'un article, engagement de l'étudiant à réaliser les corrections et à soumettre à nouveau.

Chapter 2

State of the art

In this chapter, we review research on fundamental concepts of turbulent particle laden flows: **preferential concentration, and settling velocity modification**. However, before delving into the particle turbulence interactions, we give a short recount **of the single phase turbulence cascade theory**.

Given the nature of this work and when pertinent, we will include a short discussion about the contributions of our work into the respective concept; we will refer to our published work (conducted by the author during the development of this thesis) as well as, work in preparation to be submitted, which can be found in the different chapters of this manuscript.

2.1 Turbulence cascade

Turbulence is an omnipresent physical phenomenon with direct or indirect implications in several areas of human activity via flow in pipes, industrial chemical processes, or transportation. Even every day dull events, such as; having an ordinary sour cup of coffee, to which we add sugar or milk to make it more tasty, benefits from the enhanced mixing provided by the induced turbulence coming from the stirring movement of the teaspoon, and thus, it can be difficult to extricate turbulence, or even differentiate it from the concept of mingling or blending substances.

The standard Kolmogorov scalings (see figure 2.1) propose the notion that large scales of the flow cascade -like a waterfall- into smaller scales up to the length scale where viscous effects are important [28, 29]. The graphical picture is commonly associated with large eddies, or vortices breaking up into smaller vortices, up to the point viscous attrition turns the energy of these very small eddies into heat.

Phenomenological models, experimental data, classical scalings and Kolmogorov hypotheses of statistical stationary , and isotropy have provide some support the energy cascade idea, and that at its core advances the scaling $\varepsilon = C_\varepsilon u'^3/\mathcal{L} = constant$, where ε is the energy dissipation rate, u' is the flow *root-mean squared* velocity, and $\mathcal{L}$ the integral length-scale. Furthermore, this theory proposes that if the flow separation of scales is very large, i.e, the Reynolds number $Re = u\ell/\nu$ is very large, there should exist a range of scales $\eta \ll \ell \ll \mathcal{L}$, with $\eta = (\nu^3/\varepsilon)^{1/4}$ being the Kolmogorov lengthscale, and within this range the viscosity ν has a negligible contribution, and the anisotropy from the large scales has a minimal effect on the cascade dynamics.

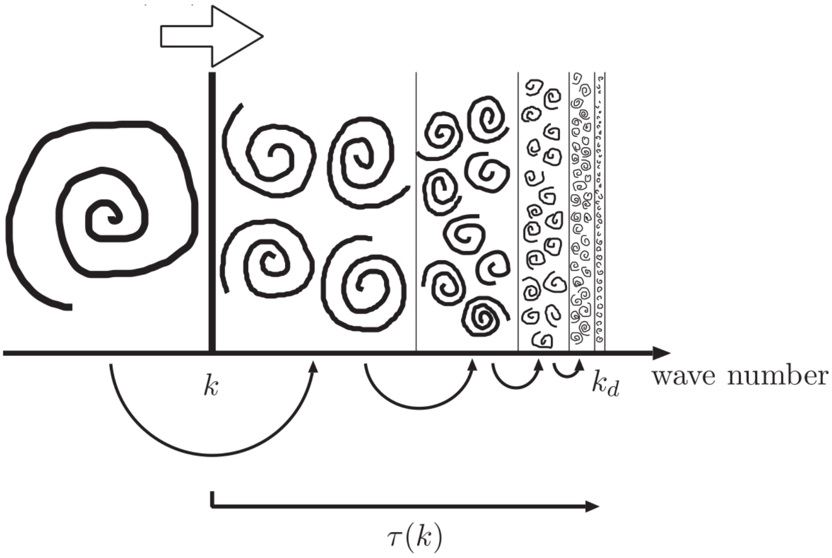

Figure 2.1 – Richardson-Kolomogorov energy cascade, taken from [27].

The latter argument leads to cornerstone assumption in turbulence [29] that the rate of energy injection at the characteristic scale of the phenomenon $\mathcal{L}$ has to be equal to the energy dissipation rate ε at small scales; a coupled process independent of the viscosity ν. It is due to the latter that sometimes the cascading processing is referred as the inviscid, or equilibrium cascade.

One of the most salient features of this classical theory is the form of energy spectrum it provides for the inertial range; $E(k) \propto \varepsilon^{2/3}k^{-5/3}$ for $1/\mathcal{L} \ll k = 1/\ell \ll 1/\eta$, where k is the wave number, and the energy dissipation rate, and Kolmogorov length scale η are averaged over time. The scaling $\varepsilon \propto u'^3(\ell)/\ell$, and shape of the spectrum in the inertial range can be analytically recovered from the Karman Howarth equation if the hypotheses of statistical stationary and isotropy are invoked [28]. However, several experimental and numerical evidence in the past ten years has cast doubt in the accuracy of this classical view [30–33]. For instance, Valente and Vassilicos [31] have found that $C_\varepsilon = f(Re_\lambda^{-1})$ in wind tunnel experiments using fractal grids, which suggest that the equilibrium cascade may not hold for certain flows. This observation has been linked to the presence of coherent structures [32, 34] in the fluid flow, and it cannot be taken lightly as several turbulence models (used in LES and RANS) have being developed considering that $C_\varepsilon = constant$ [35].

Moreover, Re_λ is key to several turbulence theories for HIT [36], as λ contains information about the topology of the flow average distance between stagnation points [35, 37, 38], and determines the threshold above which the influence of viscous terms on the scale-by-scale energy budget are negligible [35]. In addition, recent analyses of third-order structure function have point out that the assumption of an equilibrium cascade ($C_\varepsilon = constant$) may not hold in any part of the inertial range for decaying turbulence, and may only hold at the scale ℓ comparable to the Taylor length scale, i.e., $\ell \approx \lambda$ [39] .

2.1.1 Experimental generation of turbulence

The study of turbulence in experiments has been traditionally conducted by means of wind tunnels [28, 40]. However, in recent decades several facilities have been developed to study turbulence: oscillating grids [41–43], counter-rotating disks (the so called *french washing machine*) [44–46], loud speakers configurations [47, 48], or jet arrays [49, 50].

Although some of these mentioned facilities have been recently employed to study particle-turbulence interaction [10, 17, 51], we briefly introduce only wind tunnel facilities, as we conducted our experiments in such facility.

2.1.2 Passive grid

Simmons and Salter [52, 53] were the first to report that the turbulence behind a periodic grid at high Reynolds numbers is approximately isotropic (see figure 2.2). Several experimental studies [54] have shown that the turbulence intensity in the streamwise direction ($u'/\overline{U}$) decays in a powerlaw fashion [36], which depends on the separation between the bars (mesh size M), and its distance from a virtual origin x_0, i.e.,

$$\frac{\overline{U}^2}{u'^2} = A_1\left(\frac{x-x_0}{M}\right)^{-n} \tag{2.1}$$

where A_1, and n appear to depend on the grid, for instance, in their very famous study Comte-Bellot and Corrsin found $n \approx 1.28$ [55]. Empirically, it has been found that the onset of homogeneous isotropic turbulence is at $x/M \geq 30$.

Although one could consider that the properties of passive grid turbulence are more or less established, recent research has shown that fractal passive grids [56–59] generate turbulence with very interesting properties that do not follow the classical scalings seen with non-fractal passive grids, i.e., $C_\varepsilon \neq constant$. The turbulent fluctuations, however, do still have a power-law decay.

2.1.3 Non-passive grids

Despite the high quality of homogeneous isotropic turbulence (HIT), the Taylor Reynolds number achievable in wind tunnel facilities using non-fractal passive grid is of order 100 ($\mathrm{Re}_\lambda = u'\lambda/\nu = O(100)$). These limitations led some research to propose non-passive grids in wind tunnels, e.g., by using an array of air-jets in co-flow with the bulk streamwise velocity [60–62], or by moving the bar affecting solidity of the grid, and thereby, the turbulent fluctuations [59, 63, 64].

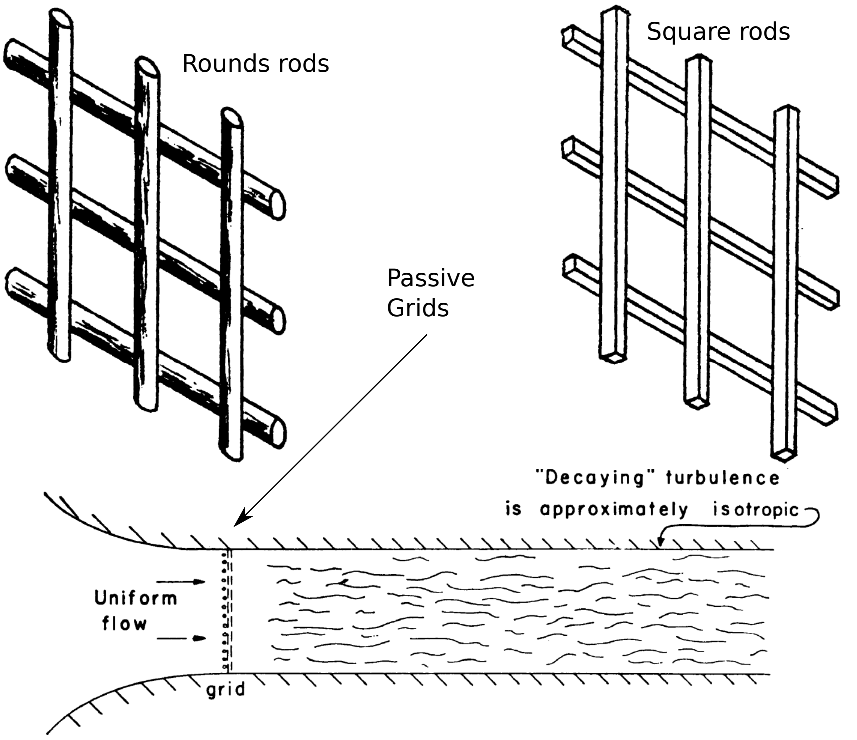

Figure 2.2 – Wind tunnel with a passive grid from [53].

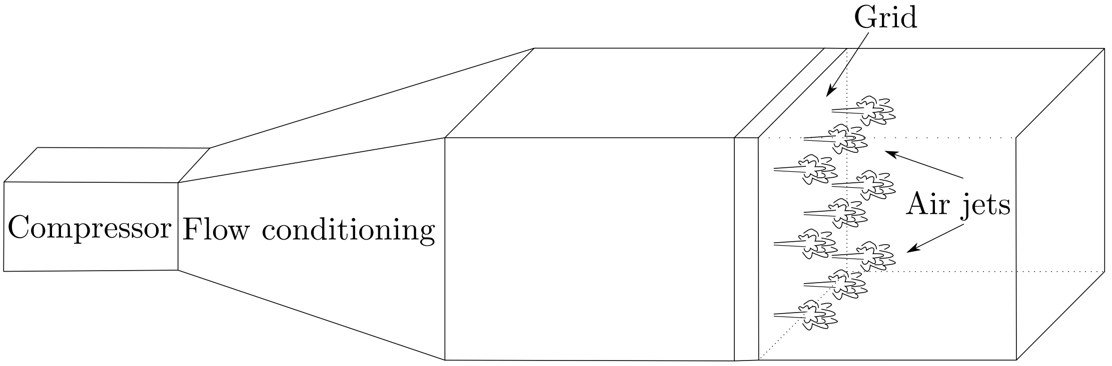

Figure 2.3 – Air jets grid adapted from [66].

2.1.3.1 Jet grids

Gad-el-Hak, and Corrsin [60] designed an array of air jets superimposed onto a classical grid (see figure 2.3) based on previous experiments showing the reasonable degree of homogeneity along with the relative high turbulence levels that could be achieved [65]. Gad-el-Hak, and Corrsin [60] found that this type of grid, generates turbulence that has acceptable isotropy levels for $x/M > 30$. The latter was further confirmed by the experiments of Tassa and Kamotani [61].

Among the may different variables controlling this setup, the injection ratio ($J = Q_{jets}/Q_{bulk}$) stands out as the main contributor to the increase in the turbulence intensity $u'^2/\overline{U}^2$. Gad-el-Hak, and Corrsin, and Tassa and Kamotani found at fixed position downstream that an increase in J leads to an increase in $u'^2/\overline{U}^2$ at a fixed position upstream, and as long as $J < 0.1$. They also observed that at increasing J the turbulence decays more slowly yielding $Re_\lambda \approx constant$ for $30 \lesssim x/M \lesssim 70$) [14, 60]

2.1.4 Active grids

Makita [63] devised a moving grid device that does not require to increase the fans, or compressors pumping air into wind tunnels. His design made of flapping winds (see figure 2.4) that allow to change the grid solidity was quickly adopted, and several new types of flaps (aside the original diamond shape) have been explored, as well as controlling protocols [59, 64, 67–70]. Taylor-Reynolds numbers (Re_λ) up to 5000 have been reported using active grids [71].

Despite the high degree of isotropic, and larger values of Re_λ these grids exhibit some pitfalls. For instance, it has been found that the type of forcing protocol could have an impact on the largest scales of turbulence [59]. More importantly, for active grid generated flows the autocorrelation function $\rho(r)$ could not cross zero leading to uncertainty into the value of the integral length scale $\mathcal{L}$[72].

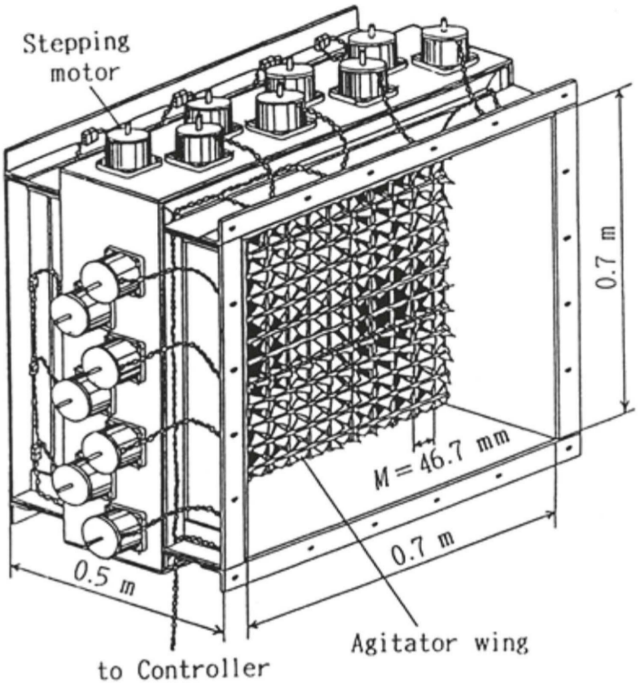

Figure 2.4 – Makita's active grid design taken from [63].

This work contribution

In this work we advance a new method (see **chapter 8**) to compute the integral length scale based on the variance of successive zero crossings of the longitudinal velocity fluctuation. This method is consistent with previous to estimate $\mathcal{L}$ [73], and can be easily extended to complicate setups, for instance, large scale experiments such as those conducted in the S1 wind tunnel in Modane [74].

2.2 Preferential concentration

Preferential concentration refers to the tendency particles have to locally accumulate under the influence of a turbulent flow. This phenomenon is also known as 'inertial clustering' given that it has been found that its underlying causes rely on the difference in inertia between the particle, and the carrier fluid [1]. Moreover, clustering could present whether or not there is a body force acting on the fluid flow.

2.2.1 Single particle dynamics

Under diluted conditions, examining the individual forces acting on a single particle seems a reasonable first step in order to understand the particle evolution while immersed in the turbulent flow. Thus, it comes to no surprise that seminal studies on clustering attempted to explain it by focusing on the forces acting on a single spherical particle [75].

How to model these forces, however, is not an easy task, and it took nearly two centuries to devise an expression that works at low Reynolds numbers. This expression is usually referred as BBOT equation (Basset, Boussinesq, Oseen, Tchen) [76, 77]. Although it is very useful for a large extent of practical applications, the BBOT equation was not fully derived from first principles, and therefore, large errors could arise [78].

In the 1980s, the studies of Gatinol [79], and Maxey and Riley [78] advanced the most accurate (up-to-date) equation for the motion of single spherical particle. This equation is derived via a perturbation approach requiring: $D_p/\eta \ll 1$ with D_p is the particle diameter, and η is the Kolmogorov length scale, Stokesian dynamics (Stokes drag), and $\mathrm{Re}_p = D_p(|\mathbf{V}_p - \mathbf{u}|)/\nu_f \ll 1$, which is the particle based Reynolds number, where $\mathbf{V}_p$ is the particle velocity, $\mathbf{u}$ is the fluid velocity (the undisturbed value of the fluid velocity field if the particle were not present), and ν_f the fluid kinematic viscosity. Under these conditions and including gravity as the unique body force, the motion of rigid sphere immersed in a turbulent flow can be written as:

$$\begin{aligned} m_p \frac{d\mathbf{V}_p}{dt} = \underbrace{3\pi D_p \mu_f (\mathbf{V}_p - \mathbf{u})}_{\text{I}} + \underbrace{\frac{1}{2} m_f \frac{d(\mathbf{V}_p - \mathbf{u})}{dt}}_{\text{II}} + \underbrace{m_f \frac{D\mathbf{u}}{dt}}_{\text{III}} + \\ \underbrace{\frac{3}{2} D_p^2 \sqrt{\pi \rho_f \mu_f} \int_{\infty}^{t} \frac{d(\mathbf{u} - \mathbf{V}_p)}{dt} \frac{d\tau}{\sqrt{t-\tau}}}_{\text{IV}} + \underbrace{(m_p - m_f) g \mathbf{e}_z}_{\text{V}} \end{aligned} \tag{2.2}$$

Where $m_f = \rho_f \pi D_p^3/6$ is the mass of displaced fluid, and the right hand terms are:

- I The Stokes drag.
- II The forced exerted by the fluid on the sphere.
- III The pressure gradient included in the material derivative $\frac{D\mathbf{u}}{Dt}$. This term assumes the force that would act in the unperturbed flow at the center of the sphere.
- IV Basset force or history term, which considers the evolution of the particle up to the time t.
- V Buoyancy force in the vertical direction (-z direction in our right hand coordinate system).

Although equation 2.2 is accurate, and derived from first principles, it can become more analytically tractable under the following conditions: heavy particles $\rho_p \gg \rho_f$, with diameters smaller than the Kolmogorov length scale $D_p < \eta$. These two conditions render negligible (see Maxey [80]) the contribution from most of the terms (e.g. added mass, or history terms) in equation 2.2 except for the Stokes drag, which is considered to be main driver of the relative motion between the fluid and the particle, equation 2.2 can be simplified to:

$$\frac{d\mathbf{V}_p}{dt} = \frac{1}{\tau_p}\big(\mathbf{u}(\mathbf{x}_p,t) - \mathbf{V}_p(t)\big) + g\mathbf{e}_z \tag{2.3}$$

with $\tau_p = (\rho_p/\rho_f)D_p^2/(18\nu_f)$. Equation 2.3 has been used extensively in direct numerical simulations (DNS) [1, 5, 12, 81, 82]. One could even argue that it is the cornerstone of the point particle approximation [1], as one assumes that the particle is very small when compared to the smallest scale of turbulence.

2.2.2 Preferential concentration models

Over the last three decades, several numerical studies and analytical approaches have, by integrating equation 2.3 and the assumption of 'one-way coupling' [7, 12, 81], proposed different models to explain preferential concentration. We review the literature available below with the following caveat: there is still no-consensus on the mechanism responsible for clustering, and whether or not the mechanism is universal for all turbulent length scales, e.g., the mechanism for clustering in the dissipate range could differ from that in the inertial range [12, 75, 83].

2.2.2.1 Centrifugation mechanism

The centrifugation mechanism was first proposed by Maxey [80], and under the assumption that particles are very small that they terminal speed is of the same order of the Kolmogorov velocity scale $V_\eta = (\nu_f \varepsilon)^{1/4}$ one could write particle velocity field as an expansion of the fluid velocity and the Stokes number $\mathrm{St}_\eta = \tau_p/\tau_\eta$ with $\tau_\eta = \sqrt{\nu_f/\varepsilon}$ being the Kolmogorov time scale [1, 84]. These assumptions lead to:

$$\mathbf{V}_p = \mathbf{u} + \mathbf{V}_{\mathrm{St}} - \mathrm{St}_\eta\left[(1-\beta)\frac{D\mathbf{u}}{Dt} + \mathbf{V}_{\mathrm{St}}\cdot\nabla\mathbf{u}\right] \tag{2.4}$$

with $\mathbf{V}_{\mathrm{St}}$ being the particle terminal speed considering Stokes drag, and $\beta = 3/(2\rho_f/\rho_p + 1)$, and all the velocity terms are normalized respect to V_η [1]. Thus, in the heavy particle limit (see section 1.2) $\rho_f \gg \rho_p$ (Maxey's result [80]) :

$$\mathbf{V}_p = \mathbf{u} + \mathbf{V}_{\mathrm{St}} - \mathrm{St}_\eta\left[\frac{D\mathbf{u}}{Dt} + \mathbf{V}_{\mathrm{St}}\cdot\nabla\mathbf{u}\right] \tag{2.5}$$

Taking into account that in derivation of equation 2.4 $\mathbf{V}_p$ is written in terms of a *continuum* velocity field (at scales smaller than η), Maxey's approach allows taking the divergence of both sides of either equation 2.4 or 2.5. The latter operation yields:

$$\nabla \cdot \mathbf{V}_p = -\mathrm{St}_\eta (1-\beta)\left[||S||^2 - ||\Omega||^2\right] \tag{2.6}$$

with $S = \frac{1}{2}(\nabla \mathbf{u} + \nabla \mathbf{u}^T)$ and $\Omega = \frac{1}{2}(\nabla \mathbf{u} - \nabla \mathbf{u}^T)$ being the strain rate and rotation rate tensor, respectively. Equation 2.6 then provides the classical picture that very heavy particles ($\beta \to 0$) accumulate ($\nabla \cdot \mathbf{V}_p < 0$) in regions where the strain rate dominates over vorticity ($||S||^2 > ||\Omega||^2$), i.e., heavy particles migrate to the strain-dominated regions [75] of the turbulent flow they are immersed in. Early studies proposed that this observation is consistent with the view of particles being expelled from vortical regions (centrifuging effects) [81, 85–87]. Moreover, several studies have also found that this migration tendency of heavy inertial particles (to regions of high strain and low vorticity) to be the strongest at $\mathrm{St}_\eta = \mathrm{O}(1)$ [6, 88, 89].

This centrifuging mechanism, although consistent in the dissipative range (i.e. at scales below η), seem to be at odds with the separation of scales (and the onset of an inertial range of scales [3]) seen at increasing values of Re_λ; a single scale could not control the particle distribution [90–92].

2.2.2.2 Sweep-stick mechanism

To bridge the multi-scale nature of turbulence [90], and the observed fractal nature of the voids found in the particles spatial distribution, Vassilicos and collaborators [7, 82, 93] proposed a mechanism to explain clustering in the inertial range, i.e., at scale r for which $\eta \ll r \ll \mathcal{L}$ where $\mathcal{L}$ is the integral length scale.

At its core, this mechanism advances that the particles spatial distribution have a strong correlation with the zero-acceleration points (ZAPs) of the carrier fluid. This correlation is initially explained by means of equation 2.3, and by considering the leading order asymptotic expansion of $\mathbf{V_p}(t)$ in terms of fluid variables [7]:

$$\mathbf{V}_p(t) \approx \mathbf{u}(\mathbf{x}_p, t) - \tau_p \mathbf{a}(\mathbf{x}_p, t) \tag{2.7}$$

where $\mathbf{a} = \frac{D\mathbf{u}}{Dt}$. First, these ZAPs are swept by the flow in direct connection with random advection hypothesis [94], and second particles that meet a ZAP stick it for a while and move with it the local fluid velocity [7]. The first part of this mechanism is justified by K41 scalings, and the expression: $\lim_{\mathrm{Re}_\lambda \to \infty} \langle (\mathbf{u} - \mathbf{V}_a)^2 | (\mathbf{a} = 0) \rangle \sim u'^2 (\mathcal{L}/\eta)^{-2/3} \approx 0$, with the acceleration velocity $V_a = d\mathbf{s}/dt$, and where $\mathbf{s}(t)$ is a position point vector with a constant in time acceleration [93]. Goto and Vassilicos [93] reported that the sweep-stick mechanism explains the particle clustering when the particle relaxation time is much smaller than time scale of ZAPS ($\tau_p \ll \tau_{ZAPs}$), as these ZAPs are more stickier. Moreover, they suggest that the particles only clusters in a way that resembles zero acceleration points when $\tau_p \ll \tau_L$ with τ_L being the flow integral time scale.

Some experimental and numerical studies have reported results consistent with this mechanism [13, 23, 26, 95] for $\tau_p \ll \tau_L$. For instance, Obligado et al. [95] found by means of Voronoï tessellations (see [75], and chapters 3 and 4) that ZAPs cluster as inertial particles. Furthermore, the experiments of Sumbekova et al. [23] (also using Voronoï tessellations [96]) observed a powerlaw behavior for the voids PDF (the opposite of clusters). The powerlaw exponent retrieved was close to -5/3 consistent with the prediction made by Goto and Vassilicos [93]. On the other hand, numerical studies with particles diameters larger than (i.e.$D_p > \eta$) by Uhlmann and Chouippe [26] did not recover the sweeping part of the mechanism, while finding strong agreement with the sticking part of it.

On the other hand, when body forces (e.g. gravity g) are present, the argument of Goto and Vassilicos [93], which underpins the Sweep-stick mechanism, suggest that inertial particle clustering should resemble the clusters if points of acceleration field where $\mathbf{a} = \mathbf{g}$. Hascoet et al. [97] found that this picture could be true for $Ro = \tau_p g/u' \ll 1$ (body forces are not very strong for fixed τ_p), but the argument fails to explain the presence of columnar clustering [97] ($Ro = \tau_p g/u' \gg 1$).

2.2.2.3 Path history mechanism

Collins, Bragg, and Ireland [12, 92, 98] have proposed the existence of an alternative mechanism (non-local) to explain particle clustering. According to these studies, at an arbitrary separation distance r particles pairs coming from larger separation $r^{>}$ will have a larger memory of their lagrangian trajectories (non-locality) than particles stemming from smaller separations $r^{<}$. This asymmetry generates ‘inertial’ clustering [99].

Before going further, it is worth mentioning that these authors [99, 100] have also introduced a distinction between the concepts of preferential concentration, and clustering. The former referred to the particle accumulation of particles due to their correlations with the flow field (e.g. high strain and low vorticity), and the latter referring to particle accumulation irrespective of their correlation with the flow field. *In this work, we use both terms interchangeably given that we study clustering as a consequence of the turbulent flow field. However, and when needed we will make the clarifications required.*

Moreover, these studies [12, 92, 98] claim that the clustering mechanisms in the inertial range are analogous to those in the dissipation range (centrifuging mechanism 2.2.2.1) when $\mathrm{St}_r = \tau_p/\tau_r \ll 1$ where St_r is the Stokes number at certain separation scale r in the inertial range, such that $\eta \ll r \ll L$, and $\tau_r = \varepsilon^{-1/3} r^{2/3}$ by following K41 scalings [3] particles are expelled from eddies of at scale $\approx r$. Interestingly, the authors show their mechanism to be consistent with the Sweep-stick mechanism when $\mathrm{St}_r = \tau_p/\tau_r \ll 1$. On the other hand, for $\mathrm{St}_r \gtrsim O(1)$, the path history effect breaking symmetries yields particle clustering [12].

Further studies from these authors [98] have also suggested that when $\mathrm{St}_r = O(1)$ the path history mechanism effects could compete with the filtering mechanism , which describes the particle modulated response to turbulent fluctuations [89]. In fact, these studies advance that at $\mathrm{St}_\eta \approx O(1)$ the path history effect domains for small $r \lesssim \eta$, whereas the filtering effect dominates for larger $r \gg \mathcal{L}$.

Although experimental verification of this mechanism is yet to be achieved, a recent study conducted in a soccer ball turbulence facility [101] has recovered that the particle pair relative velocity is independent of Re_λ in agreement with the DNS result of Ireland et al. [98] and suggesting that the path-history effects indeed dominate in the dissipation range for small r, and $\mathrm{St}_\eta \gtrsim O(1)$.

2.2.3 Clustering phenomenology

Among the different results found in previous research, numerous studies (numerical and experimental) have shown that significant particle accumulation (highest degree of clustering) occurs at the scale of order $\langle L_C \rangle = O(10-20)\eta$ [6, 26, 95, 102, 103] with $\langle L_C \rangle$ been interpreted as the characteristic linear scale of clusters. Recent experimental studies, however, have retrieved that [17, 23] this characteristic scale could strongly depend on the Taylor - Reynolds number; $\langle L_C \rangle = f(\mathrm{Re}_\lambda)$, e.g., the work of Sumbekova et al. reports $\langle L_C \rangle = O(80\eta)$ for $\mathrm{Re}_\lambda \approx 500$, whereas the work of Petersen et al. reports $\langle L_C \rangle = O(40\eta)$ for $\mathrm{Re}_\lambda \approx 500$.

This work contribution

We found that the relation $\langle L_C \rangle \approx 0.1\mathcal{L}$ seems to hold better for different experimental and numerical datasets (see **chapter 4**). This relationship seems to be consistent with previous observations experimental [23, 95] and numerical observations [104]: a larger value of the average cluster size $\langle L_C \rangle$ is seen for the active grid data which has a larger integral length scale (for the same inflow conditions in the same facility) than a passive grid [95, 105]. More precisely, Monchaux and Dejoan [16] conducted simulations at $\mathrm{Re}_\lambda \approx 40$, and reported a value of $\mathcal{L} \approx 30\eta$, and cluster sizes between 2η and 4η in agreement with the mentioned relation.

2.3 Particle settling velocity modification

Along with preferential concentration, inertial particles immersed in a turbulent flow subject to a body force (gravity) experience changes on their actual settling rate velocity V_T with respect to their terminal velocity for stagnant flow conditions (terminal velocity) $V_{st} = \tau_p g$ (for Stokes linear drag) with g being the gravitational acceleration. These changes, however, are not monotonic, and several studies (reviewed in the next sections) have reported that under certain conditions, particle could experience enhancement either $V/V_T > 1$ or reduction $V/V_T < 1$ of their settling velocity [2, 4, 6, 10, 11, 13, 16–18, 21, 106–108].

Among the different parameters involved (e.g. particle/fluid density, fluid acceleration, gravity, Re_λ, liquid fraction, or particle size D_p), dimensional analysis suggests the following relevant parameters: the ratio between fluid acceleration an gravity $\gamma = \eta/(\tau_\eta^2 g)$, the Rouse number (also known as the settling parameter Sv_ℓ) $Ro = V_T/u' = Sv_\ell$, the Stokes number $\mathrm{St}_\eta = \tau_p/\tau_\eta = O(1)$, and Re_λ, as possible non-dimensional quantities characterizing the particle settling velocity.

However, there is no-consensus on which turbulent scales are the most relevant for each regime, and on to what extent turbulence modulation by the particles [1, 16–18, 105], local hydrodynamic interactions (preferential concentration) [14], particle polydispersity play a first order role on the results seen, or turbulence characteristics (anisotropy). Also, uncertainty regarding the experimental conditions (confinement effects) are yet to be dispelled [2].

2.3.1 Settling enhancement

Several numerical and experimental studies [6, 10, 13, 16, 21, 106] have reported that for *sub-Kolmogorov* particles ($D_p \ll \eta$) the maximum enhancement in the settling $V_T/V_T > 1$ occurs at $\mathrm{St}_\eta = \tau_p/\tau_\eta = O(1)$. These studies results are consistent with preferential sampling mechanism by Wang and Maxey [81] which proposes that particles oversample downward regions of the flow.

Nevertheless, there are large discrepancies between numerical simulations, and experimental studies (and among each other) suggesting that the underlying physics are not well understood. For instance, numerical studies [10, 21] have found the magnitude of such maximum (at $\mathrm{St}_\eta = \tau_p/\tau_\eta = O(1)$) enhancement is $\Delta V/V_T = (V - V_T)/V_T \in [0.1 - 0.9]$, or $\Delta V/u' \in [0.04 - 0.16]$ with u' being the velocity of the largest eddies of the carrier phase. On the other hand, experimental studies [2, 6, 10] have found $\Delta V/V_T = (V - V_T)/V_T \in [1 - 2.5]$, or $\Delta V/u' \in [0.16 - 0.26]$.

Moreover, some studies have suggested that the effects of the mechanical coupling between discrete and carrier phases could be a necessary ingredient in numerical simulations in order to recover the magnitudes of settling [17, 21, 22, 75]. In this regard, numerical studies [1, 5, 15] proposed that the back-reaction of the disperse phase was negligible if $\phi_v < 10^{-6}$. These studies, however, do not consider the increased local concentration that occurs when clustering is present. For example, the studies of Bosse et al. [18] and Monchaux and Dejoan [16] at $\mathrm{Re}_\lambda \approx 40$ have seen an increase in $\Delta V/u'$ ranging from 30% to 200% (depending on the liquid fraction $\phi_v = O(10^{-5})$) with respect to 'one-way' coupling simulations when the 'mechanical coupling between phases ('two-way' coupling) is included. Indeed, the particles presence seems to either enhance or modulate the carrier phase turbulence dissipation rate (ε) [1, 19, 20, 24]; '1-way' DNS simulations have reported that an increase in ε leads to an increase in $\Delta V/u'$ [11, 21], .e.g., Rosa et al. reported that $\Delta V/V_T \approx f(\sqrt{\varepsilon})$. Hence, if these effects are truly intertwined, including them in theoretical analyses and computer simulations is a necessary step to reconcile numerical and experimental studies. However, in the laboratory, accurately measuring the carrier phase properties ($\varepsilon, \mathcal{L}$, or $\mathbf{u}$) in the presence of the discrete phase is very challenging due to the available technology [1, 24].

This work contribution

Trying to circumvent these technological limitations, we have developed a method [105], which can be found in **chapter 6**, to estimate the carrier phase dissipation rate in the presence of particles ε_p based on an extension of the zero crossings method (see [37, 109] and section 3.6) to compute the dissipation rate of a turbulent signal. We also advanced an alternative method to compute the integral length scale $\mathcal{L}$ (**chapter 8**) that can be extended to the particles records under similar conditions as those found in **chapter 6**.

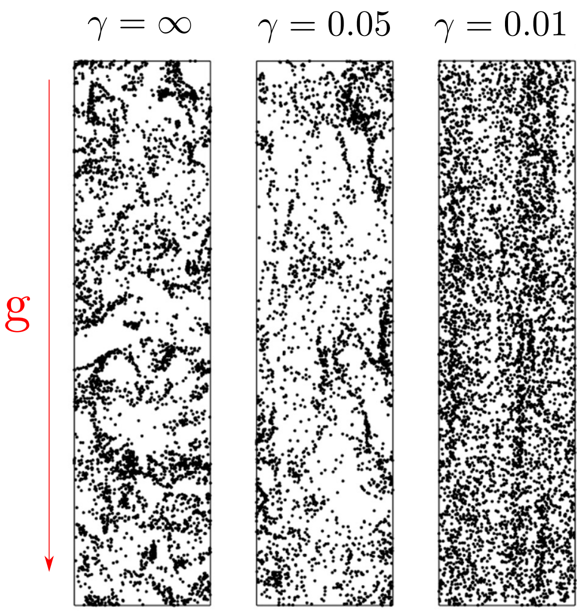

Figure 2.5 – Columnar clustering at decreasing values $\gamma = \eta/(\tau_\eta^2 g)$ (stronger gravity effects) from [11]

2.3.2 Settling enhancement mechanisms

Given the similar origin of both preferential concentration, and settling enhancement, several numerical studies and analytical approaches have suggested (under similar assumptions as for the former phenomenon) different models to explain observed enhancement in particle settling velocity. Hence, most of these models assume 'one-way' coupling [11, 22, 81, 110], and assume that the ratio between acceleration of the carrier phase, and the magnitude body force is very small, i.e., $\gamma = \eta/(\tau_\eta^2 g) \ll 1$. In the latter regime, numerical studies have reported that particles form anisotropic clusters, elongated in the direction of the body force [11, 97], at increasing magnitudes of gravity acceleration (see figure 2.5), and are assumed to follow (c.f. equation 2.3):

$$\frac{d\mathbf{V}_p}{dt} = \frac{1}{\tau_p}\big(\mathbf{u}(\mathbf{x}_p,t) - \mathbf{V}_p(t)\big) + g\mathbf{e}_z. \tag{2.8}$$

Alike the preferential concentration case, we review the literature available below with a similar caveat: there is still no-consensus on the mechanism responsible for the settling enhancement, and on what are the most relevant turbulent length scales [22, 111, 112].

2.3.2.1 Preferential sweeping

Along with their early work on the centrifugation mechanism (see section 2.2.2.1), Maxey [80] proposed that 'heavy' particles with $St_\eta \ll 1$ are ejected of vortex cores (regions of strong vorticity), and then sample downward regions of the flow. Their seminal work considering Gaussian velocity field received further support by the DNS studies of Squires and Eaton [86], and Maxey and Wang [81] that reported that these observations were the strongest at $St_\eta = O(1)$ and $V_T/u_\eta = O(1)$ with $u_\eta = (\nu\varepsilon)^{1/4}$. These studies referred to this mechanism as preferential sweeping or *fast-tracking* (see figure 2.6).

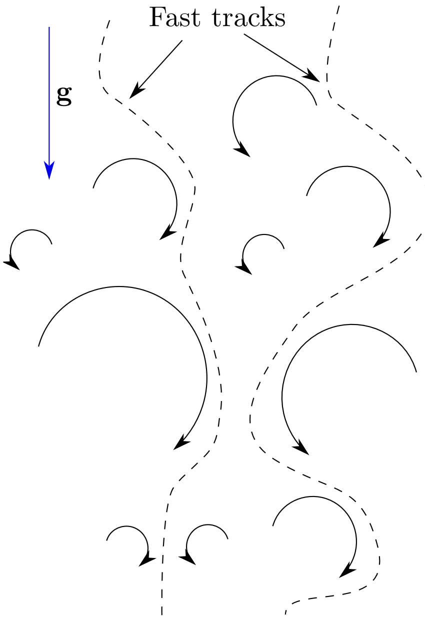

Figure 2.6 – Fast tracking illustration, adapted from [113].

On the other hand, a common observation in several studies [6, 10, 17, 21, 81, 107, 112, 114] is that the particle settling enhancement scales with $\Delta V \sim u'$; the velocity of the largest eddies of the carrier phase (see 2.3.1). Hence, if the largest scales play a non-negligible role, the impact of turbulent cascading process, and potential deviations from Kolmogorov K41 predictions [35] on the settling velocity should be considered. For instance, Mazellier and Vassilicos [37], and Goto and Vassilicos [115] have argued that normalized dissipation rate C_ε depends on the largest scales of the flow, i.e., different turbulent generators (or DNS forcing schemes) could have different values of C_ε.

This work contribution

In this regard, we have conducted experiments injecting inertial particles (see [116], and **chapter** 7) under two different turbulent cascade conditions $C_\varepsilon \neq constant = f(\mathrm{Re}_\lambda^{-1})$, and $C_\varepsilon = constant$. We have also briefly explored whether the particles presence could change the nature of the carrier phase turbulent cascade (see [105], and **chapter 6**). These preliminary results suggest that the liquid fraction ϕ_v (via 'two-way' coupling) may potentially affect the carrier phase cascade.

2.3.2.2 Multi scale preferential sweeping

By using a similar methodology and assumptions as for the path-history effect to explain preferential concentration [12] (see section 2.2.2.3), Tom and Bragg [22] have recently proposed a theoretical mechanism to explain the enhancement of the particle settling velocity in homogeneous turbulence, and as an extension of the mechanism devised by Maxey [80]. Given its potential ramifications were it found to be correct, we briefly recount the mechanism main theoretical steps, and most important consequences.

1. They define an averaging decomposition $\langle\cdot\rangle_{\mathbf{x},\mathbf{u}}^{\mathbf{x}_0,\mathbf{V}_0}$, for all realizations of $\mathbf{u}$ (the carrier phase velocity field), and all particles initial positions and initial velocities $(\mathbf{x_0},\mathbf{V}_0)$.
2. They define an evolution equation for the quantity $\Phi = \langle\delta(\mathbf{x}_p-\mathbf{x})\rangle_{\mathbf{u}}^{\mathbf{x}_0,\mathbf{V}_0}$.

$$\frac{\partial\Phi}{\partial t}+\nabla\cdot\left(\Phi\langle\mathbf{V}_p\rangle_{\mathbf{x},\mathbf{u}}^{\mathbf{x}_0,\mathbf{V}_0}(\mathbf{x},t)\right)=0. \tag{2.9}$$

3. They assume a initially uniform solution, and look for a solution of equation 2.9, and averaging for all relations of $\mathbf{u}$ yields

$$\langle u_z(\mathbf{x}_p,t)\rangle = \Big\langle u_z(\mathbf{x}_p,t)\exp\Big(-\int_0^t\nabla\cdot\left(\mathbf{V}_A(\chi(\mathbf{s}|\mathbf{x},t)ds\right)\Big\rangle^{\mathbf{u}} \tag{2.10}$$

   where $\mathbf{V}_A = \langle\mathbf{V}_p\rangle_{\mathbf{x},\mathbf{u}}^{\mathbf{x}_0,\mathbf{V}_0}$, and noting that the operator ∇ acts on the spatial coordinates of the field $\mathbf{V}_A$.

4. They introduce a coarse graining decomposition $A=\widetilde{A}+A'$ with $\widetilde{()}$ being the coarse grained fields at a scale $\ell(\mathrm{St})$, which depends on the Stokes number, and $()'$ the subgrid field component. Inserting the decomposition into equation 2.10, and with the further assumptions: K41 scalings, the separation of turbulence length scales decorrelates the divergence of particle velocity field $\mathbf{V}_a$ with the fluid velocity, and that only the length scales below $\ell<\ell_c(St)$ do affect the particles (and contribute to their enhanced settling), they obtain:

$$\langle u_z(\mathbf{x}_p,t)\rangle \approx \Big\langle u_z'(\mathbf{x}_p,t)\exp\Big(-\int_0^t\nabla\cdot\left(\mathbf{V}_A'(\chi(\mathbf{s}|\mathbf{x},t)ds\right)\Big\rangle^{\mathbf{u}}. \tag{2.11}$$

5. They relate this previous result to the ensemble averaged equation 2.8 in the z-direction $\langle d\mathbf{V}_p/dt\rangle = 0$;

$$\langle V_p|_z\rangle = \tau_p g+\langle u_z\rangle \approx \tau_p g+\underbrace{\Big\langle u_z'(\mathbf{x}_p,t)\exp\Big(-\int_0^t\nabla\cdot\left(\mathbf{V}_A'(\chi(\mathbf{s}|\mathbf{x},t)ds\right)\Big\rangle^{\mathbf{u}}}_{\text{SGF}}. \tag{2.12}$$

   The SGF (subgrid field) term contains only certain scales (due to the coarse-graining procedure conducted), and therefore, it suggests that the particle settling is not influenced by the entire range of scales present in the turbulent flow.

Then, they claim that given these theoretical analyses, it is questionable that only one length scale of turbulence dominates particle settling (e.g. $\Delta V \sim u'$), as previously reported [6, 10, 17, 21, 81, 107, 112]. They give credence to their claims by surveying DNS datasets , and among their many implications, they found that *the turbulence scales that dominate settling enhancement depend on St, with the main contribution coming from the scales* $\ell < \ell_c(\mathrm{St})$, *where* $\ell_c(\mathrm{St})$ *presents the length scale threshold beyond which particle's inertia effects are negligible.* And therefore, the range of scales that contribute to $\langle V_p|_z\rangle$ should monotonically increase with the Stokes number, and saturate when the integral length scale $\mathcal{L} > \ell(St)$ (see figure 2.7). They did not find such saturation in their study, and argued that it was due to their value of $Re_\lambda \approx 400$.

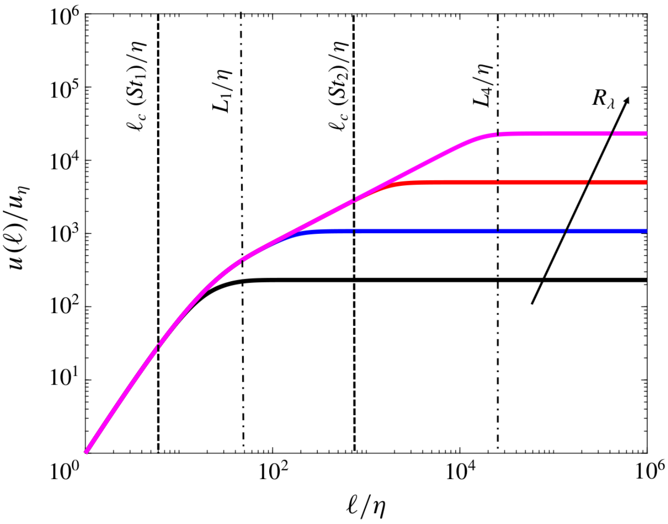

Figure 2.7 – ℓ_c dependence influencing the scales contributing to $\langle V_p|_z\rangle$ $Re_\lambda = [29, 133, 615, 2854]$. Image taken from [22].

In fact, and based on these observations, they advance that the current magnitudes (*not very large*) of Re_λ achievable in either experimental facilities, or numerical simulation computers might have lead to this presumably 'wrong' scaling (i.e. $\Delta V \not\sim u'$), which is in turn very sensitive on $(\mathrm{Re}_\lambda)^{1/2}$.

2.3.3 Settling reduction

Some experimental studies [2, 107, 108, 113, 117] have shown that the particle settling speed can be diminished (i.e., $V/V_T < 1$ or $\Delta V < 0$). This phenomenon is also known as loitering or hindering. These experiments report that the diminished settling is stronger for particles with $Ro = Sv_\ell = V_T/u' \gtrsim O(1)$ [10, 108].

The only available mechanism to explain this reduced settling rate is due to Nielsen [108], who based on the cellular flow results of Maxey and Corrsin [118], and the *fast-tracking* mechanism proposed by Maxey [80], argues that rapidly falling particles spend more time on the upwards regions of the flows: given these heavy particles cannot be trapped by eddies there should follow vortical structures (see figure

2.8). Under this picture, this increased drag grows due to the larger relative velocity between the particle and the fluid velocity field $\mathbf{w} = \mathbf{u} - \mathbf{V}_p$, and therefore, one should pose the question if the Stokes drag by itself is enough to capture the phenomenon.

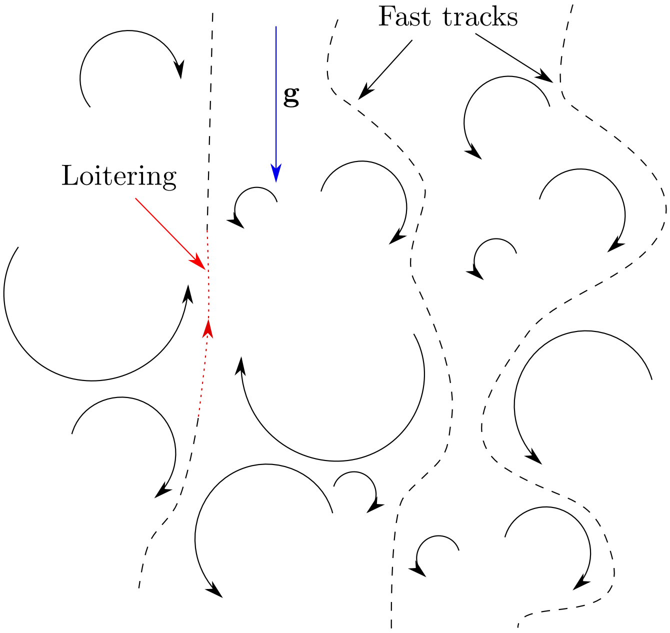

Figure 2.8 – Loitering illustration, adapted from [108].

Interestingly, in DNS simulations this 'loitering' effect is particularly elusive [10, 11, 16, 21]; Good et al.[10] recovered settling velocity reduction in numerical simulations where the confined to move vertically only, or when non-linear drag was included. Furthermore, they argued that in DNS simulations including these non-linearities was a *necessary and sufficient* step to recover particle settling reduction. On the contrary, Rosa et al.[21] did not recover such reduction when the non-linear drag was included, but did found reductions on settling when the particles lateral movements where artificially suppressed.

This work contribution

In this work, our experiment (see chapter 9) in a wind tunnel facility for moderate values of $\mathrm{Re}_\lambda \gtrsim O(200)$, provides evidence of the existence of hindering, and suggest that the crossover threshold (the Rouse number at which particle velocity is modulated) seems to depend on the average velocity of the whole (polydisperse) droplet population $\langle V \rangle|_{all} = \int V(D_p) f(D_p) dD_p$, where $f(D_p)$ is the droplets size PDF, and on a parameter $C < 1$, i.e.,

$$\frac{\langle V \rangle^c|_{all}}{u'(1-C)} \approx Ro_C. \tag{2.13}$$

The equation 2.13 applied to our data is consistent with the Ro_C values reported by Kawanisi and Shiozaki [113] Good et al. [10], and Sumbekova [2].

2.4 Preferential concentration and particle settling

Given that Maxey's [80] preferential sweeping mechanism interpretation (see section 2.3.2.1) is based on the view that inertial particles are centrifuged from eddies (see section 2.2.2.1), it is reasonable to assume that both observations are strongly coupled: preferential concentrations leads to local accumulation of particles which perturb their surrounding turbulent flow.

Experiments and numerical simulations [6, 13, 14, 17, 112] have retrieved that when conditioned on their local concentration $\mathcal{C}/\mathcal{C}_0$ (where $\mathcal{C}_0$ is the average global concentration) particles on the more dense regions fall faster than those on less dense ones, i.e., $\langle V_z|\mathcal{C}_2/\mathcal{C}_0\rangle > \langle V_z|\mathcal{C}_1/\mathcal{C}_0\rangle$ if $\mathcal{C}_2 > \mathcal{C}_1$.

Despite being these results consistent with the preferential sweeping mechanism, Tom and Bragg [22] (see section 2.3.2.2) have recently argued that *the validity of preferential sweeping cannot be (in general) tested by conditioning particle settling velocity on the particle local concentration, as it is preferential concentration, and not clustering (degree of local concentration) that is connected with preferential sweeping, and the respective particle settling speeds. They further argue that driver of the preferential sweeping mechanism is not the strength of the clustering, but the degree of correlation between particles locations and the flow characteristics (c.f. equation 2.12).* Finally, they advance that such conditioned tests are appropriate only when $\mathrm{St}_\eta \ll 1$, challenging the recent of studies Rosa and Pozorski [112], and of Petersen et al.[17].

In the literature both clustering and preferential concentration have been used interchangeably (as we will do in the remaining sections of this work), however, the subtle observation of Tom and Bragg seems to be reasonble taking into account that settling inertial particles could strongly cluster in the dissipation range $\ell < 10\eta$, in spite of having a spatial distribution uncorrelated with flow scales on that range [22, 100]. On the contrary, one could also argue one has to take into account the back reaction from particles in very dense regions (*collective effects*), as they will necessary perturb the hydrodynamic carrier phase inducing correlations between the particles position and the carrier phase evolution.

2.4.1 Collective effects

As mentioned in the previous section, the existence of preferential concentration leads to regions with higher local concentrations $\mathcal{C} = O(10\mathcal{C}_0)$ than the average global one [14]. In these very dense regions, it is expected that 'two-way' (or even 'four way') [5] coupling effects become very strong affecting the carrier phase local velocity field and its turbulent characteristics [5], and thereby, the particles settling rate. It is yet to be dispelled under which circumstances these *collective effects* become important.

Aliseda et al. [6] reported that the $\langle V_z|\mathcal{C} - V_T\rangle/u' \sim \mathcal{C}/\mathcal{C}_0$, and $\mathcal{C}/\mathcal{C}_0 \in [1-5]$; particles settling velocities increases linearly with local concentration. Petersen et al.[17] have also retrieved a monotonic increase of $\langle V_z|\mathcal{C} - V_T\rangle/u'$ with concentration.

Likewise, Huck et al. [14] recovered that the relative enhancement between the particles conditioned on concentration and its unconditioned average; $\Delta V|_{\mathcal{C}}/u' = (\langle V_z|\mathcal{C}\rangle - \langle V\rangle)/u'$ grows with $\mathcal{C}/\mathcal{C}_0$. Interestingly, the experiment of Huck et al. [14] (conducted in a wind tunnel facility and with measuring stations in the streamwise direction) suggests that energy dissipation (ε) rate could modify the magnitude of the settling rate in a non-monotonic manner. For instance, for particles in dilute regions with $\mathcal{C}/\mathcal{C}_0 \ll 1$ a larger value of ε meant a larger value of $\Delta V|_{\mathcal{C}}/u'$. On the contrary, for particles with $\mathcal{C}/\mathcal{C}_0 \gg 1$, a larger value of ε meant a smaller value of $\Delta V|_{\mathcal{C}}/u'$. By means of numerical simulations, where turbulence was forced and the value of ε was fixed, Rosa and Pozorski [112] found an opposite trend: the larger the Stokes number $\mathrm{St}_\eta = \tau_p/\tau_\eta = \tau_p\sqrt{\varepsilon/\nu}$ the smaller the enhancement with concentration.

Aside the reported difference between the characteristics of forced (DNS) and decaying turbulence (wind tunnel experiments) [35], some research has revealed that turbulence modulation by particles may be quantitative and qualitative different under both scenarios, and radically dissimilar when $\mathrm{St}_\eta < 1$ [20]. Taking into account these considerations and the scarce available data, the mechanical coupling between phases and its implications on the seen collective effects is yet to be understood.

2.5 Finite size effects

Although this work did not explore the physics involved when finite size particles $D_p > \eta$ are injected into a turbulent flow, for completeness we briefly comment the main observations found in the available literature.

Taking into account the finite size of the particles, the assumptions leading to the Maxey-Riley equation [78] do no longer hold. For instance, the expansion of the velocity field at the particle center yields

$$\mathbf{u}(x,t) = \mathbf{u}_0(x_p,t) + (\mathbf{x}-\mathbf{x}_p)\cdot\nabla\mathbf{u}_0|_{(\mathbf{x}_p,t)} + \cdots , \tag{2.14}$$

and therefore, it cannot longer be assumed that the perturbation of the velocity field at the particle position remains negligible, i.e., $\mathbf{u}(x,t) \approx \mathbf{u}_0(x_p,t)$ is no longer a reasonable approximation [1]. Thus, one has to consider in theoretical or numerical models a ‘fully’ resolved approach, e.g., the well-known work of Uhlmann [119].

2.5.1 Preferential concentration

The numerical studies of Uhlmann and Chouippe [26, 102] report that for particles with $D_p/\eta = O(10)$, and slightly more dense than the surrounding fluid ($rho_p/rho_f \approx 1.5$), there is evidence of preferential concentration (quantified by 3D Voronoï] tessellations), under HIT conditions for $Re_\lambda = O(100)$, and solid volume fraction $\phi_S = 0.005$. They also report that the relative strength of clustering reduces with increasing D_p, as one could naively expect from the principles of atomic packing: the larger the particles to closer they get to a BCC crystal cell.

The latter is consistent with the experimental work of Fiabane et al. [120] who found that at increasing Re_λ , which lead to smaller η and larger St_η, the strength of clustering decreased with increasing

St_η. In fact,the study Fiabane et al suggest that for finite size particles the Stokes number could not an adequate parameter to characterize clustering, e.g., whereas for small particles clustering occurs at $\mathrm{St}_\eta = O(1)$, it is not the case for finite size particles.

2.5.2 Settling velocity modification

Numerical simulations for slightly denser particles ($\rho_p/\rho_f \approx 1.02$) than the carrier fluid from Fornari et al. [121, 122] report that the 'hindering' effects (reduction of the particle settling velocity with respect to its quiescent value) become stronger with increasing volume fraction in the range $\phi_S \in [0.5 - 10]\%$; $\langle V_z \rangle / V_T \in [0.95 - 0.65]$.On the other hand, Uhlmann and Chouippe reported minute changes (of the order of 1%) on the particle settling velocity for particles with $D_p/\eta = O(10)$, and immersed in HIT conditions where $Re_\lambda = O(100)$.

Both studies suggest therefore that the particle-carrier phase coupling has profound implications on the settling velocity of the particles, and once the particle diameters are larger than η, a reduction in the settling velocity should be expected.

2.6 Graphical outline

A graphical outline is provided below aiming to illustrate the relationships and links between the chapters (articles published or to be submitted) (see section 1.4), and the contributions to the literature, which was review in this chapter.

Clarification: For the sake of continuity, we did not review the methods available to quantify preferential concentration (e.g. radial distribution function, box counting, Voronoï tessellations [75]). Nevertheless, during this work we also examined the influence of the Voronoï tessellations on our measurements. As it will become more clear in the next chapters (see chapters 3- 5), the Voronoï tessellation diagrams [96] play a non-negligible role on the conclusions drawn from unidimensional records. The inclusion of materials and methods in the figure 2.9 reflects this aim.

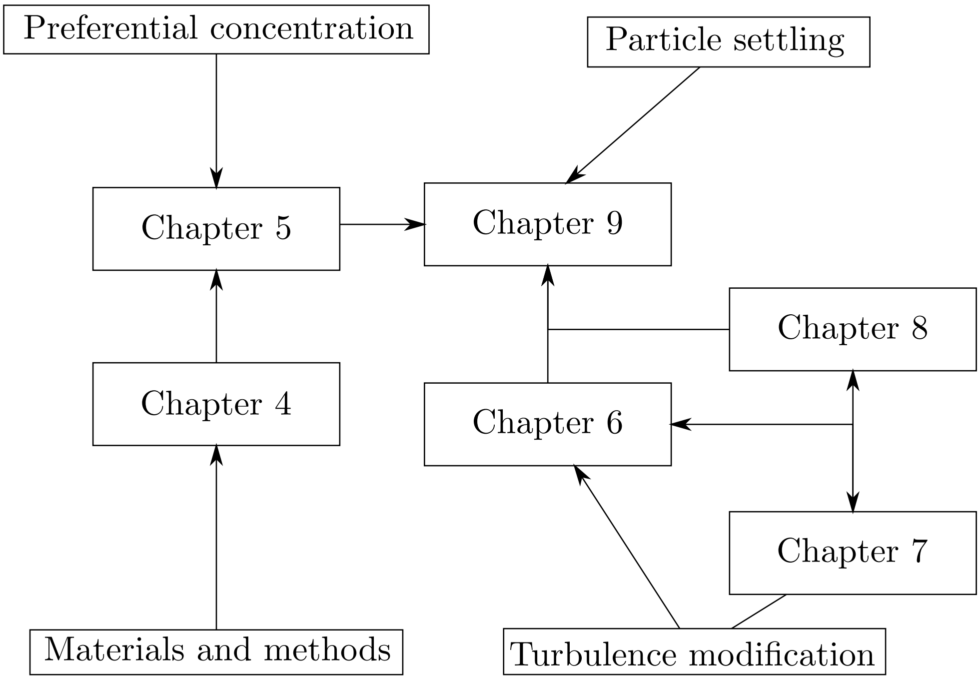

Figure 2.9 – Flowchart of the different articles and its links. See section 1.4

Chapter 3

Materials and Methods

In this work, we conducted two experimental campaigns (in LEGI, and in the University of Washington). We also used previously published data aiming at dispelling the questions posed in section 1.3. In this chapter, we will describe the experimental setups for the experiments conducted, and we will also introduce the tools used to analyze the data gathered. We will provide enough detail so that there results here presented could be reproducible. Some of these details will also be found in the remaining 'article' chapters.

3.1 Experimental setup - LEGI

The first experimental campaign was run in LEGI (*Laboratoire des Écoulements Géophysiques et Industriels*) at the Université Grenoble Alpes . We used the closed-circuit wind tunnel facility '*Lespinard* originally built in the 1950s. This facility has been used extensively, and updated in the last two decades to conduct experiments where turbulence has conditions close to homogeneous and isotropic state, and more recently it has been adapted (transparent walls and a rack of 36 water injectors were installed) to study inertial particles [2, 8, 116, 123, 124].

This low turbulence wind tunnel has a cross section of 75x75cm^2, and mean streamwise inlet velocity can be varied over wide range of values: $U_\infty \in [2-50]$ ms^{-1}. A rack of 36 injectors fed by a water pump injected water droplets in the streamwise direction, and at a variable flow rate; $Q_w \in [0.5-4]$ liters per minute. Measurements were taken 3 m downstream the grid, where turbulence has been found to be under conditions close to a homogeneous isotropic state when passive grids, or active grids (see sections 2.1.2 and 2.1.4) where employed [8, 123], and under dilute conditions $\phi_v = O(10^{-5})$.

Although the exact details of each experiment can be found in the respective chapters, a simplified sketch of its setup can be found in figure 3.1.

3.2 Experimental setup - University of Washington

The second experimental campaign was run in Multiphase and Cardiovascular Flow Lab of the Mechanical Engineering Department at the University of Washington (UW). The facility in its current form

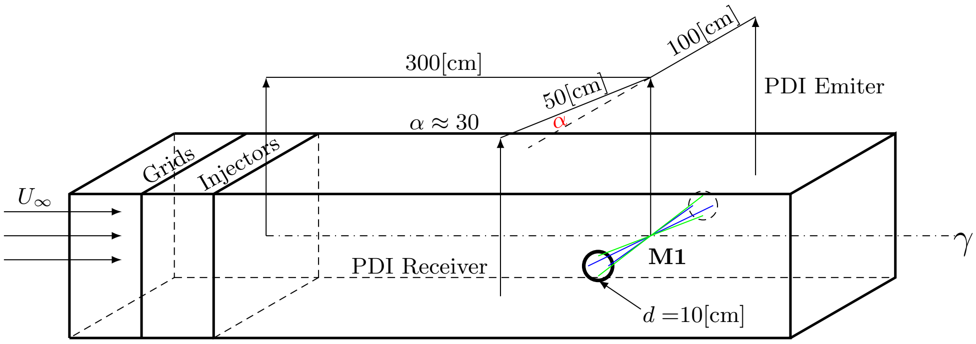

Figure 3.1 – Sketch of the experimental setup in LEGI (see chapter 9). $\mathbf{M}_1$ is the measuring station. Holes of 10cm where put on the wind walls to avoid water deposition issues with the PDI measurements.

was designed and characterised by Bateson and Aliseda [62, 66] in the early 2010s, and later used by Huck et al. [14] in 2016 to conduct experiments with inertial particles.

The facility uses a jet grid (see figure 3.2 and section 2.1.3.1 and has a cross section of $1\text{x}1\text{m}^2$. The average velocity is $U_\infty \approx 2\ \text{ms}^{-1}$, and 81 injectors insert turbulent fluctuations and water droplets. The bulk air is driven by PC fans.To collect the water deposition, when water droplets were injected, a structure called the ‘rain catcher' was placed at the end of the wind tunnel section

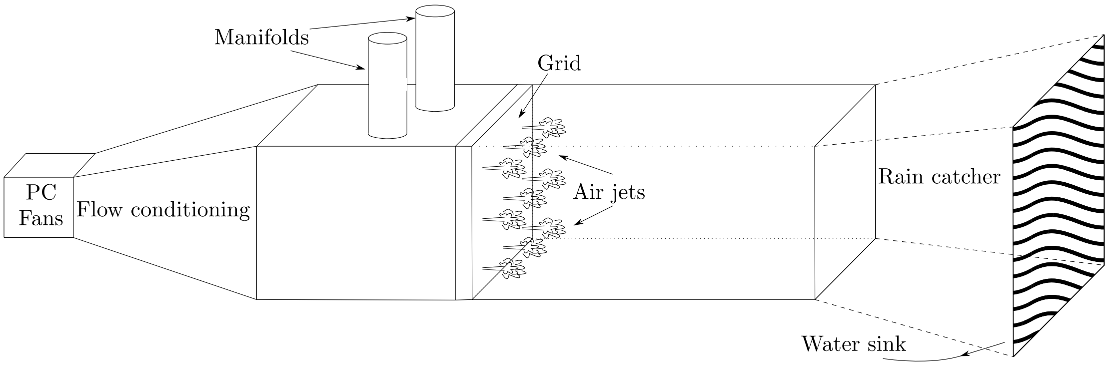

Figure 3.2 – Sketch of the experimental setup in Aliseda's lab.

A programmed relocation of the Aliseda's in Spring 2019 (before the start of the author research stay at UW) required the wind tunnel to be disassembled and moved into a new building. In this new location, the *in-situ* conditions, e.g., the available air flux to run the droplet injectors along with the space available to place the wind tunnel components entailed some modifications of the original design of Bateson and Aliseda [66]. These characterizations and reparations are described in the **chapter 10**.

3.3 Existing data used in this study

For the purposes of this work, we used existing imaging data taken previously at LEGI [125]. This data was taken by means of a high speed camera, which recorded 4500 images of the light scattered by the droplets from a 1-mm thick laser plane. These images had an area of (120×100 mm^2) and it was ensured that the images post processed were uncorrelated (statistical independent realizations) in order to compute meaningful statistics. The images were then subsequently post-processed to identify the location of the droplet centers.

Likewise, we examined 30 numerical snapshots from a DNS (Direct numerical simulation) data base [126] (`https://turbase.cineca.it/init/routes/#/logging/view_dataset/3/tabmet`). These snapshots contained inertial point particles with a Stokes number close to unity; $\mathrm{St}_\eta = \tau_p/\tau_\eta \approx 1$ where $\tau_p = \rho_p D_p^2/18\mu$ is the particle relaxation time, $\tau_\eta = \sqrt{\nu/\varepsilon}$ is the Kolmogorov timescale, D_p is the particle diameter, ε the turbulent dissipation rate, μ the dynamic viscosity of the carrier phase, and ρ_f, and ρ_p are the carrier and particle density, respectively.

As our interest was heavy inertial particles (i.e. $\rho_f \ll \rho_p$), we used the files labeled as: `RM-2008-LIGHT-512.St6.XX.h5` with the following parameters $\tau_p = 0.048282$, and $\chi = 3\rho_f/(\rho_f+2\rho_p) = 0$. Each snapshot contained the trajectories of 1280 point particles positions integrated over 3300 time steps. More details of this numerical setup ($\mathrm{Re}_\lambda \approx 185$) can be found in [127, 128].

3.4 Measuring instruments

3.4.1 Hot-wire anemometer

The hot-wire anemometry has been extensively used in experimental studies of turbulence, and that for most studies involving wind tunnels it can be considered as a very mature measurement technique, for an extended review see [129].

Its underlying principle is the forced convective heat transfer: A thin wire (with resistance R_w) is immersed in a fluid. The wire temperature is held constant (for constant temperature anemometry), and slightly larger than the surrounding flow so that as fluid passes through the wire, heat transfer will occur.

To compensate for the loss of heat (and cooling) a close loop control will adjust the current passing to the wire. The cooling (and therefore the power supplied to maintain the temperature constant), becomes a function of the convective velocity. This circuit is usually couple with a Wheatstone bridge so that the voltage at the bridge E_B is proportional to the current, and thereby to the velocity $U_\perp$(perpendicular to the cross section of the wire). Although a close solution is not directly available, King suggested a semi-empirical correlation:

$$E_B^2(T_{lab}) = f(T_{lab}) = A + BU_\perp^n, \tag{3.1}$$

where A, and B are parameters that depend on the air temperature inside the wind tunnel (T_{lab}), and the wire parameters. For turbulent flows it is common that $n \approx 0.45$, but one usually fits a curve to obtain A, B, and n. Taking into account that this temperature could change from realization to realization, one should monitor T_{lab}, and recalibrate (redo the fits) accordingly, for instance, if the temperature increases by more than two degrees Celsius.

For the two experimental campaigns, two distinct hot-wire models, were used and their details are summarized in table 3.1.

Lab	Console model	Hot-wire model	Hot-wire diameter [μm]
UW	AA CCA	Single hot wire	10
LEGI	Dantec CCT	Single normal hot wire	50

Table 3.1 – Hot-wire parameters.

3.4.2 Optical probes

Among several optical probes, monofiber optical probes have been proven useful to detect water droplets in air [130]. These probes have been developed from similar ones used to detect air bubbles in water that occur in industrial flows, such as bubble columns (see [131]). Their underlying principle is the difference in refraction between the liquid and gas phases, which can be modelled as a phase indicator function where a step decrease in voltage correlates with the presence of liquid (water droplets) (see figure 3.3).

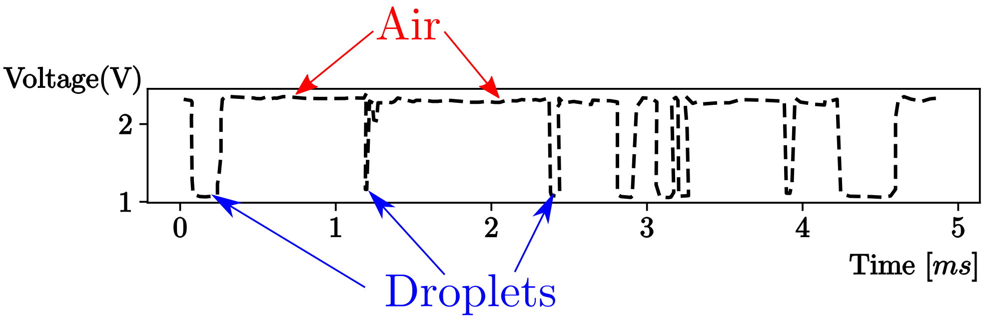

Figure 3.3 – Typical signal output of an optical probe used to detect water droplets [130].

This work contribution

Despite reporting value of droplets velocity, and liquid concentration in agreement with previous experiments, we discovered that the size of the probe (well below the Kolmogorov length scale) hinders its ability to detect preferential concentration. Under similar conditions for which clustering has been reported using 2D Voronoï tessellations, these optical probes retrieved $\sigma_{\mathcal{V}}/\sigma_{RPP} \approx 1$ (**see chapter** 4).

3.4.3 Phase doppler interferometry device

A phase Doppler interferometry device (PDI/PDPA) can measure simultaneously the settling velocity and the diameter of the particles [132, 133]. Being an eulerian measurement, it can be interpreted as a single particle counter, as one particle passing through the measuring volume at the time could be accurately, and unambiguously measured.

The fringe pattern, created at the measuring volume (where the two laser beams intersect) can be characterized by the space between fringes δ_L, which depends on the beam intersection angle γ_L, and the wave length of the laser λ_L [132];

$$\delta_L = \frac{\lambda_L}{2\sin(\gamma_L/2)}. \tag{3.2}$$

Thus, the time scale of the Doppler burst (the Doppler frequency f_D) by a particle passing through these fringes at a velocity $\mathbf{V}_p$ can be therefore related to the equation 3.2 yielding:

$$\mathbf{V}_p = \delta \mathrm{f}_D, \tag{3.3}$$

which is the basis of many laser Doppler velocimetry systems (LDV). Those systems usually use neutrally buoyant particle tracer $\mathrm{St}_\eta \approx 0$ at low concentrations. Bachalo and collaborators (see [132] and references therein) devised a system able to handle dense sprays, and allowing to measure simultaneously spherical particle speeds, and their respective diameters (D_p).

They achieved this latter aspect by measuring the phase shift between two photo detectors ϕ_{1-2} separated by a fixed distance giving the relationship:

$$\phi_{1-2} \propto \pi D_p \delta_L^{-1}. \tag{3.4}$$

For the LEGI experiment, we used commercially available phase Doppler interferometry systems that worked under these mentioned principles. The details of the specific commercial model employed, as well as the respective parameters used during our measurements during the experimental campaigns are described in tables 3.2 and 3.3. In addition, and taking into account that we measured water droplets, our PDI experimental arrangement was adapted to forward scattering, which implied a 30° angle in the plane composed of the receiver and the transmitter.

Lab	Model	Trans. / Rec. focal length [mm]	Aperture	β	δ_x/δ_y [μm]
LEGI	Artium 200 MD	1000 / 500	50	1.5°	8.9 / 8.2

Table 3.2 – Phase doppler interferometry parameters #1. *Trans.* stands for the transmitter (device emitting the laser), and *Rec.* stands for the receiver (device capturing the refraction). β is the deviation angle from the experimental setup.

Lab	Gain X/Y [mV]	$f_{sampling}$ -f_{mixer} - f_{filter} [MHz]	Res. $\Delta V_x/V_y$ [mms^{-1}]	SNR
LEGI	400±50 / 750±50	10-42.25-5/5-38.25-2.5	40/10	$\in [0.6 - 0.7]$

Table 3.3 – Phase doppler interferometry parameters #2. Gain-X/Y are the respective values needed to detect small droplets while avoiding to saturate the receiver. *Res.* stands for the resolution .

3.4.3.1 Vertical velocity finite angular position

In our experimental setup is of the foremost importance to consider the laser alignment errors (between a virtual coordinate system place in the laboratory frame of reference) introduced in the vertical velocity measurements of the phase doppler interferometry device (PDI). These alignment errors arise from the finite angular adjustment that could be attained in the different experimental rigs.

The angular errors (see figure 3.4)introduced are not negligible given that the streamwise (horizontal) velocity (V_x)is usually two orders of magnitude larger than the vertical one (V_y), i.e., $V_x/V_y = O(10^2)$. Then, even at small deviation angles (see table 3.2 β) the projected velocity $V_\beta = \overline{U}\sin\beta \approx \overline{U}\beta$ could significantly contaminate the actual value of the particle settling velocity (e.g. $\beta = 1^\circ \approx 0.02\,\mathrm{rad}$, then for $\overline{U} = O(1)$, $V_\beta = O(10^2)$ is within the same order of V_y).

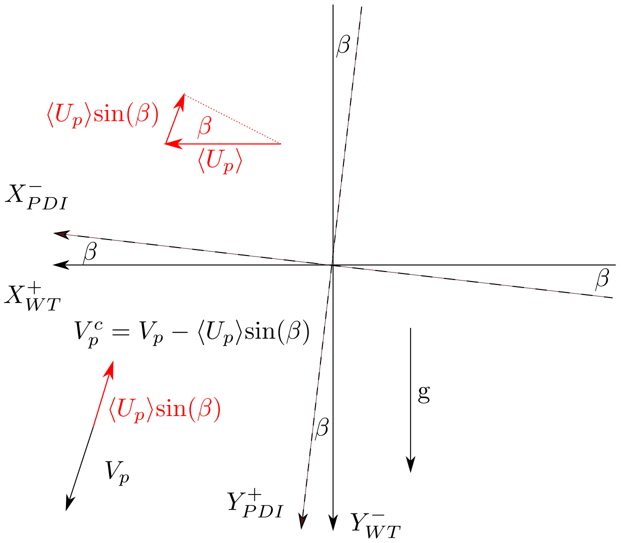

Figure 3.4 – Angle deviation illustration. The device frame of reference (PDI) is due to finite error tilted an angle β respect to the wind tunnel frame of reference (WT). For illustration purposes, the angle β shown is much larger than the actual angles found in the experiments.

Aliseda et al. [6] argued that the error introduced by V_β is the same for all particles under fixed experimental conditions given that the correction falls below the velocity fluctuation $V_\beta < u'$.

Hence, β in the PDI frame of reference could be computed from particles in the tracer limit Stokes (i.e., $\mathrm{St}_\eta \to 0$) by $\beta = \mathrm{atan}(\langle V_y \rangle / \langle V_x \rangle\big|_{PDI}$ (see figure 3.4). Although Sumbekova [2] used their smallest droplets available to compute β,in LEGI we opted instead to generate small olive oil droplets $D_p \approx 10\mu m$ under a almost laminar flow. These tests yielded $\beta = 1.5 \pm 0.3$.

3.5 Methods to quantify preferential concentration

3.5.1 Voronoï tessellations

The interest when measure preferential concentration relies on relate the carrier phase 'unladen' parameters (e.g. Re_λ , $\varepsilon, \mathcal{L}$), or the global concentration ϕ_v with the parameters, such as, the cluster size, or clustering strength.

Among the available methods (see [75] for an extended review) to quantify preferential concentration, Monchaux et al.[75] suggested that Voronoï diagrams have the upper hand with respect to other available tools to quantify clustering, and supported the latter conclusion via analyses on 2D imaging data. Voronoi diagrams *are a particular case of space tessellation where, given a set of centers, the space is divided according to their 'spheres of influence'*[96]. Monchaux et al.[8] used these diagrams on particles centers postprocessed from 2D imaging techniques. Their analyses show that PDF of areas could approximately follow a log-normal distribution, and therefore, these PDFs could be quantified by the standard deviation of the area size $\sigma_{\mathcal{V}}$, which is a measure of the voids (large gaps between particles) [23]. Furthermore, Monchaux et al. [8] proposed that clustering is present when $\sigma_{\mathcal{V}}/\sigma_{RPP} > 1$, where σ_{RPP} is the resulting standard deviation from applying the tessellation to a random Poisson distribution [96], and the degree of clustering is giving by this ratio; the larger the ratio of $\sigma_{\mathcal{V}}/\sigma_{RPP}$, the larger the degree of clustering. They also reported that the clusters PDF exhibit an algebraic exponent on its right tail, which has been retrieved by several studies [13, 23, 134], and found to be close to '-5/3' in agreement with the predictions of Goto and Vassilicos [93].

Although these diagrams, and criteria have been widely used [13, 17, 23, 26, 102, 134] in numerical and experimental realizations, their potential biases have been scarcely investigated. For instance, Uhlmann and collaborators [102, 135] have consistently reported that the clusters PDF applied on records coming from turbulence, and those coming from a 3D random poisson process exhibit similar shapes, and even may collapse. On the other hand, via '1-way' coupling simulations Coletti and collaborators [13, 17] have proposed to use only the clusters that exhibit a self-similar structure.

This work contribution

In this work, we have explored the origin of the powerlaw seen in the PDF of clusters (**see chapter** 5), which can be tracked to the probability of clusters of size *n*, and decays in a power law fashion for turbulence driven flows. Also, we retrieved that in 1D, the criteria of Monchaux et al.[8] may not be conclusive as there could be clustering in the flow, when $\sigma_{\mathcal{V}}/\sigma_{RPP} \approx 1$ (**see chapter** 4).

3.6 Methods to estimate the turbulent kinetic energy dissipation rate ε for unladen single phase flows

In homogeneous isotropic turbulence conditions (HIT), the turbulent kinetic energy dissipation rate goes as $\varepsilon = 15\nu u'^2/\lambda^2$, where λ is the Taylor length scale. In wind experiments using single hot-wires, and invoking the Taylor hypothesis, one could estimate ε (without assuming K41 scalings) via its Fourier representation, i.e., $\varepsilon = 15\nu \int_{k_{min}}^{k_{max}} k_1 F_{11} dk_1$. In addition, to reduce the contamination from electronic noise, one usually fits an exponential at large wave numbers [136]. Alternatively (and once again without assuming K41 scalings), one could use the Rice theorem, as first noted by Liepmann's [137] to compute λ, and then use $\varepsilon = 15\nu u'^2/\lambda^2$ to estimate the dissipation rate. A common procedure to estimate λ (see figure 3.5) is as follows [37, 38, 109]:

1. Take the acquired fluctuating velocity signal, and low pass filter it (with a high order filter, e.g. a fifth order butterworth filter) at different sizes $\eta_C = 2\pi/\kappa$, where κ is the wave number. Considering the use of the Taylor hypothesis, this is equivalent to filter the signal at different *frequencies.*
2. Compute the signal zero crossings, and their number density (n_s =number of zeros/duration of the signal) at at each filter size (resp. *frequency*) (see figure 3.5).
3. If a plateau of n_s is present for filter scales smaller (resp. *larger*) than a certain scale (resp. *frequency*) $\eta_C^\star$ (not to be confused with the Kolmogorov length scale η), the value of n_s is properly resolved. One could then estimate λ via $n_s^{-1}|_\star = \pi C \lambda$, with C being a constant in the order of unity which accounts for the non-gaussianity of the velocity derivative [37].

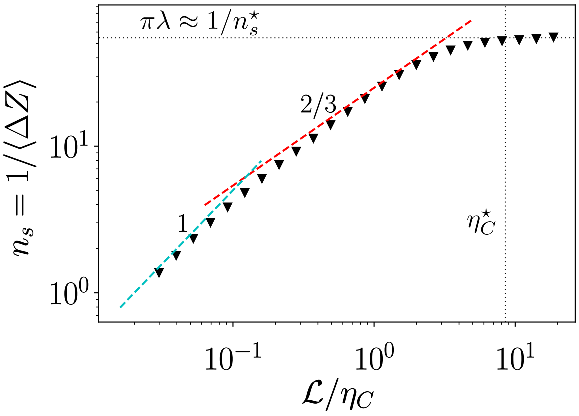

Figure 3.5 – Illustration of the estimation of λ via the zero crossings methods for a turbulent signal.

In this work, and when needed we applied both methods to the datasets recorded via hot wire anemometry.

Chapter 4

Pitfalls Measuring 1D Inertial Particle Clustering

This chapter includes the proceedings article:
Mora, D. O. *et al.* *Pitfalls Measuring 1D Inertial Particle Clustering* in *iTi Conference on Turbulence* (2018), 221–226

4.1 Summary

In this chapter, we examine the influence of 1D Voronoï tessellations analysis on particle datasets recorded by different instruments. Our results show that the *rationale* that Monchaux et al. [8] proposed to analyze particle clustering coming from 2D imaging may not be conclusive when the Voronoï tessellation is applied to 1D records coming from well-known instruments such as phase Doppler interferometers or optical probes.

More precisely, Monchaux et al. [8] propose that clustering is present if the standard deviation of the normalized Voronoï cell size is larger than the respective one coming from a random Poisson distribution (RPP) [96], i.e., $\sigma_{\mathcal{V}}/\sigma_{RPP} > 1$. The latter criterion may not extended to 1D records if the measuring volume is very small. We find that for the experiments conducted the measuring volume has to be of order η^3 (the Kolmogorov length scale) in order to recover evidence of preferential concentration. This lower bound seems to hold despite recovering adequate values of global statistics, for instance, the particles global liquid fraction or velocity distribution.

We also find evidence that concentration may play a role given that projected RPP distributions exhibit similar trends below certain concentration there is not conclusive evidence whether or not randomness is present.

Among the work developed, this thesis author had the idea of emulating the eulerian measurement via projections, he also developed the codes necessary to conduct the analyses.

Pitfalls Measuring 1D Inertial Particle Clustering

Daniel Odens Mora, A. Aliseda, Alain Cartellier and M. Obligado

Abstract We perform 1D Voronoï analysis on a time series from an optical probe detecting the passage of particles in a homogeneous. isotropic turbulent flow. The Voronoï analysis is unable to identify clustering in the particle locations along the measuring "line", despite the flow being almost identical in terms of the Reynolds number based on the Taylor scale (Re_λ), and Stokes (St) numbers to previous experiments in which 2D Voronoï analysis successfully detected and measured this phenomenon [8]. The optical probe accurately measured the particle average global concentration, and size distribution. This result stemmed from the *sub-kolmogorov* measuring volume of the probe, and seems to be in agreement with previously reported studies under totally different conditions [7] that referred to this issue as *sub-poissonian* events. If the instrument measurement window size is 'large' enough -but not too large to smooth out all correlations-, and the data satisfyies statistical convergence, 1D Voronoï diagrams effectively capture evidence of clustering, and constitute a reliable proof of preferential concentration within the flow.

1 Introduction

The study of inertial particles clustering in turbulent flows has received a large amount of attention over the last three decades. This increased interest stems from its potential applications, for instance; aerosol pollutant modelling, and rain droplets formation [8]. Several techniques have been employed to characterize particle-clusters, for example Voronoï tessellations is an increasingly popular tool in either numerical or experimental studies (see [8] and references therein). These 2D/3D Voronoï diagrams have successfully quantified the deviation from randomness (from a Random Poisson Process distribution, RPP) in the inertial particles spatial organization. From

D. O. Mora (✉) · A. Cartellier · M. Obligado
Univ. Grenoble Alpes, CNRS, Grenoble-INP, LEGI, 38000 Grenoble, France
e-mail: daniel.mora@univ-grenoble-alpes.fr

A. Aliseda
Department of Mechanical Engineering, University of Washington,
Seattle, WA 98195-2600, USA

R. Örlü et al. (eds.), *Progress in Turbulence VIII*, Springer Proceedings in Physics 226,
https://doi.org/10.1007/978-3-030-22196-6_35

an experimental point of view, it is interesting to explore whether lower dimensional techniques (1D), such as optical probes [3] are able to recover the clustering signature found in 2D/3D studies. Using these 1D measurements, along a line in space leads towards 1D Voronoï analysis. However, quantifying preferential concentration by means of unidimensional measurements, as described by Shaw [7], might lead to wrong conclusions if caution is not taken, i.e. the absence of evidence of preferential concentration might be due to a faulty method of analysis, or inadequate resolution of measuring instrument. In this context, we explore these biases where the absence of preferential concentration by means of unidimensional Voronoï analysis (1DVOA) could not discard its existence within the flow.

2 Experimental Setup and Methods

The experiment was conducted in a close-circuit wind tunnel at the LEGI-Grenoble laboratory. This wind tunnel has been extensively used to study particle clustering under homogeneous isotropic turbulent conditions [5, 8]. Turbulence is produced by means of an active grid, downstream of which a rack of 36 spray nozzles generate inertial water droplets, see [8]. The grid was operated in two different modes. In the first one, the grid is actuated with time-varying rotation rates and directions, which are chosen randomly (random grid). The second one consists in keeping the grid static and completely open (open grid). The global volume fraction ϕ_v was varied in a range $\in [1 - 5] \times 10^{-5}$ to avoid turbulence modulation by the droplets. The turbulence within the measuring region has been experimentally found to be very close to a statistically isotropic state [5, 8] under the same experimental conditions (Re_λ, and η). The signal to compute 1DVOA was acquired by means of an monofiber optical probe described in [3]. An example of the signal acquisition record is shown in Fig. 1. The probe diameter δ was well below the Kolmogorov lengthscale η ($\delta \ll \eta$). To compute the 2DVOA, a high speed camera collected 4500 images of the light scattered by the water droplets from 1 mm thick laser plan illumination, and these images were subsequently post-processed to identify the location of the centers of the droplets. The average number of droplets per image was 4000, and the illumination was normalized to remove biases, following [8]. All experimental parameters from both experiments are summarized in Table 1.

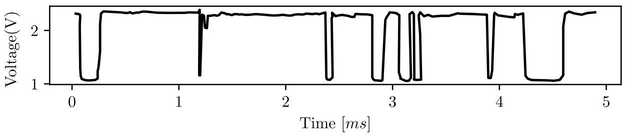

Fig. 1 Probe raw signal example. The signal reaches its maximum amplitude when the probe is surrounded by air, and whenever a droplet interacts with the probe tip, there is a sharp decrease in voltage. For details, see [3]

Table 1 ϕ_v is the volume fraction, $\lambda = \sqrt{15\nu/\varepsilon}u'$ is the Taylor length scale, and $\nu \sim 1.5 \times 10^{-5}$ $[m^2 s^{-1}]$ is the air viscosity, $Re_\lambda = u'\lambda/\nu$, D_p is the value of the most probable diameter which was used to compute the Stokes number $St_\eta = \frac{(D_p/\eta)^2}{36}(1 + 2\rho_p/\rho_f)$, see [8]. ρ_p/ρ_f is the density ratio between the particles, and the carrier phase. ε, and $\mathcal{L}$ is the carrier dissipation, and integral length scale, respectively, and OG/AG stands for open/active grid mode, respectively

Dataset	Grid mode	Re_λ	St_η	$\varepsilon\mathcal{L}^4/\nu^3$	D_p/η	$\mathcal{L}/\eta$	λ/η	ϕ_v	ρ_p/ρ_f
EXP-1D-OG	Open	105	1.4	1.0×10^8	0.125	110	20	1.0×10^{-5}	800
EXP-2D-AG-A	Random	250	0.9	4.3×10^8	0.125	175	35	1.2×10^{-5}	800
EXP-2D-AG-B	Random	250	0.9	4.3×10^8	0.125	175	35	2.3×10^{-5}	800
EXP-2D-AG-C	Random	250	0.9	4.3×10^8	0.125	175	35	4.7×10^{-5}	800

3 Results

Following [1], a unidimensional Voronoï analysis (1DVOA) was performed on the signal extracted from the optical probes. Figure 2 illustrates the diagram construction. Droplets were solely characterized by their arrival time. Considering previous 2D Voronoï analysis (2DVOA) have shown evidence of particle clustering [5, 8], it was rather surprising to find the signature of a Random Poisson Process (RPP) in the distribution of the inter-particle distance from the 1DVOA. This denotes the absence of preferential concentration (see Fig. 3a), despite the probe's accuracy in capturing global variables, such as liquid volume fraction or droplet size distribution. This result appeared to be consistent for the different vertical locations sampled in the measurement region, as well as for different values of injected droplet diameters, turbulence intensities, or the type of probe employed (single or triple cone [3]).

To discard the possibility that the underlying working principle of the probe or an incorrect configuration were responsible for the unexpected result found in Fig. 3a, 2D experimental images (see Table 1) were virtually sampled, aiming to emulate a 1D measurement to check whether the probe size δ had an impact on the 1DVOA outcome. These images were analyzed by 2DVOA, which confirmed the presence of preferential concentration in the droplet spatial distribution in this flow, as shown in Fig. 3b where the PDF shapes deviates from the corresponding RPP. This 'virtual' 1D projecting procedure was conducted as follows (see also Fig. 4a):

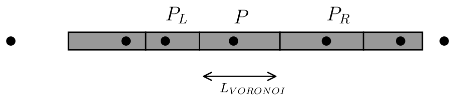

Fig. 2 For a given point **P** with left, and right neighbours points P_L, and P_R respectively, the length of the Voronoï cell is given by $L_{VORONOI} = |P_R - P_L|/2$. The time of the sharp decline in signal (droplet arrival time) illustrated in Fig. 1 was taken as the **P** point shown in this sketch

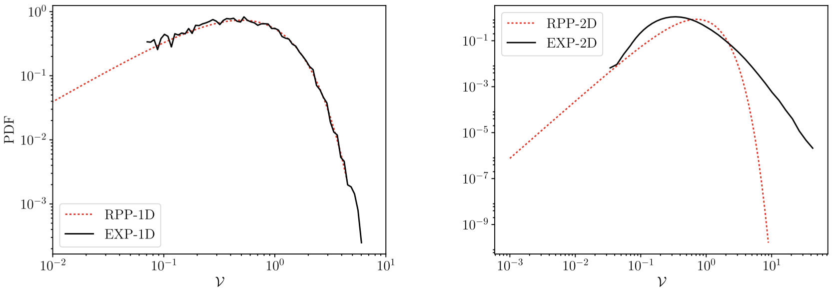

(a) (b)

Fig. 3 **a** PDF of normalized Voronoï lengths by 1DVOA, $\mathcal{V} = L_{Voronoï}/\langle L_{Voronoï}\rangle$, from our experimental data acquired by an optical probe. 2D analyses detected clustering under similar experimental conditions $Re_\lambda \sim 100$, see Fig. 3b. **b** PDF of normalized Voronoï areas by 2DVOA[4], $\mathcal{V} = A_{Voronoï}/\langle A_{Voronoï}\rangle$ for the experimental data (EXP-2D-AG-C) found in Table 1. Here, it is clearly seen that the experimental data PDF follows a different trend than the RPP

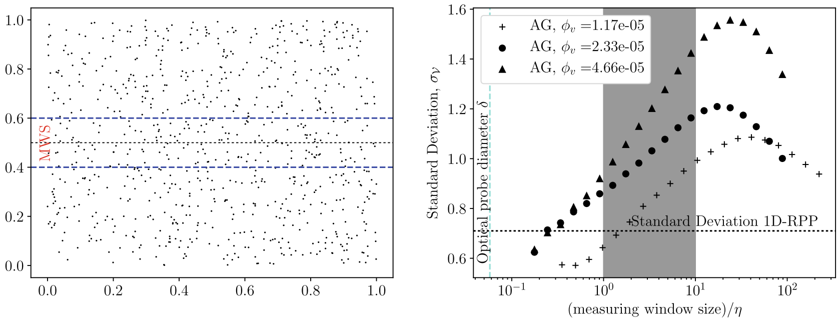

(a) (b)

Fig. 4 **a** Illustration of the procedure taken to uni-dimensionally sample the 2D experimental data $2D \rightarrow 1D$ The measuring window size (MWS) was varied to obtain the Fig. 4b. **b** Standard deviation, $\sigma_{\mathcal{V}}$ against measuring window size for the experimental data found in Table 1. Shaded region denotes the sizes of interest for several '1D' measuring instruments, e.g., PDI [6]

1. A random vertical coordinate was generated, and a measuring window or detection threshold was defined.
2. All the points/droplets *centers* that lay within this measuring strip were projected into a line, i.e., their horizontal coordinates are taken, which is basically invoking the Taylor's frozen flow hypothesis.
3. 1DVOA was performed over the projected points.

Figure 4b illustrates how the standard deviation ($\sigma_{\mathcal{V}}$) of the normalized Voronoï cells, which serves to quantify clustering via 1DVOA or 2DVOA [4, 5], varies with the measuring window size (MWS). The plot exhibits a *non-monotonic* behavior with the MWS, and shows that if it is too narrow, the signature of clustering might be lost. This "decorrelating" effect from the small probe window size is the origin

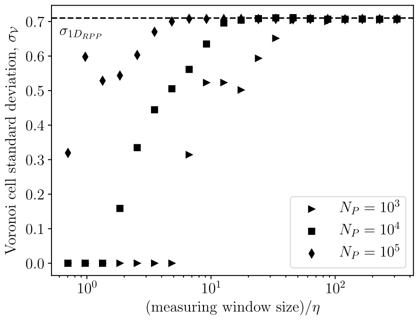

Fig. 5 'Virtual' $(3D \rightarrow 1D)$ 1DVOA standard deviation evolution versus measuring window size from 1D sampling of artificially generated 3D data using a random distribution. N_P stands for the number of points inside the 3D domain

of the false negative result reported here (see Fig. 3a) and, therefore, a signal coming from an optical probe would not be able to capture the preferential concentration that exists in the flow via 1DVOA, i.e., $\sigma_{\mathcal{V}} \sim 0.71$. For completeness, the same algorithm was applied to a "cloud" of 3D points generated by a random distribution (RPP) employing the different number of particles to check the impact of particle concentration. Interestingly, for the random cloud virtual set (see Fig. 5), even with 100 times more snapshots than the actual data, there is an evolution of the inter-particle rms with the concentration as seen in Fig. 4b, that is proportional to the number of events detected and, therefore, increases the convergence of the statistics. This plot confirms the role of convergence and projections, suggesting that *sub-poissonian* events are only a consequence of lack of convergence. More importantly, it shows that a sensitivity analysis of this type for an RPP distribution will not produce evidence of spurious clustering, or $\sigma_{\mathcal{V}} > 0.71$. The impact of volume fraction ϕ_v in $\sigma_{\mathcal{V}}$ follows previous trends found [8].

Similar studies with the radial distribution function (RDF) noticed attenuation in the 1D-RDF at lengths below the characteristic length of the instrument employed, and explained its origin by loss of information [2] due to the projection. This related phenomenon, which has been previously reported under different conditions to the ones here ($St \ll 1$, [7]), had a similar bias at small scales, with *sub-poissonian* events occurring as a result of the instrument resolution and droplets finite size. This supports the hypothesis that the optical probe actually recorded uncorrelated events, explaining the false negative result found. Hence, if the evaluation of preferential concentration by means of 1DVOA is made by comparing the standard deviation of the signal's $\sigma_{\mathcal{V}}$ against the corresponding RPP's σ_{RPP}, a positive result ($\sigma_{\mathcal{V}} > \sigma_{RPP}$) indicates without doubt the presence of clusters within the flow, whereas the opposite is not necessarily true, namely, $\sigma_{\mathcal{V}} \approx \sigma_{RPP}$ does not prove that a lack of clusters. Furthermore, our results from the optical probe and the analysis from Fig. 5 suggest that, rather than a loss of information, *sub-poissonian* events are the consequence of a lack of convergence.

4 Final Remarks

A sensitivity analysis might be required when evidence of preferential concentration by means of 1DVOA is not recovered. Conversely, when clustering is found in the 1DVOA, it is a reliable proof of its existence within the particle-laden flow. However, there are some open interesting questions concerning what is the optimal measuring window size to capture preferential concentration, and what is the impact of this analysis variable on cluster characterization.

Acknowledgements This work has been partially supported by the LabEx Tec21 (Investissements d'Avenir - Grant Agreement # ANR-11-LABX-0030).

References

1. J.S. Ferenc, Z. Néda, On the size distribution of Poisson Voronoi cells. Phys. A: Stat. Mech. Appl. **385**(2), 518–526 (2007)
2. G.L. Holtzer, L.R. Collins, Relationship between the intrinsic radial distribution function for an isotropic field of particles and lower-dimensional measurements. J. Fluid Mech. **459**, 93–102 (2002)
3. M. Hong, A. Cartellier, E.J. Hopfinger, Characterization of phase detection optical probes for the measurement of the dispersed phase parameters in sprays. Int. J. Multiph. Flow **30**(6), 615–648 (2004)
4. R. Monchaux, M. Bourgoin, A. Cartellier, Preferential concentration of heavy particles: a Voronoï analysis. Phys. Fluids **22**(10) (2010)
5. M. Obligado, T. Teitelbaum, A. Cartellier, P. Mininni, M. Bourgoin, Preferential concentration of heavy particles in turbulence. J. Turbul. **15**(5), 293–310 (2014)
6. E.W. Saw, R.A. Shaw, J.P. Salazar, L.R. Collins, Spatial clustering of polydisperse inertial particles in turbulence: II. Comparing simulation with experiment. New J. Phys. **14**(10), 105031 (2012)
7. R.A. Shaw, Particle-turbulence interactions in atmospheric clouds. Ann. Rev. Fluid Mech. **35**(1), 183–227 (2003)
8. S. Sumbekova, A. Cartellier, A. Aliseda, M. Bourgoin, Preferential concentration of inertial sub-Kolmogorov particles: the roles of mass loading of particles, Stokes numbers, and Reynolds numbers. Phys. Rev. Fluids **2**(2), 24302 (2017)

4.2 Work division

The work division was as follows:

Author	CR#1	CR#2	CR#3	CR#4	CR#5	CR#6	Score	Position
D.O. Mora	120	20	80	80	100	120	520	1
M. Obligado	60	10	20	20	50	65	225	2
A. Aliseda	30	35	-	-	30	35	130	3
A. Cartellier	40	35	-	-	20	30	125	4
Total	250	100	100	100	200	250	1000	-

The guidelines reflecting the scores and author ordering can be found in the appendix A. The thesis author (D.O. Mora) was engaged in the writing, revision, and and discussion of the paper (see also appendix B).

Chapter 5

Characterizing 1D Inertial Particle Clustering

This chapter includes the article:
Mora, D. O. *et al.* Characterizing 1D Inertial Particle Clustering, Submitted (2020)

5.1 Summary

This chapter is a continuation of the work presented in chapter 4. We, however, delved into the effects the instrument measuring volume have on the different cluster statistics (e.g. cluster average size, and probability distribution functions) extracted by means of 1D Voronoï analysis. In a similar fashion as in chapter 4, we emulate an eulerian measurement using previous experimental, and now including a numerical database. Our analyses suggest that if evidence of preferential concentration is not found by means of 1D Voronoï analysis in particle laden flows where higher dimensional techniques have found evidence of it, a sensitivity analysis involving varying the instrument measuring volume (MWS) should be carried on.

We show that a reasonable size to start such sensitivity analysis is a linear size of order η (the Kolmogorov length scale). Our results suggest that the ratio of $\sigma_{\mathcal{V}}/\sigma_{RPP}$, which quantifies the degree of clustering, as a function of the instrument measuring volume peaks at a size $\mathrm{MWS}_\star \approx 0.1\mathcal{L}$, where $\mathcal{L}$ is the carrier phase integral length scale. Alternatively, the peak correlation seems to be better correlated with the average cluster linear size $\langle L_C \rangle$, i.e., $\mathrm{MWS}_\star \approx \langle L_C \rangle$, consistent with previous studies [6].

Moreover, we studied the clusters PDF following the algorithm proposed by Monchaux et al. [8] by means of 2D imaging. Our analyses suggest that in 1D the ‘plain’ cluster PDF algorithm may not be able to distinguish between turbulence driven clusters, and spatial random fluctuations. The latter pitfall is not minor nor entirely new [26], but it strongly undermines the capacity of a 1D instrument to accurately characterize this phenomenon; strongly suggesting that in order to draw reliable conclusions about conditioned statics (e.g. particle settling conditioned on local concentration) in turbulent particle laden flows, one should use higher dimensional techniques.

To address these issues, we have modelled the steps taken in the clusters finding algorithm of Monchaux et al. [8] as a PDF mixture model [140]. Our results support that our model is an adequate representation of widely reported[8, 13, 17, 23, 26, 95, 135] power law behavior recovered in the right tail of the clusters sizes PDFs. This new tool allows us to understand the origin of previous observations, and assess amendments [13, 26] proposed to the mentioned cluster algorithm. Further analysis by means of this tool has led to propose a new test to disentangle turbulence driven clusters from those coming from random spatial fluctuations. We provide evidence that the extent of the power law behavior found in the clusters PDF has a turbulent origin that could not matched by random spatial fluctuations.

Among the work developed, this thesis author had the idea of emulating the eulerian measurement via projections, he also developed the codes necessary to conduct the analyses. The mixture PDF model approach use to analyze the clusters PDF was also this thesis author original idea.

Characterizing 1D Inertial Particle Clustering

Daniel Odens Mora, Alain Cartellier, and Martin Obligado*
Univ Grenoble Alpes, CNRS, Grenoble-INP,
LEGI, F-38000, Grenoble, France †

Alberto Aliseda
Department of Mechanical Engineering,
University of Washington, Seattle, Washington 98195-2600, USA

(Dated: June 10, 2020)

Abstract

Preferential concentration is a common phenomenon found in turbulent flows seeded with inertial particles. Although it has been studied extensively, there are still many open questions about its fundamental physics. These gaps hinder the reconciliation of different experimental and numerical studies into a single coherent quantitative view, which is needed to enable accurate high resolution modeling.

This work examines the influence of the measuring technique, and in particular of the dimensionality of the measurement (1D line, 2D planes or 3D volumes) on the characterization of cluster properties (a consequence of preferential concentration), and proposes an approach to disentangle the cluster-characterizing results from random contributions that could contaminate the cluster statistical analysis.

First, we studied this effect by projecting 2D and 3D data snapshots containing clustering onto a 1D axis. The objective was to simulate 1D sensors (widely used experimentally) with different sensing lengths.

These projected records were analysed by unidimensional Voronoï tessellations. Our results demonstrate that average mean clustering properties could be retrieved, if the measuring window is equal or larger than the Kolmogorov length scale (η), and smaller than about ten percent of the integral length scale of the turbulence $\mathcal{L}$. These observations are consistent with 2D and 3D data taken under similar experimental conditions. This agreement validates our projection approach as it adequately captures the behavior of a 1D probe immersed in a 2D, or a 3D flow.

Additionally, we found that in 1D the raw probability density function (PDF) of Voronoï cells does not provide error-free information on the clusters size or local concentration. We propose a methodology to correct for this measurement bias, based on the histograms of the number of particles within a cluster. The analysis of these histograms helps to explain the power-law behavior previously observed in the clusters size PDFs in 2D and 3D data. Moreover, the histogram analysis shows that such power law is not very robust in 1D, as it expands less than one decade.

Finally, we show that to condition the statistics with the number of particles inside each cluster also allows to discern between turbulence-driven clustering and particle concentration fluctuations due to randomness. Our test then complements the classical cluster identification algorithm.

---

* Martin.Obligado@univ-grenoble-alpes.fr

I. INTRODUCTION

Turbulent flows laden with inertial particles constitute an active research area within multiphase fluid mechanics due to their potential applications in fields such as: planetary formation, pollutant dispersion, and cloud formation [1, 2]. Hence, experiments are not only useful to validate the multiple numerical approaches, but also to disentangle their underlying physics, and finally reach comprehensive understanding.

Several methods are available to characterize particle-clusters, with Voronoï tessellations [3–6] becoming increasingly popular in both experimental studies employing visualization techniques, e.g., particle tracking velocimetry (PTV) [4, 7] and numerical simulations [8, 9].

Despite its current popularity, it was early recognized [10] that there could be pitfalls in the Voronoï method that could affect its results. The open questions are: to what extent physics from a 3D particle spatial distribution measured by 2D or 1D techniques can be captured by the Voronoï method, and how the measurement configuration (1D, 2D, line diameter, plane thickness, etc.) could impact its results. The study of Monchaux [10] was the first to survey these possible biases in context of particle laden-flows. By projecting a 3D numerical dataset onto a 2D plane, they studied the effect of the laser sheet thickness (L_{th} in their notation) on the resulting 2D Voronoï statistics. The study concludes that 2D Voronoï analysis is reliable for the most common values of laser sheet thicknesses ($L_{th} \in [2\eta - 6\eta]$) used in 2D imaging experiments, and very robust under random thinning, which simulates the effect of missed particles. However, care is needed when comparing 2D Voronoï statistics from different data sets obtained under different experimental or optical conditions, as sub-sampling results heavily depend on the particle seeding and the turbulence scales.

On the other hand, a recent study [11] reports that a 1D Voronoï analysis (referred also as 1DVOA from now on) performed on a record taken by an optical probe via phase detection [12], is unable to capture preferential concentration in experimental conditions under which clustering is observed using 2D Voronoï analysis [7]. Thus, 1D and 2D Voronoï analyses could yield contradictory results regarding the presence of preferential concentration within the flow.

The study of Mora et al.[11] suggests that the probe's measuring volume (a region in space where the instrument can detect particles transiting) has an important impact on this

---

[†] Also at Univ Grenoble Alpes, CNRS, Grenoble-INP, LEGI, F-38000, Grenoble, France

problem. This study reveals that below a certain threshold of the measuring volume, the 1D Voronoï method is unable to capture the spatial correlations between the recorded particles. This observation, however, is strongly affected by the particle concentration, as it was proven in 2D projections [10], and therefore, it cannot be attributed to insufficient resolution of the measuring instrument. Indeed, it is found that while an optical probe (with a measuring length 10 times smaller than the Kolmogorov length scale of the flow) was unable to retrieve clustering, it did recover the local liquid fraction, the particle size, and the particle velocity distributions consistent with previous measurements.

Biases involving 1D measurements have also been found in other methods to determine the existence of preferential concentration. For instance, when using 1D pair correlation functions, it has been found that excluded volume effects (due to the finite size of the droplets) could accumulate and had a combined effect across a range of scales, biasing the results obtained by this method [13, 14]. There is, however, a fundamental difference between 1D pair correlation functions and 1D Voronoï tessellations. The former method subdivides the dataset domain into segments of a certain scale, whereas, the latter method conducts analysis that is considered to be scale free. Excluded volume effects do not accumulate in 1D Voronoï tessellations given that 1D Voronoï cells are computed from their immediate neighbours. Conversely, the finite particle size impacts the value of the criterion used to assess the presence of clustering; clustering is present if the standard deviation of the Voronoi cell size $\sigma_{\mathcal{V}}$ coming from the particle dataset is larger than the respective one coming from the equivalent random Poisson distribution (RPP). Uhlmann has reported [15–17] via 3D Voronoï tessellations that, for spherical particles with diameters up to 5η, the respective magnitude of RPP standard deviation is reduced by 10%. These observations imply that the nature of the pitfalls found in pair correlation functions, and 1D Voronoï tessellations, although related, are distinct.

Given the available technology, and experimental apparatuses, one could question the use of a '1D' technique to characterize a 3D phenomenon. Still, these complementary experimental techniques, for example, phase detection optical probes [12], or phase doppler interferometry (PDI) [18], have been proven useful, as they provide additional information not so easily available from 2D/3D measurements. Moreover, when identifying the actual droplet spatial distribution within a cloud [1, 2, 19] or probing pollutant dispersion within cities [20, 21], in situ measurements are usually acquired by 1D eulerian instruments.

Hence, it is worth examining whether the 1D Voronoï statistics have any extra inherent biases when used to quantify preferential concentration, i.e., when the approach to analyze 2D or 3D data is extended to 1D records. The latter approach usually consists on building the Voronoï sizes probability density functions (PDFs), and then draw conclusions based on the particle local concentration [4, 7, 8, 15, 16, 22], which is easily available via Voronoï tessellations. The presence of these biases is not restricted to 1D probes. Analogue problems could arise in 2D and 3D measurements. The 2D Voronoi analysis, however, has been shown to be very robust for different laser sheet thicknesses and concentrations [10].

In this work, we study the impact of the instrument measuring window size (MWS) on 1DVOA statistics conducted on 'projected' records from numerical and experimental data sets. Then, different MWSs 'emulate' eulerian measurements taken with probes of different sizes in the same particle-laden flow. The later analysis allowed us to provide a range of MWSs (or probe sizes) for which evidence of preferential concentration could be consistently retrieved, under similar experimental values of the Taylor-based Reynolds number (Re_λ), and global liquid fraction (ϕ_v).

According to our analyses, this range's lower bound (labeled $\mathrm{MWS}_\dagger$) is of the same order of the Kolmogorov lengthscale (η). In other words, our analyses suggest that to retrieve clustering for similar values of Re_λ, and ϕ_v one should measure with a probe with a window size of order η, i.e., $\mathrm{MWS}_\dagger = O(\eta)$. On the other hand, we observe that for the analyzed experimental data and DNS (Direct Numerical Simulation) dataset this range's upper bound (labeled $\mathrm{MWS}_\star$), after which evidence of clustering becomes weaker, seems to be located at measuring window size close to a tenth of the integral length scale. $\mathrm{MWS}_\star \sim \mathcal{L}/10$ where $\mathcal{L}$ is the integral length scale of the carrier phase.

Furthermore, to characterize the clusters properties, we looked for biases in the probability density functions (PDFs) of cluster local concentration, and linear size. Our data strongly suggest that the method developed to analyze preferential concentration in 2D [23] cannot be (in general) directly extended to 1D Voronoï tessellations analyses. Such direct extension, under some experimental conditions, is not conclusive regarding the presence of clustering within the flow, and undermines the capacity of 1DVOA to characterize the phenomenon in 1D unambiguosly. The origin of this limitation could be attributed to the loss of information intrinsic to the 1D measuring technique, and it is supported by the weaker correlation seen among the recorded particles positions.

To further explore these biases, we developed a theoretical model to compute the PDFs of cluster sizes coming from particle positions spatially distributed according to a random Poisson process (RPP). The model underlying principles suggest that conditioning the clusters PDF by the number of particles within clusters could aid to properly find and characterize 'turbulence' driven clusters. The method, therefore, allows to disentangle randomness (as high density regions are also present within a RPP distribution due to random fluctuations of the local concentration) from turbulence (where clusters are controlled by the topology of the turbulent flow) in a 1D signal.

II. THE EXPERIMENTAL SETUP AND METHODS

A. Experimental setup and numerical database

The experiment was conducted in the close-circuit wind tunnel '*Lespinard*' that has been extensively used to study particle clustering under turbulent conditions [7, 23]. A sketch of the experimental setup is depicted in figure 1a.

Turbulence was produced by means of an active grid [24] operated in triple random or open mode [25]. At the measuring station (region #3 in fig 1a), the unladen turbulence has been experimentally found to be very close to a statistically homogeneous isotropic state (figure 1b) under similar conditions of Re_λ, and η [26] to those found in the present work.

Downstream of the grids, a rack of 36 spray nozzles generated inertial water droplets with a polydisperse diameter distribution. This polydispersity (see figure 1c) has been previously quantified via phase doppler interferometry [7].

At the measuring station, a high speed camera collected 4500 images of the light scattered by the droplets from a 1-mm thick laser plane. The images, with an area of (120×100 mm^2) and collected to be statistical independent realizations, were post-processed to identify the location of the droplet centers (more details about the experimental setup can be found in [27]).

Along with experimental data, 30 numerical snapshots from a DNS data base [28] (`https://turbase.cineca.it/init/routes/#/logging/view_dataset/3/tabmet`) were surveyed. Each file contained the trajectories of 1280 particles positions integrated over 3300 time steps.

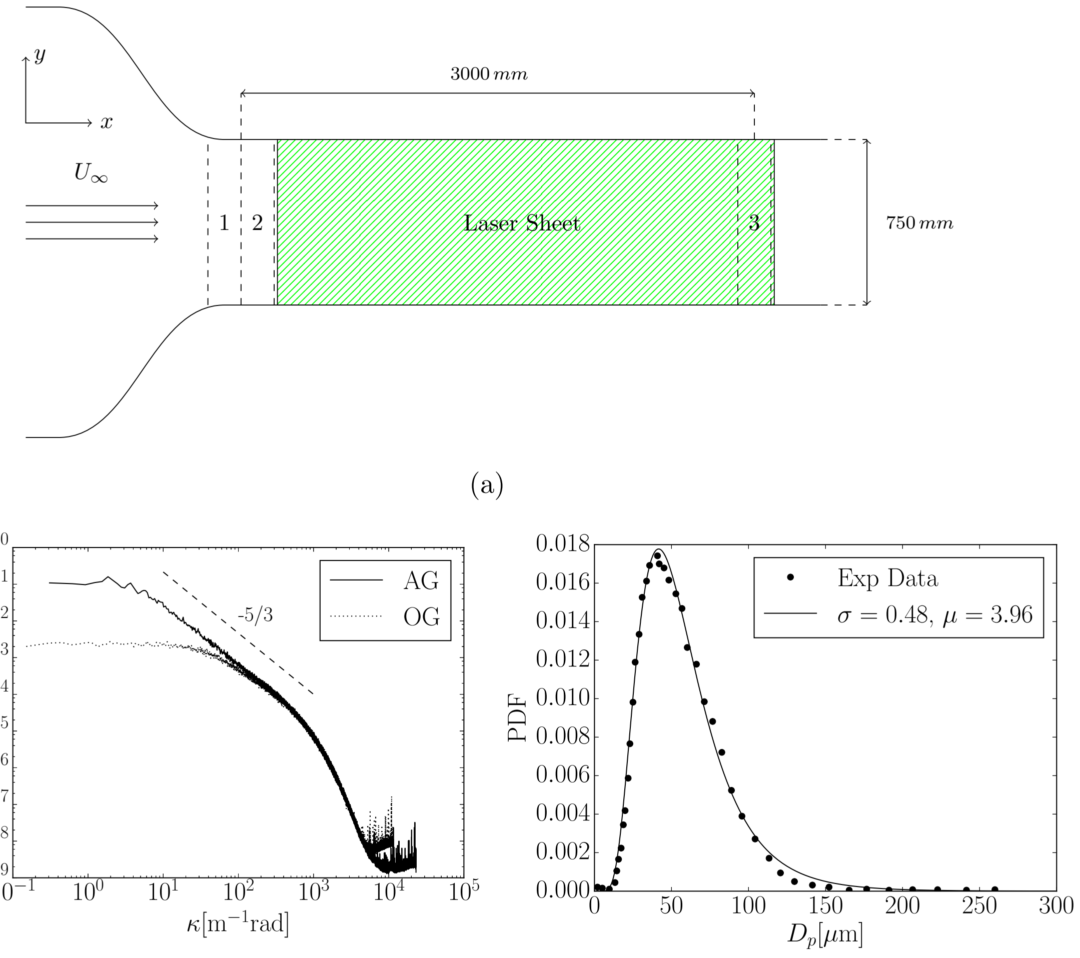

(a)

(b)

(c)

FIG. 1: a) Sketch of the wind tunnel experimental setup. 1, 2, and 3 refer to the locations of the active grid, the injection rack, and the measurement region, respectively. The measuring region downstream distance was taken from the beginning of the injector rack. The shaded region illustrates the extend of the laser sheet. The transverse square cross-section has dimensions of 750 × 750 mm^2. b) Velocity power spectral density for the active grid (AG) $Re_\lambda \approx 250$, and for the open grid (OG) $Re_\lambda \approx 30$. Both spectra were obtained via hot-wire anemometry. c) Droplet Diameter D_p distribution. The symbol (○) refers to data from [7], and the (—) line refers to a log fit (parameters shown in the plot legend)

Dataset	Grid Mode	Re_λ	St_η	$\varepsilon\mathcal{L}^4/\nu^3$	D_p/η	$\mathcal{L}/\eta$	λ/η	ϕ_v	ρ_p/ρ_f
EXP-2D-AG-A	Random	250	0.9	4.3×10^8	0.125	175	35	1.2×10^{-5}	800
EXP-2D-AG-B	Random	250	0.9	4.3×10^8	0.125	175	35	2.3×10^{-5}	800
EXP-2D-OG-A	Open	30	0.05	9.0×10^4	0.032	20	7	1.2×10^{-5}	800
EXP-2D-OG-B	Open	30	0.05	9.0×10^4	0.032	20	7	2.3×10^{-5}	800
DNS [29, 30]	-	185	1	1.1×10^{10}	-	314	26	-	$\gg 1$

TABLE I: Main turbulence parameters for experiments and DNS data used on this work. $\lambda = u'\sqrt{15\nu/\varepsilon}$ is the Taylor length scale, and $\nu \sim 1.5 \times 10^{-5}$ $[m^2 s^{-1}]$ is the air viscosity. u' is the rms of the streamwise velocity fluctuations. The turbulent Reynolds number is defined as $Re_\lambda = u'\lambda/\nu$ and D_p is the value of the most probable diameter which was used to compute the Stokes number $St_\eta = \frac{(D_p/\eta)^2}{36}(1 + 2\rho_p/\rho_f)$, see [7]. ρ_p/ρ_f is the density ratio between the particles, and the carrier phase. ε, and $\mathcal{L}$ are the carrier dissipation, and integral length scale, respectively. AG/OG stands for the random or open mode of the active grid. ϕ_v is volume fraction for the experimental data. As numerical data is a '1-way' coupling point particle simulation, we assume it is very diluted $\phi_v \ll 10^{-6}$ [31]. More details on how the experimental unladen flow parameters have been calculated can be found on [25].

These snapshots contained inertial point particles with a Stokes number close to unity; $\mathrm{St}_\eta = \tau_p/\tau_\eta \approx 1$ where $\tau_p = \rho_p D_p^2/18\mu$ is the particle relaxation time, $\tau_\eta = \sqrt{\nu/\varepsilon}$ is the Kolmogorov timescale, D_p is the particle diameter, ε the turbulent dissipation rate, μ the dynamic viscosity of the carrier phase, and ρ_f, and ρ_p are the carrier and particle density, respectively.

The snapshots files can be found in the database labeled as:
`RM-2008-LIGHT-512.St6.XX.h5`, which have particles with $\tau_p = 0.048282$, and $\beta = 3\rho_f/(\rho_f + 2\rho_p) = 0$, i.e., $\rho_f \ll \rho_p$. More details of the numerical setup ($Re_\lambda \approx 185$) can be found in [29, 30]. The experimental and simulation parameters are summarized in tables I, and II.

Dataset	N_{snap}	$\langle N_p/N_{snap}\rangle$	$\sigma_{\langle N_p/N_{snap}\rangle}$
EXP-2D-AG-A	4500	1×10^3	280
EXP-2D-AG-B	4500	5×10^3	1200
EXP-2D-OG-A	4500	3×10^3	330
EXP-2D-OG-B	4500	1×10^4	800
DNS	30	4×10^4	0
RPP	1000	$10^3, 10^4, 10^5$	0

TABLE II: Datasets summary. N_{snap} is the number of snapshots, N_p is the number of particles, $\langle N_p/N_{snap}\rangle$ is the average number of particles per snapshot, and $\sigma_{\langle N_p/N_{snap}\rangle}$ is the standard deviation of the mentioned average.

B. Voronoï Tesselations

Originally, Monchaux et al. [23] proposed the use of Voronoï tessellations to quantify preferential concentration in turbulent flows. In 2D, the Voronoï tessellation yields a collection of areas A from particles spatial positions [3]. Statistics can be then computed for this collection, e.g., the average area $\langle A\rangle$, or the area standard deviation σ_A. The Voronoï analysis is usually conducted by considering the area collection normalized by its mean $\mathcal{V} = A/\langle A\rangle$, giving $\langle\mathcal{V}\rangle = 1$.

Monchaux et al. [23] suggested that Voronoï area PDFs can be characterized by their standard deviation ($\sigma_{\mathcal{V}}$), a conclusion they substantiated by the log-normal behavior present in these PDFs, and the collapse seen under the log-normal transformation for different cases studied (with different values of Re_λ, or concentration ϕ_v). These observations led them to conclude that $\sigma_{\mathcal{V}}$ estimates the 'intensity' of clustering.

Then, to quantify 'clustering', $\sigma_{\mathcal{V}}$ is compared with the respective standard deviation coming from particles spatially distributed following a RPP distribution (σ_{RPP}), which by definition has no spatial correlations at any scale. Thus, preferential concentration is present if $\sigma_{\mathcal{V}} > \sigma_{RPP}$. It is clear that under this criterion, the voids (or area outliers of the area collection) contribute the most to the numerical value of $\sigma_{\mathcal{V}}$ [7].

Likewise, the unidimensional Voronoï tessellation (1DVOA) generates a collection of

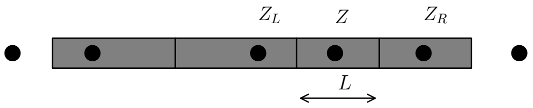

FIG. 2: Undimensional Voronoï tessellation (1DVOA). For a given particle position Z with left, and right neighbour particle Z_L, and Z_R respectively, the length of the Voronoï cell is given by $L = |Z_R - Z_L|/2$.

Dimension	PDF expression	σ_{RPP}	Model
1	$4 \times \mathcal{V}^{1.0} e^{-2.0\mathcal{V}}$	$\sqrt{1/2}$	Analytical
2	$343/15\sqrt{7/2\pi} \times \mathcal{V}^{2.5} e^{-3.5\mathcal{V}}$	≈ 0.53	Fit
3	$345/7 \times \mathcal{V}^{3.8} e^{-4.0\mathcal{V}^{1.17}}$	≈ 0.42	Fit

TABLE III: Summary of the Voronoï PDF expressions for 1,2,3 dimensions, and their respective properties as reported by Ferenc and Nedá [3] (1D and 2D) and Tanemura [32] (3D).

lengths L, not to be confused with the turbulence integral length scale $\mathcal{L}$ (figure 2). However, Mora et al.[11] reported that clustering could be present but not retrieved via 1D measurements [1, 13], and therefore, the criterion $\sigma_{\mathcal{V}} > \sigma_{RPP}$ cannot be directly extended to 1D measurements, and it may not be entirely conclusive for 1DVOA.

For clarity, we will define some acronyms below, but will often recur to the acronym's verbatim. First, angle brackets $\langle ... \rangle$ represent an ensemble average. Second: our short notation for the Voronoï tessellations variables goes as; $\mathcal{V} = \mathcal{M}_{voro}/\langle \mathcal{M}_{voro} \rangle$ where $\mathcal{M}_{voro}$ represents the length L, area A, or volume V of a Voronoï cell. Thirdly, a 1D/2D/3D Voronoï tessellation analysis will be referred as 1DVOA, 2DVOA, or 3DVOA, respectively. Finally, the respective standard deviation of a RPP distribution (σ_{RPP}), which has no correlations at any scale, can be analytically computed: $\sigma_{RPP} \approx 0.71/0.53/0.42$ for 1DVOA/2DVOA/3DVOA, respectively (see table III, and references [3, 32]). The 2D and 3D Voronoï diagrams were computed using the python library *freud* [33].

C. 1D ‘Projected’ Voronoï Analysis

Following the method proposed by Mora et al. [11], we projected particle positions coming from previous 2D and 3D data, which exhibit preferential concentration, orthogonally onto a line.

This approach aims to emulate the basic features of an Eulerian measurement: a fixed probe in space (e.g. downstream from the grid of a wind tunnel). Thus, the particle coordinates orthogonal to the bulk velocity (U_∞) were ‘frozen as the particles were advected by the flow figure 3a).

For the experimental 2D data sets, this projection process will be denoted as $2D_{EXP} \rightarrow 1D_\perp$, where $2D_{EXP}$ stands for 2D experimental images, and $1D_\perp$ is a uni-dimensional orthogonal projection into 1D, i.e., onto the streamwise axis γ (figure 3a). For the numerical 3D data, the notation is ($3D_{DNS} \rightarrow 1D_\perp$), where $3D_{DNS}$ is the 3D dimensional DNS data set (figure 3b). We applied this procedure for each data snapshot (table II).

Thus, our ‘projection’ algorithm [11] comprised the following steps:

1. A random vertical $\hat{y}$ coordinate was generated. This coordinate set the position of the axis γ onto which the particles were projected.

2. A symmetric measuring volume size (MWS) window was defined intended to quantify the effect of the instrument finite spatial resolution. At all times, the $\hat{y}$ coordinate choice was restricted so that the MWS width was inside the computational domain.

3. All the particle *centers* that lay within this measuring strip (axis γ and width MWS) were projected onto the axis γ, i.e., their horizontal coordinate was recorded.

4. 1DVOA was performed over the particle location line projections.

5. Three additional elements were considered for the 3D data :

   (a) A $\hat{z}$ transverse coordinate was generated to position a cylinder axis.

   (b) The generated cylinder diameter was equal to the measuring window.

   (c) All particles within this cylindrical volume were subsequently projected on the cylinder axis γ (see figure 3b).

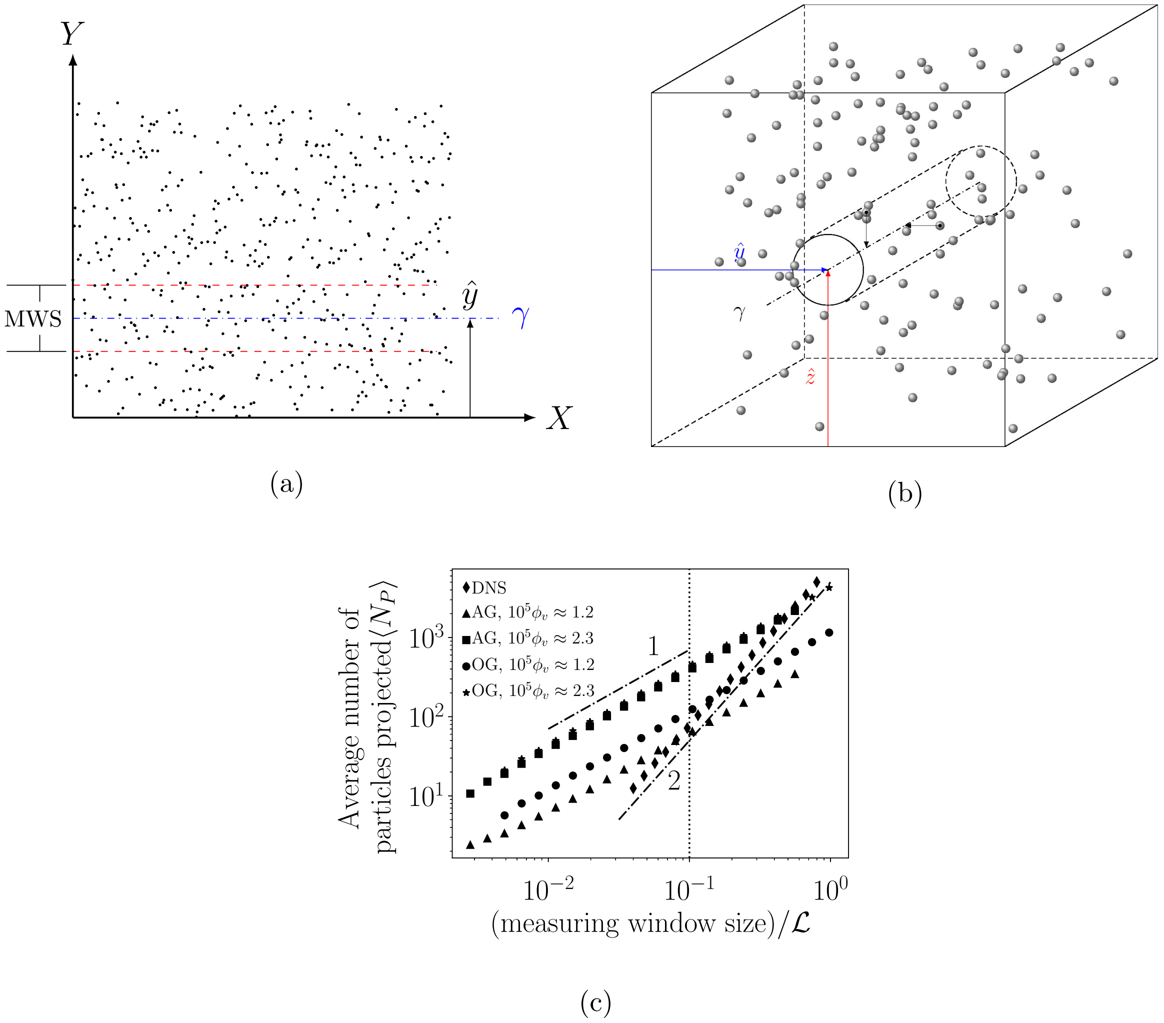

FIG. 3: a) Sketch of the $2D_{EXP} \to 1D_\perp$ particles centers projection for an arbitrary image. MWS is the measuring window size, $\hat{y}$ is the randomly generated vertical coordinate of the axis γ over which the points are orthogonally projected. b) Sketch of the $3D_{DNS} \to 1D_\perp$ particles centers projection for an arbitrary DNS snapshot. MWS is the measuring window size equal to the cylinder diameter, $\hat{y}$ and $\hat{z}$ are the randomly generated coordinates of the axis γ onto which the points are orthogonally projected. c) Average number of projected samples per snapshot from 1D sampling ($2D_{EXP}$ or $3D_{DNS} \to 1D_\perp$), and its dependency with the measuring window size. At very small MWS with respect to $\mathcal{L}$ the average number of samples captured is small, which is directly linked to lack of clustering recently reported [11].

The previous algorithm seems to capture the basic features of an equivalent experimental eulerian measurement, and is suitable to examine the effect of different measuring window sizes have on 1D Voronoï statistics. For instance, most quasi-unidimensional instruments [12, 18, 34] are particle 'counters', which usually yield a list of events with their respective eulerian 'arrival' time. One would then expect that the larger the window size (the region in space where the instrument detects the particle transiting), the larger the number of droplets is 'detected', a behavior this 'projection' approach does indeed capture (see figure 3c).

III. RESULTS

A. PDFs and Voronoï cell standard deviation

We first checked if preferential concentration was present in the 2D and 3D data. Using the same 2D datasets, Mora et al.[11] and Obligado et al.[27] have found strong evidence of preferential concentration by means of planar Voronoï tessellations. Next, we verified the existence of clustering in the 3D numerical database [29, 30] by means of tridimensional Voronoï Tessellations [3].

Visual inspection of the probability density function (PDF) (see figure 4a) of the normalized Voronoï cell volume ($\mathcal{V} = V/\langle V\rangle$) suggests the presence of preferential concentration within the DNS data. This is further confirmed by the larger value of the standard deviation of $\mathcal{V}$ (following the criterion proposed by Monchaux et al. [23]) with respect to the RPP distribution, which has no correlation at any scale (see section II B), i.e., $\sigma_{\mathcal{V}} \approx 0.62 > \sigma_{3D_{RPP}} \approx 0.42$, (see table III).

Having confirmed the presence of preferential concentration within the 3D data, we applied the projection algorithm to it (see section II C). Then, we conducted a unidimensional Voronoï tessellation analysis to these $3D_{DNS} \to 1D_{\perp}$ projections.

The probability density functions of the Voronoï cells sizes $\mathcal{V} = L/\langle L\rangle$ computed for several measuring window sizes (MWS), reveal a clear trend on these PDFs with varying window size (figure 4b): the larger the window size was, the closer the PDF shape approached the respective RPP distribution.

The right tail of the Voronoï PDFs ($\mathcal{V} \gg 1$) exhibits large changes with varying measuring

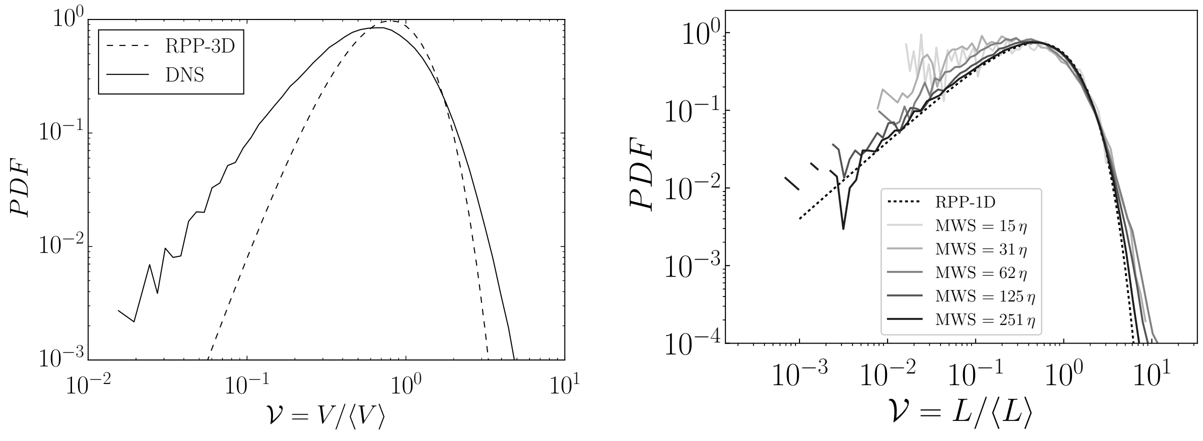

(a)

(b)

FIG. 4: a) Probability density function plot of 3DVOA for the DNS data [29, 30]. Following the criterion of Monchaux et al. [23], it is clear that the DNS data contains clustering, as $\sigma_{\mathcal{V}} \approx 0.62 > \sigma_{3D_{RPP}} \approx 0.42$ is larger than its equivalent one for a 3D RPP distribution. b) PDF plot of $(3D_{DNS} \rightarrow 1D_{\perp})$ 1DVOA for several MWS.

window size. The importance of this cannot be overstated given that the criterion proposed by Monchaux et al.[23] to determine the existence of clustering relies on the numerical value of standard deviation $\sigma_{\mathcal{V}}$, which in turn heavily depends [7] on the cell values much larger than the mean $\langle L\rangle$, i.e., $\sigma_{\mathcal{V}} = \int_0^\infty \left(\mathcal{V} - \langle\mathcal{V}\rangle\right)^2 PDF(\mathcal{V}) d\mathcal{V}$.

Furthermore, when computing $\sigma_{\mathcal{V}}$ for our 2D, and 3D projections (figure 5a), these results show that the presence of 'clustering' via this criterion can only be recovered above a certain window size ($\mathrm{MWS}_{\dagger}$), below which the evidence of clustering is not conclusive, i.e., $\sigma_{\mathcal{V}}/\sigma_{RPP} \approx 1$. In fact, for some data, $\sigma_{\mathcal{V}}/\sigma_{RPP} < 1$ could lead to the wrong conclusion of a more ordered sub-poissonian distribution [1, 11, 13].

Given the smaller number of samples available with the projection method at smaller window sizes (see figure 3c), one could attribute the result $\sigma_{\mathcal{V}}/\sigma_{RPP} < 1$ to insufficient statistical convergence. On the contrary, having statistical convergence does not necessarily guarantee that the spatial correlations within the data are captured [13].

The latter can be illustrated by applying the same projection algorithm to a three-dimensional random set (labeled $3D_{RPP} \rightarrow 1D_{\perp}$ in table II). Although this data set is, by definition, random, it shows a similar a transition region where $\sigma_{\mathcal{V}}/\sigma_{RPP} < 1$ (figure 5b). These data sets attain their 'theoretical' value of $\sigma_{\mathcal{V}}$ after a certain size which depends on to

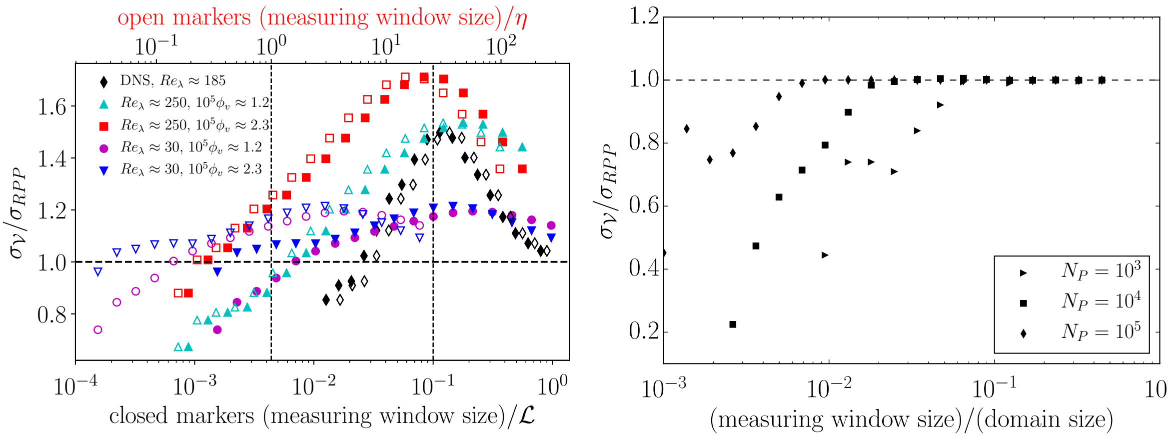

(a)

(b)

FIG. 5: a) 1DVOA standard deviation evolution for the datasets used. The larger the concentration, the higher $\sigma_{\mathcal{V}}$ for fixed measuring window size. The peak location follows the relation $\text{MWS}_\star \approx \mathcal{L}/10$, where $\mathcal{L}$ the integral length scale of the flow (see table I). However, its value depends on Re_λ, as these and previous studies have shown [7] . b) 1DVOA standard deviation evolution of projections coming from synthetic random 3D data ($3D_{RPP} \to 1D_\perp$). N_P stands for the number of points inside the 3D domain for 1000 synthetic snapshots.

the number of particles in the domain (concentration). Hence, it is the instrument and its capacity to capture particle spatial correlations which ultimately determines to which extent the 1DVOA is successful. Accurately identifying these correlations yields the proposed picture of clusters and voids [23], as there cannot be voids without clusters. Moreover, if evidence of clustering ($\sigma_{\mathcal{V}}/\sigma_{RPP} > 1$) is retrieved by means of 1DVOA, it is reliable, as a strong signature of clustering is present even after randomly removing 70% of the data points (figures 6a and 6b).

The previous observations are very relevant from an experimental point of view, as they aid to explain why two distinct measuring instruments with dissimilar window sizes could yield opposite results; as seen in the experiments of Sumbekova [35] and Mora et al. [11], ran under almost identical conditions but with different 1D measuring instruments. For the former experiment, a PDI device (MWS $\approx \eta$) was used, while for the latter, optical probes were used (MWS $\approx 0.1\eta$). This order of magnitude difference in the instrument window size is key to understand the origin of this contradiction (figure 5a).

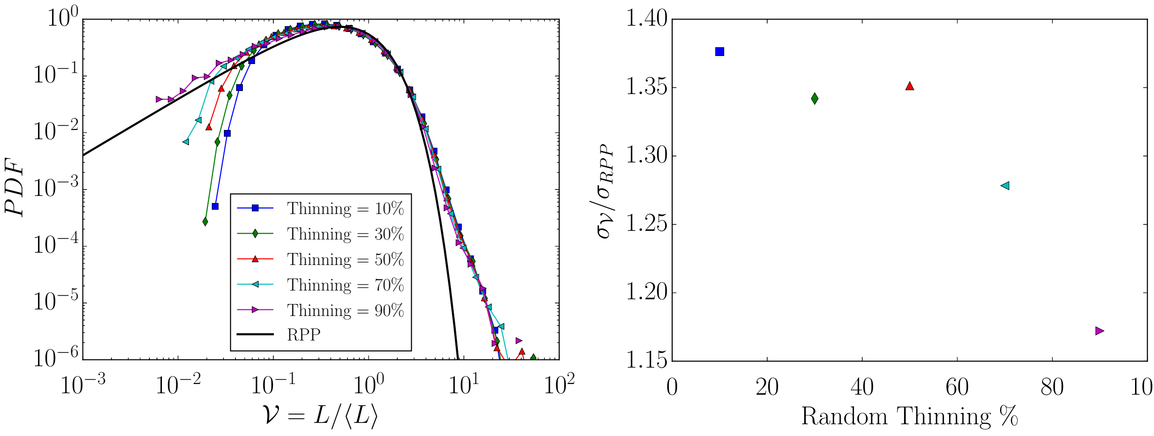

(a) (b)

FIG. 6: 1D PDI data from Sumbekova [35] for varying degrees of thinning (randomly removing samples from their records). The larger the percentage the larger the number of original particles removed. a) Thinned Voronoï PDFs b) Their corresponding normalised standard deviation ($\sigma_{\mathcal{V}}/\sigma_{RPP}$).

These results, therefore, indicate that a sensitivity analysis has to be performed if a unidimensional Voronoï analysis retrieves no clustering where higher dimensional techniques do (2DVOA or 3DVOA). However, considering the observed strong dependency of the minimum window size (MWS$_\dagger$) on the concentration values ϕ_v for which $\sigma_{\mathcal{V}}/\sigma_{RPP} > 1$ (figures 5a and 5b), and the strong dependency of $\sigma_{\mathcal{V}}/\sigma_{RPP}$ on the carrier phase conditions Re_λ, such sensitivity analysis is not straightforward, and it should be tuned to the specific conditions of the experiment.

Interestingly with our projection algorithm, we also recovered that the degree of clustering increases with Re_λ in agreement with previous studies [7, 22]. Our results, and the data of Sumbekova [35] suggest that an instrument with a measuring volume equal or larger than the Kolmogorov length scale (η) should be used if evidence of preferential concentration is to be retrieved by means of 1D Voronoï tessellation analysis. Likewise by means of RDF functions, Saw et al. [36] have recovered evidence of preferential concentration using a probe with a volume of order η.

Although the choice of η as MWS$_\dagger$ could be seen as arbitrary, it seems to be adequate for the current range of Re_λ attainable in several experimental facilities (and in our data sets) under similar experimental conditions. More importantly, this criterion does not contradict previously reported clustering at scales smaller than η [37]. If these correlations were to be present at smaller scales than η, they would be effectively captured (figure 5a).

Despite being only intended to capture the basics of an eulerian measurement, our approach also seems to capture interesting information related to preferential concentration physics, giving extra credence to its underlying hypotheses.

On the one hand, it is remarkable that the peak of the ratio $\sigma_{\mathcal{V}}/\sigma_{RPP}$ (maximum clustering degree in figure 5a) occurs at a measuring window size close to a tenth of the integral length scale, i.e., $\mathrm{MWS}_\star \approx \mathcal{L}/10$. This peak is representative of the maximum spatial correlation present at the data set, as our projection procedure does not increase the actual correlation in the data (see 3D RPP projections results in figure 5b). Hence, this window size, or scale, can be connected to the multi-scale mechanisms proposed to explain preferential concentration [38, 39].

For instance, the sweep-stick mechanism [38, 40, 41] considers that the scaling behavior for voids (the counterpart of clusters) in the inertial range is not described by a single scale, but instead follows a self-similar behavior within a range of scales (window size), $\ell_{max}/\ell_{min} = \mathcal{O}(10)$ (where ℓ denotes scales from the inertial range of the turbulent flow). We can therefore interpret $\mathrm{MWS}_\star$ as representative of the maximum interaction among all scales between the carrier turbulent flow and the particles. Also, the study of Bragg et al. [42] reports that their proposed mechanism responsible of clustering attains its peak at a scale close to $r = 200\eta$, and with $\mathcal{L} = 800\eta$, these observations are in the same order of magnitude of $\mathrm{MWS}_\star \approx \mathcal{L}/10$.

B. Average clusters size and measuring window size

We will now examine the effects that the observed biases have on the cluster linear size L_C. We started by computing L_C following the most widely accepted cluster identification algorithm [23]: first we selected all the normalized Voronoï cell sizes $\mathcal{V}$ that were below a threshold value, $\mathcal{V} < \mathcal{V}_{th}$. This threshold is defined as the closest crossing (to the left of the RPP peak) between the RPP PDF, and our data PDF (see figure 7a), i.e., $\mathcal{V}_{th} = \mathcal{V} = \mathcal{V}|_{RPP} < 1$ [10, 23, 26].

The second step in the cluster algorithm is to find (within the collection $\mathcal{V} < \mathcal{V}_{th}$) cells which share at least one edge. Then, two or more neighbouring cells were considered to be a cluster ($N_{PC} \geq 2$, where N_{PC} is the number of particles inside the cluster).

We took the same Voronoï cell threshold ($\mathcal{V}_{th} \approx 0.55$) for all 2D and 3D projections. It is important to note that this cluster identification algorithm is applied individually to each snapshot (see section II C and table II). Otherwise, spurious results in the different metrics, not shown here, could arise.

The results (see figure 7a & 7b) for the different data sets, and constrained to the MWSs for which $\sigma_{\mathcal{V}}/\sigma_{RPP} > 1$, show two distinct regions: one where the average cluster size has a power-law decay behavior with increasing measuring window, and another where $\langle L_C \rangle/\eta$ evolves slowly with MWS.

The former region occurs at larger window sizes than the minimum for which $\sigma_{\mathcal{V}}/\sigma_{RPP} > 1$ (see in figure 5a, the region where MWS$\gg$MWS$_{\dagger}$, the minimum window size). The power law behavior is a direct result of the projection method, and can be easily explained if one takes into account that: first, the average Voronoï cell value $\langle L \rangle$, which is inversely proportional to the particle number (N_p), i.e., $\langle L \rangle \propto N_p^{-1}$, also exhibits an analogous behavior with the window size (see figure 3c). Second, it has to be noted that the Voronoï cells below the threshold ($\mathcal{V} < \mathcal{V}_{th}$) are the ones that contribute the most to $\langle L \rangle$ [7]. Hence, it is not surprising that clusters become smaller (and denser) as the concentration is locally increased by projecting more particles onto a fixed domain; a leap in concentration yields a proportional reduction in $\langle L_C \rangle$, a potential setback on the applicability of 1DVOA for cluster characterization.

Given these considerations, we proceed to analyze the transition region for which $\langle L_C \rangle$ varies slowly with MWSs. The extent of this region seems heavily dependent on the liquid fraction ϕ_v and Re_λ. More importantly, the estimated average cluster lengths ($\langle L_C \rangle/\eta$) are again in agreement with previous 2D and 3D studies. Although early research shows [9, 16, 22, 43, 44] that average cluster size is of order 10η for $Re_\lambda = O(100)$, recent research has shown [7, 45, 46] that L_C may grow for larger values of Re_λ, for instance, for $Re_\lambda = O(300)$ [7, 22, 46] report $L_C = O(20 - 100\eta)$ in agreement with our observations.

In fact, the data (figures 5a and 7b) suggest that the maximum clustering window size MWS$_\star \approx \langle L_C \rangle \approx 0.1\mathcal{L}$. This conjecture seems to be supported by previously published data, for instance; Monchaux and Dejoan [9] reported $\langle L_C \rangle/\eta \approx 2 - 4$, with $\mathcal{L}/\eta \approx 30$, and $Re_\lambda \approx 30$, which is in the same order of magnitude of $\langle L_C \rangle/\eta \approx 0.1\mathcal{L}/\eta$; Obligado et al. [22] and Sumbekova et al. [7] outlined $\langle L_C \rangle/\eta \approx 10 - 20$ with $\mathcal{L}/\eta \approx 500$ and $Re_\lambda \in [200, 400]$;

and recent experiments from Petersen et al. [46] reported $\langle L_C\rangle/\eta \approx 10-40$ with $\mathcal{L}/\eta \approx 500$ and $Re_\lambda \in [200, 500]$, which are again in rough agreement with $\mathrm{MWS}_\star \approx \mathcal{L}/10$. The 3D DNS projected data also follows a similar trend, i.e., $\mathrm{MWS}_\star \approx \langle L_C\rangle \approx 40\eta$, which is close to the value found from 3D Voronoï tessellation analysis.

Thus, the expression $\langle L_C\rangle \approx \mathcal{L}/10$ could constitute a scaling for the cluster characteristic size, under similar experimental conditions. This latter consequence is remarkable, and consistent with the view of the strong role of turbulence in controlling the spatial correlation in the particle concentration field [40, 41]. For instance, despite having on average the same number of projected particles (see figures 3c and 7b), the two 2D data sets with the highest concentrations, $\phi_v = 2.3 \times 10^{-5}$, have characteristic sizes differing by almost an order of magnitude in agreement with previous 2D studies [7, 22].

Once again, these results give credence to our conservative recommendation for a minimum window size close to η, as such probe will not only be able to recover evidence of preferential concentration, but also will retrieve similar values and trends of $\langle L_C\rangle/\eta$, under similar experimental conditions of Re_λ, and ϕ_v.

IV. CLUSTER SIZE PDF

Having checked the effects of the measuring window size on the average cluster size $\langle L_C\rangle$, we proceed to study the sensitivity of the PDF of clusters length (L_C) to varying MWSs.

The analyses for experimental active grid data ($Re_\lambda \approx 250$, $10^5\phi_v \approx 2.3$, the data from the other experimental conditions exhibited a similar behavior) yield two outstanding observations (see figures 8a and 8b). First, the lack of a conclusive power law on the right tail of the L_C PDF. Second, there is a rough collapse for the PDFs of all window size with previous experimental data.

The absence of a power law behavior is surprising, as it was previously found in multiple 2D and 3D Voronoï studies [4, 8, 9, 16, 22, 46], and has been thought to be representative of the 'turbulence-driven' clusters, as the arguments of Goto and Vassilicos [38] suggest that the PDF of the voids areas should scale as $f_{AV} \sim A^{-5/3}$ based on Kolmogorov scalings, and a '-5/3' powerlaw in the velocity power spectral density. Remarkably, such power law is also found for the PDF of clusters area A_C, or cluster volume V_C in both 2D and 3D. For our unidimensional records, such power-law behaviour barely exists (if at all), as it can only be

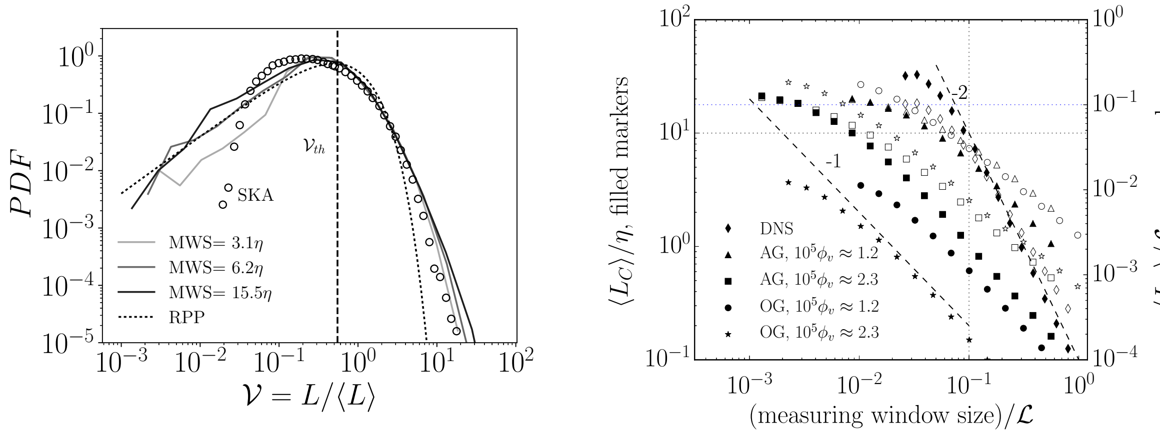

(a)

(b)

FIG. 7: a) Probability density functions (PDFs) of ($2D_{EXP} \rightarrow 1D_{\perp}$) 1DVOA (EXP-2D-AG-B) for three different measuring window sizes (MWS). The ∘ (SKA) markers correspond to the data of Sumbekova [35] for $10^5\phi_v = 2$. b) Average linear cluster size $\langle L_C \rangle$ vs different measuring window sizes (MWS) for the data analyzed. The filled markers represent the axis on the left where the cluster average size is normalized by η. The open symbols correspond to the axis on the right, where the cluster average size is normalized by $\mathcal{L}$ (the integral length scale).

identified for less than a decade for different datasets (figure 8b) .

The second observation is somehow baffling, as one could not unambiguously anticipate that these projected data PDFs (numerical and experimental) would collapse at different MWSs. The existence of relative good agreement between the projected data and previous experiments is also intriguing [35, 44] (figure 8b).

This observation has also been reported for the PDF of cluster volumes (V_C) in numerical simulations. For instance, Uhlmann and collaborators [6, 15, 16] have also found by means of 3D Voronoï tessellations that if the same clustering algorithm (and with the same threshold values $\mathcal{V}_{th}$, see section II B) is applied to data coming from a 3D random distribution, and to clustering containing data, both volume cluster PDFs attain (to some extent) a close resemblance. This pitfall is not minor, as it is critical to distinguish between the clustering coming from the turbulence and from the random fluctuations in the data. Otherwise, it is very difficult to correctly assess the influence of the turbulence on particle laden related variables such as particle settling velocity [4].

Hence, we conducted a similar analysis as the one of Uhlmann's group to explore the origin of both observations: the lack of power law behavior, and the close PDFs resemblance in 1D. Our approach was to apply the 1DVOA to synthetic data from a uniform random distribution with a uniform distribution of probability, and applying the same threshold value to those Voronoï cells with sizes smaller than 0.55, i.e., $\mathcal{V} < \mathcal{V}_{th}$ =0.55. These cells were then processed using the cluster identification algorithm described in section III B. As random datasets have no actual clusters, the algorithm then detects the high concentration regions present on the RPP. This analysis will then be useful to compare these random fluctuations with the clusters generated by the interaction between inertial particles and a background turbulent flow.

The results of this analysis evince that the PDF of cluster sizes from 1D synthetic random data collapse remarkably well with the clusters PDFs generated from previous 1D experimental PDI particle records [35, 44] under turbulent conditions (see figure 8b). As this covers most of the available clusters data, our next objective is to check whether these observations are a result of the Voronoï tessellation algorithm in 1D, or if they are a consequence of the cluster detection method [23] in any dimension.

A. Clusters PDF Model

We developed an analytical model for cluster size probability distribution $f(L_C)$ coming from synthetic 1D random data (a detailed explanation can be found in the A). Our aim with this model was to gain insight into: a very weak (if existent at all) power law, and a rather universal shape for the cluster size PDF for any input 1D data fed into the 1DVOA.

We used a mixture PDF model [47], a model based on PDFs linear superposition, and as such each PDF f_i is multiplied by a weight α_i, i.e., $f_{mix} = \sum_i^N \alpha_i f_i$, where N is the number of PDFs to combine. We then superimposed the PDFs of clusters of two, three, four, and up to N particles to construct a PDF which represents the magnitudes of L_C.

The question was, however, how to choose the coefficients α_i. A sensible approach is to propose that these weights are proportional to the probability of clusters having i particles within the cluster collection. In other words, $\alpha_{N_{PC}}$ = counts of clusters of size N_{PC} / the total number of clusters. We then obtained these weights by computing histograms (S_N) conditioned on the number of particles in a cluster; N_{PC} (see figure 9a, and equations A10

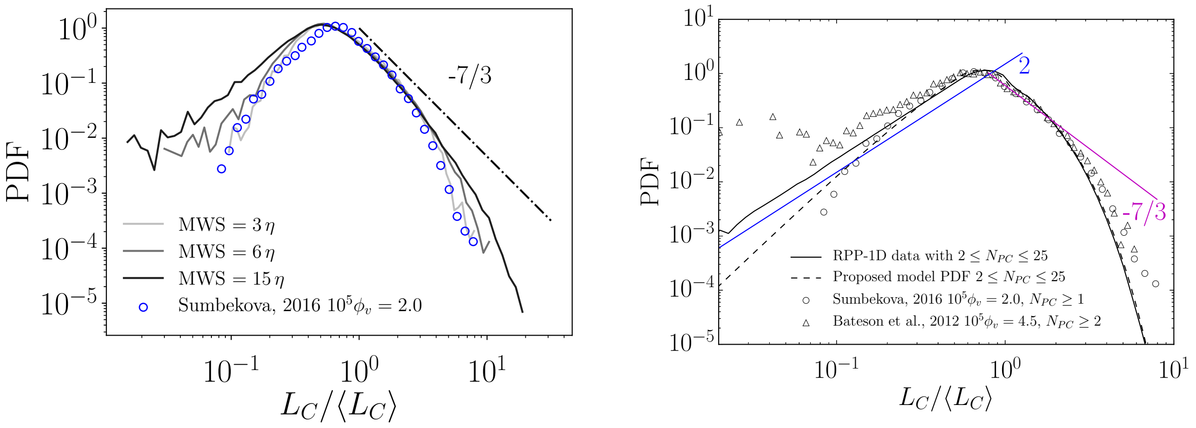

(a)

(b)

FIG. 8: In the figures, the markers (○) and (△) correspond to the experimental data from Sumbekova [26], and Bateson et al.[44] (taken in a different facility), respectively. a) PDFs of 1DVOA of linear cluster size $L_C/\langle L_C\rangle$ for several window sizes (MWSs). b) PDFs of 1DVOA of linear cluster size $L_C/\langle L_C\rangle$ for a random uniform distribution (RPP [3]), experimental data, and the model proposed. For all clusters having between 2 and 25 cluster cells (N_{PC}). The model proposed here represents well the right tail of the RPP data when $N_{PC} \geq 2$. The condition $\mathcal{V} \leq \mathcal{V}_{th} = 0.55$ was employed for clustering computation.

- A12).

Our PDF mixture model based on these weights (see open symbols in figure 9a), has good agreement with the clusters PDF found by applying the cluster identification algorithm to synthetic 1D RPP data (see figure 8b), and therefore, it strongly supports the absence of a power law decay in the cluster size PDF coming from a 1D RPP distribution.

Moreover, the construction of the histograms S_N for turbulence-induced data reveals that S_N histograms are power law distributed (see filled symbols in figure 9a) up to certain extent for the data containing preferential concentration both in 1D and 2D, whereas they decay exponentially for randomly generated RPP data both in 1D and 2D. On the contrary, 3D randomly generated data still shows a power-law similar to the one present for the turbulent DNS dataset.

It therefore appears that the existence of a power law behavior in the clusters PDF is correlated to the functional dependency of the weights distribution (S_N) in any dimension (see figure 9a). This observation then suggests that the individual PDFs (f_i) should attain a particular shape at increasing values of N_{PC}. Given that our model estimates the PDF of $L_C|_{N_{PC}}$ assuming a sum of independent random variables, i.e., $L_C|_{N_{PC}} = X_1 + X_2 + X_3 + \ldots + X_{N_{PC}}$ (see in the appendix figure 15c, and equations A1 and A9), we found that at increasing N_{PC} this PDF tends to a Gaussian distribution, as stated by the central limit theorem [48].

Although this theorem is valid for sums of independently distributed random variables, it has been rigorously proven [49] (invoking strong-mixing conditions [50, 51]) that some consequences of it can extended to sums of correlated variables having limited normal or gamma distributions; $f_\Gamma(\mathcal{V}, p, k) = k^p \mathcal{V}^{p-1} e^{-k\mathcal{V}}/\Gamma(k)$. Taking into account that; the Voronoï cells ($\mathcal{V}$) PDF (see table III) are special cases, or numerical fits of the gamma distribution (for instance, in 1D $k = p = 2$ [3, 52]), and that sums of random correlated variables are implied when computing the clusters PDF, a central limit theorem [49] should hold for the cluster algorithm of Monchaux et al. [23]. We can then conclude that the histograms of S_N indeed control shape of the cluster size PDF, and thereby, they provide a robust criterion to identify turbulence-driven clusters.

From these previous results, three conclusions can be drawn. First, the weak power law regime seen in the right tail of the cluster size PDF in 1D is due to the limited extend of such behavior in their respective 1D S_N histograms, as shown by the S_N behavior computed from the experimental records of Sumbekova [35], and Bateson et al.[44]. This behavior in the S_N histograms is really robust and independent of the number of samples (for the PDI). For instance, the data of Sumbekova had 10^6 samples, whereas the data of Bateson et al. had 10^4 samples. Hence, this weaker power law behavior is more likely to come from the loss of correlation inherent to the 1D measurements, and not due to insufficient statistical convergence.

Second, the small 'compact' clusters sizes, which are on the left tail of the PDF, have also a behavior close to a power law, i.e., $f_C(\mathcal{M}_C/\langle\mathcal{M}_C\rangle < 1) \approx (\mathcal{M}_C/\langle\mathcal{M}_C\rangle)^a$, where $\mathcal{M}$ stands for length L, area A or volume V, and a is twice the absolute value of the algebraic exponent found in the base RPP Voronoï cell PDFs (see table III), i.e., $a \approx 2/5/8$ in 1D/2D/3D, respectively.

Third, the stronger power law behavior previously reported for the 2D/3D area/volume clusters PDF [8, 22] can be alternatively explained by the much wider extent (compared to 1D) of such powerlaw behavior in the histograms of S_N (figure 9a). Our analysis is

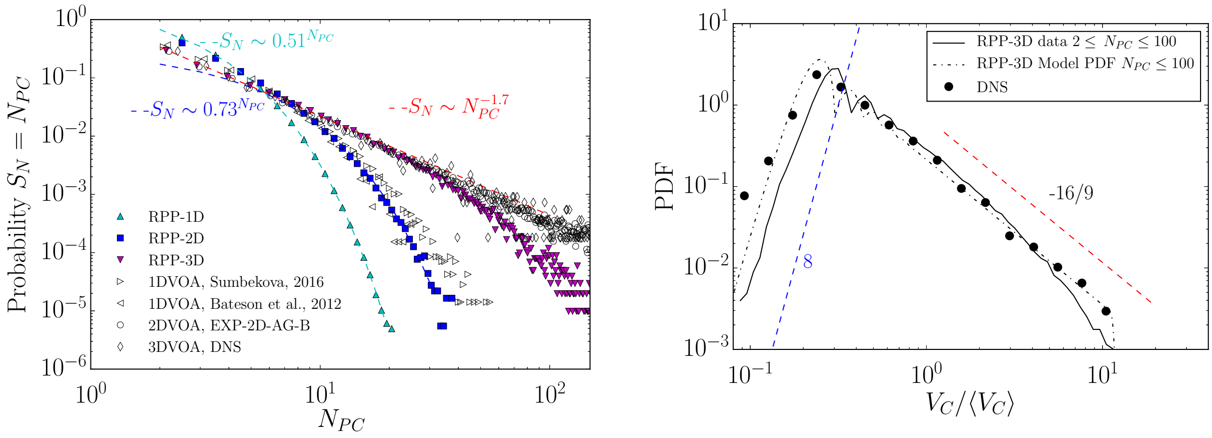

(a) (b)

FIG. 9: a) Histogram for number of particles within a cluster the different datasets. Filled symbols represent random data, whereas open symbols represent the turbulent datasets. b) Probability distribution function of clusters volume $V_C/\langle V_C\rangle$ for 3D DNS data, synthetic data, and the PDF mixture model using the weights found in figure 9a. The condition $\mathcal{V} \leq \mathcal{V}_{th} = 0.62$ was employed for clustering computation.

also in agreement with the findings of Uhlmann and collaborators [6, 15, 16] who report the presence of a power law for the clusters volume PDF (3DVOA) when the clustering algorithm is applied to a random Poisson distribution with no correlations at any scale. The latter result further supports the strong role that the S_N histograms have on the clusters PDF despite the increased uncertainty of our mixture PDF model in higher dimensions due to the approximations involved in the base Voronoï PDFs in 2D and 3D (for details see A 1, and table III).

Thus, it seems justified to use this model to analyze some properties, and possible biases found in 2D, and 3D Voronoï analyses, as our model for the PDFs of cluster areas/volumes have the same leading order behavior: with the absence/presence of power laws if the weights S_N have exponential/power law distributions (see figures 9b , 10a and 10b).

For instance, in the context of 2D Voronoï tessellations, an additional step has been recently suggested to suppress spurious edge effects [46, 53]. According to these studies, these edge effects cause ripples in the cluster areas PDFs, $A_C/\langle A_C\rangle$, and therefore, one has to require that all cells surrounding the detected clusters have a cell size below the threshold $\mathcal{V}_{th}$.

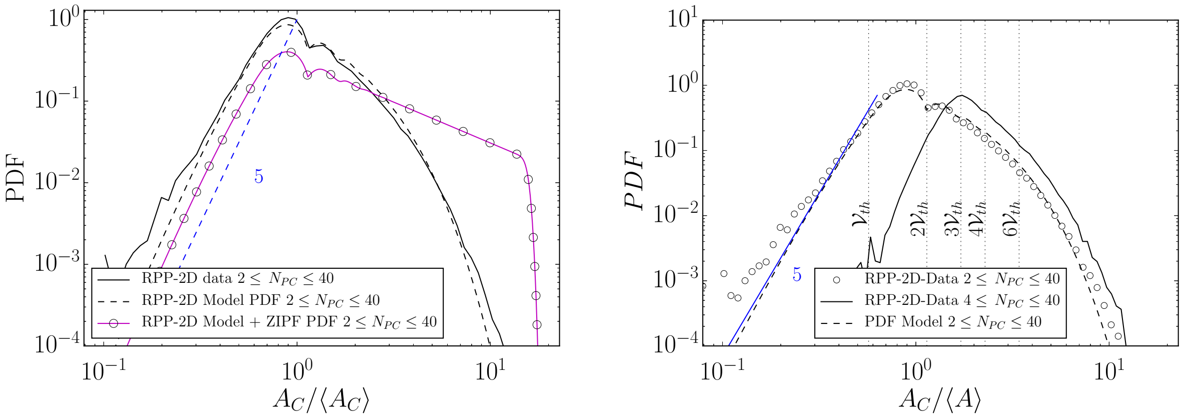

(a) (b)

FIG. 10: a) Probability distribution function of cluster area $A_C/\langle A_C\rangle$ for a random uniform distribution, and the model proposed using the weights found in figure 9a, and using weights from a ZIPF distribution $\alpha_i \propto N_{PC}^{-1}$. Indeed using the latter weights yields a strong power behavior. b) PDf of clusters area normalized by average Voronoï cell area $\langle A\rangle$ for the synthetic data, our model. The presence of ripples within the analytical PDF seems to challenge the argument of Zamansky et al. [53] to cater for the 2DVOA edge effects.

Although we recovered ripples in the 2D cluster area PDFs (figures 10a and 10b), it is questionable that we could attribute the existence of these ripples to edge effects, as our analytical model (convolutions via Fourier transforms) should not be affected by them. From our model construction, it appears that these ripples occur at the boundary that mixes the individual PDFs, e.g., where the PDF for clusters containing 2 particles merges with the PDF for clusters containing 3 particles. Given that having clusters on these boundaries is less likely, it could explain such oscillations in the PDF. These ripples, however, disappear or become less ‘intense’ for larger clusters sizes containing many particles. From our analysis, filtering out these ripples is equivalent to leaving out small, power law dependent clusters.

B. An approach to disentangle turbulence from random fluctuations

Considering the results of the previous section, a complementary methodology to the classical algorithm [23] is needed to discern turbulence-driven clusters from concentration fluctuations of random uncorrelated particles.

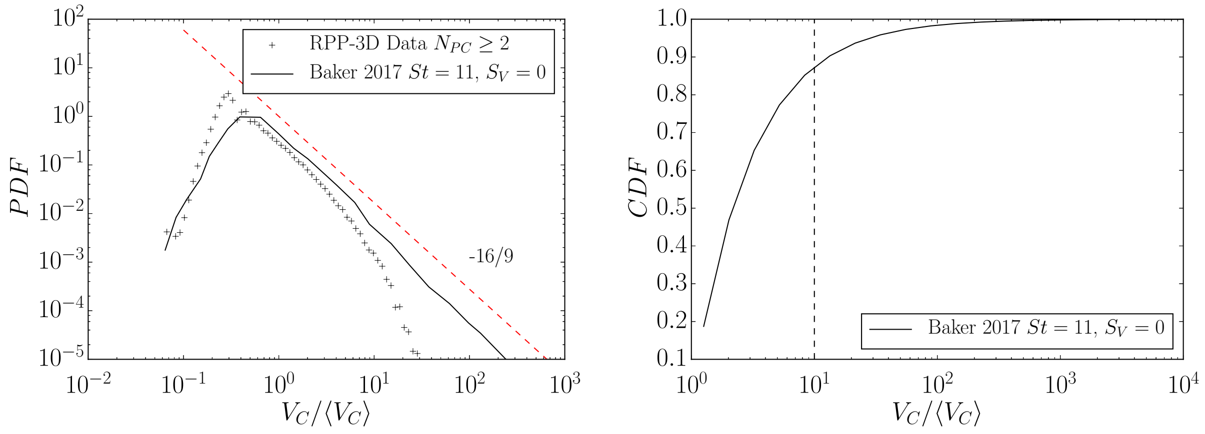

(a)

(b)

FIG. 11: PDFs of 3DVOA (DNS data of Baker et al. [8] for $St = 11$, and $S_v = \tau_p g/u' = 0$) for normalized cluster volume $V_C/\langle V_C \rangle$. Baker et al. suggest that turbulence driven clusters are the ones for which for $V_C > \eta^3$ or $V_C/\langle V_C \rangle > 1$. The figure shows that their criterion might fail (see figure 11b) for almost the first decade of clusters (several points). b) CDF of 3DVOA (DNS data of Baker et al. [8] for $St = 11$, and $S_v = \tau_p g/u' = 0$) for normalized cluster volume $V_C/\langle V_C \rangle$. The vertical dashed line (- - -) line represents up to the range where RPP-3D generated data follows a distinguishable power law (see figure 11a).

With this goal, we briefly recount proposed fixes found in the literature, and analyze their fitness to solve the mentioned problem. Baker et al. [8] have proposed an amendment in the context of 3D Voronoï tessellations. Their underlying principle is that only the clusters lying on the right tail of $V_C/\langle V_C \rangle$ (see figure 11a) should be considered as turbulence-driven 'coherent' clusters. However, our data, and histogram analyses (figures 9a, and 9b) challenge this argument, since the clustering algorithm applied to synthetic 3D RPP data still yields a self-similar behavior for the clusters volume distribution ($V_C/\langle V_C \rangle$). This behavior lasts for at least a decade, before transitioning into an exponential decaying behavior in agreement with the S_N analysis. Thus, by following strictly this criterion, a large number of 'random' (see figure 11b) clusters could remain after the additional step proposed, and be counted as turbulence-induced clusters (see figures 11a and 11b), defeating the purpose of such amendment.

An alternative test to distinguish randomness from turbulence-driven clusters has been proposed by Uhlmann and collaborators [6, 15]. It involves comparing the 3D clusters mean aspect ratio when clustering is present, as turbulence-driven clusters would have larger aspect ratio than randomly generated cells, due to gravity and enhanced particle settling. This criterion, however, could become less accurate as the clusters become less columnar.

On the other hand, the analyses presented in the previous section suggest a methodology based on segregated cluster probability S_N (figure 9a). According to these analyses, one expects that the right tail of the turbulence-driven cluster size distribution (in any dimension), conditioned on the number of particles in the cluster (N_{PC}) would preserve the powerlaw behavior at increasing thresholds of N_{PC}; whereas for random data this behavior would be eventually lost at increasing N_{PC}.

For the 1D case, this segregation approach seems promising, as despite having a very weak power-law dependency (perhaps due to the limited amount of data from the records from Sumbekova [35]), the clustering containing data seems to preserve its power law behavior up to cluster of four or more points ($N_{PC} \leq 4$) (see figure 12a).

In 2D, the segregation approach is very effective (figure 12b) as the right tail PDF power law behavior (figure 9a) is conserved at increasing the values of N_{PC}. This is in agreement with the S_N analysis (figure 9a), and consistent with the mentioned conjecture that turbulence-driven clustering will preserve its power law behavior at increasing values of increasing N_{PC}.

In 3D, the clustering containing results apply to a larger extent their power law dependency, and the respective 3D random data eventually decays exponentially at around $N_{PC} > 20$ (see figure 12c), consistent with the transition found in S_N (figure 9a).

Thus, an analysis of the clusters histograms conditioned on the number of particles N_{PC}, is a promising complementary step to detect the presence of turbulence-driven clusters, as it seems capable of detecting and avoiding the possibles biases present in cluster identifying algorithms [8, 23] in any dimension.

V. CLUSTERS CONCENTRATION 1D

A. Average cluster concentration

Knowledge of the particle local concentration is of the foremost importance in the study of particle-laden flows [31], and its potential applications. The easy access to local concentration maps is what gives Voronoï tessellations the upper hand with respect to different available methods [10, 23].

However, taking into account the results from sections III A-III B , the probe measuring volume will have an impact on the estimated local concentration values, when these tessellations are applied to 1D records. In this section, we conduct a sensitivity analysis on the projected data (analogous to the one found in section III B for the average cluster size), and for the same data found in table I. We then define the cluster concentration as $C_C = N_{PC}/L_C$, where N_{PC} is the number of particles inside the cluster, and L_C is its length. The average concentration of the entire record is defined as $C_0 = N_P/L_R$, where N_P is the total number of particles detected over the total length recorded L_R, which is close to the inverse of the average Voronoï length [3] $C_0 \sim 1/\langle L\rangle = f(\mathrm{MWS})$.

The analysis by varying windows shows that the average cluster concentration value $\langle C_C/C_0\rangle$ has a non-monotonic behavior which depends on the measuring window size, and the bulk liquid fraction ϕ_v (although only one dataset is shown in figure 13 the remaining data sets -not shown here- exhibited the same behavior). There is also a transition region similar to the one found in the normalized average cluster size $\langle L_C\rangle/\eta$ (see figure 7b), and after this region the concentration tends to a value close to 3.

For the transition region, the data points with a measuring size of order η are in good agreement with previous 1D and 2D experimental data, i.e., $\langle C_C/C_0\rangle \in [2.0 - 5.0]$ [23, 27, 35]. Although a comparison between the 1D and the 2D average cluster concentration values $\langle C_C/C_0\rangle$ was not conclusive due to the uncertainty in the lower to higher dimension extrapolation [54], it seems that our approach also captures the leading order evolution of the average cluster concentration.

The latter supports again that under similar experimental conditions an instrument with with measuring window size of order η, is able to recover global average clustering parameters which are in agreement with previous data captured with higher dimensional techniques.

On the other hand, at increasing MWSs values, the cluster concentration approaches asymptotically to $\langle C_C/C_0\rangle \approx 3.0$; cluster density varies proportionally with the MWS in agreement with arguments of section III B. It is, however, important to notice that $\langle C_C/C_0\rangle \approx 3.0$ is very close to the value attained when the same algorithm is applied to the denser regions of RPP distributions in any dimension. We can estimate this concentration analytically for the RPP distribution, if we take account that $C_0/C \approx \langle L\rangle|_0^{\mathcal{V}_{th}} =$

$K\int_0^{\mathcal{V}_{th}} \mathcal{V}^2 e^{-2\mathcal{V}} d\mathcal{V}$ (K is a normalization constant see equation A2) for $\mathcal{V}_{th} = 0.55$, $C_0/C \approx \langle L\rangle|_0^{\mathcal{V}_{th}} \approx 0.332$, or $C/C_0 \approx 3$. Given the similarity between the RPP, and turbulence-driven values, care has to be taken when drawing conclusions based on average cluster concentration.

B. Concentration PDFs

We now explore the concentration PDFs, and their sensitivity to variations with the measuring window size. Similar to the clusters PDF, the 1D concentration PDFs of synthetic random and clustering containing data have a close resemblance (figure 14a).

The concentration PDF also follows a -4 exponent, as reported by Sumbekova via PDI measurements [26]. This exponent, however, is a trivial result of the unidimensional tessellation, as it can be analytically estimated; given that $C_C \sim L_C^{-1}$, so that $\mathrm{PDF}_{C_C}(C_C) \sim \mathrm{PDF}_{L_C}(1/C_C) \times C_C^{-2}$ by the chain rule [55]. Then, for the region $L_C/\langle L\rangle \ll 1$, $C_C \gg 1$, where the cluster size PDF_{L_C} exhibits a power law with exponent of 2 (figure 8b), it follows that $\mathrm{PDF}_{C_C}(C_C) \sim L_C^4 \sim C_C^{-4}$, and thereby, the -4 exponent.

Thus, to gain more insight into the effects of turbulence on C_C, we conditioned the clusters based on their number of particles, as proposed in section IV B. Although mild differences are found between clustering, and random generated data at very small N_{PC}, the preferential concentration data shows that it is almost an order of magnitude more likely to find very dense regions $C_C/C_0 > 4$ than in the RPP (see figure 14b) when $N_{PC} > 8$. Previous experiments have shown that particles belonging to ‘compact’ (very dense) clusters exhibit peculiar properties, for instance, enhanced settling velocity due to collective effects [4, 43]. Given these results, it is questionable to neglect those ‘compact’ clusters found at the left region of the clusters PDFs, as proposed by the amendment of Baker et al. [8] also discussed in section IV B.

As a final observation, it seems advisable that future experiments should acquire very long records in order to disentangle, and correctly study statistics conditioned on local concentration as 1D measurements are unable to register enough turbulence-driven clusters events. For instance, the PDI data of Sumbekova [35], contained in its entirety 10^6 samples, which yielded 10^4 clusters with $N_{PC} \geq 2$, and 10^3 clusters for $N_{PC} \geq 10$, which undeniably impacts the convergence of any conditioned statistic.

VI. CONCLUSIONS

Unidimensional Voronoï tessellations to analyse preferential concentration provide results consistent with the mean values of cluster size and concentration reported in previous studies under the same experimental conditions. However, quantifying preferential concentration by means of this analysis has some biases that need to be considered.

It is clear that if unidimensional measurements via 1DVOA recover evidence of particle clustering, i.e., $\sigma_{\mathcal{V}}/\sigma_{RPP} > 1$ following the criteria of Monchaux et al.[23], this evidence is reliable as random distributions cannot create spurious traces of clustering given adequate statistical convergence.

On the contrary, if 1DVOA yields $\sigma_{\mathcal{V}}/\sigma_{RPP} \approx 1$, it cannot be directly concluded that preferential concentration is absent within the flow.

The origin of this effect has been tracked to the measuring window size (MWS): if it is too small or too wide, it might not be able to detect preferential concentration present within the turbulent flow by means of the unidimensional Voronoï Analysis (1DVOA). Thus, MWS plays an important role on preferential concentration measurements that needs to be understood and taken into account.

To capture preferential concentration with 1DVOA, MWS should be a fraction of the expected cluster length, $\langle L_C \rangle$. In the experimental conditions reported here, our results suggest the range of MWS that retrieve preferential concentration may have as lower bound the Kolmogorov length scale (η).

This guidelines are justified by our sensitivity analysis, which shows that the maximum degree of clustering (the magnitude of $\sigma_{\mathcal{V}}$) is found at $\text{MWS}_\star \sim \mathcal{L}/10$, where $\mathcal{L}$ is the integral length scale of the carrier phase. In general, this expression seems to follow $\text{MWS}_\star \sim \langle L_C \rangle$, which combined with $\text{MWS}_\star \sim \mathcal{L}/10$, yields that this window should be of order η consistent with previously reported values of $L_C = \mathcal{O}(10-20)\eta$ under similar conditions.

Hence, a MWS within the latter range may be able to recover meaningful values of the average cluster linear size $\langle L_C/\eta \rangle$, as well as the average cluster concentration $\langle C_C/C_0 \rangle$.

However, it seems that these thresholds (in general) could depend on specific experimental conditions, or DNS simulation conditions, and therefore an iterative procedure for varying the MWS should be put in place if evidence of preferential concentration is not recovered at the first try by unidimensional analysis. This conclusion is supported by the 1DVOA performed on the numerical projections of 3D numerical, and 2D experimental data ($3D_{DNS} \to 1D_{\perp}$, $2D_{EXP} \to 1D_{\perp}$, respectively), and previously reported quasi-unidimensional PDI data.

A pitfall of the 1DVOA is that the 'raw' cluster linear size $L_C/\langle L_C \rangle$ and cluster concentration C_C/C_0 probability density functions (PDFs) might not be insightful for characterizing preferential concentration, as the loss of information inherent to the 1D projections in quasi-unidimensional experimental methods, e.g., PDI, or optical probes, weakens the correlations present within data, and yields as consequence the disapperance of a power law behavior in the right tail of the cluster size PDF.

We develop a simple theoretical model for cluster PDFs from random distributions, which ruled out the existence of a power law within the resulting PDF. However, given the urgent need of characterizing these PDFs, we proposed an alternative filtering approach to disentangle randomness from turbulence clustering. This approach conditions the cluster size PDF by the number of particles in a cluster, N_{PC}, and is based on the premise that if preferential concentration is present in the data, the right tail of the clusters PDF will conserve its power law dependence, as in respective clusters histogram S_N. This could have deep implications when analyzing the impact of collective effects on particles settling velocity via quasi-unidimensional measuring techniques.

Our data suggests that the 2D and 3D Voronoi tessellations (2DVOA/3DVOA) are much more robust to characterize the cluster size PDF than its 1D counterpart. In fact, 2DVOA is very robust and its biases are minimal, as previously demonstrated [56].

3DVOA, however, presents biases that a recently proposed cutoff criterion [8] does not consider. The results presented for the classical cluster detection algorithm [23] applied to 3D random synthetic data, which does not contain correlations at any scale, yielded the presence a power law on the right tail of the cluster size PDF, as reported elsewhere [15, 16]. In 3D, our filtering approach seems promising, as it allows to clearly determine whether the clusters data is coming from a random, or turbulent origin. In the latter case our results confirm that a powerlaw is preserved for a larger extent when compared to the former case.

VII. ACKNOWLEDGMENTS

The authors would like also to thank A2PS for all the material, and support provided during the study of the optical probe. We thank Markus Uhlmann and Agatha Chouippe from KIT for fruitful discussions, and Laure Vignal for her help and insight regarding the experimental setup. The numerical (DNS) Lagrangian data set was provided by the TurBase [28] repository under the project EuHIT: a European High performance Infrastructures in Turbulence (Grant agreement # 312778). Our work has been partially supported by the LabEx Tec21 (Investissements dAvenir Grant Agreement No. ANR-11-LABX-0030), and by the ANR Project No. ANR-15-IDEX-02.

Appendix A: Clusters PDF Model RPP Distribution

In order to model the normalized cluster size PDF for $L_C/\langle L_C\rangle$ coming from randomly generated data (RPP distribution, see table III). The following assumptions were made:

- The normalized cluster size PDF for a cluster population with an arbitrary number of cluster points $L_C/\langle L\rangle|_{N_{PC}}$, where $N_{PC} \geq 2$ is the number of points inside the cluster, is equal to the sum N_{PC} of the independent and identically distributed [57] variables X_i, with $i = 1, 2, 3, \ldots, N_{PC}$;

$$\frac{L_C|_{N_{PC}}}{\langle L\rangle} = X_1 + X_2 + X_3 + \ldots + X_{N_{PC}} \tag{A1}$$

The random variable X_i is distributed as:

$$f(\mathcal{V}) = K_f \begin{cases} \mathcal{V}e^{-2\mathcal{V}} & \text{if } 0 < \mathcal{V} < \mathcal{V}_{th} \\ 0 & \text{otherwise} \end{cases} \tag{A2}$$

$$\langle \mathcal{V}\rangle|_{0<\mathcal{V}<\mathcal{V}_{th}} = \frac{e^{2\mathcal{V}_{th}} - 2\mathcal{V}_{th}^2 - 2\mathcal{V}_{th} - 1}{e^{2\mathcal{V}_{th}} - 2\mathcal{V}_{th} - 1} \tag{A3}$$

$$\frac{\langle L_C|_{N_{PC}}\rangle}{\langle L\rangle} = N_{PC}\langle \mathcal{V}\rangle|_{0<\mathcal{V}<\mathcal{V}_{th}} \tag{A4}$$

where $\mathcal{V}$ is the normalized cell size, $K_f = 0.25\big(1 - (2\mathcal{V}_{th} + 1)\exp(-2\mathcal{V}_{th})\big)$ a constant that accounts for the normalization of the PDF, namely,

$\int_0^{\mathcal{V}_{th}} f(\mathcal{V})d\mathcal{V} = 1$. f is the theoretical model PDF for $\mathcal{V}$ proposed by Ferenc et Néda [3] but with its domain bounded by $\mathcal{V}_{th}$, which is the threshold to compute the clusters.

The sum of N_{PC} independent variables has a PDF equal to the convolution of their respective individual PDFs [55], e.g., $N_{PC} = 2$ (the simplest case):

$$f_2(Z) = \int_{-\infty}^{\infty} f_X(X) f_Y(Z - X) dX \tag{A5}$$

with $Z = X + Y$ (these are dummy random variables, it is equally valid $Z = X_1 + X_2$), considering the support of components distribution, a traditional technique consist in dividing the range of the new random variable in two:

$$f_2(Z) = K_2 \begin{cases} \int_0^Z X e^{-2X}(Z - X)e^{2(X-Z)} dX & 0 < Z \leq \mathcal{V}_{th} \\ \int_{Z-\mathcal{V}_{th}}^{\mathcal{V}_{th}} X e^{-2X}(Z - X)e^{2(X-Z)} dX & \mathcal{V}_{th} < Z \leq 2\mathcal{V}_{th} \end{cases} \tag{A6}$$

Where K_2 is a normalizing constant. As the original variables had a support from $0 < Z \leq \mathcal{V}_{th}$ is straight forward to see that the new support is $0 < Z \leq 2\mathcal{V}_{th}$, further simplifying:

$$f_2(Z) = K_2 e^{-2Z} \begin{cases} \int_0^Z XZ - X^2 dX & 0 < Z \leq \mathcal{V}_{th} \\ \int_{Z-\mathcal{V}_{th}}^{\mathcal{V}_{th}} XZ - X^2 dX & \mathcal{V}_{th} < Z \leq 2\mathcal{V}_{th} \end{cases} \tag{A7}$$

After carrying on the integration:

$$f_2(Z) = K_2 e^{-2Z} \begin{cases} Z^3 & 0 < Z \leq \mathcal{V}_{th} \\ 6Z\mathcal{V}_{th}^2 - Z^3 - 4\mathcal{V}_{th}^3 & \mathcal{V}_{th} < Z \leq 2\mathcal{V}_{th} \end{cases} \tag{A8}$$

The figure 15a illustrates that there is good agreement with the right tail of the distribution between numerically generated data, and the model here proposed. The disagreement in the left tail comes from the nature of this assumption, as we ignore the influence of the neighbours in the construction of the Voronoï cells. However, it seems that this approximation is satisfactory for the right tail of the distribution.

For larger values of N_{PC}, the convolution in 'physical' space becomes cumbersome, and thereby, the duality between the convolution and the Fourier transform, i.e., $\mathcal{F}\{F *$

$G\} = \widehat{F} \cdot \widehat{G}$ is going to be employed to compute the PDF of $L_C/\langle L\rangle|_{N_{PC}}$, for $N_{PC} \geq 3$, whence:

$$f_{N_{PC}} = \mathcal{F}^{-1}\{\prod_{k=1}^{N_{PC}} \widehat{F}\} \tag{A9}$$

being $\widehat{F}$ the Fourier transform of the PDF found in equation A2. This approach (see figures 15a-15b) has good agreement regarding the PDF right tail despite the increase in statistical uncertainty due to the decrease in the number of samples for an increasing N_{PC} (see figure 9a)

It is expected that as $N_{PC} \to \infty$ the PDF collapses into a normal/gaussian distribution due to the central limit theorem [55], as seen in figure 15c. The average of this distribution is given by equation A4, e.g., for $N_{PC} = 30$, $\langle L_C\rangle/\langle L\rangle|_{N_{PC}=30} \approx 10$.

- The second assumption deals with the composition of the PDF for clusters having between $2 \leq N_{PC} \leq N^{\star}_{PC}$, with $N^{\star}_{PC} = 3, 4, \ldots, N$ points.

  The approach taken was to make a mixture model [47], i.e., the composite PDFs will be a weighted sum of the **normalized PDFs** for each N_{PC}. This is written as:

$$f_{2\leq N_{PC}\leq N} = \sum_{k=2}^{N} \alpha_{k-2} f_k l \tag{A10}$$

$$\sum_{k=2}^{N} \alpha_{k-2} = 1 \tag{A11}$$

$$\int_0^{n\mathcal{V}_{th}} f_n(\mathcal{Z}) d\mathcal{Z} = 1 \tag{A12}$$

Being able to compute f_k, the weights α_{k-2} were modeled following a numerical experiment (see figure 9a), which revealed that in 1D there is a predominantly presence of 2-point clusters, and that in turn this presence halves for 3-points clusters, and halves again for 4-point clusters, and so on. This can also be seen as the probability of finding a n-point cluster. The result is plotted in Figure 8b, and it is repeated here for clusters between $2 \leq N_{PC} \leq 25$ (see figure 15d), the latter being the larger cluster detected in the numerical experiment. To change from $L_C/\langle L\rangle$ to $L_C/\langle L_C\rangle$, it is straight forward following the chain rule [55];

$$f_Y(y) = f_X(v(y))|v'(y)| \tag{A13}$$

which completes the explanation of the model here proposed.

Given these previous results and the central limit theorem, one conjectures that for $L_C/\langle L\rangle \gg 1$ the right tail of the clusters PDF will be within an envelope determined only by the weights α_i distribution, regardless of the presence of turbulence. Hence, it validates our model, as our interest is to examine right tail of such PDF.

The left tail however (as explained in the main text) behave as $f(\mathcal{M}_C/\langle\mathcal{M}\rangle < 1) \approx (\mathcal{M}_C/\langle\mathcal{M}\rangle)^\alpha$ behaves as twice this exponent, e.g., $\alpha \approx 2/5/8$ in 1D/2D/3D. The lower exponent than the respective on from our model $\alpha = 3$ is due to our assumptions, as we independently N_{PC} cells PDFs, whereas in reality, due to the tessellation construction the distance between the cells 'centers' is **correlated**, and such correlation seems to be particularly important for small, 'compact' clusters, as for large clusters the joint PDF can successfully modeled as a product of marginal PDFs, as shown.

1. Higher Dimensions

The extension to the previous arguments to higher dimensions has the pitfall of not having analytical PDFs available to do the computations, but rather fits proposed by Ferenc and Néda [3], and therefore, a mismatch is expected. The weights also have a different behavior than their counter part in 1D (see figure 9a). For instance, in 2DVOA the figures 16a-16b reveal that there is an acceptable agreement again with the right tail of the numerical experiment. Proceeding into the compound PDF (equation A10), figure 10a shows that the model captures the changes in the behavior of the numerical PDF (inflection points), however the slope is not *completely* well captured, and effect that might be due to not enough numerical samples, or the inaccuracy of the fits proposed by Ferenc and Néda [3] (error propagation).

---

[1] R. A. Shaw, Particle-turbulence interactions in atmospheric clouds, Annual Review of Fluid Mechanics **35**, 183 (2003).

[2] M. L. Larsen, R. A. Shaw, A. B. Kostinski, and S. Glienke, Fine-scale droplet clustering in atmospheric clouds: 3d radial distribution function from airborne digital holography, Physical review letters **121**, 204501 (2018).

[3] J. S. Ferenc and Z. Néda, On the size distribution of Poisson Voronoi cells, Physica A: Statistical Mechanics and its Applications **385**, 518 (2007), arXiv:0406116 [cond-mat].

[4] P. Huck, C. Bateson, R. Volk, A. Cartellier, M. Bourgoin, and A. Aliseda, The role of collective effects on settling velocity enhancement for inertial particles in turbulence, Journal of Fluid Mechanics **846**, 1059 (2018).

[5] W. Yuan, L. Zhao, H. I. Andersson, and J. Deng, Three-dimensional voronoï analysis of preferential concentration of spheroidal particles in wall turbulence, Physics of Fluids **30**, 063304 (2018).

[6] A. Chouippe and M. Uhlmann, On the influence of forced homogeneous-isotropic turbulence on the settling and clustering of finite-size particles, Acta Mechanica , 1 (2019).

[7] S. Sumbekova, A. Cartellier, A. Aliseda, and M. Bourgoin, Preferential concentration of inertial sub-Kolmogorov particles: The roles of mass loading of particles, Stokes numbers, and Reynolds numbers, Physical Review Fluids **2**, 24302 (2017), arXiv:1607.01256.

[8] L. Baker, A. Frankel, A. Mani, and F. Coletti, Coherent clusters of inertial particles in homogeneous turbulence, Journal of Fluid Mechanics **833**, 364 (2017).

[9] R. Monchaux and A. Dejoan, Settling velocity and preferential concentration of heavy particles under two-way coupling effects in homogeneous turbulence, Physical Review Fluids **2**, 104302 (2017).

[10] R. Monchaux, M. Bourgoin, and A. Cartellier, Analyzing preferential concentration and clustering of inertial particles in turbulence, International Journal of Multiphase Flow **40**, 1 (2012).

[11] D. O. Mora, A. Aliseda, A. Cartellier, and M. Obligado, Pitfalls measuring 1d inertial particle clustering, in *iTi Conference on Turbulence* (Springer, 2018) pp. 221–226.

[12] M. Hong, A. Cartellier, and E. J. Hopfinger, Characterization of phase detection optical probes for the measurement of the dispersed phase parameters in sprays, International Journal of

multiphase flow **30**, 615 (2004).

[13] A. B. Kostinski and R. A. Shaw, Scale-dependent droplet clustering in turbulent clouds, Journal of fluid mechanics **434**, 389 (2001).

[14] R. A. Shaw, A. B. Kostinski, and M. L. Larsen, Towards quantifying droplet clustering in clouds, Quarterly Journal of the Royal Meteorological Society **128**, 1043 (2002).

[15] M. Uhlmann and T. Doychev, Sedimentation of a dilute suspension of rigid spheres at intermediate galileo numbers: the effect of clustering upon the particle motion, Journal of Fluid Mechanics **752**, 310 (2014).

[16] M. Uhlmann and A. Chouippe, Clustering and preferential concentration of finite-size particles in forced homogeneous-isotropic turbulence, Journal of Fluid Mechanics **812**, 991 (2017), arXiv:1612.00318.

[17] M. Uhlmann, Voronoï tesselation analysis of sets of randomly placed finite-size spheres, Physica A: Statistical Mechanics and its Applications , 124618 (2020).

[18] W. Bachalo and M. Houser, Phase/doppler spray analyzer for simultaneous measurements of drop size and velocity distributions, Optical Engineering **23**, 235583 (1984).

[19] A. Jaczewski and S. P. Malinowski, Spatial distribution of cloud droplets in a turbulent cloud-chamber flow, Quarterly Journal of the Royal Meteorological Society **131**, 2047 (2005).

[20] R. E. Britter and S. R. Hanna, Flow and Dispersion in Urban Areas, Annual Review of Fluid Mechanics **35**, 469 (2003).

[21] S. D. Sabatino, R. Buccolieri, and P. Salizzoni, Recent advancements in numerical modelling of flow and dispersion in urban areas: a short review, International Journal of Environment and Pollution **52**, 172 (2013).

[22] M. Obligado, T. Teitelbaum, A. Cartellier, P. Mininni, and M. Bourgoin, Preferential concentration of heavy particles in turbulence, Journal of Turbulence **15**, 293 (2014).

[23] R. Monchaux, M. Bourgoin, and A. Cartellier, Preferential concentration of heavy particles: A Voronoï analysis, Physics of Fluids **22**, 10.1063/1.3489987 (2010).

[24] L. Mydlarski, A turbulent quarter century of active grids: from Makita (1991) to the present, Fluid Dynamics Research **49**, 061401 (2017).

[25] D. O. Mora, E. Muñiz Pladellorens, P. Riera Turró, M. Lagauzere, and M. Obligado, Energy cascades in active-grid-generated turbulent flows, Phys. Rev. Fluids **4**, 104601 (2019).

[26] S. Sumbekova, *Concentration préférentielle de particules inertielles : la structure et la dynamique de clusters*, Ph.D. thesis, Universite Grenoble Alpes (2016).

[27] M. Obligado, A. Cartellier, A. Aliseda, T. Calmant, and N. de Palma, Study on preferential concentration of inertial particles in homogeneous isotropic turbulence via big-data techniques, Physical Review Fluids **5**, 024303 (2020).

[28] R. Benzi, L. Biferale, F. Bonaccorso, H. Clercx, A. Corbetta, W. Möbius, F. Toschi, F. Salvadore, C. Cacciari, and G. Erbacci, Turbase: a software platform for research in experimental and numerical fluid dynamics, in *2017 International Conference on High Performance Computing & Simulation (HPCS)* (IEEE, 2017) pp. 51–57.

[29] J. Bec, L. Biferale, A. Lanotte, A. Scagliarini, and F. Toschi, Turbulent pair dispersion of inertial particles, Journal of Fluid Mechanics **645**, 497 (2010).

[30] J. Bec, L. Biferale, M. Cencini, A. Lanotte, and F. Toschi, Intermittency in the velocity distribution of heavy particles in turbulence, Journal of Fluid Mechanics **646**, 527 (2010).

[31] S. Balachandar and J. K. Eaton, Turbulent Dispersed Multiphase Flow, Annual Review of Fluid Mechanics **42**, 111 (2010).

[32] M. Tanemura, Statistical distributions of poisson voronoi cells in two and three dimensions, FORMA-TOKYO- **18**, 221 (2003).

[33] V. Ramasubramani, B. D. Dice, E. S. Harper, M. P. Spellings, J. A. Anderson, and S. C. Glotzer, freud: A software suite for high throughput analysis of particle simulation data (2019), arXiv:1906.06317.

[34] A. Cartellier and E. Barrau, Monofiber optical probes for gas detection and gas velocity measurements: conical probes, International Journal of Multiphase Flow **24**, 1265 (1998).

[35] S. Sumbekova, A. Aliseda, A. Cartellier, and M. Bourgoin, Clustering and Settling of Inertial Particles in Turbulence, in *Proceedings of the 5th International Conference on Jets, Wakes and Separated Flows (ICJWSF2015)*, Vol. 185 (2016) pp. 475–482.

[36] E. W. Saw, R. A. Shaw, J. P. Salazar, and L. R. Collins, Spatial clustering of polydisperse inertial particles in turbulence: II. Comparing simulation with experiment, New Journal of Physics **14**, 105031 (2012).

[37] F. Toschi and E. Bodenschatz, Lagrangian Properties of Particles in Turbulence, Annual Review of Fluid Mechanics **41**, 375 (2009).

[38] S. Goto and J. C. Vassilicos, Self-similar clustering of inertial particles and zero-acceleration points in fully developed two-dimensional turbulence, Physics of Fluids **18**, 1 (2006).

[39] P. J. Ireland, A. D. Bragg, and L. R. Collins, The effect of reynolds number on inertial particle dynamics in isotropic turbulence. part 1. simulations without gravitational effects, Journal of Fluid Mechanics **796**, 617 (2016).

[40] S. Goto and J. C. Vassilicos, Sweep-stick mechanism of heavy particle clustering in fluid turbulence, Physical Review Letters **100**, 1 (2008).

[41] S. W. Coleman and J. C. Vassilicos, A unified sweep-stick mechanism to explain particle clustering in two- and three-dimensional homogeneous, isotropic turbulence, Physics of Fluids **21**, 1 (2009).

[42] A. D. Bragg, P. J. Ireland, and L. R. Collins, Mechanisms for the clustering of inertial particles in the inertial range of isotropic turbulence, Physical Review E **92**, 023029 (2015).

[43] A. Aliseda, A. Cartellier, F. Hainaux, and J. C. Lasheras, Effect of preferential concentration on the settling velocity of heavy particles in homogeneous isotropic turbulence, Journal of Fluid Mechanics **468**, 77 (2002).

[44] C. P. Bateson and A. Aliseda, Wind tunnel measurements of the preferential concentration of inertial droplets in homogeneous isotropic turbulence, Experiments in fluids **52**, 1373 (2012).

[45] T. Wittemeier and J. S. Shrimpton, Explanation of differences in experimental and computational results for the preferential concentration of inertial particles, Computers & Fluids **173**, 37 (2018).

[46] A. J. Petersen, L. Baker, and F. Coletti, Experimental study of inertial particles clustering and settling in homogeneous turbulence, Journal of Fluid Mechanics **864**, 925 (2019).

[47] S. Frühwirth-Schnatter, *Finite mixture and Markov switching models* (Springer Science & Business Media, 2006).

[48] S. M. Ross, S. M. Ross, S. M. Ross, S. M. Ross, and E.-U. Mathématicien, *A first course in probability* (Prentice Hall Upper Saddle River, NJ, 1998).

[49] D. DeRiggi, A central limit theorem for correlated variables with limited normal or gamma distributions, Communications in Statistics-Theory and Methods **48**, 5213 (2019).

[50] I. A. Ibragimov, A note on the central limit theorems for dependent random variables, Theory of Probability & Its Applications **20**, 135 (1975).

[51] R. C. Bradley Jr, Central limit theorems under weak dependence, Journal of Multivariate Analysis **11**, 1 (1981).

[52] T. Kiang, Random fragmentation in two and three dimensions, Zeitschrift fur Astrophysik **64**, 433 (1966).

[53] R. Zamansky, F. Coletti, M. Massot, and A. Mani, Turbulent thermal convection driven by heated inertial particles, Journal of Fluid Mechanics **809**, 390 (2016).

[54] B. Spinewine, H. Capart, M. Larcher, and Y. Zech, Three-dimensional Voronoï imaging methods for the measurement of near-wall particulate flows, Experiments in Fluids **34**, 227 (2003).

[55] R. V. Hogg, J. McKean, and A. T. Craig, *Introduction to mathematical statistics* (Pearson Education, 2005).

[56] R. Monchaux, Measuring concentration with Voronoi diagrams: The study of possible biases, New Journal of Physics **14**, 095013 (2012).

[57] N. L. Johnson, S. Kotz, and N. Balakrishnan, *Continuous univariate distributions, vol. 2* (John Wiley\& Sons, 1994).

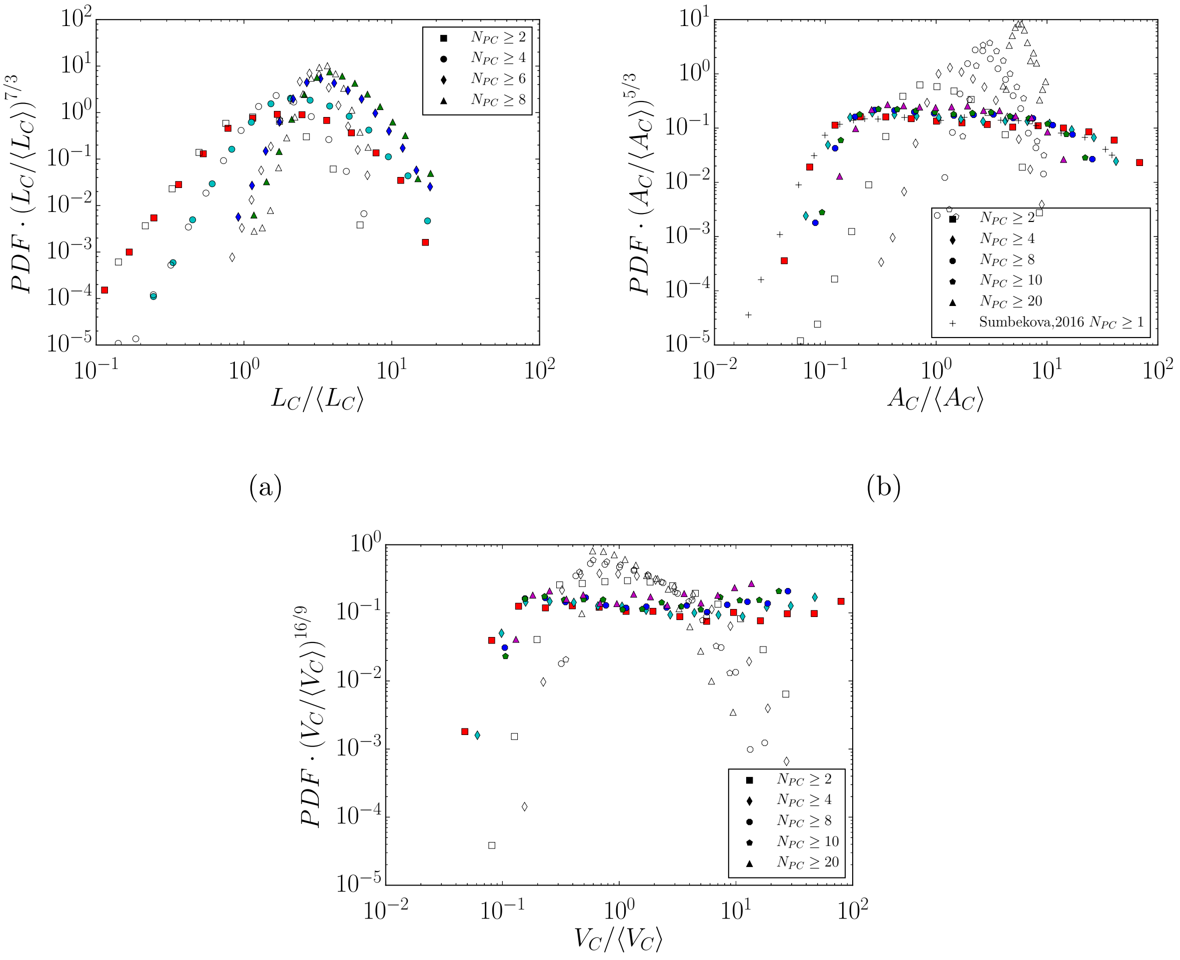

(a)

(b)

(c)

FIG. 12: PDFs of characteristic cluster sizes compensated by the respective voids exponents given by the work of Goto and Vassilicos [38] (7/3 and 5/3 for 1D and 2D in the order given), by Uhlmann and collaborators [15, 16] (16/9 for 3D). Filled symbols the come from the data from in table I, whereas open symbols are data coming from their respective RPP. a) PDFs of $L_C/\langle L_C\rangle$. Filled symbols are experimental data PDI from Sumbekova [35] and the 1D-RPP. b) PDFs of $A_C/\langle A_C\rangle$ for our 2D experimental data base, and the 2D-RPP c) PDFs of normalized cluster volume $V_C/\langle V_C\rangle$ for the DNS data, and the 3D-RPP.

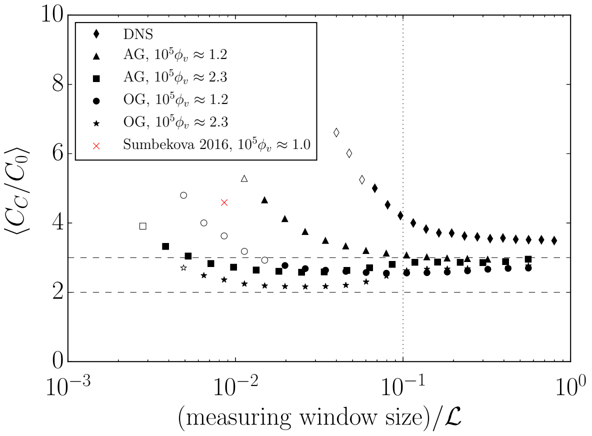

FIG. 13: Average cluster concentration $\langle C_C/C_0 \rangle$ vs the measuring window scale for numerical and experimental data. Filled symbols refer to MWS for which $\sigma_{\mathcal{V}}/\sigma_{RPP} > 1$, whereas blank symbols refer to $\sigma_{\mathcal{V}}/\sigma_{RPP} < 1$ (figure 5a). The X refers to the PDI data from Sumbekova[26] $\langle C_C/C_0 \rangle \sim 4.56$. The larger the number of points projected, the closer the cluster concentration to the value of 3.

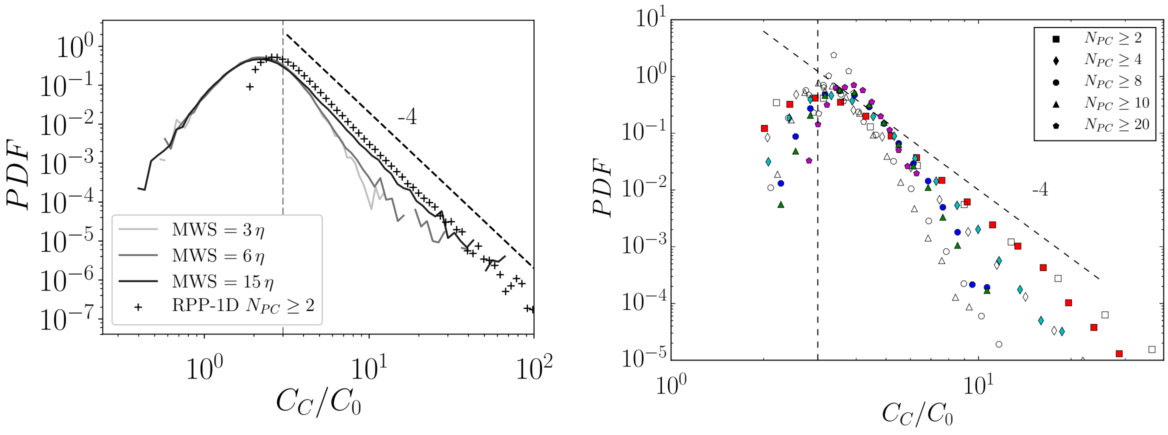

(a)

(b)

FIG. 14: a) PDF of the cluster concentration over global concentration C_C/C_0. For experimental sampled data (EXP-2D-AG-B) ($2D_{EXP} \rightarrow 1D_{\perp}$), and different measuring window sizes (MWS). b) PDF of the cluster concentration over global concentration C_C/C_0. Solid symbols are experimental PDI data [26], whereas open symbols are from RPP-1D data. The vertical (- - -) line represents the asymptotic value $C_C/C_0 \approx 3.0$ found in figure 13. It can be seen that large cluster concentrations have higher probability in clustering containing data than in random data.

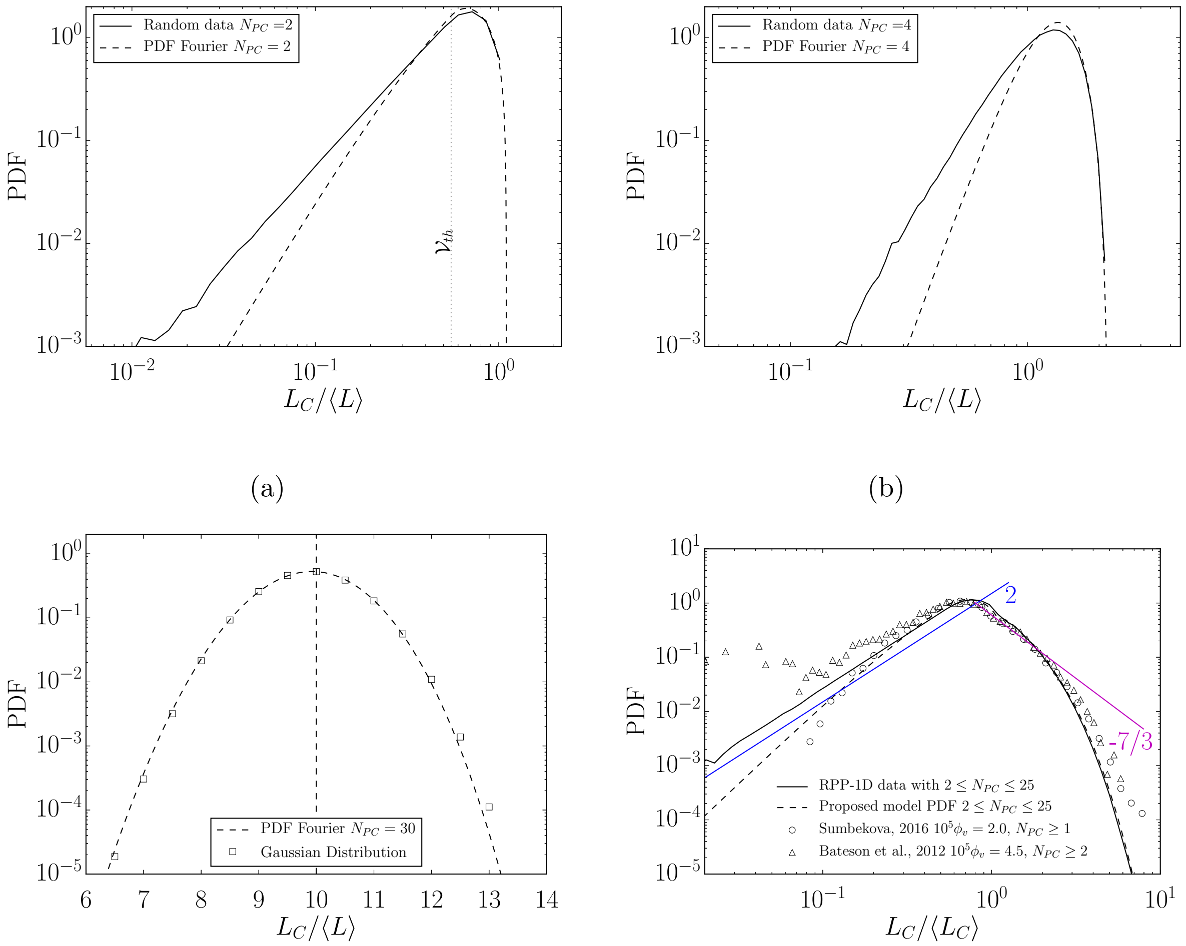

(a)

(b)

(c)

(d)

FIG. 15: a) PDF of the cluster size $L_C/\langle L\rangle$, where $\langle L\rangle$ is the average Voronoï cell size. The plot reveals that the model (equation A8) has good agreement with the right tail of numerical generated data. The plot also shows the Fourier computed PDF. b) PDF of the cluster size $L_C/\langle L\rangle$. The plot reveals that the model (equation A8) has good agreement with the right tail of numerical generated data. The plot also shows the Fourier computed PDF. c) PDF of the cluster size $L_C/\langle L\rangle$ for $N_{PC} = 30$. This figure illustrates that as N_{PC} increases the PDF tends to a normal distribution as expected by the central limit theorem [55]. d) PDF of 1DVOA for normalized linear cluster size $L_C/\langle L_C\rangle$ for a random uniform distribution, experimental data, and the model proposed. For all clusters having between 2 and 25 points (N_{PC}). The model here proposed represents well the right tail of the RPP data, and the marker (□) corresponds to data from [26], which computed the clusters with the condition $N_{PC} \geq 1$. The condition $\mathcal{V} \leq \mathcal{V}_{th} = 0.55$ was employed for clustering computation.

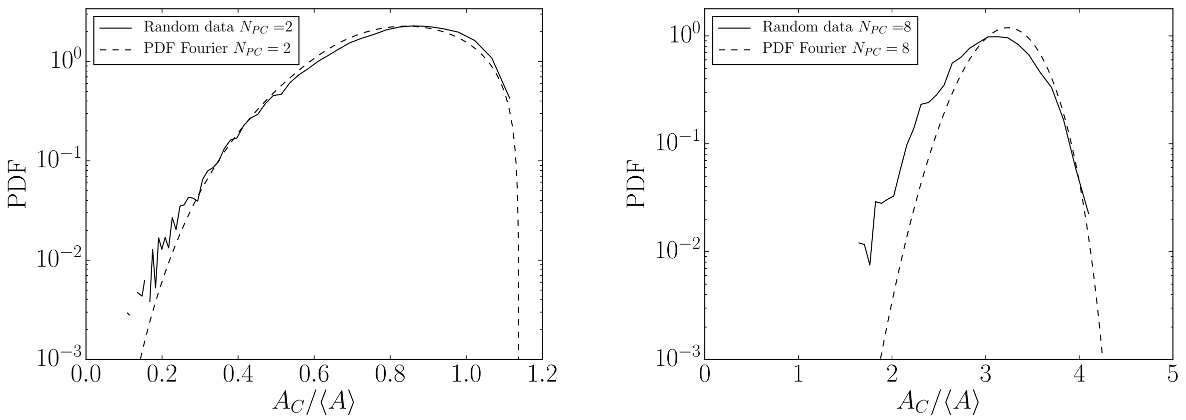

(a) (b)

FIG. 16: a) PDF of the cluster size $A_C\langle A\rangle$. The plot reveals that the model (equation A8) has good agreement with the right tail of numerical generated data. The plot also shows the Fourier computed PDF. b) PDF of the cluster size A_C. The plot reveals that the model (equation A8) has good agreement with the right tail of numerical generated data. The plot also shows the Fourier computed PDF.

5.2 Work division

The work division was as follows:

Author	CR#1	CR#2	CR#3	CR#4	CR#5	CR#6	Score	Position
D.O. Mora	150	20	80	70	100	150	570	1
M. Obligado	50	10	20	20	50	65	215	2
A. Aliseda	10	35	-	-	30	35	110	3
A. Cartellier	40	35	-	10	20	-	105	4
Total	250	100	100	100	200	250	1000	-

The guidelines reflecting the scores and author ordering can be found in the appendix A. The thesis author (D.O. Mora) was engaged in the writing, revision, and and discussion of the paper (see also appendix B).

Chapter 6

Experimental estimation of turbulence modification by inertial particles at moderate Re$_\lambda$

This chapter includes the article:
Mora, D. O. *et al.* Experimental estimation of turbulence modification by inertial particles at moderate Re$_\lambda$**. *Phys. Rev. Fluids* 4, 074309 (7 2019)**

6.1 Summary

In this chapter, we explore the consequences of the mechanical coupling between the carrier and discrete phases on the carrier phase dissipation rate. Some research points out that this coupling [16, 18, 141], and its implications for the turbulent carrier phase could be responsible for the discrepancies found between numerical simulations, and experiments. Balanchandar and Eaton [1] describe it succinctly:

> "Turbulence modulation is important because it can be so large as to qualitatively change the behavior of natural or engineering systems. The mechanisms of turbulence modulation are poorly understood because the wide range of relevant length scales from the particle diameter to the size of the largest eddies causes problems for detailed simulations. Also, ..., it is difficult to acquire accurate turbulence data for the carrier phase in particle-laden flows. ... several different mechanisms can cause turbulence modulation, and sometimes multiple mechanisms act simultaneously. Because of these competing factors, the present state of our knowledge is incomplete, and many contradictory results have been published."

To partially address these open questions, we aimed at estimating the turbulence modification by the particles presence on the carrier phase turbulent dissipation rate ε_p. To achieve this aim, we propose that under some assumptions (e.g. *sub-Kolmogorov* particles) and high enough sampling rate, it is plausible that to estimate the energy dissipation rate coming from a particle record via the extension of the zero crossings method. A method based on the Rice theorem [142], and used as an surrogate to estimate the carrier phase turbulence dissipation rate ε [37, 105, 109].

The results obtained by this method show that the 'two-way' coupling effects could indeed affect the small scale dynamics and may be a key ingredient to understand the underlying physics of particle laden flows. Interestingly, these coupling effects were observed at volume concentrations as lower as $\phi_v = O(10^{-5})$ very close to the limits proposed by Elgobashi [5] via numerical simulations. In other words, it seems that the threshold for two-way coupling effects is much lower than the predicted by Elgobashi. Petersen et al. [17] has also retrieved under similar experimental conditions ($\phi_v = O(10^{-5})$) that the small turbulence scales are indeed affected by the presence of particles, and suggest that preferential concentration may play a role in such turbulence modification.

Among the work developed, this thesis author had the original idea of extending the zero crossing method to estimate λ to the multiphase turbulent flows.

6.1.1 Recent developments

During the course of publication of the article comprising this chapter, two works were also published addressing the influence of the mechanical coupling between the carrier and discrete phases on the particle statistics collected.

First, the PhD thesis of Jérémy Vessaire [143] reports experimental measurements of turbulence modulation taken in a Von-Karman flow seeded with particles of different sizes. The carrier fluid was water, and the particles were made of silica $\rho_p/\rho_f \approx 2.2$. Their experiments run a several rotation rates show that in order to achieve the same rotation rate Ω a higher energy has to be supplied even at even at very small volume fractions. Although the latter effect could explained as a trivial consequence of the increased inertia, they identified that for small particles (i.e. $D_p < 160\mu m$), the additional energy required comes from the particle - turbulence interactions. Given that these small particles have a scale comparable to the carrier phase dissipation range, they suggest that these turbulence-particle interactions have an impact on the carrier phase evolution, and thereby, modify its effective viscosity (rheology effects) leading to the modulation, and the extra energy requirements observed. In our work, we also noticed the trivial observation: more energy was required to drive the particles to a comparable speed than the one found in unladen experiments.

The second recent development is the work of Saito et al.[144]. These authors propose the use of a Damköler number $Da = \phi_v(\mathcal{T}/\tau_p)(\rho_p/\rho_r)$, where $\mathcal{T}$ is the time scale of the largest eddies. They observe that modulation is significant when $Da \gg 1$, and negligible when $Da \ll 1$. They validate this observations by means of two-way coupled simulations, and linear-drag. To compare their predictions with ours results we rewrite the Damköler number as $Da = \phi_v(\mathcal{L}/u)(\rho_p/\rho_r)$, where $\mathcal{L}$ is the integral length scale, and u the velocity fluctuations. Our results (see table I in [105], also shown in the previous section) suggest that at a fixed carrier phase conditions the Damköler number should increase with phi_v, a trend consistent with the larger dissipation rate recovered by our results of St/St_0 (see figure 2b in [105], also shown in the previous section). Likewise, at a fixed concentration ϕ_v, we recovered a smaller dissipation rate with increasing Re_λ. The latter trend (smaller Da) also seems to be consistent with the values of $\mathcal{L}$, and u reported by our experiments (see table I in [105], also shown in the previous section).

We, however, do not have quantitative agreement with Da numbers reported by Saito et al. [144]. An explanation of this discrepancy could be due to the distinct behavior of turbulence modulation in decaying (our experiments) and in forced (Saito et al. study) turbulence [20] .

PHYSICAL REVIEW FLUIDS **4**, 074309 (2019)

Experimental estimation of turbulence modification by inertial particles at moderate Re_λ

D. O. Mora, A. Cartellier, and M. Obligado[*]
Université Grenoble Alpes, CNRS, Grenoble-INP, LEGI, F-38000 Grenoble, France

(Received 10 May 2019; published 29 July 2019)

We advance a method to estimate the carrier-flow dissipation ε_p in the presence of inertial *sub-Kolmogorov* particles at moderate Re_λ. Its foundations rely on the unladen flow dissipation calculation using the Rice theorem, and the density of zero crossings of the longitudinal velocity fluctuation $u'(x)$ coming from a laser Doppler anemometry device. Our experimental results provide strong evidence regarding the non-negligible effect that sub-Kolmogorov particles have on the carrier-flow energy cascade at $\phi_v = O(10^{-5})$, and $\mathrm{Re}_\lambda \in [200–600]$.

DOI: 10.1103/PhysRevFluids.4.074309

I. INTRODUCTION

Several experimental and numerical studies have aimed at quantifying the impact of inertial particles on the turbulent kinetic energy (TKE) and turbulent kinetic energy dissipation (ε) of particle-laden flows. Classical numerical studies have shown that the carrier-phase turbulence remains almost unchanged if the discrete phase volume fraction (ϕ_v) is very small, i.e., $\phi_v \leqslant 10^{-6}$, and very small particles are present ($D_p < \eta$) [1,2], with η the Kolmogorov length scale. Moreover, recent numerical simulations [3–6] have further explored the consequences of slightly larger concentrations [$\phi_v = O(10^{-5})$], and have reported enhancement or damping of ε. These observations show the lack of consensus regarding how ε from the carrier phase is affected by the presence of particles at similar ϕ_v. Furthermore, the underlying mechanism behind such modulation at larger Re_λ is still unclear. For instance, Malloupas *et al.* [6] conducted several fully resolved "four-way" coupling simulations with varying ϕ_v (which consider the particle feedback on the carrier phase, as well as the collisions between particles), and reported the consequences on the energy and dissipation spectra at $\mathrm{Re}_\lambda \approx 35$, which were not present at $\mathrm{Re}_\lambda \approx 58$. Considering that the traditional approach (also known as "one-way coupling," and which considers negligible the impact of the particles on the carrier-phase turbulence) has propelled the development of several theoretical models to describe these flows [7–10], a key improvement including the interaction between the two phases (two-way coupling) would be needed if the latter approach did not hold. Indeed, the one-way coupling hypothesis has not been strictly validated by experiments due to the inherent difficulty [2] to measure the energy dissipation ε with traditional methods, e.g., classical optical techniques; particle image velocimetry (PIV) or particle tracking velocimetry (PTV) resolution is still unable to reliably capture the particle movements at moderate Re_λ.

A classical way to model the particle-fluid interaction has been to consider them to behave as point particles [11], and therefore, they follow the equation

$$\frac{d\mathbf{V}_p}{dt} = -\frac{1}{\tau_p}[\mathbf{V}_p - \mathbf{u}(\mathbf{X}_p, t)], \tag{1}$$

---

[*] Martin.Obligado@univ-grenoble-alpes.fr

with $\mathbf{V}_p$ the particle velocity and $\mathbf{u}(\mathbf{X}_p, t)$ the carrier's flow velocity evaluated at the particle's location $\mathbf{X}_p$, and τ_p is the particle viscous response time $\tau_p = \rho_p D_p^2/18\mu$, with μ the carrier-flow dynamic viscosity, and ρ_p the particle density. Equation (1) is valid given that the particle diameters are less than or equal to the Kolmogorov length scale ($D_p \leqslant \eta$), i.e., *sub-Kolmogorov* particles. The Fourier transform of Eq. (1) yields

$$\hat{\mathbf{V}}_p = \frac{\hat{\mathbf{U}}}{i\omega\tau_p + 1}. \tag{2}$$

Hence, the particle field velocity is a low-pass filtered version of the carrier-phase one, and with the filter being a function of the Stokes number [$\mathrm{St} = \tau_p/\tau_\eta$, with $\tau_\eta = (\nu/\varepsilon)^{1/2}$ the Kolmogorov timescale of the flow, and ν is the air kinematic viscosity, i.e., $\nu = 1.5 \times 10^{-5}\ \mathrm{m^2\,s^{-1}}$] with a cutoff frequency of $f_c = \tau_p^{-1}/2\pi$, or $f_c\tau_\eta = (2\pi\ \mathrm{St})^{-1}$.

Several authors [12–15], starting from Liepmann, have proposed and extended a way to estimate the Taylor microscale (λ) in an unladen flow from the density of zero crossings n_s of the longitudinal velocity fluctuation component $u'(x)$ [13–15] where the temporal measurements are translated into space by means of the Taylor hypothesis. These zero crossings follow a power-law function dependent on the ratio between the flow integral length scale (L) and the size of a low-pass filter η_C (not to be confused with the Kolmogorov length scale η) applied to the "raw" signal. Interestingly, the relation $n_s = f(L/\eta_C)$ reaches a plateau above the cutoff length $\eta_C^\star$ for which $n_s \approx$ const, if $\eta_C \geqslant \eta_C^\star$. More precisely, this plateau occurs when the product of n_s compensated by the average zero crossing distance of the whole signal $\bar{l}$ approaches one, i.e., $n_s\bar{l} \approx 1$, and it provides a criterion to determine whether or not n_s is well resolved. From these observations, and via the Rice theorem, Liepmann [12] proposed $n_s^{-1} = B\lambda$, with B being a constant that accounts for intermittency. Recently, Vassilicos and collaborators [14,16] have used the latter expression in conjunction with $\varepsilon = 15\nu u^2/\lambda^2$ and $u = \langle u'^2\rangle^{1/2}$ to suggest a reliable method to estimate ε, and to ultimately study the effects of the larger scales on the dissipation constant $C_\varepsilon = L\varepsilon/u^3$.

From Eq. (2), if the cutoff frequency f_c is large enough to resolve the dissipation scales, n_s should be recovered regardless of the particle size distribution [provided Eq. (2) still holds]. Thus, it would be feasible to deduce the value of λ from a set of particle velocities, and thereby provide a method to compute ε, at such moderate Re_λ, which is prohibitive for current standard experimental techniques. Hence, under these mild assumptions and having numerous small particles to sample the flow, it is sensible to extend the mentioned approach to particle-laden flows considering that the cutoff wave number $2\pi/\eta_C$, after which Vassilicos and collaborators [14,15] found a plateau in the density of zero crossings n_s, was at least one order of magnitude larger than the Kolmogorov length scale, i.e., a low-pass filtered particle velocity record could still be able to resolve the value of λ, namely, $f_c\tau_\eta = (2\pi\ \mathrm{St})^{-1} > 10^{-2}$, for our data. Therefore, it is reasonable to extend the zero crossing method to particle-laden records with enough particles to sample the carrier flow [see Fig. 2(a) for criteria], and to which Eq. (2) holds. More importantly, as we are aiming at measuring λ, we are directly estimating the effect that particles ("two-way" coupling) have on the carrier-flow dissipation, i.e., the value of the modulated Taylor length scale λ_p, which in turn enables us to compute the modulated dissipation rate ε_p in the presence of particles.

In this paper, we apply the method described above to provide measurements of two-way coupling between the inertial particles and the carrier flow for active-grid-generated turbulence in a wind tunnel at $\mathrm{Re}_\lambda \in [200\text{–}600]$ and at liquid fractions ranging from $\phi_v \in [0.5\text{–}4.4] \times 10^{-5}$. We describe the method to estimate the modulated dissipation rate ε_p (at this moderate value of Re_λ) for particle-laden flows from records taken by a phase Doppler interferometer (PDI) device [17] [a laser Doppler anemometry (LDA)-like instrument] by means of extending the single-phase approach proposed by Vassilicos and collaborators. We also compute L_p from the resampled unidimensional spectrum via $L = \lim_{\kappa\to 0} F_{11}(\kappa)\pi/u^2$ [18], which complies with our low-pass filtering argument [see Eq. (2)] [18], and ultimately leads to the estimation of C_ε, which allows us to partially study the consequences of the turbulence modulation on the carrier-flow energy cascade. First, we briefly comment on the experimental setup. Second, we review the signal postprocessing. Next, we expose a criterion to discard spurious or poorly sampled signals. Finally, we use our results to show two important consequences of the mechanical coupling between the two phases on this system: First, we show that the particles' Stokes number is significantly modified compared to the "one-way" coupling approach, as τ_η is strongly affected by the presence of particles. This has important consequences in terms of scalings, for both preferential concentration and settling velocity modification [3,5,19]. Then, we show that the particles' presence leads to modifications to the dissipation constant C_ε (defined via the relation $\varepsilon = C_\varepsilon u^3/L$). Our results suggest that C_ε evolves with Re_λ and ϕ_v in a nontrivial manner that may suggest changes on the nature of the energy cascade.

II. EXPERIMENTAL SETUP AND SIGNAL PROCESSING

The experiment was conducted in the Lespinard wind tunnel, a closed-circuit wind tunnel with a $75 \times 75\ \mathrm{cm}^2$ square cross section and 4 m long at LEGI laboratory. High levels of turbulence were generated by means of an active grid [20]. Just downstream of it, a rack of spray nozzles produced polydisperse inertial water droplets [21]. This wind tunnel has been extensively used to study the particle-turbulence interaction under homogeneous isotropic turbulent (HIT) conditions (more experimental details are described in Refs. [22–24]). The measuring station was located 3 m downstream the active grid, and at the center line of the wind tunnel, where HIT and the classical scalings from Kolmogorov's theory of 1941 (K41) have been recovered [15]. At this position we set a PDI device (Artium Technologies PDI-200), with an experimental setup, which was almost identical as the one described in Sumbekova [21], with the only difference being two circular holes of 10 cm on each window. The latter was aimed to counteract the water accumulation on the walls (the holes were as small as possible to reduce the perturbation to the fluid flow), which had an impact on the droplet detection, a problem encountered by Sumbekova [21]. The unladen flow was measured by hot-wire anemometry (HWA) (for details, see Ref. [15]), and its characteristics are summarized in Table I. We tried to mimic as closely as possible the horizontal speed U_∞ of the unladen flow, and to vary the volume fraction ϕ_v as much as possible within our experimental limits (see Table I). Each realization consisted of roughly 500×10^3 samples with individual records spanning 10^5 sample points. These records are unevenly sampled due to the very nature of LDA measurements—we treated the records and resampled them to an average acquisition frequency as explained below.

The possibility of estimating the energy spectrum from LDA measurements was recognized early on [26], and several methods are available to account for the bias regarding the nonuniform sampled signal recorded by LDA [27]. These methods aim mainly at computing the autocorrelation function (ACF), which, via the Wierner-Kinchin theorem and the Fourier transform, yields the energy spectrum. Our approach, even though related to these ideas, relies on a different argument. We have resampled the horizontal velocity particle records using a piecewise cubic Hermite interpolating polynomial (PCHIP) [28], at a frequency equal to the average acquisition frequency, i.e., $\langle f_p \rangle = [\text{No. of events}]/[\text{signal length}]$ (see Table I). The longitudinal spectrum for the droplet signals is shown in Fig. 1(a); most of the data sets exhibit a power law close to $-5/3$ over almost two decades.

In general, $\langle f_p \rangle$ is not large enough to properly resolve the Kolmogorov length scale η. The latter, however, does not invalidate our approach, as we are still able to resolve the density of zero crossings [14,16,29], and thereby λ_p from the longitudinal velocity fluctuation u'_p, given that the signal resolution via Taylor hypothesis satisfies the criteria $U_\infty/\langle f_p \rangle = \eta_{pC} = O(\eta_C^\star)$ (sufficient particles to sample the flow), and that $f_c \tau_\eta = (2\pi\ \mathrm{St})^{-1} > 10^{-2}$ (enough resolution to capture the carrier-phase temporal fluctuations responsible for λ at our Re_λ values; see Table I). The latter is supported by the exact relation $\lambda/\eta = 15^{1/4}\,\mathrm{Re}_\lambda^{1/2}$ [18] (see Table I) and the Taylor hypothesis. The selection of the low-pass filter (of length scale η_C) has to be done with care, as some filter types could have a strong impact on the variable $A = \eta_C/\eta$. For instance, in the same facility for the single-phase flow [15], it was found that an antialiasing low-pass filter overestimated the value of A

TABLE I. Parameters of the unladen phase (measured by HWA) at the measuring station 3 m downstream the active grid. L was computed following Ref. [25]. The notation p refers to particle values measured by the PDI device. $\phi_v \approx Q_W/Q_A$, where Q_W and Q_A are the volumetric flux of water and air, respectively. D_p is the droplet diameter. $\langle f_p \rangle$ is the average droplet acquisition frequency.

Re_λ	U_∞ (ms^{-1})	$\langle f_p \rangle$ (kHz)	u/U_∞	u_p/u	$10^{-5}\phi_v$	D_p (μm)	L (m)	ε (m^2 s^{-3})	λ (m)	η (μm)
232	2	[0.35,1.32,1.37]	0.1273	[0.93, 0.95, 1.21]	[0.9, 3.0, 4.4]	[10–200]	0.0570	0.0777	0.0136	457
321	3	[0.39,0.96,1.86,1.85]	0.1343	[0.98, 1.01, 0.99, 1.04]	[0.6, 1.0, 2.0, 3.0]	[10–200]	0.0721	0.2577	0.0119	338
404	4	[0.42,1.08,1.94,2.33]	0.1405	[0.98, 1.01, 1.04, 1.05]	[0.4, 0.7, 1.5, 2.2]	[10–200]	0.0845	0.6058	0.0108	273
503	5	[0.39,1.23,2.23,2.64]	0.1476	[0.97, 1.02, 1.02, 1.05]	[0.4, 0.6, 1.2, 1.8]	[10–200]	0.0980	1.1667	0.0102	231
601	6	[1.33,2.21,2.96,3.74]	0.1541	[0.99, 1.01, 1.00, 1.02]	[0.5, 1.0, 1.5, 2.0]	[10–200]	0.1110	2.1116	0.0098	200
648	7	[1.41,2.38,3.17,4.47]	0.1578	[1.01, 1.01, 1.01, 1.02]	[0.4, 0.8, 1.3, 1.7]	[10–200]	0.1158	3.3862	0.0090	178

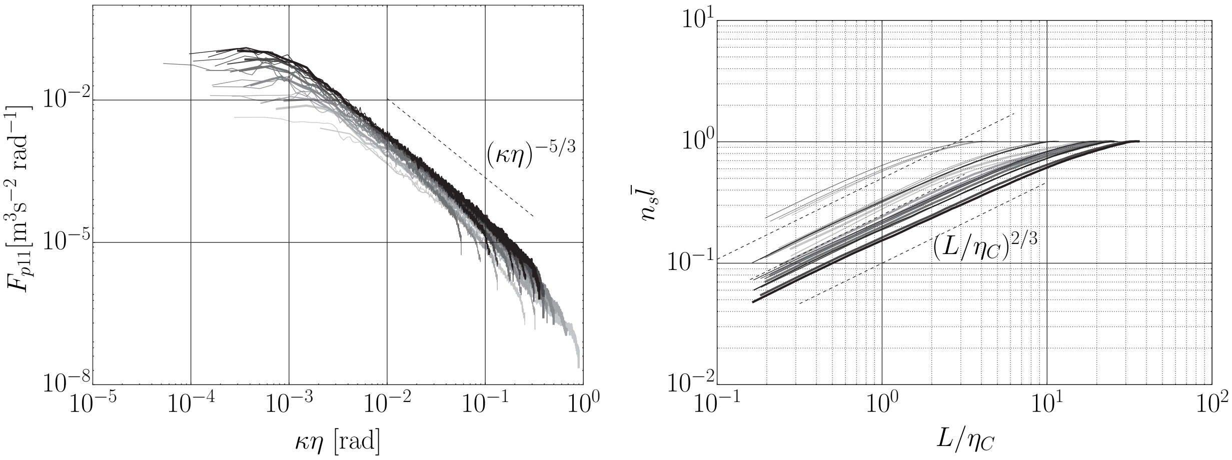

(a) (b)

FIG. 1. (a) Longitudinal energy density spectra F_{p11}. The darker the color, the larger is the mean velocity U_∞. (b) Normalized zero crossing density $n_s\bar{l}$ against the normalized filter size L/η_C. The thicker the line, the larger is the liquid fraction ϕ_v (see Table I).

by 50% (without modifying the obtained values of C_ε and λ). To counter it, we used a sixth-order Butterworth filter [30], as did Mazellier and Vassilicos [14]. This latter filter has proven to be more robust and will allow us directly to compare the values of A obtained on that work.

III. RESULTS AND DISCUSSION

Figure 1(b) shows the normalized zero crossing density $n_s\bar{l}$ for the resampled PDI data, where $\bar{l}$ has been independently obtained by averaging distances between consecutive zero crossings of the unfiltered signal [14], i.e., before applying the filters at different length scales. In order to validate our data for the criterion $U_\infty/\langle f_p\rangle$, we consider the unladen flow values reported by Vassilicos and collaborators [14,29]. They reported that the parameter $A = \eta_C/\eta = O(10)$ for large Re_λ, which quantifies the filter cutoff length η_C [defined as the intersection between a 2/3 power law fitted to the data, and the horizontal line $n_s\bar{l} \approx 1$; see Fig. 1(b)] to the Kolmogorov length scale. The latter value of A has been also recovered at our facility using unladen flow measurements [15].

Figure 2(a) illustrates an expected result; if the average frequency of events is too small, we are unable to properly resolve λ_p. Taking all the records for which $A < 40$ (it has been shown that A is a function of Re_λ [14], and the fits of Mazellier and Vassilicos were slightly wide, hence the value taken of A), the multiphase flow dissipation could be estimated via the expressions $n_s^{-1}|_{\eta^*_{pC}} = B\lambda_p$, where we took $B = 1.2\pi$ as the one found for the unladen flow [15], and $\varepsilon_p = 15\nu u_p^2/\lambda_p^2$, with $u_p = \langle u_p'^2\rangle^{1/2}$. Figure 2(b) illustrates $\mathrm{St}/\mathrm{St}_0 = (\varepsilon_p/\varepsilon)^{1/2}$. We compared the modulated dissipation rate to the unladen dissipation $(\varepsilon_p/\varepsilon)$ rate taken in the same facility via HWA (and computed by integrating the dissipation spectrum; see Ref. [15]), which has a larger temporal resolution that our PDI records, e.g., 50 kHz vs 5 kHz. Next, we compared our data with the two-way coupling direct numerical simulation (DNS) results of Monchaux and Dejoan [5] and Bosse *et al.* [3], which are close in terms of ϕ_v, but are one order of magnitude smaller in Re_λ. We have good agreement at $\phi_v \approx 2\times10^{-5}$. This estimate is remarkably accurate considering the rather simple algorithm followed. Moreover, the results confirm that at fixed concentration $\phi_v \approx 2\times10^{-5}$ the flow becomes less dissipative at increasing Re_λ, consistent with the DNS of Mallouppas *et al.* [6]. On the contrary, for increasing concentration values ϕ_v at fixed Re_λ, ε could be dampened or enhanced by the particles' presence, which is again consistent with the previous DNS results [3,5]. Furthermore, the experimental work from Poelma *et al.* [31] proposed the parameter $\Phi_{\mathrm{St}} = 6\pi^{-1}\phi_v(\eta/D_p)^3\,\mathrm{St}$ to quantify $\varepsilon_p/\varepsilon$, and reporting that for $\Phi_{\mathrm{St}} > 0.003$ this ratio was larger than one (with this relationship being

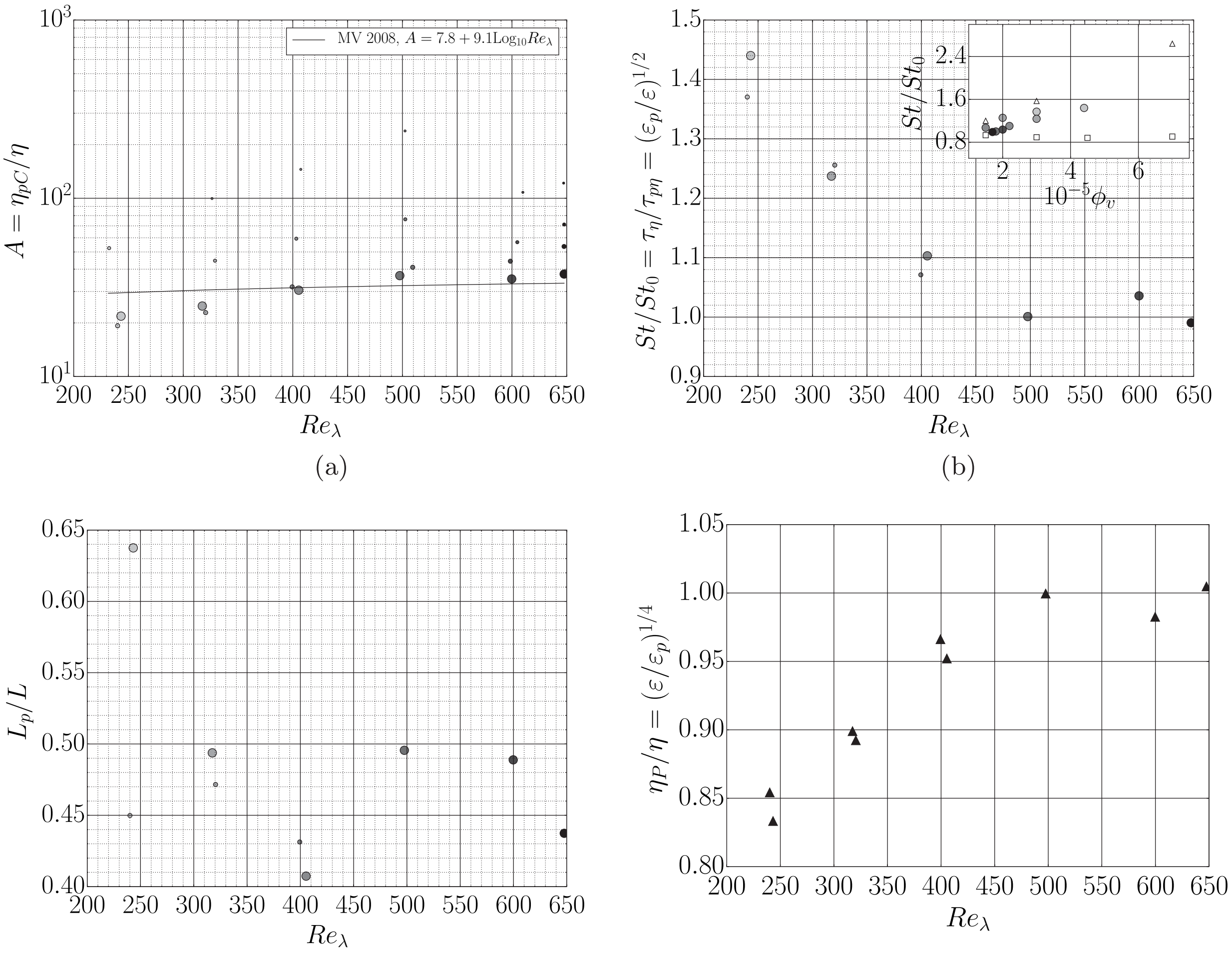

(a) (b)

(c) (d)

FIG. 2. Several parameters plotted against the unladen Re_λ. In all figures, the larger the marker size, the larger is the concentration, and the darker its color, the larger is the Re_λ (see Table I). (b) and (c) cover the data sets from (a) with the condition $A < 40$, $\phi_v \in [1.2\text{–}4.4] \times 10^{-5}$. (a) $A = \eta_{pC}/\eta$. Our values of A are in good agreement with previously reported unladen flow values of (MV 2008: Mazellier and Vassilicos) [14,15,29], i.e., $A = O(10) \approx 7.8 + 9.1 \log_{10} \mathrm{Re}_\lambda$ [14]. (b) Stokes number modification $\mathrm{St}/\mathrm{St}_0 = (\varepsilon_p/\varepsilon)^{1/2}$. In the inset, (△) represents the results of Dejoan and Monchaux [5] for $V_T/u = 1$ (in their notation V_T is the particle terminal velocity), and (□) illustrate the results of Bosse *et al.* [3]. (c) Ratio of integral length scales L_p/L, a factor close to 2 with respect to the unladen flow [15] is due to the method [25] to estimate L_p. (d) Ratio of Kolmogorov length scales; $\eta_P/\eta = (\varepsilon/\varepsilon_p)^{1/4}$.

linear). If we take the Sauter diameter ($D_{23} \approx 60$ μm; $\mathrm{St}_{32} \in [1\text{–}5]$) as representative of our droplet distribution [23], we recover values of $\Phi_{St} \in [0.001\text{–}0.035]$, which are in agreement with the results reported in Fig. 2(b), despite the fact that these authors did their experiments at $\mathrm{Re}_\lambda \approx 30$, and $\phi_v = O(10^{-3})$.

These observations therefore invalidate any approach that does not include the effects of two-way coupling on the carrier-flow turbulence at similar concentration values $\phi_v = O(10^{-5})$, which are very close to the common threshold of $\phi_v = O(10^{-6})$ considered in one-way coupling DNS simulations. On the other hand, one could inadvertently argue that as the Kolmogorov length scale η [see Fig. 2(d)] does not exhibit an abrupt change, the one-way coupling hypothesis could be still valid under certain conditions. Such an argument could have masked these observations and their consequences given that Kolmogorov length scale $\eta = (\nu^3/\varepsilon)^{1/4}$ depends on the fourth root of ε, and could have concealed the physics behind the turbulence modulation phenomenon in previous studies [5].

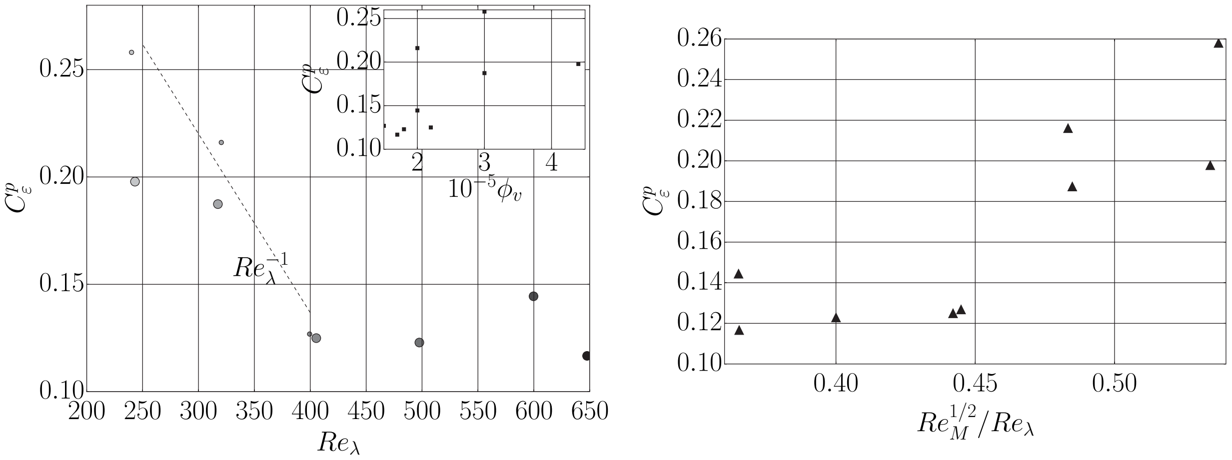

(a) (b)

FIG. 3. Several parameters plotted against the unladen Re_λ for the data found in Fig. 2(b). In the figures, the larger the marker size, the larger is the concentration, and the darker its color, the larger is the Re_λ (see Table I). (a) $C_\varepsilon^p = \varepsilon_p L_p / u_p^3$. The inset shows C_ε^p vs ϕ_v. (b) C_ε^p vs $\mathrm{Re}_M^{1/2}/\mathrm{Re}_\lambda$ as in Ref. [34].

Including these modulation effects could be crucial considering that ε has a strong role enhancing the particle settling velocity in particle-laden flows [8,19,32,33]. In fact, Rosa *et al.* [19] have reported one-way coupling DNS simulations with $\mathrm{Re}_\lambda \approx 200$, where the particle settling velocity enhancement is at least 15% when the turbulence dissipation rate is doubled. Thus, it is necessary to incorporate the two-way coupling in order to properly model the flow physics, for instance, given that $(\varepsilon_p/\varepsilon)^{1/2} = (2)^{1/2} \approx 1.4$ could happen at these values of Re_λ and "low" concentrations as shown in Fig. 2(b).

Finally, we investigate if the energy cascade is being affected by the presence of droplets. Consider that analogous Kolmogorov K41 scalings $\varepsilon = C_\varepsilon u^3/L$ (with C_ε constant for fixed boundary conditions) [35] are applicable to our particle-laden flow, i.e., $\varepsilon_p = C_\varepsilon^p u_p^3/L_p$. The integral length scale for our particle-laden data sets was computed by $L = \lim_{\kappa\to 0} F_{11}(\kappa)\pi/u^2$ [18]. This is the most reasonable method to compute this quantity, given that our records do not possess the characteristics required to apply alternative procedures [25,36]. Hence, an expected discrepancy with a factor close to 2 was found with respect to the unladen data sets [15], which ultimately does not change the functionality of ε.

After applying the latter method to the spectra found in Fig. 1(a) [which, at low values of κ, is unaffected by the low-pass filtering effect of the particles, cf. Eq. (2)], the value of C_ε^p can be estimated. Figure 3(a) reveals that at large Re_λ (computed from unladen phase), C_ε^p reaches a "plateau." The latter can be explained by the following argument: As the turbulence intensity increases, the particle feedback on the carrier-phase turbulence is less and less important, ultimately becoming negligible at $\mathrm{Re}_\lambda \to \infty$, and equal to the single-phase one. However, there is a transition region (that might not necessarily can be classified as finite Re_λ effects [35]) where C_ε^p is roughly inversely proportional to Re_λ, i.e., $C_\varepsilon^p = f(\mathrm{Re}_\lambda^{-1})$. The inset in Fig. 3(a) further illustrates the entanglement between Re_λ and ϕ_v. The latter behavior was previously reported by Valente and Vassilicos [34,35] studying the unladen cascade in grid experiments at similar Re_λ. Although our results were taken at only one position (contrary to the results of Valente and Vassilicos [34], who performed streamwise profiles within the test section), they provide evidence that the carrier-phase cascade might be altered by the presence of *sub-Kolmogorov* particles at similar concentrations ϕ_v and values of Re_λ. Figure 3(b) illustrates C_ε^p against $\mathrm{Re}_M^{1/2}/\mathrm{Re}_\lambda$ as done by Valente and Vassilicos [34]. Re_M is a global Reynolds number that only depends on the inlet conditions (defined here as $\mathrm{Re}_M = U_\infty M/\nu$, with M the mesh size of the grid). From it, there is again a rough linear dependence between C_ε^p and Re_λ^{-1}. The underlying principles of this observation should be addressed in future works. However, this conjecture (if proven correct) critically undermines the one-way coupling approach, widely used in theoretical approaches to model these types of flows, and in numerical simulations [37]. For instance, Bec *et al.* [8], Rosa *et al.* [19], Baker *et al.* [38], and Tom and Bragg [39] have recently reported (by means of the two-way coupling DNS simulations at $\mathrm{Re}_\lambda = O(100)$) several consequences on the particle settling velocity without considering the impact of the turbulence modulation by the particles. For instance, Goto and Vassilicos [29] have shown that the type of DNS forcing has an impact on C_ε. If C_ε were to change, it directly impacts on the scalings via $\tau_\eta = (\nu/\varepsilon)^{1/2}$. In light of our results, future numerical simulations at similar volume fractions should model somehow the feedback of the particles on the flow, and assess whether or not these consequences are captured by the one-way coupling approach. With that given, our observations might be biased by the very nature of our approximation via Eq. (2), as the Lagrangian trajectories of particles do not sample randomly the carrier-flow velocity field (as we know that inertial particles in the range of St, Re_λ, and ϕ_v explored in this work experience preferential concentration). The consistency of our results seems to indicate this effect is not important, but further study is needed to isolate such a contribution.

IV. CONCLUSIONS

We have developed a method to estimate the carrier-phase turbulent kinetic energy dissipation ε_p in the presence of sub-Kolmogorov particles. Our method relies on the extension of the Rice theorem, and the fact that there are enough particles to sample the flow. We proposed criteria to select adequate records, and to avoid excessive bias. Our experimental results show that at $\phi_v = O(10^{-5})$ and $\mathrm{Re}_\lambda \in [200, 600]$ the particles affect the carrier-phase energy dissipation and the turbulent energy cascade in a nontrivial manner. Our observations are consistent with previous two-way coupling DNS studies at similar concentrations. Our results may also have an impact on distinct phenomena on particle-laden flows that depend on the coupling of the particles with the flow, such as preferential concentration and settling velocity modifications.

ACKNOWLEDGMENTS

Our work has been partially supported by the LabEx Tec21 (Investissements d'Avenir Grant Agreement No. ANR-11-LABX-0030), and by the ANR Project No. ANR-15-IDEX-02. We also thank Laure Vignal for her continuous support, and help during the setup of the PDI device.

---

[1] S. Elghobashi, On predicting particle-laden turbulent flows, Appl. Sci. Res. **52**, 309 (1994).

[2] S. Balachandar and J. K. Eaton, Turbulent dispersed multiphase flow, Annu. Rev. Fluid Mech. **42**, 111 (2010).

[3] T. Bosse, L. Kleiser, and E. Meiburg, Small particles in homogeneous turbulence: Settling velocity enhancement by two-way coupling, Phys. Fluids **18**, 027102 (2006).

[4] A. H. Abdelsamie and C. Lee, Decaying versus stationary turbulence in particle-laden isotropic turbulence: Turbulence modulation mechanism, Phys. Fluids **24**, 015106 (2012).

[5] R. Monchaux and A. Dejoan, Settling velocity and preferential concentration of heavy particles under two-way coupling effects in homogeneous turbulence, Phys. Rev. Fluids **2**, 104302 (2017).

[6] G. Mallouppas, W. George, and B. van Wachem, Dissipation and inter-scale transfer in fully coupled particle and fluid motions in homogeneous isotropic forced turbulence, Int. J. Heat Fluid Flow **67**, 74 (2017).

[7] S. Coleman and J. Vassilicos, A unified sweep-stick mechanism to explain particle clustering in two-and three-dimensional homogeneous, isotropic turbulence, Phys. Fluids **21**, 113301 (2009).

[8] J. Bec, H. Homann, and S. S. Ray, Gravity-Driven Enhancement of Heavy Particle Clustering in Turbulent Flow, Phys. Rev. Lett. **112**, 184501 (2014).

[9] P. J. Ireland, A. D. Bragg, and L. R. Collins, The effect of Reynolds number on inertial particle dynamics in isotropic turbulence. Part 1. Simulations without gravitational effects, J. Fluid Mech. **796**, 617 (2016).

[10] R. Dhariwal and A. D. Bragg, Small-scale dynamics of settling, bidisperse particles in turbulence, J. Fluid Mech. **839**, 594 (2018).

[11] M. R. Maxey and J. J. Riley, Equation of motion for a small rigid sphere in a nonuniform flow, Phys. Fluids **26**, 883 (1983).

[12] H. Liepmann and M. Robinson, *Counting Methods and Equipment for Mean-Value Measurements in Turbulence Research* (National Advisory Committee for Aeronautics, Washington, DC, 1953).

[13] K. Sreenivasan, A. Prabhu, and R. Narasimha, Zero-crossings in turbulent signals, J. Fluid Mech. **137**, 251 (1983).

[14] N. Mazellier and J. Vassilicos, The turbulence dissipation constant is not universal because of its universal dependence on large-scale flow topology, Phys. Fluids **20**, 015101 (2008).

[15] D. O. Mora, P. Riera Turró, E. Muñiz, M. Lagauzere, and M. Obligado, Energy cascades in active-grid-generated turbulent flows, arXiv:1903.04258.

[16] J. Davila and J. C. Vassilicos, Richardson's Pair Diffusion and the Stagnation Point Structure of Turbulence, Phys. Rev. Lett. **91**, 144501 (2003).

[17] W. Bachalo and M. Houser, Phase/Doppler spray analyzer for simultaneous measurements of drop size and velocity distributions, Opt. Eng. **23**, 235583 (1984).

[18] H. Tennekes and J. L. Lumley, *A First Course in Turbulence* (MIT Press, Cambridge, MA, 1972).

[19] B. Rosa, H. Parishani, O. Ayala, and L.-P. Wang, Settling velocity of small inertial particles in homogeneous isotropic turbulence from high-resolution DNS, Int. J. Multiphase Flow **83**, 217 (2016).

[20] L. Mydlarski, A turbulent quarter century of active grids: From Makita (1991) to the present, Fluid Dyn. Res. **49**, 061401 (2017).

[21] S. Sumbekova, Concentration préférentielle de particules inertielles: La structure et la dynamique de clusters, Ph.D. thesis, Université Grenoble Alpes, 2016.

[22] M. Obligado, T. Teitelbaum, A. Cartellier, P. Mininni, and M. Bourgoin, Preferential concentration of heavy particles in turbulence, J. Turbul. **15**, 293 (2014).

[23] S. Sumbekova, A. Cartellier, A. Aliseda, and M. Bourgoin, Preferential concentration of inertial sub-Kolmogorov particles: The roles of mass loading of particles, Stokes numbers, and Reynolds numbers, Phys. Rev. Fluids **2**, 24302 (2017).

[24] D. O. Mora, A. Aliseda, A. Cartellier, and M. Obligado, in *Pitfalls Measuring 1D Inertial Particle Clustering, in Progress in Turbulence VIII*, edited by R. Örlü, A. Talamelli, J. Peinke, and M. Oberlack, Springer Proceedings in Physics Vol. 226 (Springer, Berlin, 2019).

[25] A. J. Puga and J. C. LaRue, Normalized dissipation rate in a moderate Taylor Reynolds number flow, J. Fluid Mech. **818**, 184 (2017).

[26] R. Adrian and C. Yao, Power spectra of fluid velocities measured by laser Doppler velocimetry, Exp. Fluids **5**, 17 (1986).

[27] N. Damaschke, V. Kühn, and H. Nobach, A fair review of non-parametric bias-free autocorrelation and spectral methods for randomly sampled data in laser Doppler velocimetry, Digital Signal Process. **76**, 22 (2018).

[28] F. N. Fritsch and R. E. Carlson, Monotone piecewise cubic interpolation, SIAM J. Numer. Anal. **17**, 238 (1980).

[29] S. Goto and J. Vassilicos, The dissipation rate coefficient of turbulence is not universal and depends on the internal stagnation point structure, Phys. Fluids **21**, 035104 (2009).

[30] G. Bianchi and R. Sorrentino, *Electronic Filter Simulation & Design* (McGraw-Hill, New York, 2007).

[31] C. Poelma, J. Westerweel, and G. Ooms, Particle-fluid interactions in grid-generated turbulence, J. Fluid Mech. **589**, 315 (2007).

[32] A. Aliseda, A. Cartellier, F. Hainaux, and J. C. Lasheras, Effect of preferential concentration on the settling velocity of heavy particles in homogeneous isotropic turbulence, J. Fluid Mech. **468**, 77 (2002).

[33] G. Good, P. Ireland, G. Bewley, E. Bodenschatz, L. Collins, and Z. Warhaft, Settling regimes of inertial particles in isotropic turbulence, J. Fluid Mech. **759** (2014).

[34] P. C. Valente and J. C. Vassilicos, Universal Dissipation Scaling for Nonequilibrium Turbulence, Phys. Rev. Lett. **108**, 214503 (2012).

[35] J. C. Vassilicos, Dissipation in turbulent flows, Annu. Rev. Fluid Mech. **47**, 95 (2015).

[36] B. Pearson, P.-Å. Krogstad, and W. van de Water, Measurements of the turbulent energy dissipation rate, Phys. Fluids **14**, 1288 (2002).

[37] S. Elghobashi, Direct numerical simulation of turbulent flows laden with droplets or bubbles, Annu. Rev. Fluid Mech. **51**, 217 (2019).

[38] L. Baker, A. Frankel, A. Mani, and F. Coletti, Coherent clusters of inertial particles in homogeneous turbulence, J. Fluid Mech. **833**, 364 (2017).

[39] J. Tom and A. D. Bragg, Multiscale preferential sweeping of particles settling in turbulence, J. Fluid Mech. **871**, 244 (2019).

6.2 Work division

The work division was as follows:

Author	CR#1	CR#2	CR#3	CR#4	CR#5	CR#6	Score	Position
D.O. Mora	120	20	70	60	80	150	500	1
M. Obligado	130	10	20	20	60	65	305	2
A. Cartellier	-	30	-	10	60	35	135	3
Laure Vignal	-	40	10	10	-	-	60	4
Total	250	100	100	100	200	250	1000	-

The guidelines reflecting the scores and author ordering can be found in the appendix A. The thesis author (D.O. Mora) was engaged in the writing, revision, and and discussion of the paper (see also appendix B).

CHAPTER 7

Energy cascades in active-grid-generated turbulent flows

This chapter includes the article:
Mora, D. O. *et al.* Energy cascades in active-grid-generated turbulent flows. *Phys. Rev. Fluids* 4, 104601 (10 2019)

7.1 Summary

In this chapter, we analyze the unladen phase turbulence characteristics in the wind tunnel test section in LEGI. The interest of exploring these characteristics is due to the recent evidence [31] suggesting that turbulence, even under homogeneous isotropic conditions (HIT), appears to be affected by its turbulence generator, i.e., turbulence seems to remember its initial conditions. The latter phenomenon also referred as *non-equilibrium turbulence*, contrary to the standard 'universality' (memoryless) of small scale scale turbulence given by Kolmogorov K41 scalings (i.e. $C_\varepsilon = constant$), has been confirmed in multiple canonical flows [35] including wind tunnels.

By the same token, research has shown that the turbulence generator, equivalent to the turbulent forcing in DNS simulations, does change the carrier phase topology [37, 115].This observation is relevant for turbulent particle laden flows, as most theoretical approaches to explain preferential concentration and/or particle settling velocity modification assume that the carrier phase follow K41 scalings and/or its consequences, and thereby derive analytical expressions [7, 22]. More importantly, a recent numerical study has advance that the type of forcing used to sustain turbulence in DNS simulation does indeed affect the degree of clustering observed [145].

The objective of this chapter is to investigate whether the active grid could exhibit non-equilibrium turbulence scalings, namely $C_\varepsilon = f(Re_\lambda) \neq constant$, in any operating mode, e.g., triple random or open mode. Our study rules out the presence of non-equilibrium turbulence for active-grid generated flows actuated under a triple random mode, i.e., we recover $C_\varepsilon = constant$ for these flows. On the other hand, we found that when an active grid is set in open mode (minimum blockage) it exhibits turbulence characteristics similar of a flow generated by fractal grids [31], i.e., $C_\varepsilon = f(Re_\lambda)$.

Among the work developed, this thesis author took most measurements of the experimental campaign, *validated the codes to compute the single phase quantities, examined the raw data, and drew some conclusions of this study.*

PHYSICAL REVIEW FLUIDS **4**, 104601 (2019)

Energy cascades in active-grid-generated turbulent flows

D. O. Mora,[*] E. Muñiz Pladellorens, P. Riera Turró, M. Lagauzere, and M. Obligado[†]
Université Grenoble Alpes, CNRS, Grenoble INP, LEGI, 38000 Grenoble, France

(Received 6 May 2019; published 4 October 2019)

The energy cascade and diverse turbulence properties of active-grid-generated turbulence were studied in a wind tunnel via hot-wire anemometry. To this end, two active grid protocols were considered. The first protocol is the standard triple-random mode, where the grid motors are driven with random rotation rates and directions, which are changed randomly in time. This protocol has been extensively used due to its capacity to produce higher values of Re_λ than its passive counterpart, with good statistical homogeneity and isotropy. The second protocol was a static or open grid mode, where all grid blades were completely open, yielding the minimum blockage attainable with our grid. Center-line streamwise profiles were measured for both protocols and several inlet velocities. It was found that the turbulent flow generated with the triple-random protocol evolved in the streamwise direction consistently with an energy dissipation scaling of the form $\varepsilon = C_\varepsilon u'^3/L$, with C_ε being a constant, L the longitudinal integral length scale, and u' the rms of the longitudinal velocity fluctuations. Conversely, for the open-static grid mode, the energy dissipation followed a nonequilibrium turbulence scaling, namely, $C_\varepsilon \sim \mathrm{Re}_G/\mathrm{Re}_L$, where Re_G is a global Reynolds number based on the inlet conditions of the flow and Re_L is based on the local properties of the flow downstream the grid. Furthermore, this open-static grid mode scaling exhibits important differences with other grids, as the downstream location of the peak of turbulence intensity is a function of the inlet velocity; a remarkable observation that would allow one to study the underlying principles of the transition between equilibrium and nonequilibrium scalings, which are yet to be understood. It was also found that a rather simple theoretical model can predict the value of C_ε based on the number density of zero crossings of the longitudinal velocity fluctuations. This theory is valid for both active grid operating protocols (and therefore two different energy cascades).

DOI: 10.1103/PhysRevFluids.4.104601

I. INTRODUCTION

Since the first active grid was proposed by Makita [1], active-grid-generated turbulence has become a standard way to generate moderate-to-high Reynolds numbers in wind/water tunnels [2]. They present several advantages over classical passive grids for wind/water tunnel research, as bespoke nonstationary or inhomogeneous turbulence with relatively large values of Reynolds numbers based on the Taylor microscale, Re_λ, and reasonable homogeneous isotropic turbulence (HIT) conditions, can be generated with active grids. Their use has therefore become widespread in several active research fields, such as two-phase [3,4] and atmospheric flows [5], wind energy [6], and fundamental turbulence [7–10].

In many of these applications, these grids are used to "tune" the turbulence intensity and/or the Reynolds number Re_λ. Several grid protocols are then available to explore the parameter space,

---

[*] Department of Mechanical Engineering, University of Washington, Seattle, Washington 98195-2600, USA.
[†] martin.obligado@univ-grenoble-alpes.fr

but little or no attention has been paid yet to the consequences of them on the energy cascade. For instance, some studies have focused on the characteristics of the turbulent flow for a given blade geometry and initial conditions [11]. Furthermore, other studies have reported values of the turbulent kinetic energy dissipation constant C_ε [12,13], primarily by employing one operating protocol with subtle variations (the one defined as triple random below), with the intent to corroborate the validity of the scalings derived from Kolmogorov's 1941 theory (K41), also detailed below. C_ε is a key parameter to understand these flows, as it can be used to determine the properties of the energy cascade on them (for further details, we refer to the review from Vassilicos [14]).

Therefore, it remains unclear whether the nature of the energy cascade would remain unchanged if strong changes were to be introduced in the grid controlling protocol. The traditional view, derived from Kolmogorov's scalings (and compatible with both of his 1941 and 1962 theories), is that the turbulent kinetic energy dissipation follows the law $\varepsilon = C_\varepsilon \frac{u'^3}{L}$, where u' is the standard deviation of streamwise velocity fluctuations u and L is the longitudinal integral length scale. C_ε is a constant that may depend on the boundary conditions but remains constant for a fixed grid geometry. Recently, several separate studies have reported that these scalings may also be fulfilled within a balanced non-equilibrium cascade [15]. From now on, we will refer to these scalings as "standard" dissipation scalings.

It has been known for some time that grids can generate a region where turbulence is at odds with these laws, i.e., C_ε is not constant, but instead it goes as $C_\varepsilon \sim \mathrm{Re}_G^m/\mathrm{Re}_L^n$, where Re_G is a Reynolds number that depends on the inlet conditions and Re_L is a local, streamwise position-dependent one [14]. The exponents n and m have been found to be very close to unity; $m = n = 1$ for large values of Re_λ. For grid turbulence, $\mathrm{Re}_G = MU_\infty/\nu$, with M being the mesh spacing, U_∞ the inlet velocity, and ν the kinematic viscosity of the flow. The local Reynolds number is defined as $\mathrm{Re}_L = Lu'/\nu$. These high Reynolds nonequilibrium scalings have been recovered in both regular and fractal grids, at a range of downstream positions which starts close to the peak of turbulent kinetic energy and extends well beyond it. Typically, this region spans $x_{\max} < x < 5x_{\max}$, where x is the downstream coordinate from the grid and $x_{\max}$ (see details below) can be predicted as the position where the wakes of the grid bars meet, which hinges on the grid geometry.

The presence of diverse energy cascades would create limitations for the applicability of active grids in some situations, as their respective consequences regarding scales separation, and the number of degrees of freedom (quantified by L/λ), would follow separate laws. "Standard" scalings verify the relation $L/\lambda \sim C_\varepsilon \mathrm{Re}_\lambda$, while high Reynolds nonequilibrium scalings preserve $L/\lambda \sim \sqrt{\mathrm{Re}_G}$ (where both formulas assume $\varepsilon \sim \nu u'^2/\lambda^2$). The latter are independent of Re_λ at fixed Re_G.

This work summarizes a series of experiments on active-grid-generated turbulence. We found evidence that different operating protocols produce different energy cascades. Given the myriad of possible operating protocols, we focused on two extreme cases: one where the grid was static and fully opened, and the other where the grid moved randomly (via the triple-random protocol, explained in the next section). Finally, we show that it is possible to check the consistency of the values of C_ε obtained via an adaptation of the Rice theorem to turbulent flows.

II. EXPERIMENTAL SETUP

Experiments were conducted in the Lespinard wind tunnel at LEGI: a large wind tunnel with a measurement section 4 m long and a square cross section of $0.75 \times 0.75\ \mathrm{m}^2$. Turbulence is generated with an active grid made of 16 rotating axes (eight horizontal and eight vertical, with a mesh size $M = 10$ cm) mounted with coplanar square blades (with also a 10 cm side; see Fig. 1). Each axis is driven independently with a step motor whose rotation rate and direction can be changed dynamically. Two different protocols were tested: one where the blades move randomly and one where they remain static. For the random mode (hereafter referred as active grid or AG), the motors were driven with random rotation rates and directions, which were changed randomly in time (the velocity was varied between 1 and 3 Hz, and changes for a lapse were between 1 and 3 s). This mode

FIG. 1. Picture of the active grid used on the present work.

is of widespread use to generate moderate-to-high Re_λ with good HIT conditions and is usually called the triple-random mode. The second protocol employed was the static open mode (referred as open grid or OG), where the grid was completely open (thus minimizing blockage) and static (and therefore generating low values of Re_λ). More details on the active grid and the wind tunnel can be found in a previous work [3].

All measurements were made by means of a single hot wire, using a Dantec Dynamics 55P01 hot-wire probe, driven by a Dantec StreamLine constant temperature anemometer (CTA) system. The Pt-W wires were 5 μm in diameter, 3 mm long, with a sensing length of 1.25 mm. Acquisitions were made for 300 s at 25 and 50 kHz (while a low-pass filter was always set at 30 kHz to counteract aliasing). It was checked that for all the data sets where C_ε results are reported we have at least $\kappa\eta = \frac{2\pi}{U} f\eta = 1$ (with U the local mean velocity).

For each operating protocol, two different kinds of measurements were done: streamwise profiles at constant inlet velocity U_∞, and measurements at fixed streamwise positions ($x = 150$ and $x = 300$ cm) and varying U_∞. The range of U_∞ explored is imposed by the inherent instabilities of the wind tunnel at low velocities, and by the fact that at high U_∞ the grid motors do not have enough power to compensate for the drag force of incoming wind, i.e., it impairs the randomness of the active grid protocol and the closing of the open grid.

For AG (the active grid protocol), one streamwise profile at fixed inlet velocity was recorded at $U_\infty = 6.7$ m/s between $x = 45$ cm and $x = 325$ cm. Next, profiles at fixed downstream position were taken at five different values of U_∞ (1.8, 2.6, 3.6, 5.2, and 6.8 m/s).

For OG (the open grid protocol), three streamwise profiles at fixed inlet velocity were recorded on a similar range as for AG ($U_\infty = 8.6$, 11.9, and 17.0 m/s). Likewise, the profiles for the fixed downstream position were taken at five different values of U_∞ (4.4, 7.0, 9.7, 12.2, and 14.7 m/s).

The registered time signals were subsequently converted into the spatial domain via the Taylor hypothesis. To account for bias of this method, a modified Taylor hypothesis that takes into account a local mean velocity of the flow [16] was also checked, giving almost identical results in both cases. Figure 2 shows the velocity fluctuations' power spectral density obtained for the whole range of velocities—and modes—at the downstream position $x = 300$ cm. It can be observed that they all exhibit a power law close to $-5/3$. Nevertheless, at low values of U_∞, the OG has a less clear

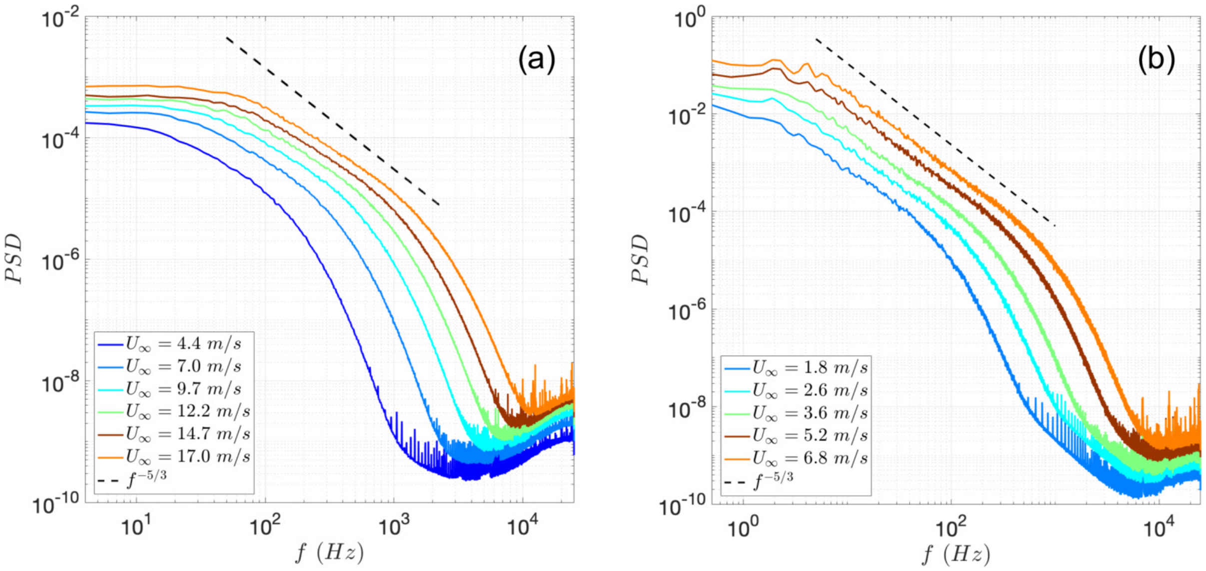

FIG. 2. Power spectral densities of velocity fluctuations obtained at $x = 300$ cm for different values of U_∞ for the open (a) and the active (b) modes. The black dashed line is a $-5/3$ power law.

$-5/3$ exponent, but its shape still remains very similar to other regular static grid spectra previously reported [17].

Large-scale isotropy was quantified with a Cobra probe manufactured by TFI, which is able to compute the three fluctuating velocity components with a resolution of ∼500 Hz. Figure 3 shows the ratios between the three components of the fluctuating velocity vector $\vec{U}' = (u, v, w)$. The active mode exhibits acceptable isotropy conditions, with ratios below 10% for moderate distances away from the grid, i.e., $x > 1$ m. Surprisingly, the isotropy ratios for the open mode are larger (in the order of 30%), and consistent with values reported for fractal grids in the range which comprises nonequilibrium turbulence [18]. Hence, it is seen that reasonable isotropy conditions are found on both modes. However, caution has to be taken when analyzing results coming from the open mode.

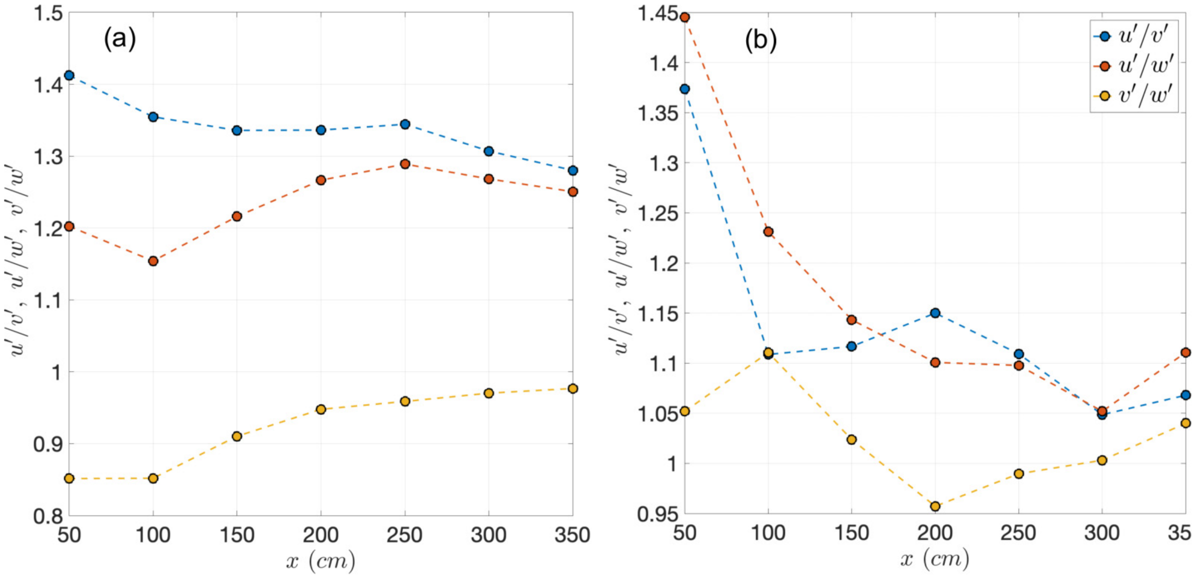

FIG. 3. Ratios between the fluctuating velocity vector $\vec{U}' = (u, v, w)$ components for the open (left) and the active (right) modes. Measurements were taken at $U_\infty = 11.5$ m/s for the first mode and at $U_\infty = 4.9$ m/s for the latter modes.

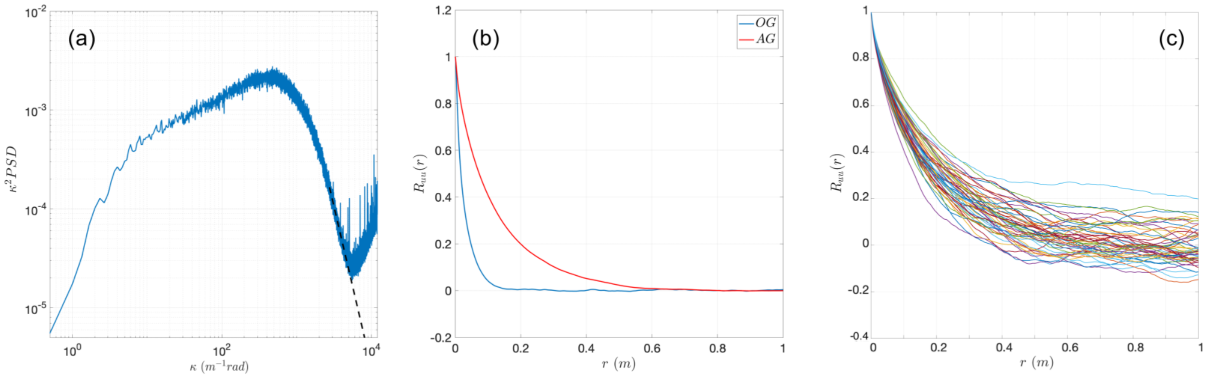

FIG. 4. (a) Estimation of ε via the dissipation spectra; the black dashed line corresponds to the modeled frequencies. (b) Typical autocorrelation functions R_{uu} obtained for both operating modes. (c) Example of the method applied to estimate L for the active mode.

There have been a few studies regarding the turbulence homogeneity in wind or water tunnels employing active grids (see, for instance, [11,19] and the review [2]). Interestingly, Larssen and Devenport ([20]) reported that the flow can be considered as homogeneous if the measuring station is located at two integral length scales from the walls. Another proposed criterion to have homogeneity at the center of the section is to have a mesh size M roughly equal to 10% of the tunnel width [2]. Our measuring station ($75 \times 75\ \mathrm{cm}^2$), and mesh size ($\sim$10 cm) fall within the limits of these criteria, and we will therefore consider our flow to be close to a homogeneous state.

The turbulent dissipation rate ε was estimated via the dissipation spectrum. It was calculated as $\varepsilon = \int 15\nu k_1^2 E_{11} dk_1$ where $E_{11}(k_1)$ is the one-dimensional power spectrum, $k_1 = 2\pi f/U$ is the respective wave number, and f is the Fourier frequency in Hz. The latter involves assuming local, small-scale isotropy and applying the Taylor hypothesis. The noise at high frequencies has been removed and modeled as a power law, fitted for each time signal [Fig. 4(a)]. The Taylor microscale has been obtained from ε as $\lambda = \sqrt{15\nu\langle u^2\rangle/\varepsilon}$.

The integral length scale L was estimated via the streamwise velocity autocorrelation function R_{uu} [Fig. 4(b)]. For OG, it was estimated as $L = \int_0^{r_0} R_{uu} dr$, with r_0 being the smallest value at which $R_{uu} = 0$, and r estimated again via the Taylor hypothesis.

The estimation of L for the AG is more difficult, as the autocorrelation function has the pitfall of not always crossing zero. Thus, it was estimated using a method proposed by Puga and LaRue [13], which consists of dividing the velocity signal into small, not-converged segments, that present a typical dispersion δ in R_{uu} [Fig. 4(c)]. Therefore, L can be computed as $L = \int_0^{r_\delta} R_{uu} dr$, where now r_δ is the smallest value for which $R_{uu} = \delta$. This method, however, presents some ambiguity regarding the absolute value of L, as it strongly depends on the length of the segments chosen to estimate δ. It can be appreciated in Fig. 4 that our choice of small segments yielded large values of δ. This choice reduces the dispersion of L between data sets, but it also reduces the value of L. We have examined for biases with respect to this decision, and it was found that different averages present the same trends.

The previous discussions show that both C_ε and L were estimated without assuming any K41 scalings. Thus, it is possible to compute $C_\varepsilon = \varepsilon L/u'^3$ without any assumptions except for the presence of local homogeneity, which would allow a cascade to operate without interference of one-point flow statistics gradients. The range of turbulence parameters obtained for each operating protocol is shown in Table I. Considering that we have ensured that all our turbulent quantities have reached statistical convergence (as stated, signals were acquired for 300 s), the main error on these parameters comes from the measurement of U_∞ during the calibration of the hot wire (and the subsequent use of the Taylor hypothesis) and from the temperature oscillations (that influence ν). We estimate those errors are roughly ± 0.2 m/s for U_∞, and $\pm 0.5\,^\circ$C (due to possible temperature fluctuations between different calibrations).

TABLE I. Typical turbulence parameter ranges for the open (OG) and active (AG) modes: inlet velocity U_∞, turbulence intensity $u'/\langle u\rangle$, Reynolds number based on the Taylor microscale Re_λ, Taylor microscale λ, Kolmogorov length scale $\eta = (\nu^3/\varepsilon)^{1/4}$, and streamwise integral lengthscale L.

Parameter	OG	AG
U_∞ (m/s)	4.4–17.0	1.8–6.8
$u'/\langle u\rangle$ (%)	2.0–10.0	12.5–45.0
Re_λ	50–200	200–950
λ (mm)	3.0–8.0	7.0–14.0
η (μm)	100–400	100-500
L (cm)	1.0–3.0	5.0–13.0

III. RESULTS

A. Active grid mode

In this section we present results for the grid operated in the active, triple-random, mode. Figure 5 shows different turbulence parameters obtained for the measured streamwise profiles. No peak was observed for the turbulence intensity, including previous measurements done at distance much closer to the grid ($x \sim 10$ cm, not shown here). It can be observed that turbulence intensity has a considerable magnitude, and therefore the Taylor hypothesis should be used with care. Hence, we will only show results in the following for $x > 130$ cm, where the turbulence intensity remains below 25%, similar to results reported in other works [8]. However, the validity of this approach (using the Taylor hypothesis under these conditions) remains an open question and the validity of the use of this hypothesis on active-grid-generated turbulence should be addressed in detail in future works.

From the figures, it can be seen that, first, the magnitude of Re_λ is considerable, and it significantly changes during the downstream evolution of the flow, the latter being an important requirement to disentangle standard from nonequilibrium energy cascade scalings. Second, the length scale L estimated via the method detailed in the previous section is smooth and slightly decreases with x (a surprising result, but similar trends for L have been reported by Thormann and Meneveau for fractal active grids at large x/M [12]). Finally, all parameters from Fig. 5 are quite sensitive to U_∞, even the turbulence intensity (that usually remains constant at fixed x for static grids) and λ and η (not shown in the figure). This phenomenon was also reported in a previous work [11].

The properties of the energy cascade were studied for $x > 1.3$ m (for the reasons previously explained). Figure 6(a) shows C_ε vs Re_λ. There, it can be observed that for all conditions studied C_ε

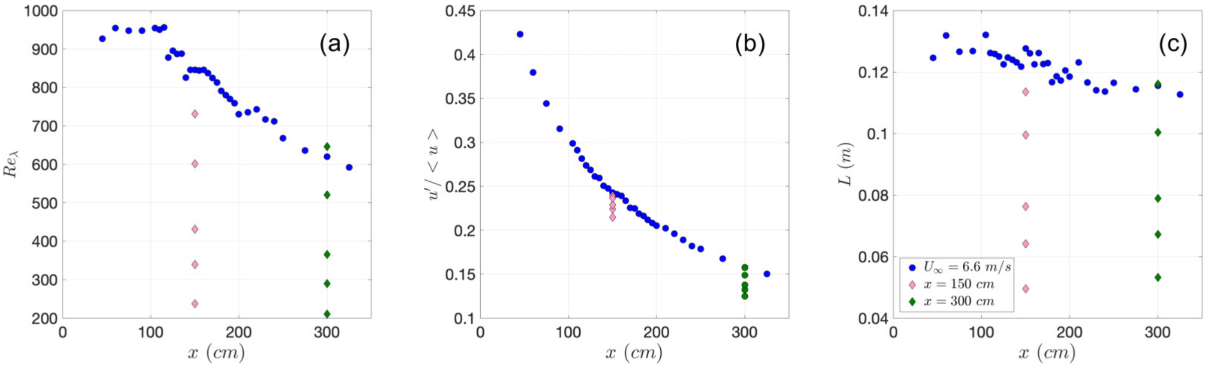

FIG. 5. Streamwise evolution of Re_λ (a), turbulence intensity (b), and integral length scale L (c) for all results obtained for the active mode (AG).

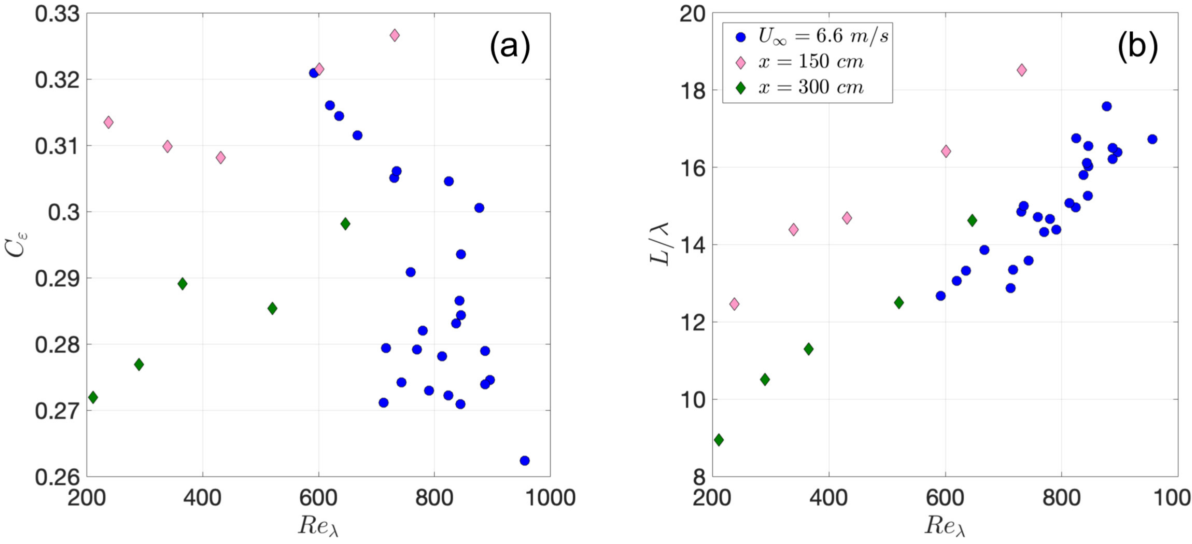

FIG. 6. (a) Plot of C_ε vs Re_λ. (b) L/λ vs Re_λ. Results correspond to all data sets obtained for the active mode.

remains constant: $C_\varepsilon \sim 0.30 \pm 0.03$. This is consistent with standard dissipation scalings and with the relation $L/\lambda \sim C_\varepsilon \mathrm{Re}_\lambda$, that also matches our data [Fig. 6(b)]. The robustness of this outcome validates the use of the Taylor hypothesis in this study and the assumption that the turbulent flow is approximately close to HIT conditions.

Our results, however, differ from those from Puga and LaRue [13] in two ways. First, we do not observe any variation of C_ε with Re_λ (while in the cited work the correlation $C_\varepsilon = 2e^{-0.0108\mathrm{Re}_\lambda} + 0.647$ is proposed). Second, we find smaller values of C_ε. The discrepancy in the magnitudes of C_ε can be attributed to the underestimation of L, as previously detailed. Thus, an alternative method that allows one to check the validity and consistency of the values is required. This will be covered in Sec. III C.

B. Open grid mode

The results for the grid operated in open static mode (OG) are presented below. This case presents important differences with respect to the AG results: for instance, lower values of Re_λ [Fig. 7(a)] and L and much lower values of turbulence intensity. Interestingly, and contrary to the AG, a peak in the downstream evolution of the intensity of the turbulence intensity was captured.

Previous works by Mazellier and Vassilicos [21] and refinements by Gomes-Fernandes and collaborators [22] (for both regular and fractal grids) proposed that the location of turbulence intensity peak could be obtained via the wake interaction length $x_\star$. This model assumes that the maximum of turbulence intensity is a consequence of the interaction between plane wakes, and its downstream location can be therefore modeled, for regular grids, as $x_\star \sim M^2/(C_d t)$, with t being the thickness of the bars and C_d their respective drag coefficient. The value of $x_\star$ depends only on the geometry of the grid and is independent of U_∞ for either regular or fractal grids at large Reynolds numbers.

Conversely, our results with the OG hint that $x_\star$ is an increasing function of U_∞ [Fig. 7(d)]. This is an important difference from previous results in static grids, as it suggest an alternative turbulence generation mechanism not explained by the interaction between wakes, possibly coming from interactions between laminar boundary layers or laminar shear layers, which grow on the surface of the grid blades pointing streamwise. To disentangle the underlying physics of this phenomenon, a broader range of U_∞ should be explored (not currently possible with the present wind tunnel and current grid) in conjunction with a particle image velocimetry (PIV) study close the grid or in the lee of it.

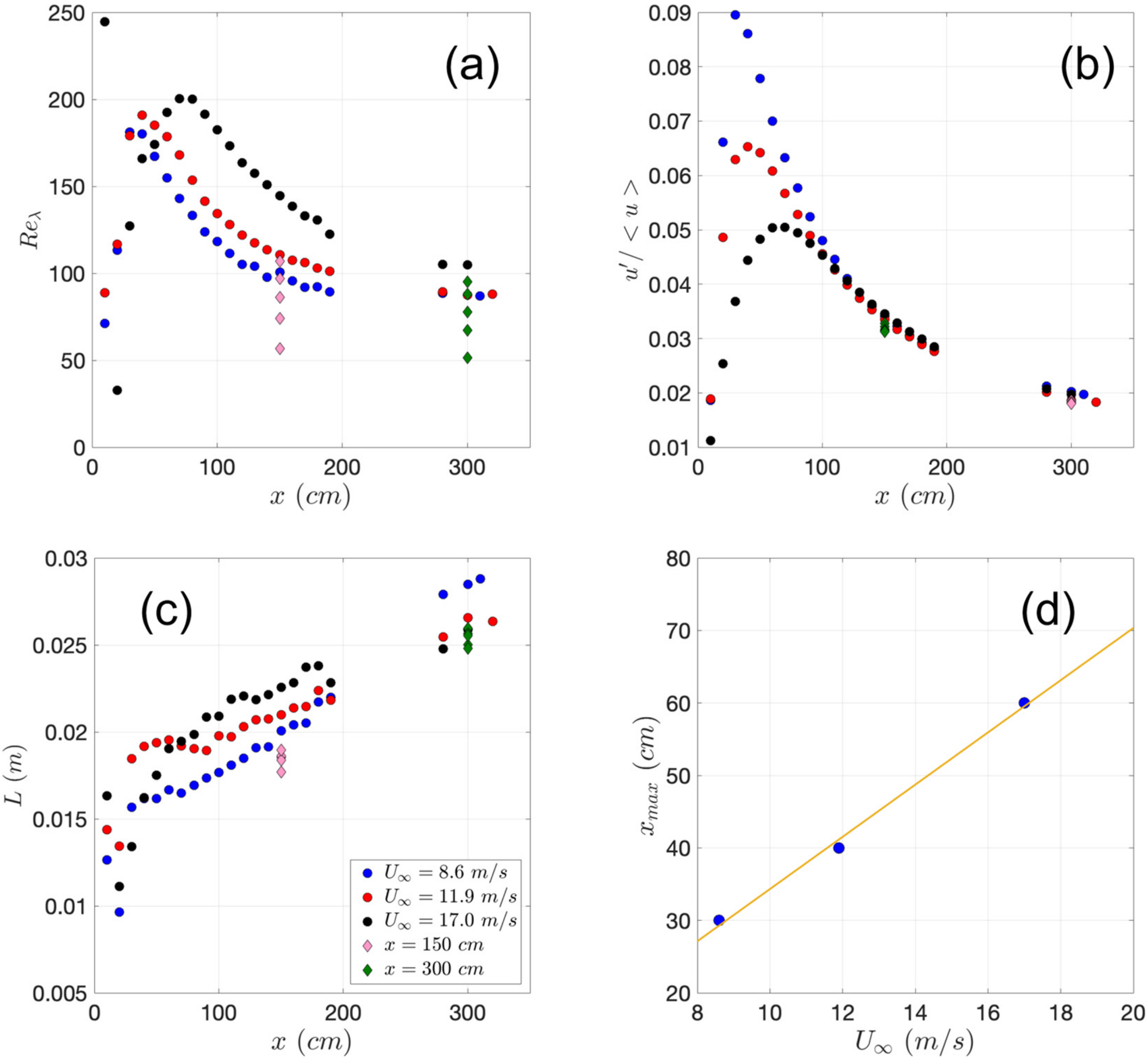

FIG. 7. Streamwise evolution of Re_λ (a), turbulence intensity (b), and integral length scale L (c) for all results obtained for the open mode. (d) Downstream position of the turbulence intensity maximum $x_{\max}$ vs U_∞.

The criterion of Gomes-Fernandez and Vassilicos [22] for the intensity peak is independent of U_∞; it is a consequence of the streamwise scalings of turbulent plane wakes [23,24]. On the other hand, our results exhibit a clear dependence on the inlet velocity, suggesting that the turbulent flow is not entirely (if at all) a result of the interactions between wakes. At our facility, reliable experiments cannot be performed for $U_\infty > 17$ m/s. A broader range of velocities would help to verify how this phenomenon scales with U_∞ and relate it with other mechanisms that may generate turbulent flows, such as laminar and/or turbulent boundary or shear layers interactions. Moreover, it will be very interesting to see how far downstream the peak of turbulence intensity can be shifted (with the consequence that $C_\varepsilon \neq$ constant), and whether or not its downstream location continues to grow with U_∞ or if it has a dependence on the grid or blade parameters. These experiments are of foremost importance, taking into account the research of Mazellier and Vassilicos [25], which cast doubt on the universality of C_ε and its strongly dependence on the flow initial conditions.

As our data for the active mode only exhibit decaying turbulence, we will focus on the same regime for the open mode. We therefore report data only downstream the turbulence intensity peak. Figure 8(a) illustrates that C_ε is a function that varies with $\mathrm{Re}_G/\mathrm{Re}_L$ (and ultimately with Re_λ). Furthermore, at low values of $\mathrm{Re}_G/\mathrm{Re}_L$ it collapses to a straight line, consistent with the high

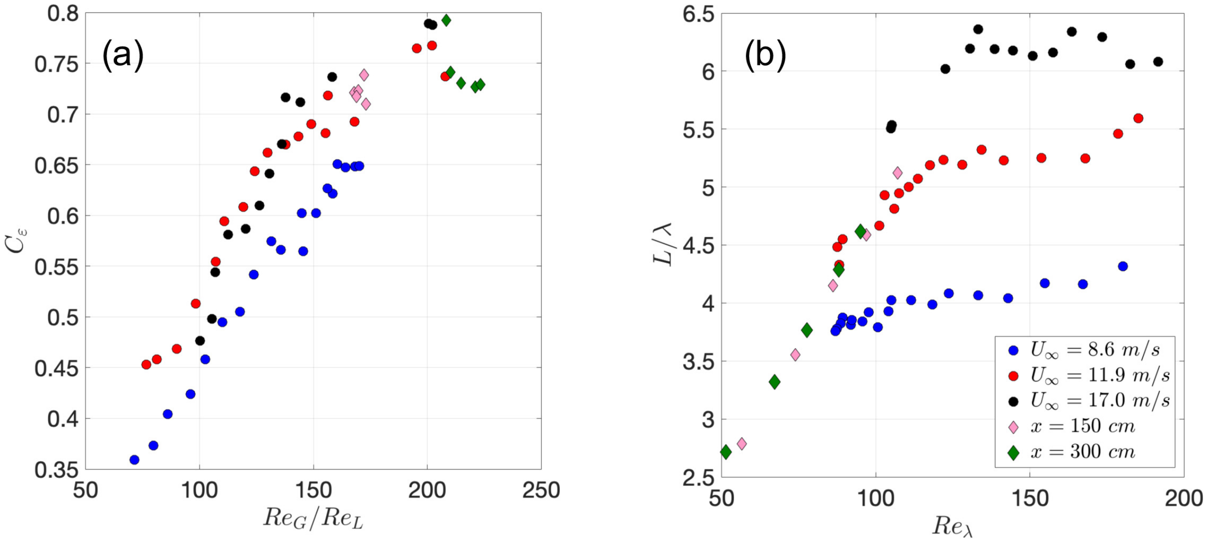

FIG. 8. (a) Plot of C_ε vs $\mathrm{Re}_G/\mathrm{Re}_L$. (b) L/λ vs Re_λ. Results correspond to all data sets obtained for the open mode.

Reynolds nonequilibrium scalings. We also observe that L/λ approaches a constant [Fig. 8(b), the constant having a trend consistent with $\sqrt{\mathrm{Re}_G}$] at large Re_λ (i.e., low $\mathrm{Re}_G/\mathrm{Re}_L$). On the other hand at large $\mathrm{Re}_G/\mathrm{Re}_L$ we note that C_ε becomes constant with Re_λ, and that $L/\lambda \sim C_\varepsilon \mathrm{Re}_\lambda$, consistent with standard dissipation scalings. These figures, similar to those reported by Valente and Vassilicos [26], provide evidence of the presence of both scalings (in separate regions of the flow), i.e., high Reynolds nonequilibrium scalings close downstream from the kinetic energy peak and standard ones after a transition region downstream. The outstanding fact of this transition (previously observed for fractal and regular static grids [26] and in direct numerical simulations of periodic turbulence [15]) is that it occurs at relatively large values of x (while in standard static grids it happens a few cm from the grid), allowing one to capture both regimes in the same experiment. Moreover, the unfixed position of $x_\star$ implies that the open mode can be used to tailor the crossover downstream position between the two scalings. However, the presence of relatively large anisotropy values on the transition downstream position (visible in Fig. 3) suggests that the latter result may not be conclusive. Despite this, and given that the anisotropy barely changes in magnitude for different streamwise positions, the values of C_ε estimated with the full kinetic energy instead of u' follow a similar trend. Further studies on a larger wind tunnel (or with a grid with smaller M) may help to shed light on this phenomenon.

At present, our data suggests that the active grid, depending on the operating protocol selected, will produce different energy cascades, with important consequences for several applications. For instance, apart from the number of degrees of freedom and scale separation, the nature of the cascade will be related to or affected by the persistence of coherent large-scale structures and the turbulent kinetic energy budget, and these will have consequences in terms of turbulence modeling [14,15]. This reinforces the idea to develop an alternative method that allows one to estimate and validate the values of C_ε here obtained.

C. Estimation of ε via the zero crossings of the streamwise velocity fluctuations

Lieppman [27] noticed that the Rice theorem could be applied to the zero crossings of velocity fluctuations to estimate the Taylor microscale λ in turbulent flows. In particular, he mathematically proved that λ is proportional to the average distance $\bar{l}$ between zero-crossings points: $\bar{l} = B\lambda$. The constant B is also defined as $B = C\pi$, where C is a constant that quantifies the non-Gaussianity of velocity derivatives ($\partial u/\partial x$), where $C = 1$ for a Gaussian distribution and $C > 1$ for an intermittent turbulent flow.

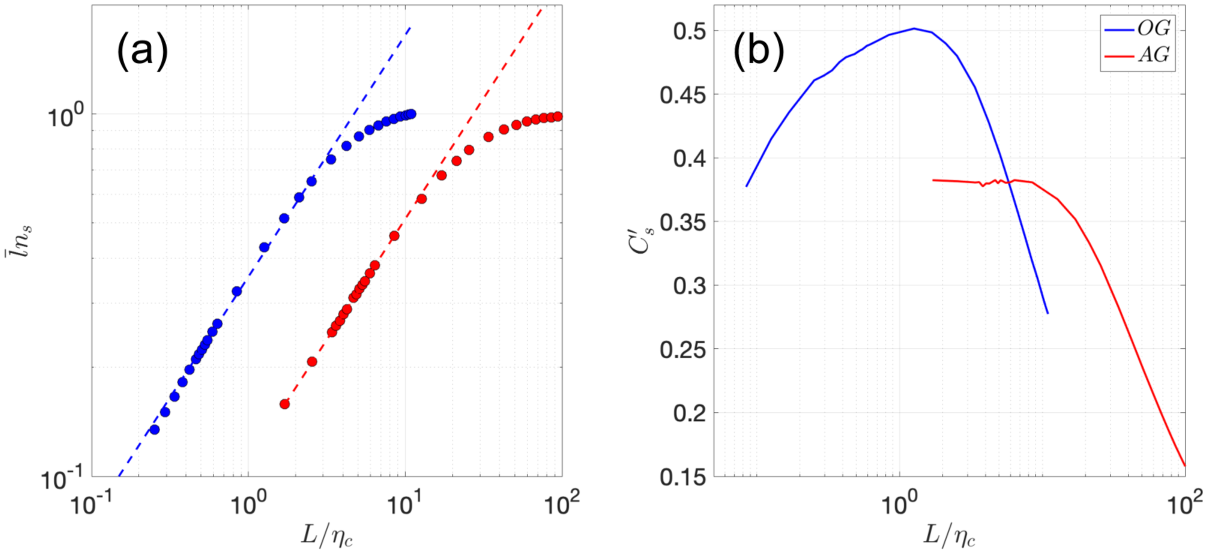

FIG. 9. $\bar{l}n_s$ vs L/η_c (a). The dashed lines are a 2/3 power law. Cs' vs L/η_c (b). Blue lines correspond to the open mode and the red ones to the active one.

However, a theory that allows one to relate C_ε to the number density of zero crossings, n_s, was recently developed by Mazellier and Vassilicos (see [25] for more detailed explanations). This theory relies on the expectation that n_s is a power-law function of L/η_c (as proposed by Sreenivasan and collaborators [28] and by Davila and Vassilicos [29]), n_s being computed after low-pass filtering the turbulent signal with a cutoff frequency $2\pi/\eta_c$ (η_c being the length scale of the filter, not to be confused with the Kolmogorov length scale η). Hence,

$$n_s = \frac{C_s'}{L}(L/\eta_c)^{2/3}, \tag{1}$$

with C_s' a dimensionless constant that characterizes the large scales. The 2/3 exponent is a consequence of the $-5/3$ power-law decay of the power spectral density of the streamwise velocity fluctuations [29]. The constant C_s' also should not be confused with the intermittency constant C (we use the exact same notation and definitions of constants from the seminal work of Mazellier and Vassilicos [25]).

By combining Eq. (1) and the relations $\varepsilon = C_\varepsilon \frac{u'^3}{L}$ and $\lambda = \sqrt{\frac{15\nu u'^2}{\varepsilon}}$, the value of C_ε can be computed as

$$C_\varepsilon = (15B^2)^{3/2}\left(\frac{C_s'}{A^{2/3}}\right)^3, \tag{2}$$

with $A = \eta_*/\eta$. η_* is the value of η_c that corresponds to the intersection of the 2/3 power law and the value $\bar{l}n_s = 1$. At large values of Re_λ, it was found [25] that the latter expression goes as $C_\varepsilon \sim C_s'^3$, which in turn implies that dissipation is controlled by the large scales of the flow. We remark that in the deduction we never required that C_ε be constant (or dependent on $\mathrm{Re}_G/\mathrm{Re}_L$), and therefore Eq. (2) remains valid for any energy cascade (within only approximate HIT conditions, as Mazellier and Vassilicos used the model even for measurements at the center line of a round jet), and in particular for our results for both the open and active modes.

To check the previous prediction, we first checked whether the number density of zero crossings, n_s, followed a 2/3 power law when u was low-pass filtered with different cutoff wave numbers $2\pi/\eta_c$. Figure 9(a) shows that indeed the law was recovered by our data set. As the 2/3 power law has been shown to be a consequence of the $-5/3$ spectrum [30], Fig. 9(a) supports the validity of the results for the OG, that do not clearly follow a power law close to the $-5/3$ law of the velocity

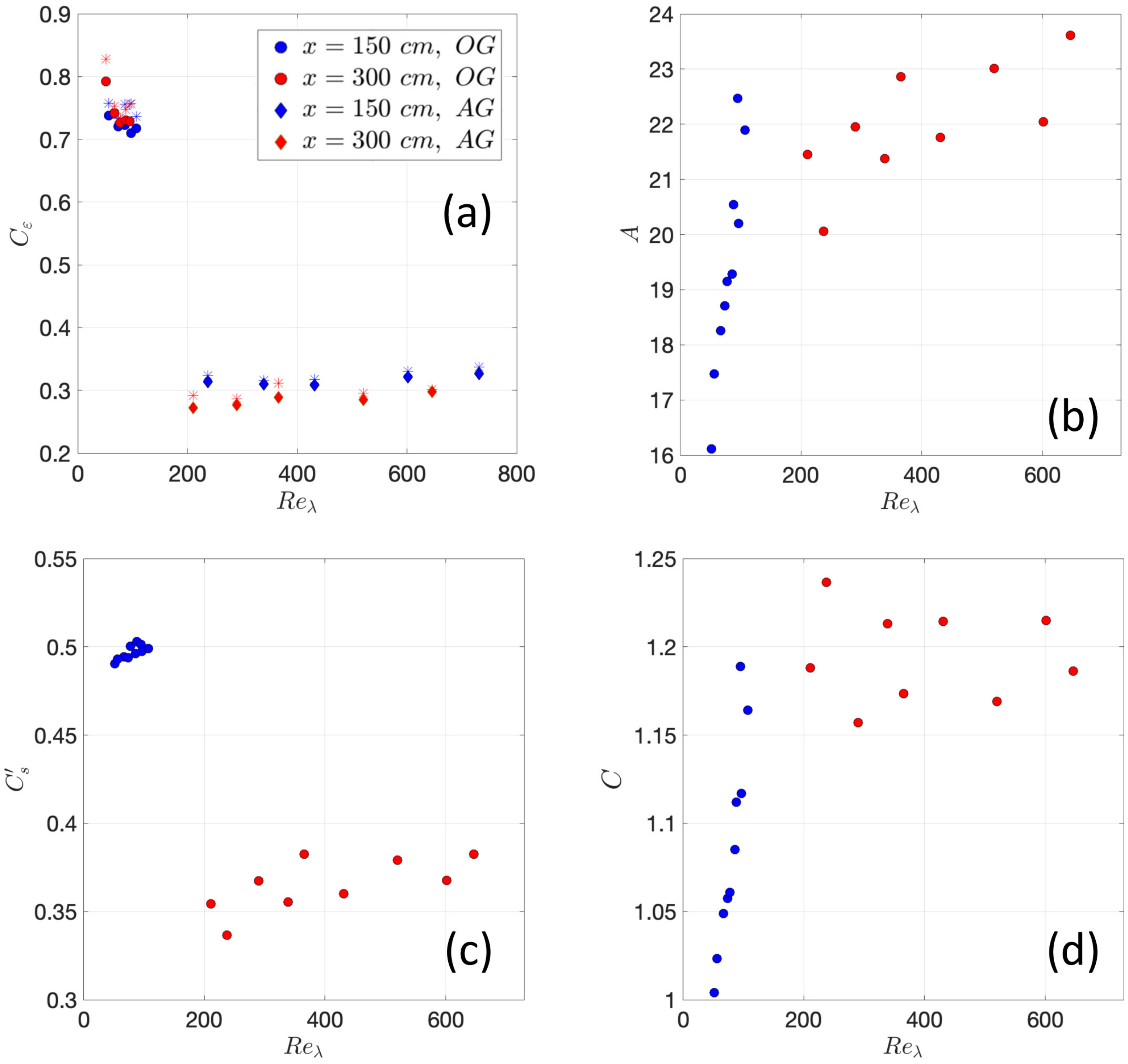

FIG. 10. (a) Comparison of the values $C_\varepsilon^{\text{model}}$ obtained using equation (2) (star symbols) and the experimental ones $C_\varepsilon^{\text{exp}} = \varepsilon L/u'^3$ (filled symbols). Value of A (b), C'_s (c) and the intermittency constant C (d) vs Re_λ for all data sets.

power spectral density (Fig. 2). Furthermore, Fig. 9(b) shows that C'_s is properly defined within the region that follows the power law. The value of C'_s presents a maximum instead of a plateau for the open mode, a consequence of the low values of Re_λ (also observed in previous regular grid measurements at similar values of Re_λ [25]). Therefore, we took the maximum values of C'_s for the open mode.

The results reported here correspond to an antialiasing finite impulse response low-pass filter. We found that the parameter η_* depends on the properties and type of filter used, affecting the values of both A and C'_s. Nevertheless, for all cases, the values of C_ε deduced are very robust [as the dependence on η_* is canceled in Eq. (2)].

Once these requirements were verified, the validity of Eq. (2) could be assessed. The value of C could, in principle, be deduced from the velocity derivatives. However, as the active mode has large values of Re_λ, the convergence of the probability density function of $\partial u/\partial x$ was not completely achieved. Instead, we took this value as $C = \frac{\bar{l}}{\lambda\pi}$.

Figure 10(a) shows streamwise profiles of C_ε for our experimental data and computed from $C_\varepsilon^{\text{exp}} = \varepsilon L/u'^3$ and from Eq. (2) ($C_\varepsilon^{\text{model}}$) for every inflow conditions. The model predictions have good agreement with all values for the whole range of Re_λ. This remarkable result is an observation of the validity of this model for nonequilibrium turbulence, and, more importantly, it confirms the consistency of the values $C_\varepsilon^{\mathrm{exp}}$ here obtained.

Figures 10(b)–10(d) show the values of A, C_s', and C, respectively. It can be clearly seen that these values strongly depend on the operating mode (OG or AG). The intermittency (indirectly quantified by C) increases with Re_λ and seems to reach a constant value of $C \sim 1.2$ for the active grid mode. As A and B tend toward constant values at large Re_λ, we confirm the prediction that $C_\varepsilon \sim C_s'^3$ for large Re_λ.

IV. CONCLUSIONS

We present a systematic study of the streamwise evolution of active-grid-generated turbulence for two paradigmatic operating modes: a high Re_λ active and random mode and a low Re_λ static one. We found clear evidence that the energy cascade may be strongly influenced by the operating protocol. This outcome has important consequences for active-grid-related research, e.g., the interaction of wind turbines with background turbulence, the formation and development of clusters of inertial particles [31], and other phenomena that rely on the nature of a given energy cascade.

We corroborated previous experimental measurements, which showed that C_ε is constant for active-grid turbulence in the triple-random mode (and therefore consistent with both the Richardson-Kolmogorov cascade and a balanced nonequilibrium energy cascade). On the other hand, we observed that, in a region close downstream the turbulent kinetic energy peak, the open mode followed recently proposed high-Reynolds-number nonequilibrium scalings. Furthermore, this mode seems to be generating a particular type of turbulence (not observed before), which is possibly controlled by the boundary and/or shear layers at the blades of the grid, as the wake interaction length (as defined) is an increasing function of the inlet velocity and is not only dependent on the grid geometry.

Furthermore, we find that the mesh size of the grid is no longer a good estimation of L for any of the tested operating modes. The active mode produces integral length scales on the order of the measurement section (as proposed already in [1]). On the other hand, the open mode has an integral scale of around $1/5$ the mesh size. Remarkably, the same relation between L and M is reported by Mazellier and Vassilicos [21] for fractal-grid-generated nonequilibrium turbulence. Although more studies are needed, this coincidence may point towards a general law relating these two length scales of the flow.

Further studies of intermediate protocols, between the static and random ones, could shed light on underlying mechanics behind the transition from standard to nonequilibrium cascades. Our results seem to agree with the suggestion that nonequilibrium turbulence is related to the presence of large-scale coherent structures [15], as the active mode may destroy them very fast while it could be expected that they are more persistent for the open one. Interestingly, in this work the nonequilibrium energy cascade occurs for the flow at globally lower Re_λ, while for a fixed grid geometry these type of cascade occur close downstream from the grid (and therefore where Re_λ is larger). This is consistent with the findings from [15]: nonequilibrium turbulence does not seem to be a phenomenon that depends uniquely on the Reynolds number of the flow.

Finally, we verified that the model developed by Mazellier and Vassilicos [25] extends to nonequilibrium scalings. This theoretical model, that predicts the value of C_ε from the zero crossings of velocity fluctuations, is a powerful tool to assess the validity of the results obtained when different operating protocols are employed.

ACKNOWLEDGMENTS

We thank Sebastien Torre for his help with installing and operating the traverse system. This work has been partially supported by the LabEx Tec21 (Investissements d'Avenir Grant Agreement No. ANR-11-LABX-0030), and by the ANR Project No. ANR-15-IDEX-02.

[1] H. Makita and K. Sassa, Active turbulence generation in a laboratory wind tunnel, in *Advances in Turbulence 3* (Springer, Berlin, 1991), pp. 497–505.

[2] L. Mydlarski, A turbulent quarter century of active grids: From Makita (1991) to the present, Fluid Dyn. Res. **49**, 061401 (2017).

[3] M. Obligado, T. Teitelbaum, A. Cartellier, P. Mininni, and M. Bourgoin, Preferential concentration of heavy particles in turbulence, J. Turbul. **15**, 293 (2014).

[4] V. N. Prakash, Y. Tagawa, E. Calzavarini, J. Martínez Mercado, F. Toschi, D. Lohse, and C. Sun, How gravity and size affect the acceleration statistics of bubbles in turbulence, New J. Phys. **14**, 105017 (2012).

[5] P. Knebel, A. Kittel, and J. Peinke, Atmospheric wind field conditions generated by active grids, Exp. Fluids **51**, 471 (2011).

[6] R. B. Cal, J. Lebrón, L. Castillo, H. S. Kang, and C. Meneveau, Experimental study of the horizontally averaged flow structure in a model wind-turbine array boundary layer, J. Renewable Sustainable Energy **2**, 013106 (2010).

[7] N. Mordant, Experimental high Reynolds number turbulence with an active grid, Am. J. Phys. **76**, 1092 (2008).

[8] M. Sinhuber, E. Bodenschatz, and G. P. Bewley, Decay of Turbulence at High Reynolds Numbers, Phys. Rev. Lett. **114**, 034501 (2015).

[9] K. P. Griffin, N. J. Wei, E. Bodenschatz, and Gregory P. Bewley, Control of long-range correlations in turbulence, Exp. Fluids **60**, 55 (2019).

[10] L. Mydlarski and Z. Warhaft, On the onset of high-Reynolds-number grid-generated wind tunnel turbulence, J. Fluid Mech. **320**, 331 (1996).

[11] R. J. Hearst and P. Lavoie, The effect of active grid initial conditions on high Reynolds number turbulence, Exp. Fluids **56**, 185 (2015).

[12] A. Thormann and C. Meneveau, Decay of homogeneous, nearly isotropic turbulence behind active fractal grids, Phys. Fluids **26**, 025112 (2014).

[13] A. J. Puga and J. C. LaRue, Normalized dissipation rate in a moderate Taylor Reynolds number flow, J. Fluid Mech. **818**, 184 (2017).

[14] J. C. Vassilicos, Dissipation in turbulent flows, Annu. Rev. Fluid Mech. **47**, 95 (2015).

[15] S. Goto and J. C. Vassilicos, Unsteady turbulence cascades, Phys. Rev. E **94**, 053108 (2016).

[16] J.-F. Pinton and R. Labbé, Correction to the Taylor hypothesis in swirling flows, J. Phys. II **4**, 1461 (1994).

[17] R. A. Antonia, L. Djenidi, and L. Danaila, Collapse of the turbulent dissipative range on Kolmogorov scales, Phys. Fluids **26**, 045105 (2014).

[18] D. Hurst and J. C. Vassilicos, Scalings and decay of fractal-generated turbulence, Phys. Fluids **19**, 035103 (2007).

[19] R. E. G. Poorte and A. Biesheuvel, Experiments on the motion of gas bubbles in turbulence generated by an active grid, J. Fluid Mech. **461**, 127 (2002).

[20] J. V. Larssen and W. J. Devenport, On the generation of large-scale homogeneous turbulence, Exp. Fluids **50**, 1207 (2011).

[21] N. Mazellier and J. C. Vassilicos, Turbulence without Richardson–Kolmogorov cascade, Phys. Fluids **22**, 075101 (2010).

[22] R. Gomes-Fernandes, B. Ganapathisubramani, and J. C. Vassilicos, Particle image velocimetry study of fractal-generated turbulence, J. Fluid Mech. **711**, 306 (2012).

[23] A. A. R. Townsend, *The Structure of Turbulent Shear Flow* (Cambridge University Press, Cambridge, 1980).

[24] W. K. George, The self-preservation of turbulent flows and its relation to initial conditions and coherent structures, in *Advances in Turbulence* (Hemisphere, New York, 1989), p. 3973.

[25] N. Mazellier and J. C. Vassilicos, The turbulence dissipation constant is not universal because of its universal dependence on large-scale flow topology, Phys. Fluids **20**, 015101 (2008).

[26] P. C. Valente and J. C. Vassilicos, Universal Dissipation Scaling for Nonequilibrium Turbulence, Phys. Rev. Lett. **108**, 214503 (2012).

[27] H. W. Liepmann and M. S. Robinson, Counting methods and equipment for mean-value measurements in turbulence research (National Advisory Committee for Aeronautics, Washington, DC, 1953).

[28] K. R. Sreenivasan, A. Prabhu, and R. Narasimha, Zero-crossings in turbulent signals, J. Fluid Mech. **137**, 251 (1983).

[29] J. Davila and J. C. Vassilicos, Richardson's Pair Diffusion and the Stagnation Point Structure of Turbulence, Phys. Rev. Lett. **91**, 144501 (2003).

[30] S. Goto and J. C. Vassilicos, The dissipation rate coefficient of turbulence is not universal and depends on the internal stagnation point structure, Phys. Fluids **21**, 035104 (2009).

[31] R. Monchaux, M. Bourgoin, and A. Cartellier, Analyzing preferential concentration and clustering of inertial particles in turbulence, Int. J. Multiphase Flow **40**, 1 (2012).

7.2 Work division

The work division was as follows:

Author	CR#1	CR#2	CR#3	CR#4	CR#5	CR#6	Score	Position
D.O. Mora	80	-	20	60	80	140	380	1
M. Obligado	140	-	-	20	100	110	370	2
E. Muniz and P. Riera	30	30	30	20	20	-	120	3
M. Lagauzere	-	70	50	-	-	-	100	4
S. Torre[†]	-	-	20	-	-	-	20	5
Total	250	100	100	100	200	250	1000	-

The guidelines reflecting the scores and author ordering can be found in the appendix A. The thesis author (D.O. Mora) was engaged in the writing, revision, and and discussion of the paper (see also appendix B). *E. Muniz and P. Riera* are counted as a single author given that they developed together the report of their internship in LEGI this article was based on.

[†] We pay homage to Sebastien Torre who kindly provided his expertise in the setting up of the experiments that lead to this publication.

Chapter 8

Estimating the integral length scale on turbulent flows from the zero crossings of the longitudinal velocity fluctuation

---

This chapter includes the article:
Mora, D. O. & Obligado, M. Estimating the integral length scale on turbulent flows from the zero crossings of the longitudinal velocity fluctuation. *Experiments in Fluids* 61 (2020)

8.1 Summary

This chapter builds upon the research found in chapter 7. During those single phase unladen experiments, we noticed that the velocity autocorrelation functions in active grid generated flows under a triple random random do not cross zero. The latter implies that standard methods [73], which rely on this crossing, to estimate the integral length scale $\mathcal{L}$ cannot be directly applied. This pitfall is not minor given that $\mathcal{L}$ is a key input parameter in theoretical approaches, and numerical simulations that aim at modelling the carrier phase turbulence.

Although in chapter 7 we partially circumvented this problem by following the work of Puga and LaRue [72] to estimate $\mathcal{L}$, we noticed that their method is very sensitive to the threshold δ used to compute $\mathcal{L}$. Our objective was therefore to develop a more robust method to obtain the carrier phase integral length scale.

We propose two new methods to estimate $\mathcal{L}$ based on the variance of the length between successive zero crossings, use similar assumptions as those used to estimate the Taylor length scale [37, 109, 137] under analogous conditions. We tested these methods using four different turbulent flows, and for their velocity autocorrelation function crosses zero, they have good agreement with previous standard methods. Due to the sensitivity of the threshold δ in the method proposed by Puga and LaRue [72], we find that for the active grid generated flows in triple random mode, our the integral length scale computed in chapter 7 might have been by a factor of 2.

More importantly, these two methods are not restricted to active grid generated flows, they have potential applications in several types of flow, and field experiments, where the instrument calibration is very difficult or cumbersome.

Among the work developed, this thesis author had original idea of using the variance of the length between successive zero crossings to estimate the integral length scale. It was also his original idea to use 1D Voronoï tessellations on the hot-wire records.

Experiments in Fluids (2020) 61:199
https://doi.org/10.1007/s00348-020-03033-2

RESEARCH ARTICLE

Estimating the integral length scale on turbulent flows from the zero crossings of the longitudinal velocity fluctuation

D. O. Mora[1,2] · **M. Obligado**[1]

Received: 13 May 2020 / Revised: 27 July 2020 / Accepted: 7 August 2020

Abstract

The integral length scale ($\mathcal{L}$) is considered to be characteristic of the largest motions of a turbulent flow, and as such, it is an input parameter in modern and classical approaches of turbulence theory and numerical simulations. Its experimental estimation, however, could be difficult in certain conditions, for instance, when the experimental calibration required to measure $\mathcal{L}$ is hard to achieve (hot-wire anemometry on large scale wind-tunnels, and field measurements), or in 'standard' facilities using active grids due to the behaviour of their velocity autocorrelation function $\rho(r)$, which does not in general cross zero. In this work, we provide two alternative methods to estimate $\mathcal{L}$ using the variance of the distance between successive zero crossings of the streamwise velocity fluctuations, thereby reducing the uncertainty of estimating $\mathcal{L}$ under similar experimental conditions. These methods are applicable to a variety of situations such as active grids flows, field measurements, and large-scale wind tunnels.

Graphic abstract

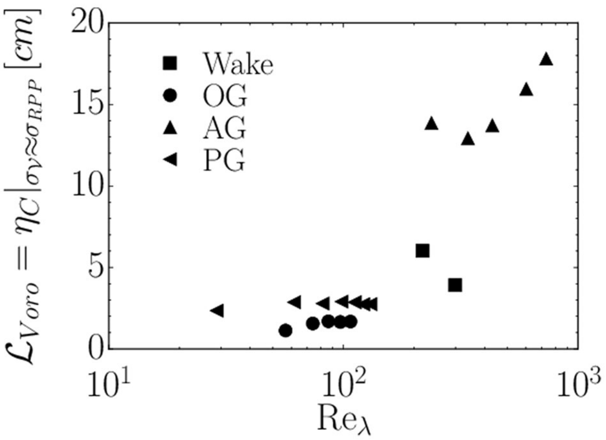

1 Introduction

The integral length scale ($\mathcal{L}$) is widely interpreted as the characteristic length scale of the energy containing eddies in a turbulent flow. $\mathcal{L}$ is defined as the integral of the normalised velocity autocorrelation function: $\mathcal{L} = \int_0^\infty \rho(r)\mathrm{d}r$, where $\rho(r) = \langle u'(x)u'(x+r)\rangle/\sigma_u^2$ (Tennekes and Lumley 1972), and σ_u is the standard deviation of the streamwise velocity fluctuations u'. Moreover, $\mathcal{L}$ is central to different attempts aiming to understand turbulence evolution

---

✉ M. Obligado
Martin.Obligado@univ-grenoble-alpes.fr

[1] Université Grenoble Alpes, CNRS, Grenoble-INP, LEGI, 38000 Grenoble, France

[2] Department of Mechanical Engineering, University of Washington, Seattle, USA

and its cascading process (Pope 2000; Vassilicos 2015). For instance, for turbulence close to a statistically homogeneous and isotropic state (HIT), the dissipation constant $C_\varepsilon = \varepsilon\mathcal{L}/\sigma_u^3$ depends on two large-scale quantities, $\mathcal{L}$ and σ_u.

In experiments, noise and non-stationary experimental conditions can pollute the large separation values, which are denoted by increments of r. This prevents the computation of the integral $\int_0^\infty \rho(r)\mathrm{d}r$ up to infinity. Therefore, the value of $\mathcal{L}$ is usually estimated by different methods. These include integrating up to the first zero crossing (O'Neill et al. 2004); integrating up to a minimum value of the autocorrelation function (O'Neill et al. 2004; Tritton 2012); integrating up to the value where the autocorrelation falls below e^{-1} (O'Neill et al. 2004; Bewley et al. 2012) or via standard Kolmogorov scalings. Besides these methods, other practical considerations have also been explored. Valente and Vassilicos (2011) also propose to integrate the autocorrelation function up to a length scale which is about ten times $\mathcal{L}$. Krogstad and Davidson (2010) suggest to apply a high-pass filter to the time signal at 0.1 Hz to counteract the effect of non-stationary low frequencies on the estimation of $\mathcal{L}$. These previous estimations are usually accompanied by the assumption that Taylor's hypothesis holds, $r = U\tau$, where τ refers to time and U is the local convective velocity.

Despite their widespread use, these approaches to estimate $\mathcal{L}$ may fail or result in ambiguities. For instance, some experimental studies using facilities that generate turbulence by means of active grids (Mydlarski 2017) have reported that $\rho(r)$ sometimes does not decay exponentially nor cross zero (Puga and LaRue 2017; Mora et al. 2019b). These observations pose the problem of how to compute $\mathcal{L}$ under such conditions. Likewise, in large-scale experiments (Gagne et al. 2004), or in field measurements, conducting the equipment calibration procedure could be very cumbersome, and therefore, such uncertainty would contaminate the reported values of the turbulent quantities.

To cater for the atypical autocorrelation function behaviour, Puga and LaRue (2017) have recommended estimating the integral length scale as $\mathcal{L} \approx \int_0^{r_0} \rho(r)\mathrm{d}r$ with $r_0 = U\tau_0 = U\tau(\rho(\tau) = \delta)$. The parameter δ quantifies the dispersion on the estimation of $\rho(r)$. It is usually found by averaging different segments extracted from the velocity time signal. Therefore, when $\int_0^{r_0} \rho(r)\mathrm{d}r$ is estimated by this method, δ plays an important role in the value of $\mathcal{L}$ obtained. Nevertheless, the choice of δ is ambiguous as it strongly depends on the averaging chosen for the computation of $\rho(r)$. This is not a minor issue considering the influence $\mathcal{L}$ exerts on the normalised dissipation rate constant C_ε, e.g., Mora et al. (2019b) reported $C_\varepsilon \approx 0.3$ in disagreement (by a factor of 2) with the value $C_\varepsilon \approx 0.6$ reported by Puga and LaRue (2017) for similar values of Re_λ, despite the high degree of turbulence isotropy and turbulence homogeneity present in both experiments.

Puga and LaRue (2017) anticipated that their method could not be general to all active grid generated flows, as it has been reported that the active grid protocol could affect the largest scales of the flow (Hearst and Lavoie 2015; Griffin et al. 2019). Then the choice of δ, which under this method may change between different experimental conditions and data analyses, could impact $\mathcal{L}$ and C_ε making it difficult to compare different results available in the literature.

To address this problem, we study the zero crossings of u' for different datasets. Zero crossing analysis has been used to characterise the small-scale features of the flow via the Taylor microscale (λ) (Sreenivasan et al. 1983; Mazellier and Vassilicos 2008; Mora et al. 2019b; Akinlabi et al. 2019). Given that the zero crossings of a velocity signal usually do not depend on the equipment calibration (as far as the mean velocity is known), this analysis is suitable even under challenging experimental conditions.

Our first approach is solely based on the work of McFadden (1958), whereas the second one relies on the observation that the velocity field filtered at a scale equal to the integral length scale seems to exhibit uncorrelated zero crossings. Both approaches are able to estimate the integral length scale in several turbulent flows in good agreement with standard well established methods (e.g., direct integration of the autocorrelation function). We also briefly analyse the structure of the zero crossings for different turbulent signals by means of Voronoï tessellations (Ferenc and Néda 2007; Monchaux et al. 2010) to gain insight into the trends seen in our methods. Finally, we discuss potential extensions of this work.

Table 1 Typical turbulence parameters range for the open (OG), active (AG) (Mora et al. 2019b), and passive (PG) grids

Parameter	OG	AG	PG	Wake
U_∞ (m/s)	4.4–17.0	1.8–6.8	1.5–18.0	10.0
σ_u/U (%)	2.0–10.0	12.5–15.0	3.0-2.50	3.0-8.0
λ (mm)	8.0–3.0	16.0–9.0	9.0–4.0	10–5.4
Re_λ	50–200	200–731	30–130	200–300
η (μm)	400–100	500–180	918–191	340–163
$\mathcal{L}$ (cm)	1.0–3.0	5.0–11.0	1.7–2.8	4–6.2
Signal size	(1–3) $10^5\mathcal{L}$	(1–4) $10^4\mathcal{L}$	(1–4) $10^5\mathcal{L}$	(1–3) $10^6\mathcal{L}$

AG refers to the active grid being operated in a random mode while OG to the same grid, completely open and static. We also employed records from the wake of a bluff body (Dairay et al. 2015). In the table, inlet velocity U_∞, turbulence intensity σ_u/U (with U the mean local velocity), Taylor micro-scale λ, Reynolds number based on the Taylor micro-scale $Re_\lambda = \lambda\sigma_u/\nu$ (ν being the kinematic viscosity of the flow), Kolmogorov length scale $\eta = (\nu^3/\varepsilon)^{1/4}$, streamwise integral length scale $\mathcal{L}$ obtained via $\int \rho(r)\mathrm{d}r$ and total length of signals in $\mathcal{L}$ units

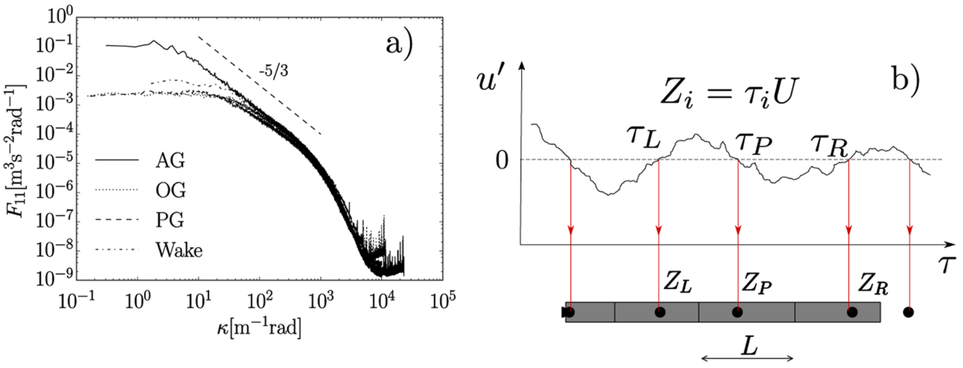

Fig. 1 **a** Longitudinal energy density spectra (F_{11}) for the data found in Table 1. **b** Zero crossings and 1D Voronoï tessellation illustration. For a given zero crossing position Z_P with left, and right neighbour crossings Z_L, and Z_R, respectively, the length of the Voronoï cell (centered on Z_P) is given by $L = |Z_R - Z_L|/2$

2 Methodology

We analysed measurements taken via hot-wire anemometry (HWA). These measurements, except for those using a passive grid, have been previously published in the literature (Dairay et al. 2015; Mora et al. 2019b), and span a variety of turbulent flows generated by different mechanisms (see Table 1): downstream of active grids or passive grids, and downstream of the wake of an irregular bluff plate (Fig. 1a).

All grid experiments were conducted in the *Lespinard* wind tunnel in LEGI, a low-turbulence wind tunnel facility with a measurement cross section of 75 × 75 cm^2, which has been extensively used to conduct experiments under homogeneous isotropic turbulence conditions (Mora et al. 2019b). Both the active and passive grids have a mesh size of 10 cm. The passive grid is composed of 18 circular cylinders (9 horizontal and 9 vertical distributed homogeneously on space) and each bar has a diameter of 20 mm. The passive grid was placed in the wind tunnel converging section, where it has an area of 94.4 × 94.4 cm^2. Likewise, the active grid, located at the inlet of the measurement section, is composed of 16 rotating axes (8 horizontal and 8 vertical also distributed homogeneously on space) and each rotating axis can be actuated independently. All motors were driven with random rotation rates and directions, which were changed randomly in time. Measurements were taken 3 m downstream the measurement section inlet, where turbulence has been found to be close to HIT for all grids (Mora et al. 2019b). The measuring instrument used to record the velocity fluctuations was a single Dantec Dynamics 55P01 hot-wire probe, driven by a Dantec StreamLine constant temperature anemometer (CTA) system. The Pt–W wires were 5 μm in diameter, 3 mm long, with a sensing length of 1.25 mm. Acquisitions were made for 300 s at 25 kHz and 50 kHz. For all measurements reported here, the Kolmogorov frequency was always smaller than half our sampling frequency.

The wake experiments were conducted in the 3 × 3 wind tunnel at Imperial College London, using the same HWA system as in the grid experiments. Measurements were taken at the centreline at the streamwise distances $D = 15$ and $D = 50$ from a plate with a characteristic length $D = \sqrt{\mathcal{A}} = 64$ mm (with $\mathcal{A}$ being the frontal area of the plate).

To avoid potential confusion among the different estimations of the integral length scale, we use the following notation: the symbol $\mathcal{L}$ (with no subscripts) stands for the integral length scale magnitudes reported in Table 1. For all datasets except for the active grid (AG) measurements, these magnitudes were estimated by direct integration of the autocorrelation function (i.e. $\mathcal{L} = \int \rho(r)\mathrm{d}r$) up to the first zero of $\rho(r)$. For the AG datasets, $\rho(r)$ was integrated up to a threshold δ. Other estimates will use the symbol $\mathcal{L}$ with a specific subscript related to the method employed, e.g., $\mathcal{L}_{\mathrm{Voro}}$ refers to the integral length scale estimated via Voronoï tessellations.

2.1 Zero crossing computation

For this study, we employed a Reynolds decomposition for the streamwise velocity ($u = U + u'(\tau)$) to extract the Eulerian fluctuating velocity u'. We then computed the fluctuating velocity $u'(\tau)$ zero crossings, i.e., the set of times τ_i^c for which $u'(\tau_i^c) = 0$ (see top of Fig. 1b), and

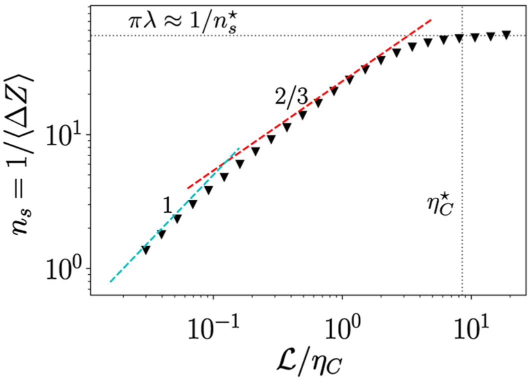

Fig. 2 Zero-crossing computation example for one of the PG datasets in Table 1

translated this list of zero crossings from time into space by assuming the Taylor hypothesis $Z_i = \tau_i^c U$ (see Fig. 1b). It was verified that all measurements had enough temporal resolution to estimate λ (Mora et al. 2019b) via the zero crossings. A common procedure to verify the latter condition (Sreenivasan et al. 1983; Mazellier and Vassilicos 2008) is as follows:

1. Take the acquired fluctuating velocity signal, and low-pass filter it (with a high-order filter, e.g. a fifth-order Butterworth filter) at different sizes $\eta_C = 2\pi/\kappa$, where κ is the wavenumber. Considering the use of the Taylor hypothesis, this is equivalent to filter the signal at different frequencies.
2. Compute the signal zero crossings, and their number density (n_s =number of zeros/duration of the signal) at at each filter size (resp. frequency) (see Fig. 2).
3. If a plateau of n_s is present for filter scales smaller (resp. larger) than a certain scale (resp. frequency) $\eta_C^\star$ (not to be confused with the Kolmogorov length scale η), the value of n_s is properly resolved. One could then estimate λ via $n_s^{-1}|_\star = \pi C \lambda$, with C being a constant in the order of unity which accounts for the non-Gaussianity of the velocity derivative (Mazellier and Vassilicos 2008).

The analysis we present in this work uses the mean and the standard deviation of the interval times between successive zero crossings. Therefore, all records have to be long enough so they achieve adequate statistical convergence. To fulfil this condition, our records had between 10^4 and 10^6 integral length scales (see Table 1), which is consistent with previous studies at similar values of Re_λ. We find, in agreement with the results reported from Mazellier and Vassilicos (2008) ($Re_\lambda \in [50–2000]$), that all our datasets require in the order of 10^4 integral length scales to converge both parameters.

2.2 Variance of the intervals between zero crossings

The seminal work of McFadden (1958) was the first to derive for Gaussian processes closed expressions to compute the variance of the interval distance between two successive zero crossings ($\Delta Z = Z_{i+1} - Z_i$) under two analytically tractable conditions: intervals between zeros are statistically independent, or intervals between zeros make a Markov chain. We proceed to apply McFadden's work to our turbulent signals, as single point velocity fluctuations exhibit similar properties as those of Gaussian processes (Tsinober et al. 2019). Recent research has advanced stochastic tools (e.g. Fokker–Planck equation) can also be used to gain insight into the turbulence cascading process (for a recent review, see Peinke et al. 2019). While this is an interesting ramification of the discussion we present in this work, we focus our effort on deriving a first-order estimation of the integral length scale for experimental conditions under which traditional methods to estimate $\mathcal{L}$ might be ambiguous. It is left for future work an in-depth stochastic analysis of the relationship between the turbulence cascade and the variance of ΔZ.

Within McFadden's theory, the first assumption is that intervals between zeros are statistically independent. This assumption yields an analytically convenient expression (contrary to the Markov chain case, see, for instance, Wilson and Hopcraft 2017) for the variance for intervals between successive zero crossings:

$$\mathrm{Var}(\Delta Z) = 2\langle \Delta Z\rangle \int_0^\infty \frac{2}{\pi} \arcsin(\rho(\tau))\mathrm{d}\tau. \tag{1}$$

The latter expression, and assuming Taylor hypothesis, provides an estimate for $\mathcal{L}$ if the assumption of independent zero crossing intervals approximately holds for turbulent signals:

$$\begin{aligned}\frac{\mathrm{Var}(\Delta Z)}{2\langle \Delta Z\rangle} &= \int_0^\infty \frac{2}{\pi}\arcsin(\rho(\tau))\mathrm{d}\tau \\ &= \int_0^\infty \frac{2}{\pi}\left(\rho(\tau) + \frac{\rho(\tau)^3}{6} + \frac{\rho(\tau)^5}{40} + \cdots\right) \le \int_0^\infty \rho(\tau)\mathrm{d}\tau. \end{aligned} \tag{2}$$

By truncating the integral up to the first term, we obtain a relation between the Fano factor ($\mathrm{Var}(\Delta Z)/\langle \Delta Z\rangle$) (Smith et al. 2008), and the integral time ($\mathcal{T}$) and length scales,

$$\mathcal{L}_{\mathrm{McF}} = \frac{\pi}{4}\frac{\mathrm{Var}(\Delta Z)}{\langle \Delta Z\rangle} \approx U \int_0^\infty \rho(\tau)\mathrm{d}\tau = U\mathcal{T} = \int_0^\infty \rho(r)\mathrm{d}r. \tag{3}$$

From now on, $\mathcal{L}_{\mathrm{McF}}$ refers to the estimation of the integral length scale via Eq. 3.

2.3 Successive zero crossings and 1D Voronoï tessellation

Interestingly, if McFadden's assumption of statistically independent intervals holds, the variance of the length between two successive intervals (Bendat and Piersol 2011) could be written as

$$\mathrm{Var}(\Delta Z_1 + \Delta Z_2) = \mathrm{Var}(\Delta Z_1) + \mathrm{Var}(\Delta Z_2) + \cancelto{0}{\mathrm{Cov}(\Delta Z_1, \Delta Z_2)}. \tag{4}$$

This equation paves the way to analyze the implications of the decorrelation between ΔZ_1 and ΔZ_2 (as statistical independence implies decorrelation) using 1D Voronoï tessellations (Ferenc and Néda 2007), a convenient tool to analyze spatial clustering (Monchaux et al. 2012). These two frameworks (Voronoï tessellations and 'raw' inter-crossing distances) are related by their respective definitions. For instance, if a random variable ΔZ represents the distance between successive crossings, the respective

Voronoï cell length L (also a random variable) is given by $L = 1/2(\Delta Z_L + \Delta Z_R)$, where $\Delta Z_L = |Z_P - Z_L|$ and $\Delta Z_R = |Z_R - Z_P|$ are the crossing lengths (random variables) at the left, and at the right of the crossing Z_P (see Fig. 1b). From these definitions, $\langle L\rangle = \langle \Delta Z\rangle = n_s^{-1}$.

If we assume that the covariance between ΔZ_L and ΔZ_R is very weak, then the variance of the ensemble of normalized Voronoï cells ($\mathcal{V} = L/\langle L\rangle$) is half the variance of $\Delta Z/\langle \Delta Z\rangle^2$,

$$\mathrm{Var}(L) = \mathrm{Var}\left(\frac{\Delta Z_L + \Delta Z_R}{2}\right) = \frac{1}{4}\mathrm{Var}(\Delta Z) + \frac{1}{4}\mathrm{Var}(\Delta Z) + \frac{\cancelto{\approx 0}{\mathrm{Cov}(\Delta Z_L, \Delta Z_R)}}{2},$$

that is then equivalent to,

$$\frac{1}{2}\frac{\mathrm{Var}(\Delta Z)}{\langle \Delta Z\rangle^2} = \frac{\mathrm{Var}(L)}{\langle L\rangle^2} = \sigma_{\mathcal{V}}^2. \tag{5}$$

This formula holds for zero crossings spatially distributed as a random Poisson process (RPP), which has no spatial correlations at any scale and, therefore, their Voronoï cells are statistically independent (Ferenc and Néda 2007). For a RPP process (Ferenc and Néda 2007), $\langle \Delta Z\rangle = 1$, $\mathrm{Var}(\Delta Z) = 1$, which yields $\mathrm{Var}(L)/\langle L\rangle^2 = 1/2$. We will refer to the standard deviation of this RPP process as $\sigma_{\mathrm{RPP}} = \sqrt{1/2}$, and to the respective standard deviation coming from our Voronoï analysis of turbulent signals as $\sigma_{\mathcal{V}}$.

3 Results

3.1 Estimation of the integral length scale via McFadden's equation

To examine the accuracy of McFadden's equation ($\mathcal{L}_{\mathrm{McF}}$) for the different datasets, we need to estimate $\mathrm{Var}(\Delta Z)$ and $\langle \Delta Z\rangle$. These estimates are computed by following a standard procedure found in the literature (Sreenivasan et al. 1983; Mazellier and Vassilicos 2008), described in Sect. 2.1: we low-pass filter u' with a range of filter sizes η_C, and compute the signal zero crossings and zero crossings statistics at each filter size. In other words, we collect statistics as a function of the filter size, i.e., $\langle \Delta Z\rangle = f(\eta_C)$,$\mathrm{Var}(\Delta Z) = g(\eta_C)$. The presence of a plateau (as shown in Fig. 2, which was present for all our datasets) for $\langle \Delta Z\rangle = f(\eta_C < \eta_C^\star) \approx constant$ indicates that number density of zero crossings (n_s) is well resolved (Sreenivasan et al. 1983) and, therefore, λ can be computed as $n_s^{-1} = \langle \Delta Z\rangle \approx \pi\lambda$ (see Fig. 2). After checking that our signals resolve λ, we proceed to test the accuracy of McFadden's equation.

We compare the values of $\mathcal{L}_{\mathrm{McF}}$ (c.f. Eq. 3) against $\mathcal{L}$, the integral length scale estimated by the direct integration of the autocorrelation function (see Table 1). We make this comparison for all velocity signals and for all filter scales (see Fig. 3). First, we note that $\mathcal{L}_{\mathrm{McF}}$ has a residual dependency on Re_λ coming from the variance value at the plateau, as expected from previous analyses (Mazellier and Vassilicos 2008). Next,

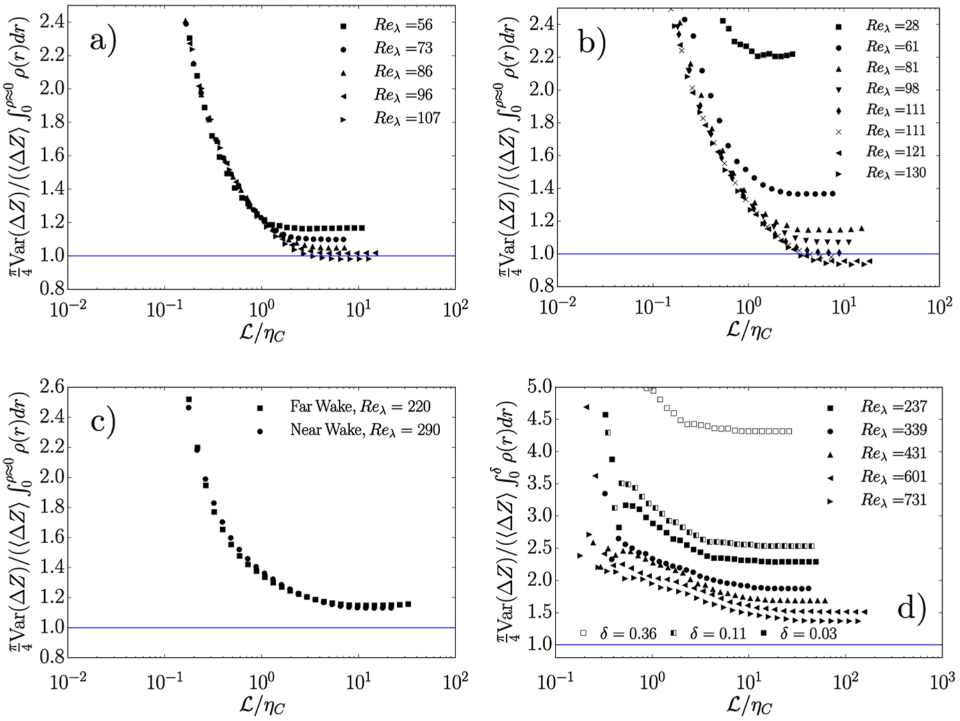

Fig. 3 Ratio between the integral length scales $\mathcal{L}_{\mathrm{McF}}/\mathcal{L} = \frac{\pi}{4}(\mathrm{Var}(\Delta Z)/\langle \Delta Z\rangle)/\mathcal{L}$. **a** OG. **b** PG. **c** Wakes. **d** AG. For the AG datasets Mora et al. (2019b), the autocorrelation integrals were estimated by the method of Puga and La Rue Puga and LaRue (2017). We also show the sensitivity of this parameter to different values of δ for the lowest value of Re_λ (square)

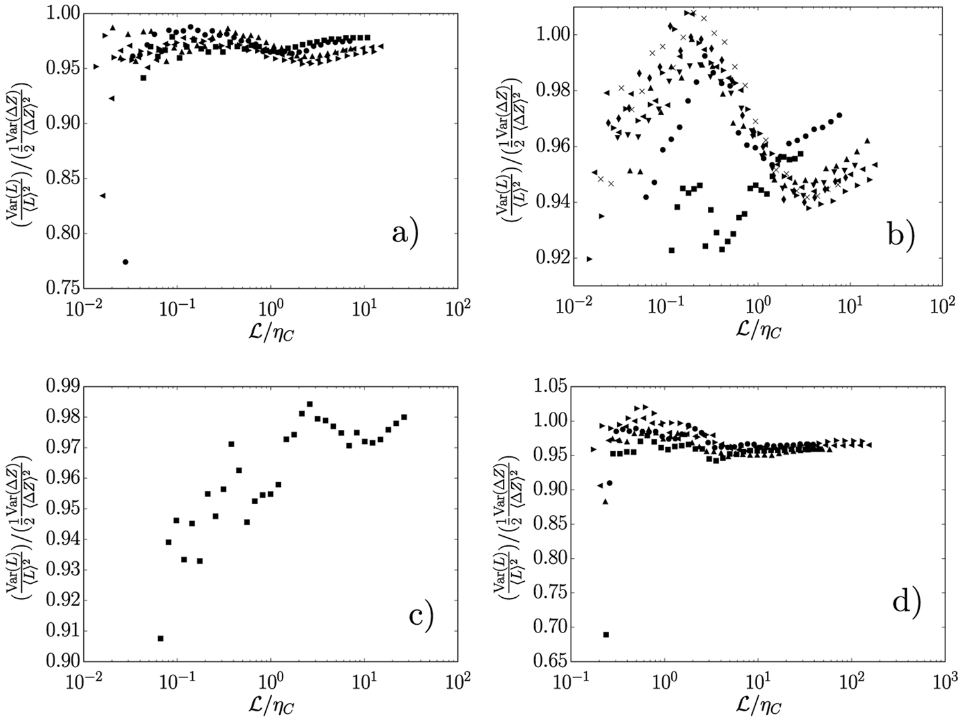

Fig. 4 Ratio between the variance of Voronoï cells $\mathrm{Var}(L) = \langle (L - \langle L\rangle)^2\rangle$, and the respective one of the interval distance between two successive zero crossings; $\mathrm{Var}(\Delta Z) = \langle \Delta Z^2\rangle - \langle \Delta Z\rangle^2$. Note that $\langle L\rangle = \langle \Delta Z\rangle$. **a** OG. **b** PG. **c** Wakes. **d** AG

we observe that $\mathcal{L}_{\mathrm{McF}}$ better agrees with $\mathcal{L}$ for large values of Re_λ, and at the smaller filter scales η_C. Based on the agreement seen for the OG, PG, and Wake datasets, we conjecture that for the AG data (Fig. 3d) the integral length scale values (Table 1) may be underestimated [already discussed in Mora et al. (2019b)]. For the AG dataset, the integral length scale is estimated as $\mathcal{L} \approx \int_0^\delta \rho(r)\mathrm{d}r$. Evidently, the magnitude of $\mathcal{L}$ strongly depends on the value of δ selected; as δ increases $\mathcal{L}$ decreases.

Also, the agreement between the values of $\mathcal{L}$ and $\mathcal{L}_{\mathrm{McF}}$ (see Eq. 3) advance that the assumption of independent successive zero crossings could approximately hold in turbulent signals. Although decorrelation does not imply independence, the Pearson coefficient, computed for the last point on the plateau is small, and negative, i.e., $-0.1 < \mathrm{Cov}(\Delta Z_L, \Delta Z_R)/\left(\sigma_{\Delta Z_L}\sigma_{\Delta Z_R}\right) < 0$ (for all our datasets). This observation along with our results found (Fig. 3) suggests that Eq. 3 is a reasonable approximation of the integral length scale for the range of Re_λ here explored. On the other hand, Eqs. 4 and 5 are valid for two uncorrelated variables (a weaker condition than statistical independence). We estimate this degree of correlation between successive intervals by looking at the ratio $\mathrm{Var}(L)/\left((1/2)\mathrm{Var}(\Delta Z)\right)$ (see Fig. 4a–d). This ratio relates the variance of Voronoï tessellation length $\sigma_{\mathcal{V}}^2$ (see Fig. 1b) to the variance of the interval distance between two successive zero crossings $\mathrm{Var}(\Delta Z)$. For the different datasets, this ratio of variances (see Eq. 5) yields:

$$0.90 < \sigma_{\mathcal{V}}^2 / \left(\frac{1}{2}\frac{\mathrm{Var}(\Delta Z)}{\langle \Delta Z\rangle^2}\right) = \left(\frac{\mathrm{Var}(L)}{\langle L\rangle^2}\right) / \left(\frac{1}{2}\frac{\mathrm{Var}(\Delta Z)}{\langle \Delta Z\rangle^2}\right) < 1.02, \quad (6)$$

at all filter scales of interest for the data found in Table 1. These results suggest that Eq. 5 (i.e. intervals between zeros are approximately decorrelated) is valid within 10% error for our datasets, enough to get a good first-order estimation of the integral length scale.

3.2 Voronoï analysis

Considering the previous bounds, and the respective decorrelation seen, we proceed to apply 1D Voronoï tessellation analysis (Ferenc and Néda 2007) to the signals' zero crossings (see Fig. 1b) at each filter scale.

Our results reveal that $\sigma_{\mathcal{V}}$ (see Fig. 5a–d) has complex behaviour with the filter scale η_C which can be divided in three parts. First, a plateau regime at low values of $\kappa_C \sim \eta_C^{-1}$ representative of a band-limited Gaussian white noise signal. Second, an intermediate regime where $\sigma_{\mathcal{V}}$ may attain a power law behaviour with an exponent close to 1/4 for large values of Re_λ; despite of its persistence among different datasets, the existence of this intermediate regime remains unexplained and is left for future research as the limited extent of our data does not allows us to unambiguously conclude the accuracy of the exponent. Third, a second plateau consistent with the one found for the zero crossing number density $n_s^{-1} = \langle \Delta Z\rangle$ is found.

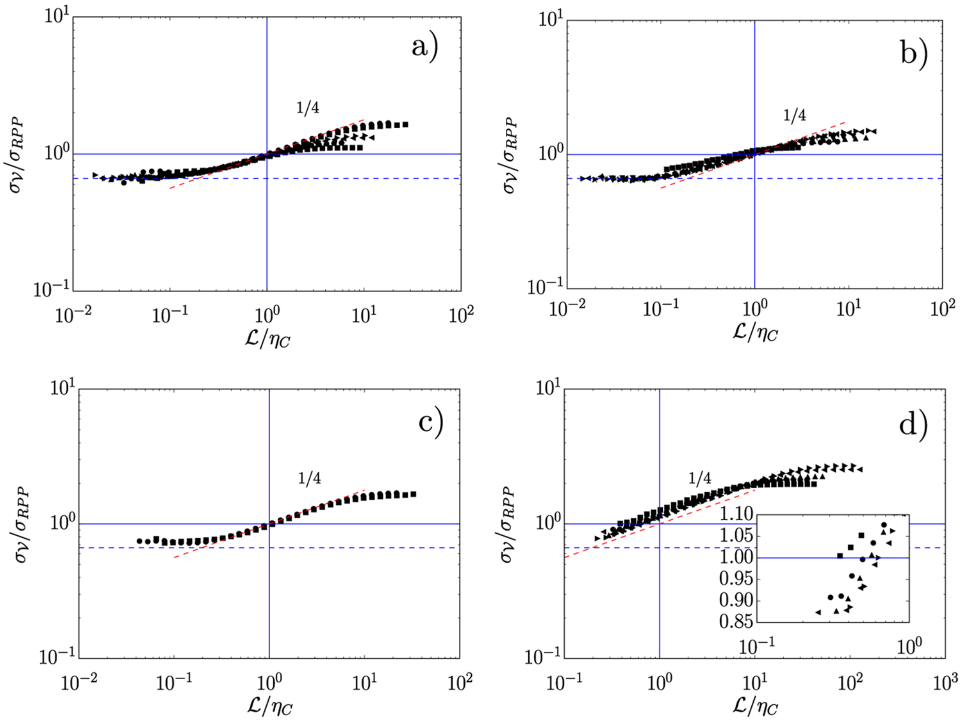

Fig. 5 Evolution of $\sigma_\mathcal{V}$ against the filter scale. In the figures $\mathcal{L}$ refers to the integral length scale estimated from integrating the autocorrelation function (see Table 1). **a** OG. **b** PG. **c** Wakes. **d** AG. In **d**, we are only plotting the AG data for $\delta = 0.03$ (see Fig. 3d). In the figures the horizontal dashed line corresponds to the standard deviation corresponding to a band-limited Gaussian white noise process (McFadden 1958); $\sigma_\mathcal{V}/\sigma_{\mathrm{RPP}} \approx 0.67$

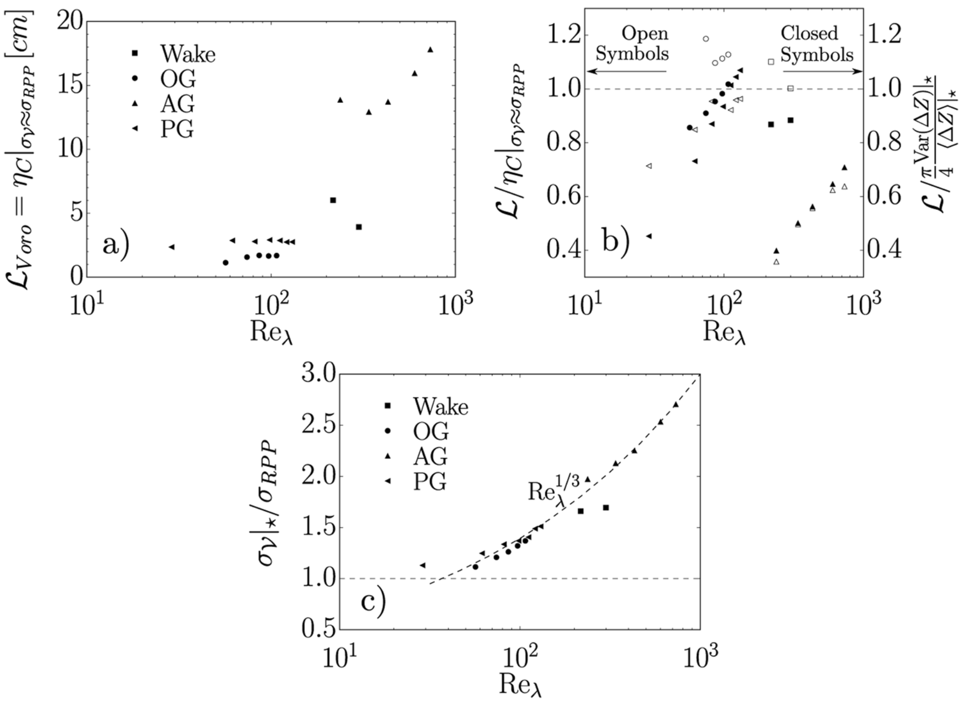

Fig. 6 **a** Evolution of $\mathcal{L}_{\mathrm{Voro}} = \eta_C|_{\sigma_\mathcal{V} \approx \sigma_{\mathrm{RPP}}}$ with Re_λ. **b** Comparison between the two methods to estimate the integral length scale via $\mathcal{L}_{\mathrm{Voro}} = \eta_C$ for which $\sigma_\mathcal{V} \approx \sigma_{\mathrm{RPP}}$, and via $\mathcal{L}_{\mathrm{McF}}$ estimated from Eq. 3 with respect to $\mathcal{L}$, the integral of the autocorrelation function. The $\star$ represents the last value at the plateau of $\sigma_\mathcal{V}$ in Fig. 5a–d. **c** Standard deviation of the Voronoï cells at the last point (filter) on the plateau. In the figures, we are only plotting the AG data for $\delta = 0.03$ (see Fig. 3d)

Moreover, there seems to be a strong correlation (especially for the OG, PG, and wake datasets) between the filter scale at which $\sigma_\mathcal{V}/\sigma_{\mathrm{RPP}} \approx 1$, and $\mathcal{L}$, i.e., apparently $\sigma_\mathcal{V}/\sigma_{\mathrm{RPP}} \approx 1$ when $\eta_C = \mathcal{L}$. These results hint that we could estimate the integral length scale as the length scale at which the zero crossing interval topology is somewhat decorrelated, i.e., $\mathcal{L}_{\mathrm{Voro}} = \eta_C|_{\sigma_\mathcal{V} \approx \sigma_{\mathrm{RPP}}} \approx \mathcal{L}$. Interestingly, $\mathcal{L}_{\mathrm{Voro}}$ (see Fig. 6a) is strongly dependent on Re_λ for active grids (AG) at large U_∞, whereas $\mathcal{L}_{\mathrm{Voro}}$ is roughly constant (i.e. a weak function of Re_λ Mazellier 2005; Gad-el Hak and Corrsin 1974) for the passive grids (OG and PG, see also Table 1).

Fig. 7 PDF of the normalized Voronoï cell length $\mathcal{V} = L/\langle L \rangle$ for the last data point on the plateau (Fig. 5a–d) and the data found in Table 1. **a** OG. **b** PG. **c** Wakes. **d** AG. In the figures, the RPP label refers to a random Poisson process with no correlations at any scale (Ferenc and Néda 2007; Monchaux et al. 2010)

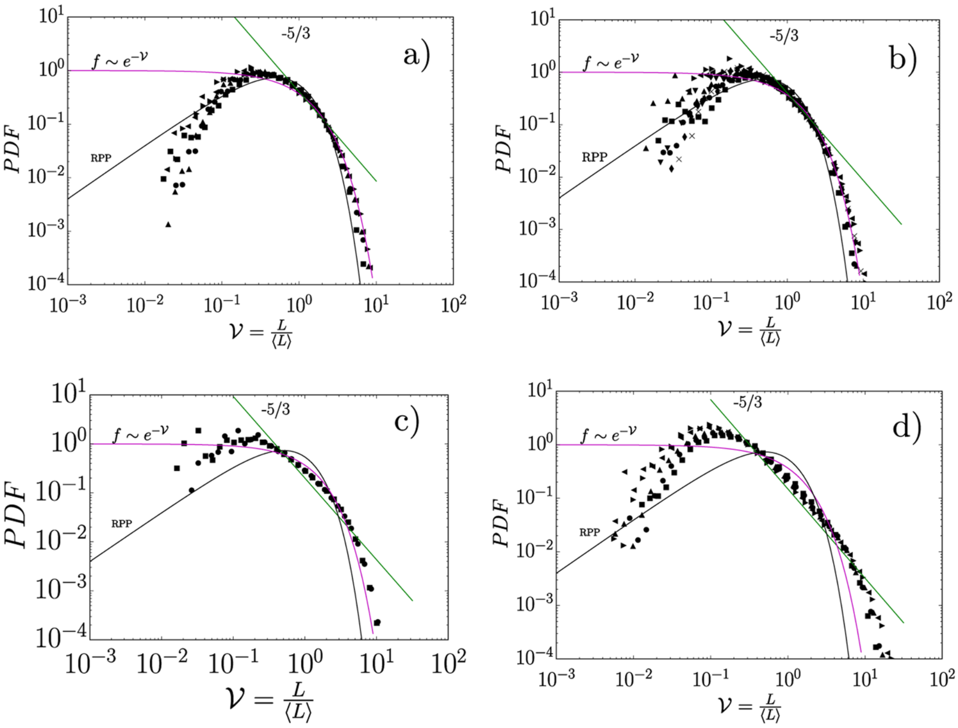

Furthermore, a comparison between the values estimated from McFadden's equation (taking the last points of the plateaus of n_s, and $\sigma_{\mathcal{V}}$), and the values extracted from $\sigma_{\mathcal{V}}/\sigma_{\mathrm{RPP}} \approx 1$ when $\eta_C = \mathcal{L}$ (see Figs. 3d, 4, 5, 6b) points out again that for the AG data, the integral length scale $\mathcal{L}$ could have been originally underestimated by a factor of 2 explaining the discrepancy in C_ε between the studies of Mora et al. (2019b), and Puga and LaRue (2017). This underestimation occurs, when integrating the autocorrelation by the method proposed by Puga and LaRue (2017), as a consequence of the arbitrary choice of the value δ; smaller values converge to a closer value of $\mathcal{L}$, while larger values of δ reduce the noise while keeping the trends. We, therefore, conclude that while $\mathcal{L}_{\mathrm{McF}}$ gives a good estimation of the integral length scale, a better estimation might be $\mathcal{L}_{\mathrm{Voro}} = \eta_C|_{\sigma_{\mathcal{V}} \approx \sigma_{\mathrm{RPP}}}$. Despite both methods relying on similar hypotheses, $\mathcal{L}_{\mathrm{Voro}}$ can estimate the integral length scale even for non-stationary and non-calibrated data.

On the other hand, and following the cluster-detection method of Monchaux et al. (2010), we argue that zero crossing clustering is present when the ratio $\sigma_{\mathcal{V}}|_\star/\sigma_{\mathrm{RPP}} > 1$ (where $\sigma_{\mathcal{V}}|_\star$ is the value of $\sigma_{\mathcal{V}}$ at the plateau observed at small values of η_C) and that this clustering intensity depends on this ratio magnitude. Being the standard deviation mainly set by the 'voids' (Sumbekova et al. 2017) (large intervals without zero crossings), these observations suggest again that at the length scale ($\eta_C = \mathcal{L}_{\mathrm{Voro}}$) for which $\sigma_{\mathcal{V}}|_\star/\sigma_{\mathrm{RPP}} \approx 1$, the 'large' intervals contributing the most to $\sigma_{\mathcal{V}}$ are decorrelated. An observation consistent with the interpretation of integral length scale. On the other hand, our results show that the degree of clustering of zero crossings increases with $Re_\lambda^{1/3}$ (see Fig. 6c), in agreement with the observations of Mazellier and Vassilicos (2008).

3.2.1 Zero crossing interval PDFs

Considering that $\mathcal{L}_{\mathrm{McF}}$ depends on the magnitude of $\sigma_{\mathcal{V}}|_\star$, we expect that the estimation of the integral length scale via Eq. 3 is highly dependent on the large intervals without zero crossings. To check this conjecture, we briefly examine the probability density functions (PDF) of Voronoï cells $\mathcal{V} = L/\langle L \rangle$.

The probability density function of the inter-arrival distance between zero crossings from turbulent signals, and Gaussian processes has been extensively studied in the last decades. Several studies retrieved that this PDF exhibits an exponential behaviour and clustering (Sreenivasan et al. 1983; Smith et al. 2008). For instance, Smith et al. (2008) propose that these PDFs should have a power-law behavior if the underlying stochastic process is fractal. Some other studies have reported (Chamecki 2013; Cava et al. 2012) that the onset of an exponential cut-off present in the PDF is due to the randomisation effects (at scales larger than $\mathcal{L}$) that bend the coherent structures present in the flow reducing the probability of larger intervals between zero crossings.

Our analysis for the last point on the plateau, by means of the 1D Voronoï tessellation, is consistent with those results: first, the PDFs deviate from a RPP distribution suggesting the presence of clustering (Monchaux et al. 2010) (see Fig. 7a–d). This deviation appears to become stronger with increasing Re_λ in agreement with behavior found for $\sigma_\mathcal{V}$ (Fig. 6c). Also, the zero's clustering seems to correlate with the wider extent of a power law behaviour (with an exponent close to '$-$ 5/3') found in the PDFs at increasing Re_λ. These observations, in the context of McFadden equation (3), are consistent with previous experiments showing that the integral length scale is a function of Re_λ in active grid generated flows (Hearst and Lavoie 2015), whereas such dependency is much weaker for passive grids (see Fig. 6a). Second, we retrieved an exponential cut-off transition in our dataset PDFs (see Fig. 7a–d). While it is not in the scope of this work, these figures also suggest the possibility of using Voronoï tessellations to do a local analysis of the zero crossing cluster and void properties (e.g. average cluster size) analogous to those conducted for inertial particles (Monchaux et al. 2010).

4 Concluding remarks

The velocity autocorrelation function $\rho(r)$ coming from active-grid-generated flows may present a non-decaying behavior that could make ambiguous the estimation of the integral length scale by well-established methods. In the previous sections, our analysis of the variance of the distance between zero crossings of the fluctuating velocity via Voronoï tessellations in conjunction with the theoretical work of McFadden (1958) allowed us to propose two methods ($\mathcal{L}_{\mathrm{Voro}}$ and $\mathcal{L}_{\mathrm{McF}}$) to estimate the integral length scale. These methods are applicable to hot-wire records from flows generated by active grids, and thereby, circumvent the problem of the non-standard behavior of $\rho(r)$. They are also consistent traditional techniques to estimate $\mathcal{L}$ in several flows: turbulent wakes, and passive grids. Thus, these two methods have potential applications in field experiments where calibration could be difficult, or in particle laden flows, where under certain conditions, zero crossing analysis has been used to estimate the energy dissipation rate the presence of inertial particles (Mora et al. 2019a). Our work shows that all global turbulence parameters (such as ε, $\mathcal{L}$, λ, ...) can be estimated even with a non-calibrated hot-wire, provided that the mean velocity of the flow is known (needed for the Taylor hypothesis).

Acknowledgements Our work has been partially supported by the LabEx Tec21 (Investissements d'Avenir—Grant agreement # ANR-11-LABX-0030), and by the ANR project ANR-15-IDEX-02.

References

Akinlabi EO, Wacławczyk M, Mellado JP, Malinowski SP (2019) Estimating turbulence kinetic energy dissipation rates in the numerically simulated stratocumulus cloud-top mixing layer: evaluation of different methods. J Atmos Sci 76(5):1471–1488

Bendat JS, Piersol AG (2011) Random data: analysis and measurement procedures, vol 729. Wiley, New York

Bewley G.P, Chang K, Bodenschatz E, for Turbulence Research, I.C. (2012) On integral length scales in anisotropic turbulence. Phys Fluids 24(6):061702

Cava D, Katul GG, Molini A, Elefante C (2012) The role of surface characteristics on intermittency and zero-crossing properties of atmospheric turbulence. J Geophys Res Atmos 117(D1):D01104

Chamecki M (2013) Persistence of velocity fluctuations in non-Gaussian turbulence within and above plant canopies. Phys Fluids 25(11):115110

Dairay T, Obligado M, Vassilicos JC (2015) Non-equilibrium scaling laws in axisymmetric turbulent wakes. J Fluid Mech 781:166–195

Ferenc JS, Néda Z (2007) On the size distribution of poisson voronoi cells. Phys A 385(2):518–526

Gad-el Hak M, Corrsin S (1974) Measurements of the nearly isotropic turbulence behind a uniform jet grid. J Fluid Mech 62(1):115–143

Gagne Y, Castaing B, Baudet C, Malécot Y (2004) Reynolds dependence of third-order velocity structure functions. Phys Fluids 16(2):482–485

Griffin KP, Wei NJ, Bodenschatz E, Bewley GP (2019) Control of long-range correlations in turbulence. Exp Fluids 60(4):55

Hearst RJ, Lavoie P (2015) The effect of active grid initial conditions on high reynolds number turbulence. Exp Fluids 56(10):185

Krogstad PÅ, Davidson P (2010) Is grid turbulence saffman turbulence? J Fluid Mech 642:373

Mazellier N (2005) Dynamique spatio-temporelle du champ de vorticité en turbulence: mesures par corrélation acoustique dynamique. Ph.D. thesis

Mazellier N, Vassilicos J (2008) The turbulence dissipation constant is not universal because of its universal dependence on large-scale flow topology. Phys Fluids 20(1):015101

McFadden J (1958) The axis-crossing intervals of random functions-ii. IRE Trans Inf Theory 4(1):14–24

Monchaux R, Bourgoin M, Cartellier A (2010) Preferential concentration of heavy particles: a Voronoï analysis. Phys Fluids. https://doi.org/10.1063/1.3489987

Monchaux R, Bourgoin M, Cartellier A (2012) Analyzing preferential concentration and clustering of inertial particles in turbulence. Int J Multiph Flow 40:1–18

Mora DO, Cartellier A, Obligado M (2019a) Experimental estimation of turbulence modification by inertial particles at moderate re$_\lambda$. Phys Rev Fluids 4:074309. https://doi.org/10.1103/PhysRevFluids.4.074309

Mora DO, Muñiz Pladellorens E, Riera Turró P, Lagauzere M, Obligado M (2019b) Energy cascades in active-grid-generated turbulent flows. Phys Rev Fluids 4:104601. https://doi.org/10.1103/PhysRevFluids.4.104601

Mydlarski L (2017) A turbulent quarter century of active grids: from Makita (1991) to the present. Fluid Dyn Res 49(6):061401

O'Neill P.L, Nicolaides D, Honnery D, Soria J, et al (2004) Autocorrelation functions and the determination of integral length with reference to experimental and numerical data. In: 15th Australasian fluid mechanics conference, vol 1, pp 1–4. University of Sydney Sydney, NSW, Australia

Peinke J, Tabar MR, Wächter M (2019) The Fokker–Planck approach to complex spatiotemporal disordered systems. Annu Rev Condens Matter Phys 10:107–132

Pope SB (2000) Turbulent flows. Cambridge University Press, Cambridge

Puga AJ, LaRue JC (2017) Normalized dissipation rate in a moderate Taylor Reynolds number flow. J Fluid Mech 818:184–204

Smith J, Hopcraft K, Jakeman E (2008) Fluctuations in the zeros of differentiable Gaussian processes. Phys Rev E 77(3):031112

Sreenivasan K, Prabhu A, Narasimha R (1983) Zero-crossings in turbulent signals. J Fluid Mech 137:251–272

Sumbekova S, Cartellier A, Aliseda A, Bourgoin M (2017) Preferential concentration of inertial sub-Kolmogorov particles: the roles of mass loading of particles, Stokes numbers, and Reynolds numbers. Phys Rev Fluids 2(2):24302. https://doi.org/10.1103/PhysRevFluids.2.024302

Tennekes H, Lumley JL (1972) A first course in turbulence. MIT Press, Cambridge

Tritton DJ (2012) Physical fluid dynamics. Springer Science & Business Media, Berlin

Tsinober A, Tsinober, Jacobs (2019) Essence of turbulence as a physical phenomenon. Springer, Berlin

Valente P, Vassilicos JC (2011) The decay of turbulence generated by a class of multiscale grids. J Fluid Mech 687:300–340

Vassilicos JC (2015) Dissipation in turbulent flows. Annu Rev Fluid Mech 47:95–114

Wilson LR, Hopcraft KI (2017) Periodicity in the autocorrelation function as a mechanism for regularly occurring zero crossings or extreme values of a Gaussian process. Phys Rev E 96(6):062129

8.2 Work division

The work division was as follows:

Author	CR#1	CR#2	CR#3	CR#4	CR#5	CR#6	Score	Position
D.O. Mora	150	30	50	60	120	200	610	1
M. Obligado	100	70	50	40	80	50	390	2
Total	250	100	100	100	200	250	1000	-

The guidelines reflecting the scores and author ordering can be found in the appendix A. The thesis author (D.O. Mora) was engaged in the writing, revision, and and discussion of the paper (see also appendix B).

CHAPTER 9

Poly disperse particle settling velocity in decaying homogeneous isotropic turbulence

---

This chapter includes the article:
Mora, D. O. *et al.* Polydisperse particle settling velocity in decaying homogeneous isotropic turbulence, To be submitted (2020)

9.1 Summary

In this chapter, we reported the data from a experimental campaign aimed at measuring the particle settling modification of poly disperse inertial particles under homogeneous isotropic turbulence. These experiments were conducted in LEGI's wind tunnel using an active grid in triple random mode to generate turbulence at moderate Taylor Reynolds numbers $Re_\lambda \in [200 - 700]$. The liquid fractions studied, $\phi_v \leq 10^{-5}$, were the lowest attainable at the time in this facility. The particles velocities were measured by means of Doppler interferometry.

Under the mentioned experimental conditions, we observe that the settling behavior mainly depends on Re_λ, which in our facility scales with the incoming bulk velocity $Re_\lambda = f(U_\infty)$. We find that at increasing values of Re_λ (i.e., at increasing values of the carrier phase velocity fluctuation u') the particles fall slower (their speed is hindered) in the direction of gravity regardless of flux bulk concentration. A similar behavior has been recently reported in different experimental facility [148].

It is, however, uncertain whether or not this global settling reduction is due to the existence of a *facility-dependent* weak mean flow (i.e. a confinement effect) that acts in conjunction with the background turbulence. The existence of such weak mean flow has been proposed by Good et al. [10, 107] in a different wind tunnel facility and by Sumbekova in the same facility [2]. To explore this potential bias, we plot our results with respect to a translating frame of reference moving at a velocity equal to the global distribution average, i.e., $\langle V\rangle|_{all} = \int V(D_p)f(D_p)dD_p$, where $f(D_p)$ is the particle size distribution. Our results reveal a better collapse of the data when plotted in this framework suggesting that further research has to be done to quantitatively estimate the impact of these effects on the settling data.

On the other hand, this research was constrained by the results found in chapters 4, and 5, and therefore, we did not conducted 1D Voronoï analysis conditioned on the particle the local concentration.

Among the work developed, this thesis author took all the measurements, and did preliminary analyses. The author also had the original idea of plotting the results in a translating frame of reference.

The effect of Re_λ and Rouse Ro numbers on the settling of inertial particles in homogeneous isotropic turbulence

Daniel Odens Mora* and Martin Obligado
UGA, CNRS, Grenoble-INP, LEGI, F-38000, Grenoble, France

Alberto Aliseda†
Department of Mechanical Engineering,
University of Washington, Seattle, Washington 98195-2600, USA

Alain Cartellier
Univesité Grenoble Alpes, CNRS, Grenoble-INP, LEGI, F-38000, Grenoble, France

(Dated: June 29, 2020)

Abstract

Using phase Doppler interferometry, we observe that the settling behavior of polydiperse inertial particles in homogeneous isotropic turbulence downstream mainly depends on the values of Re_λ. We recover that average settling behavior decreases at increasing values of Re_λ. On the contrary, we do not retrieve a strong correlation between the particle settling weakly and on the ratio between the fluid, and gravity accelerations ($\gamma \sim (\eta/\tau_\eta^2)/g$). Moreover, we find that the boundary between the hindering, and enhancement regimes occurs at smaller Rouse numbers with increasing values of Re_λ. Thus, the particle settling strongly depends on the values of the velocity fluctuation u'.

I. INTRODUCTION

Turbulent particle-laden flows have a widespread presence in industrial and natural processes, e.g., pollen dispersion, spray combustion, planetoids growth, and clouds formation [1, 2]. Among the several consequences of particle turbulence interactions, two observations: preferential concentration (PC), and particle settling velocity modification (SVM) have received considerable attention in the last decades [3, 4]. Preferential concentration describes the tendency of particles to agglomerate and form clusters. In contrast, particle settling modification accounts for the enhanced (or reduced) particles settling velocity in the direction of the body force acting on them, for instance, gravity.

Several theoretical approaches have suggested mechanisms that relate the topology of the turbulent flow to the observed phenomena. Classical contributions have suggested that the *sub-Kolmogorov* particles, which have a characteristic scale smaller than η, tend to concentrate in regions of high strain and low vorticity [3, 5]. However, this classical picture does not fit well with the multiscale nature of turbulence. Recent research has advanced that this classical picture does not take into account the multiscale nature of turbulence. Under this framework, some studies have proposed that particles accumulate at the different (coarse-grained) scales of high strain and low vorticity [6]. Alternatively, others have retrieved evidence that particles mimic the clustering of the carrier phase zero acceleration points [7, 8], which exhibits a self-similar behavior [9].

---

[*] Also at Department of Mechanical Engineering, University of Washington, Seattle, Washington 98195-2600, USA

[†] aaliseda@uw.edu

Classical studies have suggested that modification of particles settling speed may be due to centrifuging effects: inertial particles are expelled of eddies, fast-tracking downward eddies and thereby, enhancing their respective settling speed [5, 10, 11]. Recent studies have also attempted to include the multiscale nature of turbulence to understand the observed particle settling behavior. Some works content that the centrifuging effect (and enhanced settling) depends on the relationship between the particle inertia, and the carrier phase length scales, i.e., at particles of different inertia are affected by different length scales of the turbulent flow [12]. The opposite effect has also been observed: particles settling velocity is reduced instead of being enhanced [13]. Some research has conjectured that this phenomenon occurs when particles sample upward regions of the flow[13–15].

Considering the complex interactions between the turbulent carrier phase, and the discrete particle phase, most studies treat the mentioned phenomena (i.e., PC and SVM) independently. Recent research [16–21] has, however, aimed at relating both PC, and SVM in a casual manner. For instance, some studies have reported that the increased particle enhanced particle settling is due to the increased local concentration [20, 22]. In other words, particles in high density regions settle (on average) faster with respect to particles in low density regions [7, 22–27].

Numerical and experimental studies do exhibit similar trends on the behavior of preferential concentration and settling velocity with global flow parameters, such as the Taylor-based Reynolds number $Re_\lambda = u\lambda/\nu$ and the Stokes number $St = \tau_p/\tau_\eta$. Nevertheless, quantitative consensus has yet to be reached [12, 18, 21, 23, 26, 28]. Moreover, the origin of these discrepancies could be multi-fold [18, 23, 24, 29], for instance, the numerical and experimental study of Good et al. [24] at similar values of Re_λ, and ϕ_v have shown that particle settling *hindering* effects cannot be captured in DNS simulations that only consider linear drag. Conversely, DNS simulations of Rosa et al. [29] report no variation in the particle settling velocity with the drag model, i.e., their results were insensitive to the choice of the drag law used (e.g., linear, non-linear).

Another source of discrepancy may stem from the mechanical coupling between particle phase and the turbulent carrier phase interaction ignored in most DNS studies (also known as '1-way' Another source of discrepancy may stem from the mechanical coupling between the particle phase and the turbulent carrier phase. The need to include these inter-phase mechanical coupling effects was early recognized by Aliseda et al. [22]. They suggested modifying the carrier phase pressure field to account for the flow regions with high particle density. Most DNS studies ignore this coupling and assume that the particles do not affect the carrier phase, a regime known as 'one-way' coupling. However, Bosse et al. [23], and Monchaux et al. [18] observed a larger particle velocity when the mechanical coupling between phases, a regime known as 'two-way' coupling, was included in the simulations. Their simulations, however, were run at rather small Reynolds numbers ($Re_\lambda \approx 40$). Rosa et al. [30] has recently arrived at similar conclusions at higher Reynolds numbers ($Re_\lambda \approx 100$). These findings hint that including two-way coupling interactions seems necessary to describe the phenomena underlying physics accurately.

In this work, we report experimental measurements of (polydispersed) inertial particles settling under homogeneous isotropic turbulence downstream of an active grid. Our results suggest that the Taylor-Reynolds (Re_λ) is the leading contributor to the particles' behavior. For instance, the global particle settling decreases at increasing Re_λ, the boundary between the hindering (particles falling slower than their quiescent speed), and enhancement (particles falling faster than their quiescent speed) regimes shifts to smaller Rouse numbers at increasing values of Re_λ.

II. METHODS

A. Experimental Setup

The experiments were performed in a close-circuit wind tunnel '*Lespinard*' in the *Laboratoire des Écoulements Géophysiques et Industriels* (LEGI) at Université Grenoble Alpes. This facility has been regularly employed to study particle clustering under *Homogeneous Isotropic Turbulence* (HIT) conditions [2, 31, 32]. A sketch of our experimental setup is depicted in figure 1.

In our experiments, the turbulent flow was generated utilizing an active grid [33] in triple random mode (AG). We measured the turbulent unladen velocity streamwise (with no particles) through hot-wire anemometry. We computed the turbulent parameters using standard methods and assumptions (e.g., Taylor hypothesis). The most relevant parameters are summarized in table I. For detailed explanations, see [34]. Figure 2c shows the energy spectra at the measuring station (see label '**M1**' in figure 1).

Downstream of the 'grids' section (see figure 1) a rack of 18, or 36 spray nozzles –at smaller concentrations fewer injectors were used, see figure 2a– injected inertial water droplet particles with diameters D_p between 20 and 300 microns , i.e, $D_p \in [20 - 300]\,\mu$m. This polydispersity was measured by phase Doppler interferometry (PDI) (see figure 2b, where the particle distribution has been log-normally fitted) for details , see[35]. The droplets were considered as spherical particles as their Weber number parameter was, for most droplets, below unity (see in Sumbekova [35] section 6.3).

The measuring station was placed 3m downstream of the droplet injection (see figure 1). The measuring volume lies at the centerline of the wind-tunnel. We used a PDI (Artium-PDI-200) apparatus, which can measure the settling velocity and the particles' diameter simultaneously [36, 37]. The PDI setup has two components: the receiver and the laser emitter. The laser emitter was placed perpendicular to the gas flow. The receiver (see figure 1) was on the same horizontal plane but rotated 30 degrees to ensure adequate capture of spherical water droplets in the airflow.

For the particle datasets here reported, the number of samples/droplets recorded was close to half a million (5×10^5). The velocity resolution for the vertical (resp. horizontal) component is 0.010 m/s (resp. 0.04 m/s). These conditions were maintained for all experimental conditions.

At the measuring station the particles' velocity distribution (see figures 3a-3b) were almost Gaussian. These Gaussian statistics suggest that injection transients. And therefore, we are confident that we measured the effects of the background turbulence on the particle behavior.

Considering that the carrier phase turbulence may change in the presence of particles in our facility [34], we run the experiments with the smallest liquid fractions attainable. Then, we attempted to match, as close as possible, the particles' mean velocity $\langle U \rangle$ to respective unladen mean velocity U_∞ so that we could quantify the effects of the carrier phase turbulence on the particles.

The validation rate (valid droplet measurements) reported by the PDI software was above 70% or higher in all experimental realizations. The acquisition rate (particles per second) varied between 400 and 3000 Hz depending on the liquid fraction, and bulk velocity, i.e., a higher concentration at a higher bulk velocity gave a higher acquisition rate.

Global experimental parameters of the unladen carrier turbulence phase are summarized

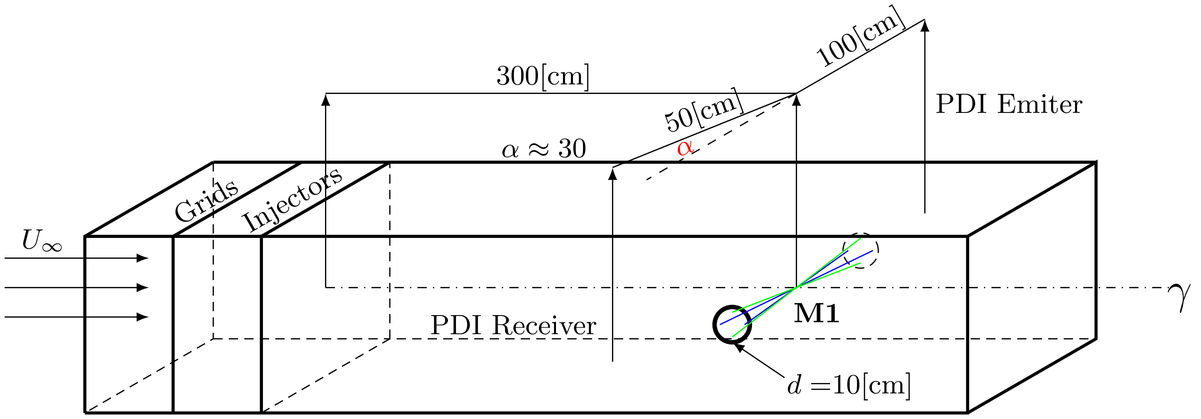

FIG. 1: Sketch of our experimental setup (not to scale). The wind-tunnel cross-section is 75x75 cm^2. Its center line is labeled as γ in the figure. The emitter and receiver components of the PDI are on the same horizontal plane. However, the receiver is positioned at 30 degrees (see α in the figure) with respect to the emitter to maximize the capture of the water droplets refraction [16, 36]. Two holes of approximately 10 cm were carved onto the walls to counteract the water accumulation on them. The measuring station was located at the position labeled as **M1** on the wind-tunnel center line, and 3 meters downstream of the droplets injection.

in table I. The particle-laden parameter space explored aimed at the smaller concentrations, and at large Reynolds numbers, attainable in our facility, respectively (see figure 2d).

This parameter space represents our effort to reduce the effects of the mechanical coupling between phases; we, therefore, present the data for the smallest liquid fractions (ϕ_v), namely, $\phi_v < 10^{-5}$.

B. Velocity measurements and angle correction

Vertical velocity measurements will contain optical alignment errors. These errors arise because we can align the PDI measuring axes only with finite precision. Therefore, there will be a small deviation angle between the PDI axes, and the wind tunnel frame of reference (see figure 4b). Considering that the particles' horizontal velocity is an order of magnitude larger than the vertical one, the horizontal component's projection onto the vertical component in the PDI frame of reference requires attention.

We address this problem by subtracting the projected mean bulk velocity from the vertical

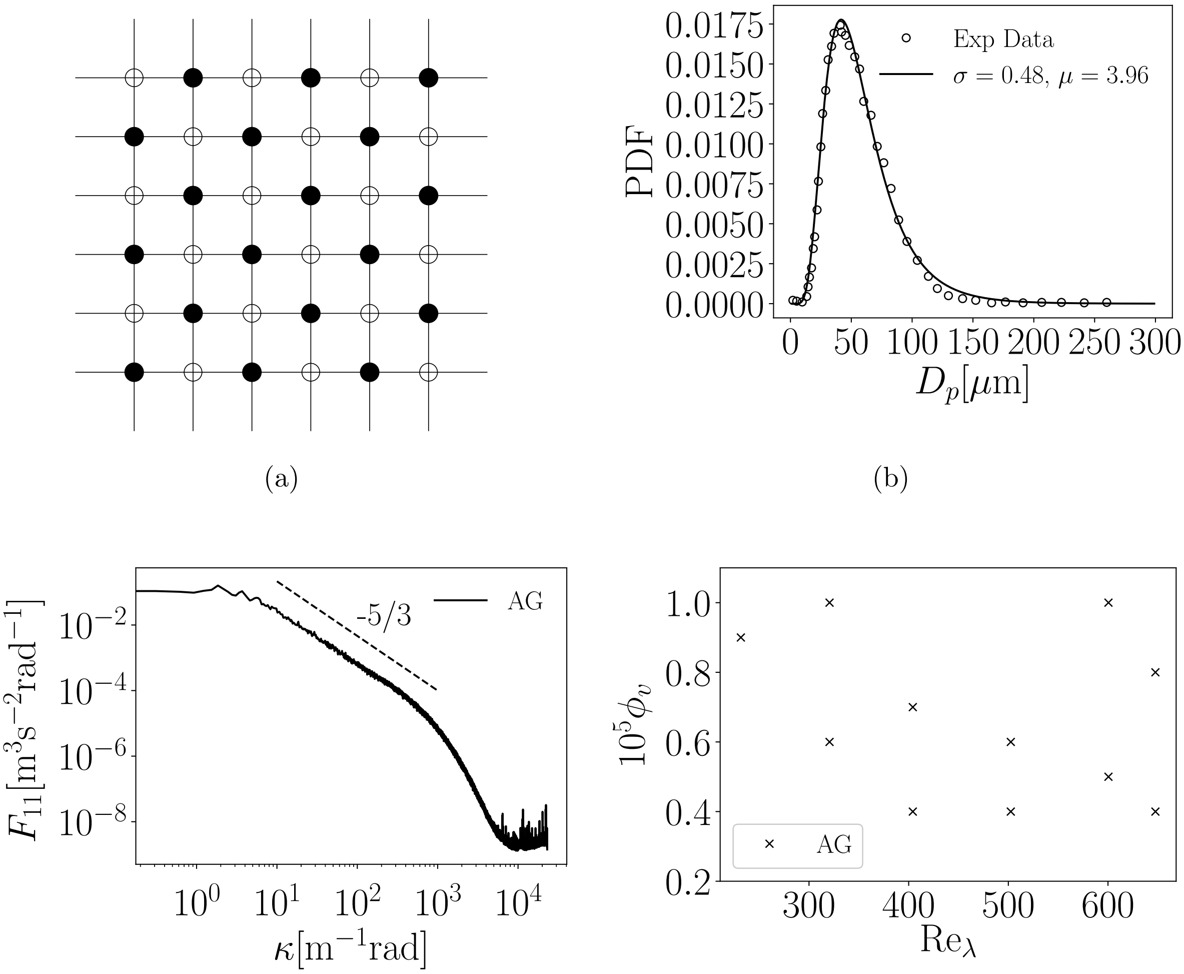

(a)

(b)

(c)

(d)

FIG. 2: a) Injector rack sketch. For the lowest volume fractions half of the injectors (filled markers) were utilized. b) Spray characterization coming from PDI data , see [35]. c) Energy spectra coming from hot wire records at measuring station **M1** (see figure 1). d) Parameter space for the experiments conducted. The global liquid fraction was estimated as $\phi_v \approx Q_W/Q_A$, where Q_W, and Q_A are the volumetric flux of water, and of air, respectively.

velocity in the PDI frame of reference. Thus, we define the angle corrected velocity as

$$V_j^c = V_j - U_\infty \sin(\beta) = V_j - V_\beta, \quad V_\beta = U_\infty \sin(\beta) \tag{1}$$

Grid Type	Re_λ	U_∞ [ms^{-1}]	u/U_∞	u_p/u	L [cm]	ε [m^{2}s^{-3}]	λ [cm]	η [μm]	Fr
Active	232	2	0.1273	[0.93, 0.95,1.21]	5.70	0.0777	1.36	457	0.24
Active	321	3	0.1343	[0.98, 1.01, 0.99, 1.04]	7.21	0.2577	1.19	338	0.59
Active	404	4	0.1405	[0.98, 1.01, 1.04, 1.05]	8.45	0.6058	1.08	273	1.12
Active	503	5	0.1476	[0.97, 1.02, 1.02, 1.05]	9.80	1.1667	1.02	231	1.84
Active	601	6	0.1541	[0.99, 1.01, 1.00, 1.02]	11.10	2.1116	0.98	200	2.87
Active	648	7	0.1578	[1.01, 1.01, 1.01, 1.02]	11.58	3.3862	0.90	178	4.09

TABLE I: Parameters of the unladen phase measured by means of hot wire anemometry at the measuring station 3m downstream the grids. The parameters are defined as, $u = \langle u' \rangle^{1/2}$, $\varepsilon = 15\nu u^2/\lambda^2$, $\eta = \left(\nu^3/\varepsilon\right)^{1/4}$, and L is the integral length scale computed following [38]. The kinematic viscosity of the air $\nu = 1.5 \times 10^{-5}$. u_p is particles stream-wise velocity standard deviation for the different cases (see figure 2d) coming from the PDI device. $Fr = \varepsilon^{3/4}/(g\nu^{1/4})$. The values in brackets represent the concentrations found in figure 2d at increasing values from left to right.

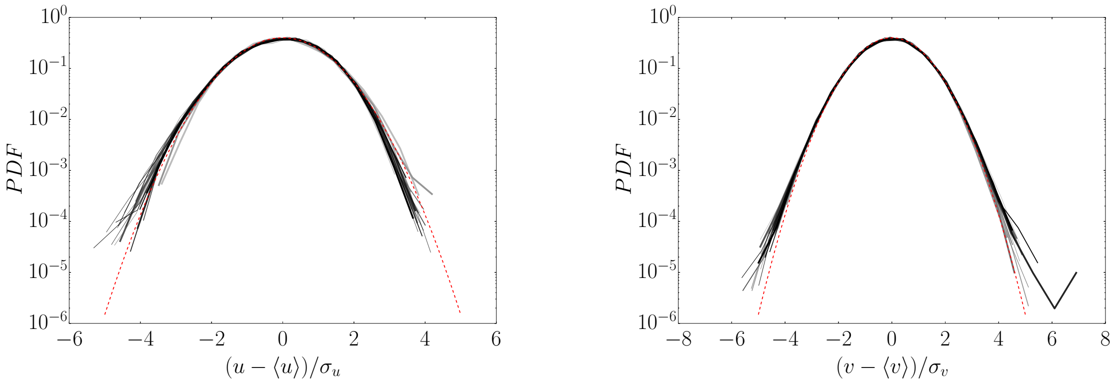

(a)

(b)

FIG. 3: PDFs of the particles velocity for the different records. a) Horizontal component. b) Vertical component. The darker the color the larger Re_λ. In the figures, the normal distribution is plotted as a dashed line (- - -).

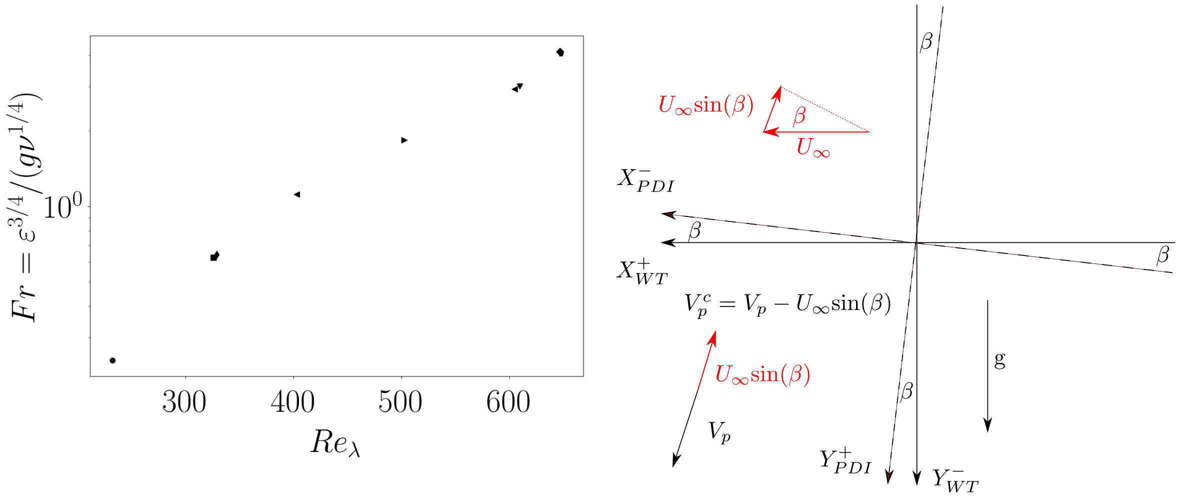

(a)

(b)

FIG. 4: a) Froude against Taylor Reynolds number for the conditions found in table I. b) Frame of reference for the wind tunnel, and the PDI device.

We obtained V_β by using a separate injector positioned at the grid. We then left the grid open, and circulated air at 3.5 ms^{-1} so that small olive oil droplets, with very narrow distribution, and mean diameter $\approx 8\mu m$, were convected downstream. We measured these droplets' velocities at **M1** (see 1). The velocity statistics collected for 2000 droplets in the PDI frame of reference (see figure 4b) were $\langle V_x \rangle = -3.52 \pm 0.02$, $\sigma_{V_x} = 0.11 \pm 0.02$, and $\langle V_y \rangle = -0.09 \pm 0.005$, $\sigma_{V_y} = 0.11 \pm 0.005$. The latter values and our resolution yielded $\beta = -1.5° \pm 0.3°$, a correction angle we used for all experimental realizations. The angle uncertainty comes the resolution available.

The latter correction is justified for all polydisperse particles under our turbulent conditions because this correction is smaller than the standard deviation of the carrier phase velocity, i.e., $V_\beta/u = \sin(\beta) \times U_\infty/u \approx \sin(1.5°) \times O(100) < 1$ (see table I, and figure3).

III. MEASUREMENTS

A. Raw settling velocity

We will consider the particles' vertical velocity to be positive towards gravity consistent with the PDI frame of reference (figure 4b). We also binned our datasets by their diameters.

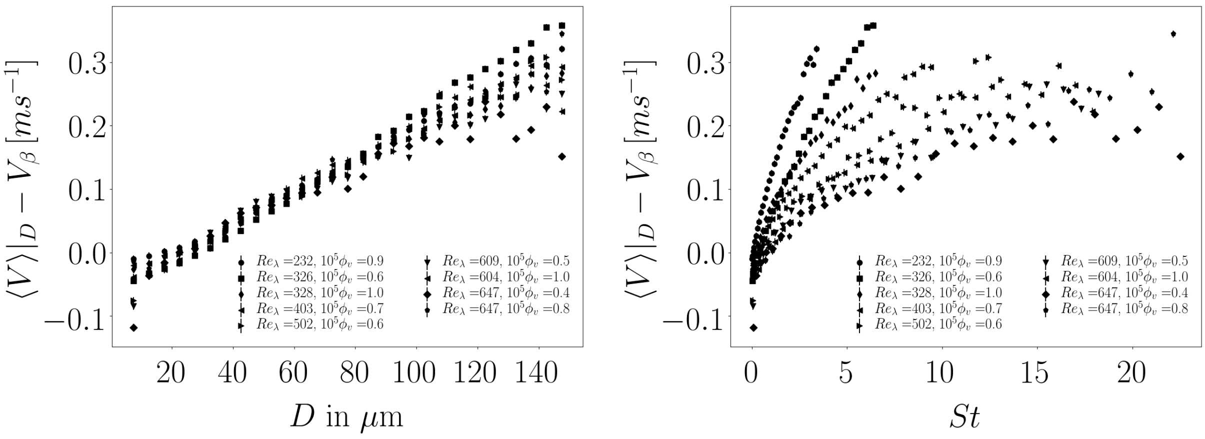

(a) (b)

FIG. 5: Active grid datasets (AG). Particle vertical velocity measurements binned by diameter size. a) Against the binned diameter. b) Against the binned Stokes number. Error bars have a size $\pm 5 \times 10^{-3} ms^{-1}$ (half of the PDI resolution).

These bins had a size of $5\mu m$ (an operation represented by $\langle\rangle|_D$) and spanned $D_p \in [10-150]$. This latter consideration is due to the injector droplet size distribution (see figure 2b). It has some consequences: smaller droplets are less common, and therefore, our first bins may have a larger variation. We, nevertheless, collected enough samples to have meaningful statistics.

Our raw velocity measurements show that with increasing diameter, the particles fall faster (see figure 5a). However, there are two sources of uncertainties in our results for the smallest droplets: first, the finite optical alignment, and second the vertical resolution used (0.010 m/s). In the latter case, the resolutions results from a trade-off between an adequate acquisition rate and the statistics needed.

Interestingly, for all particle sizes, the particles' velocities decrease with increasing Re_λ (i.e., slower settling in our convention). The polydispersity of our droplet generator, and our active grid turbulence characteristics (e.g., higher values of ε, see table I) allows us to explore a wide range (almost a decade) of particle Stokes numbers $St = \tau_p/\tau_\eta$ (see section) for the different experimental conditions (see figure 5b).

B. Settling parameters, and non-dimensional numbers

The carrier phase is usually characterized by the Taylor Reynolds number $Re_\lambda = u\lambda/nu$, where λ is the Taylor length scale [39], and ν the kinematic viscosity. Conversely, there is still an open debate (see [35] and references therein) about which parameters are adequate to describe the dynamics of the discrete phase. A complete discussion on how to derive these parameters from dimensional analysis (or from first principles) is beyond the scope of this study (see, for instance, see Sumbekova [35] section 6.5.). Thus, we briefly summarize the most common non-dimensional numbers proposed to analyze the particles settling velocity.

Classical numerical and experimental studies [11, 22] plot the particles settling velocity against the Stokes number $St = \tau_p/\tau_\eta$ (see figure 5b), where τ_p , is the particle characteristic time considering or not non-linear drag, and $\tau_\eta = (\nu/\varepsilon)^{1/2}$ is the Kolmogorov timescale; changes in the turbulence dissipation rate lead to changes in the Stokes number (figure 5b).

Other non-dimensional parameters of interest involve the ratio between the particle terminal speed (V_T) and the background turbulence RMS fluctuation ($u = \langle u'^2\rangle^{1/2}$). This ratio is known as the Rouse number $Ro = V_T/u$ [18, 35] (some authors also refer to this non-dimensional number as the settling parameter Sv [21, 24]). Algebraic manipulations allow combining Rouse and Stokes numbers as follows:

$$St = \frac{\tau_p}{\tau_\eta} \rightarrow St = \frac{\tau_p}{\tau_\eta}\frac{u}{u}\frac{g}{g} \rightarrow St = Ro\frac{u}{\tau_\eta g}, \tag{2}$$

where the particle relaxation time includes the non-linear drag from Schiller, and Nauman [40],

$$\tau_p = \frac{\rho_p D_p^2}{18\mu_f(1 + 0.15Re_p^{0.687})}. \tag{3}$$

In addition to St and Ro, some research suggest that the ratio between the turbulent acceleration (η/τ_η^2) and gravity may play a role on the results. Some authors refer to this ratio as $\gamma = \eta/(g\tau_\eta^2)$ [13, 20, 24], while others refer to it as a *Froude* number [12, 25] (Fr). In this work, we will follow the latter notation. From equations (2 - 4), and taking into account that $\lambda = \sqrt{15}\tau_\eta u$ (small scale isotropy), and that $u_\eta = \eta/\tau_\eta$, one gets;

$$Fr = \frac{\varepsilon^{3/4}}{g\nu^{1/4}} = \frac{\eta}{\tau_\eta^2 g}, \quad (4) \qquad St = \frac{RoFrRe_\lambda^{1/2}}{15^{1/4}}, \quad (5) \qquad Ro = 15^{1/4}\frac{St}{FrRe_\lambda^{1/2}}. \quad (6)$$

Moreover, combinations of these parameters such as $RoSt$ (involving the Rouse and Stokes numbers) have recently gained momentum, as they appear to give a better collapse of the data [10, 21, 24]. For the $RoSt$, one gets from equations 5, and 6 that

$$RoSt = \frac{V_T}{u}\frac{\tau_p}{\tau_\eta} \sim V_T\frac{\tau_p}{\lambda}, \tag{7}$$

which seems to gauge the influence of the background turbulence on the particle settling velocity; the ratio between the particle stopping distance to the Taylor microscale λ, which scales with the average distance between velocity stagnation points [34, 41–44].

In our experiments, we cannot change the magnitude of gravity acceleration (g) or the magnitude of the air kinematic viscosity (ν). As a result, we cannot easily disentangle or individually vary, Ro, St, and Fr. Therefore, we can only increase the turbulence dissipation rate ε by increasing the inlet velocity U_∞. These constraints yield similar functional behaviors for Fr, and Re_λ (see figure 4a). Thus, to overcome these restrictions, we use other experimental datasets taken from different experimental studies.

C. Normalized settling velocity

To quantify the degree of settling enhancement the velocity difference between the particle settling velocity and its terminal speed is computed, i.e., $\Delta V = \langle V\rangle|_D - V_T - V_\beta$, where V_β includes the misalignment effects. ΔV is usually normalized by the carrier phase fluctuations u, or by the particle terminal speed V_T [3, 11, 16, 21, 22, 25, 29].

Interestingly when normalized by u, ours and previous experiments reveal that the particle velocity is hindered (slowed down) when Re_λ increases (see figures 6a, and 6b). Akutina et al. [45] have reported similar results for experiments done in a turbulent column. Particles with small Rouse and Stokes numbers have settling velocities that depend strongly on the liquid fraction ϕ_v and Re_λ. For large Rouse numbers, the normalized particle settling ($\Delta V/u$) seems to have a quasi-linear behavior. The behavior of $\Delta V/u$ against Stokes depends on Re_λ, i.e., the larger Re_λ, the milder the settling reduction rate versus St. These observations imply each other due to the relationships between Rouse and Stokes numbers (see equation 5).

Even though our data exhibits hindering effects at very small St, and Rouse numbers, other experimental facilities recover similar behaviors, e.g., experiments in grid tanks [46] and in a box of turbulence [21]. However, we must note that these conclusions require further research given the difficulty of recovering the 'tracer' behavior in similar experimental measurements, i.e., a particle that almost perfectly follows a fluid parcels. To recover this behavior using optical techniques (e.g. PDI) and imaging (e.g. PIV, PTV), it is required that the optical alignment is very accurate so that the absolute zero is properly set. Besides proper alignment, we also need two extra elements: very dilute conditions $\phi_v \rightarrow 0$, and, in our specific case, very small particles $St \rightarrow 0$. Thus, it is not surprising that most experiments have reported values of $\Delta V \neq 0$ for $St \rightarrow 0$ [16, 22, 24, 47].

Moreover, our measurement resolution could also have an impact on the measurements taken in this regime. These resolutions limitations can be clearly observed when the velocity ΔV is normalized against V_T (see large error bars for small Rouse in figures 7a, and 7b).

Besides, we note that these conclusions could be biased by a condition that may exist due to the spatial domain where the experiments take place (confinement effects): weak recirculation currents that perturb the settling dynamics of the settling particles. These perturbations could be of the order of the settling velocity for small inertia particles biasing the results measured. These biases imply that the tracer behavior may not be recovered $\Delta V/V_T \neq 0$ for $St \rightarrow 0$, and therefore, measuring the true values of $\Delta V/V_T$ for $Ro \ll 1$ or $St \ll 1$ is not straightforward (figures 7a and 7b).

For instance, Good et al. [47] reports $\Delta V/V_T \rightarrow O(100)$ for $Ro \ll 1$ in wind tunnel experiments. In a following publication, Good et al. [24] suggest their previous experimental observation (i.e. $\Delta V/V_T \geq O(10)$ for $Ro \ll 1$) was due to a weak mean flow.

Likewise, Akutina et al. [45] reports a similar phenomenon in grid-tank experiments: "*The intensity of these mean fluid motions can be of the order of the particle settling velocity and therefore strongly affects the measurements.*"

Given the difficulty of measuring both phases simultaneously, we are unable to gauge the impact of these recirculation cells on our results. Future research should address the impact these weak mean flows have on the small Rouse regime in wind tunnel experiments. To circumvent these mean currents effects, we present in section V an analysis in a translating frame of reference.

Considering the experimental difficulties found in the double limit of $\phi_v \rightarrow$, and $St \rightarrow 0$, we will focus our analysis on bulk trends of the moderate Rouse regime, which is less sensitive to these measuring uncertainties.

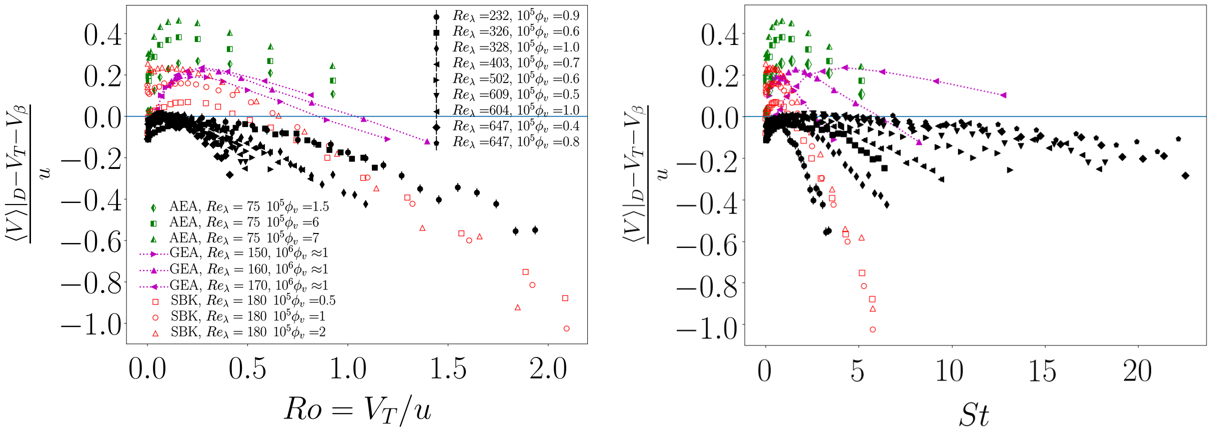

(a) (b)

FIG. 6: Particle velocity over the carrier phase fluctuations. In the figures legend GEA refers to the data of Good et al.[24]. AEA refers to the data of Aliseda et al. [22], and SBK refers to the data of Sumbekova [16]. a) Against Rouse number. b) Against the Stokes number. Error bars denote the resolution uncertainty.

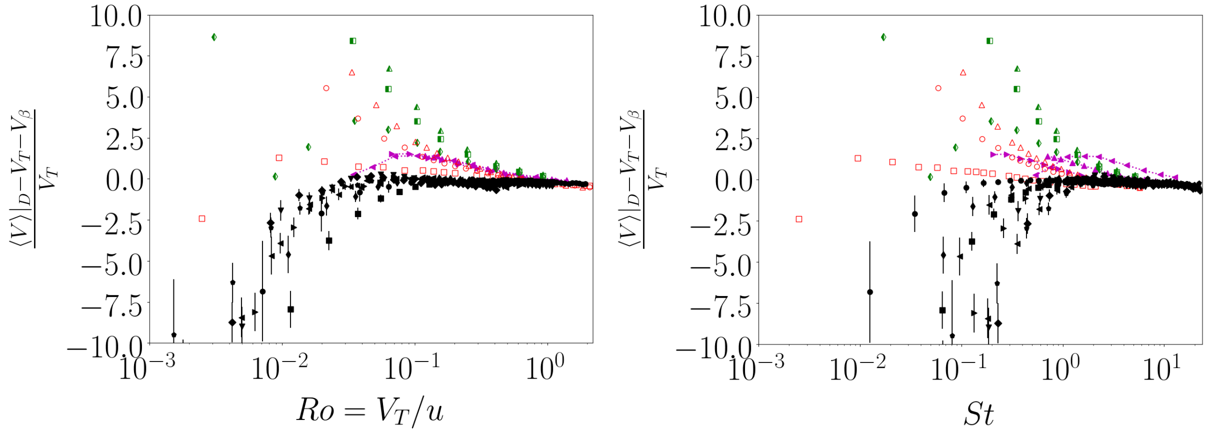

(a) (b)

FIG. 7: Particle velocity over the particle terminal speed. a) Against Rouse. b) Against stokes. The markers follow the legend of figure 6a.

IV. MODERATE ROUSE REGIME

A. Global behavior

We focus on the regime $Ro > O(0.1)$, and analyze different geometrical elements for the velocity settling curves against Rouse (see figure 8). These parameters include: their slope, their intercept or their crossover between hindering and enhancement. For those datasets that have not reached hindering, we extrapolated the crossing over from quasi-linear fits.

First, we consider the scaling of Sumbekova et al. [16] for a similar range of Rouse numbers (other scalings proposed for this regime are included in the appendix B) . They propose that the crossover Ro_{cr}, which defines the boundary between hindering and enhancement, increases with $\gamma_a = a_0^{1/2} Fr$, where $a_0 = 0.13 Re_\lambda^{0.64}$ is the Lagrangian acceleration fit proposed by Sawford [48]. This proposal seems to hold to some extent for previous datasets (see figure 9a) but it does not for the AG data, which seems to be less affected (if at all) with variations of the fluid acceleration.

Interestingly, our data reveal that Ro_{cr} (figure 9b) becomes smaller with increasing Re_λ, an effect previously reported in [15]. These results are also in agreement with the wind tunnel experiments of Good et al. [47]. Although the liquid fraction does impact Ro_{cr}, the leading order contribution comes from Re_λ. It is then left for future research to assess whether these effects could be facility dependent (e.g., due to mean weak flows present [24, 35, 45]).

Although not show here (see table II in the appendix), the linear fits intercepts (i.e. the fit in the limit $Ro \to 0$) also decrease with increasing Re_λ. This trend is consistent with the observed reduced settling at increasing Re_λ (figure 8). On the other hand, the fitted linear slopes are of order 1, i.e., $(\Delta V/u)/Ro = \Delta V/V_T = O(1)$, and they seem to become steeper with Re_λ. The correlation with Re_λ, however, is not conclusive, as multiple factors (e.g., re circulation cells, and volume fraction ϕ_v) could be influencing the results. Interestingly, this quasi-linear behavior has also been recovered in numerical simulations (see appendix A), where the lateral movements of the particles were suppressed [29].

The maximum settling enhancement (figure 9d) also decreases with Re_λ. This trend is consistent with the findings of Sumbekova et al. [17]. In particular, they report that the particles global average settling velocity decreases with increasing Re_λ using 2D PTV measurements. Likewise, the Rouse number corresponding to the maximum velocity decreases

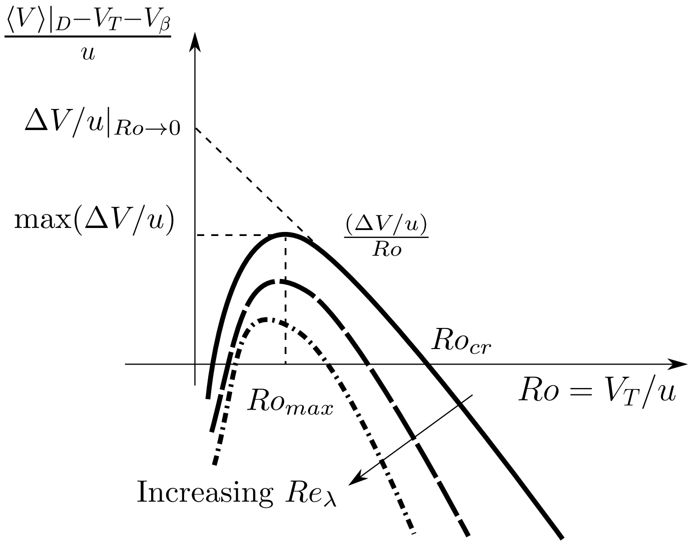

FIG. 8: Parameters computed for the data the data found 6a . The different line styles refer to different values of Re_λ.

with Re_λ (figure 9d). The latter observation may be a direct consequence of the coupling between u and Re_λ in our experiment: they both scale with the inlet velocity U_∞. Thus, $Ro = V_T/u$ decreases with increasing Re_λ. The latter results are summarized in table II in appendix A. .

B. Local concentration effects

Some experimental studies report that the increased local concentration due to preferential concentration has an impact on the particles settling velocity [20, 22]. These settling speed modifications due to local concentration are usually referred to as *collective effects.* For our experimental conditions, previous research has found evidence of preferential concentration in the same facility utilizing 2D imaging [2].

Taking into account these previous results, we decided to normalize ΔV by the clusters velocity V_{cl} based on the approach of Obligado et al. [49]. These authors take $V_{cl} \sim \langle C_{cl}\rangle\langle A_{cl}\rangle \rho_p g/(\rho_{air}\nu)$, where ρ_p is the particle density, $\langle C_{cl}\rangle$, and $\langle A_{cl}\rangle$ are the clusters concentration, and area, respectively. We estimate the latter quantities from correlations found in the same facility via 2D imaging $\langle C_{cl}\rangle \approx 4\phi_v$ [2, 20, 31], and $\langle A_{cl}\rangle = 2.1\times10^{-5} St_{max}^{-0.25} Re_\lambda^{4.7} \phi_v^{1.2}$ [2]. The latter mean concentration range has also been reported in anisotropic turbulence [50] for mass loadings between 1% to 7%.

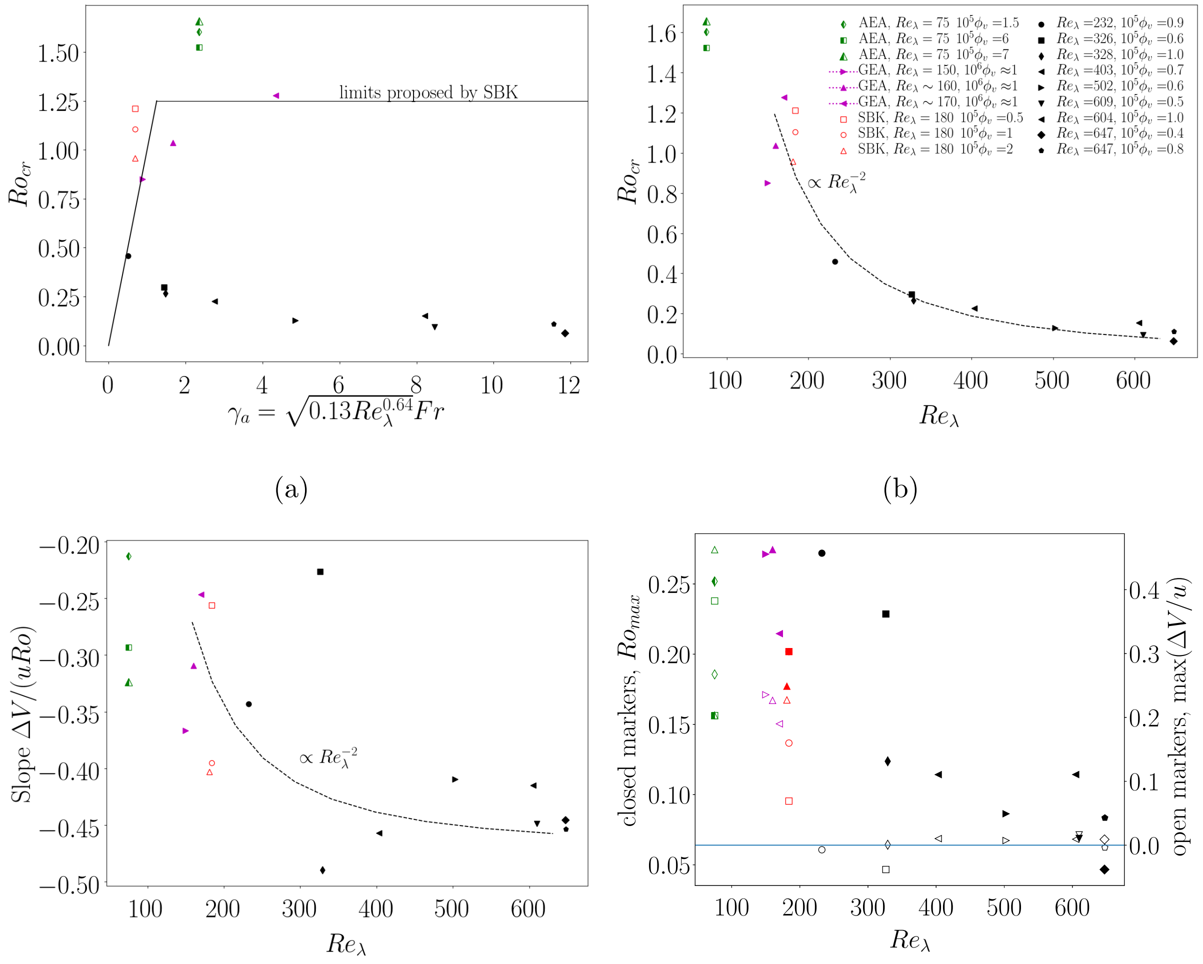

(c) (d)

FIG. 9: a) Ro_{cr} cross over between enhancement to hindering against $\gamma_a = \sqrt{0.13 Re_\lambda^{0.64}} Fr$. The solid lines refer to the proposal of Sumbekova [35]. b) Ro_{cr} cross over between enhancement to hindering against Re_λ. c) Slope of the velocity settling against the Rouse number $(\Delta V/u)/Ro$. d) Maximum settling velocity and Rouse value for these maxima. Markers follow the color convention found in figure 9b. GEA refers to the data of Good et al.[24]. AEA refers to the data of Aliseda et al. [22], and SBK refers to the data of Sumbekova [16].

Once again, the normalization by a single velocity scale fails to account for the different trends observed (figure 10a). Tom and Bragg [12] that normalizing the settling velocity results with a single length scale may not be adequate due to the multi-scale nature of the turbulence. They advance that the particle settling is affected by the many scales, and

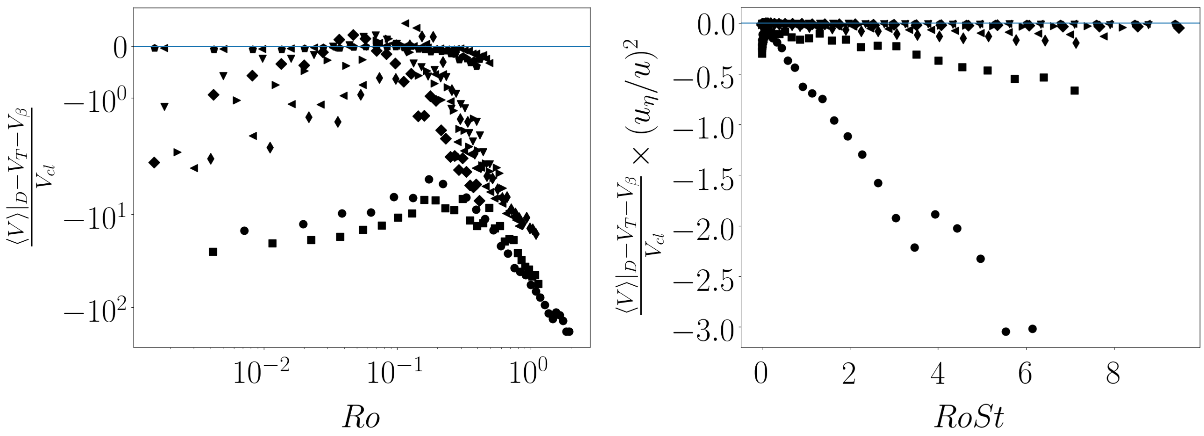

(a) (b)

FIG. 10: Active grid data settling velocity normalized by respect to different length scales including the estimated settling velocity V_{cl} following the approach of Obligado et al. [49]. The vertical axis in figures a) and b) is negative log, i.e., -1 × log.

therefore, some physics may be lost by using a single length scale.

Tom and Bragg further argue the multi-scale nature of particle settling explains the better data collapse brought by the use of the mixed length scales normalizations (small velocity scaling combined by large scale Stokes [24]). Consistent with their observations, we see a slightly better collapse when we plot using mixed scalings (small and large scales combined) (see figure 10b). However, we cannot rule out that the potential existence of a weak mean flow biases the trends seen, as proposed by Sumbekova [35]. Future experiments with higher resolution should address these claims.

V. ANALYSIS ON A MOVING FRAME OF REFERENCE

Weak mean flow effects could potentially impact the results here presented in the laboratory setting frame of reference. To address these biases, we conduct a final analysis considering the particle settling velocity in a frame of reference moving at the particle distribution global average; $\langle V\rangle|_{all} = \int V(D_p) f(D_p) dD_p$, where $f(D_p)$ is the particle distribution PDF (see figure 2b).

In this moving frame of reference, we do not need to correct for the angle deviation effects. In the regime $RoSt > 0.1$, the relative particle settling velocity has a slow evolution (see figure 11a). This slow evolving behavior can be written as

$$\frac{\langle V\rangle|_D - \langle V\rangle|_{all}}{V_T} \approx C, \tag{8}$$

with $C \in [0.4 - 0.5]$, and which after algebraic manipulation gives;

$$\frac{\langle V\rangle|_D - \langle V\rangle|_{all} - V_T}{u} \approx (C-1)Ro. \tag{9}$$

The latter expression is consistent with the quasi-linear behavior found in figure 6a. Although the datasets present some dispersion at small Rouse numbers, we observe a power-law dependency for small $RoSt \ll 10^{-2}$. If we were to apply this observed exponent, algebraic manipulations yields

$$\frac{\langle V\rangle|_D - V_T - \langle V\rangle|_{all}}{u} \approx C_{\dagger}\Big(\frac{15^{1/4}}{FrRe_{\lambda}^{1/2}}\Big)^{1/2} - Ro. \tag{10}$$

This result suggests that at very small Rouse numbers, it would be possible to bound these profiles within the values of parameter $C_{\dagger}$. The data has a better collapse in this framework when pre-multiplied by latter scaling (see figure 11b).

Although this result seems very encouraging, we cannot directly extract the physics involved in this translation moving frame. Moreover, this approach requires $\langle V\rangle|_{all}$, and thus, it is limited to datasets with polydisperse distributions. The effects of particles' polydispersity, which have been hardly explored, seem to have interesting consequences on the settling velocity. For instance, some experiments have advanced that a bidisperse particle distribution may fall faster than any of the two monodisperse ones [51], an enhancement that cannot be explained by simple linear superposition, i.e., by taking an effective diameter of the bidisperse distribution.

VI. CONCLUDING REMARKS

We have examined the particle settling velocity modification of a polydisperse droplet distribution under homogeneous isotropic turbulence downstream of an active grid in a wind tunnel facility. Our results suggest that at increasing values of Re_{λ}, the particles settling velocity decreases for the entire distribution; for all Stokes and particle diameters. Akutina et al. [45] reports similar findings in grid tank experiments.

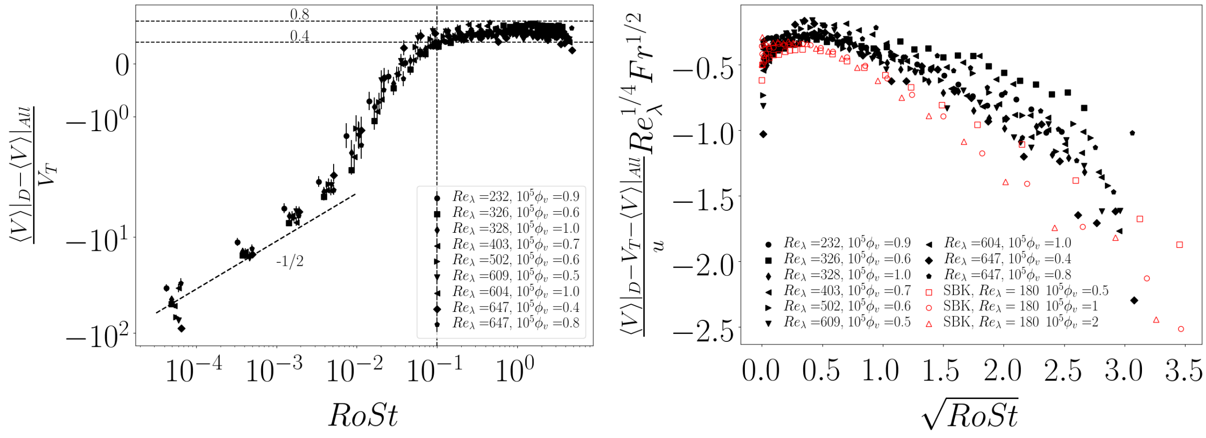

(a) (b)

FIG. 11: a) Settling Velocity in a relative frame. Error bars account for the velocity vertical resolution $\pm 0.005ms^{-1}$. b) Scaling of equation 10 applied in the relative moving frame of reference.

Our analyses suggest that Re_λ plays the leading order role in the particle settling velocity behavior. For instance, the particle velocity settling curves against the Rouse number (V_T/u) may exhibit a quasi-linear behavior, i.e., the settling velocity decreases at increasing values of Rouse. Also, the cross-over point between particle settling enhancement, and particle hindering, occurs at smaller Rouse with increasing Re_λ consistent with previous observations [15].

On the other hand, we do not find a strong correlation between the settling velocity and the Froude number (i.e. gravity-to-fluid accelerations) and the measured particle settling velocity. This could be due to the entanglement between both Re_λ and Fr in our experiments, which cannot be independently varied.

Finally, we cannot rule out that our wind tunnel experiments might be affected by a weak mean flow, as proposed by previous research [24, 35]. To address this potential bias, we have plotted our data in a translating frame of reference moving at the mean velocity of our particle distribution. Concerning such frame, ours, and previous experimental data seems to better collapse, and aids to explain some of the quasi-linear behavior seen in the absolute (laboratory) frame of reference.

	$10^5\phi_v$	Re_λ	Fr	ε	η	Slope	$\Delta V/u\|_{Ro\to 0}$	Ro_{cr}	Ro_{max}	(max($\Delta V/u$)
AEA 1	1.5	75	1.630	1.000	241	-0.213	0.341	1.602	0.252	0.267
AEA 2	6.0	75	1.630	1.000	241	-0.293	0.446	1.523	0.156	0.382
AEA 3	7.0	75	1.630	1.000	241	-0.324	0.536	1.657	0.156	0.463
GEA E1	0.1	150	0.500	0.200	360	-0.367	0.312	0.851	0.215	0.190
GEA E2	0.1	160	0.900	0.460	290	-0.309	0.321	1.037	0.274	0.227
GEA E3	0.1	170	2.300	1.600	220	-0.247	0.315	1.277	0.271	0.236
SBK 1	0.5	185	0.490	0.200	400	-0.256	0.310	0.555	0.202	0.069
SBK 2	1.0	185	0.490	0.200	400	-0.395	0.436	0.671	0.202	0.160
SBK 3	2.0	185	0.490	0.200	400	-0.405	0.386	0.624	0.177	0.227
AG	0.9	232	0.243	0.078	455	-0.343	0.157	0.459	0.272	-0.007
AG	0.6	326	0.625	0.277	332	-0.226	0.067	0.297	0.229	-0.038
AG	1.0	329	0.641	0.286	330	-0.490	0.130	0.266	0.124	0.001
AG	0.7	403	1.118	0.601	274	-0.457	0.104	0.227	0.114	0.010
AG	0.6	503	1.840	1.168	232	-0.410	0.052	0.128	0.086	0.007
AG	0.5	610	3.014	2.255	197	-0.449	0.042	0.094	0.069	0.016
AG	1.0	605	2.934	2.176	198	-0.415	0.064	0.153	0.114	0.009
AG	0.4	647	4.141	3.444	177	-0.445	0.028	0.063	0.047	0.009
AG	0.8	648	4.040	3.333	178	-0.454	0.050	0.110	0.083	-0.004

TABLE II: Summary of the parameters extracted from figures 9b to 9d.

Appendix A: Global settling velocity behavior against Rouse number trends

Table II summarizes the different parameters collected from the analysis made in section IV A.

Appendix B: Alternative scalings

The scaling of Sumbekova et al. [16] (figure 12a) does not show a better collapse when compared to those of include in the main text. In the figure, some of the curves look closer, but this could be an effect of the y scale used. On the other hand, when large and small

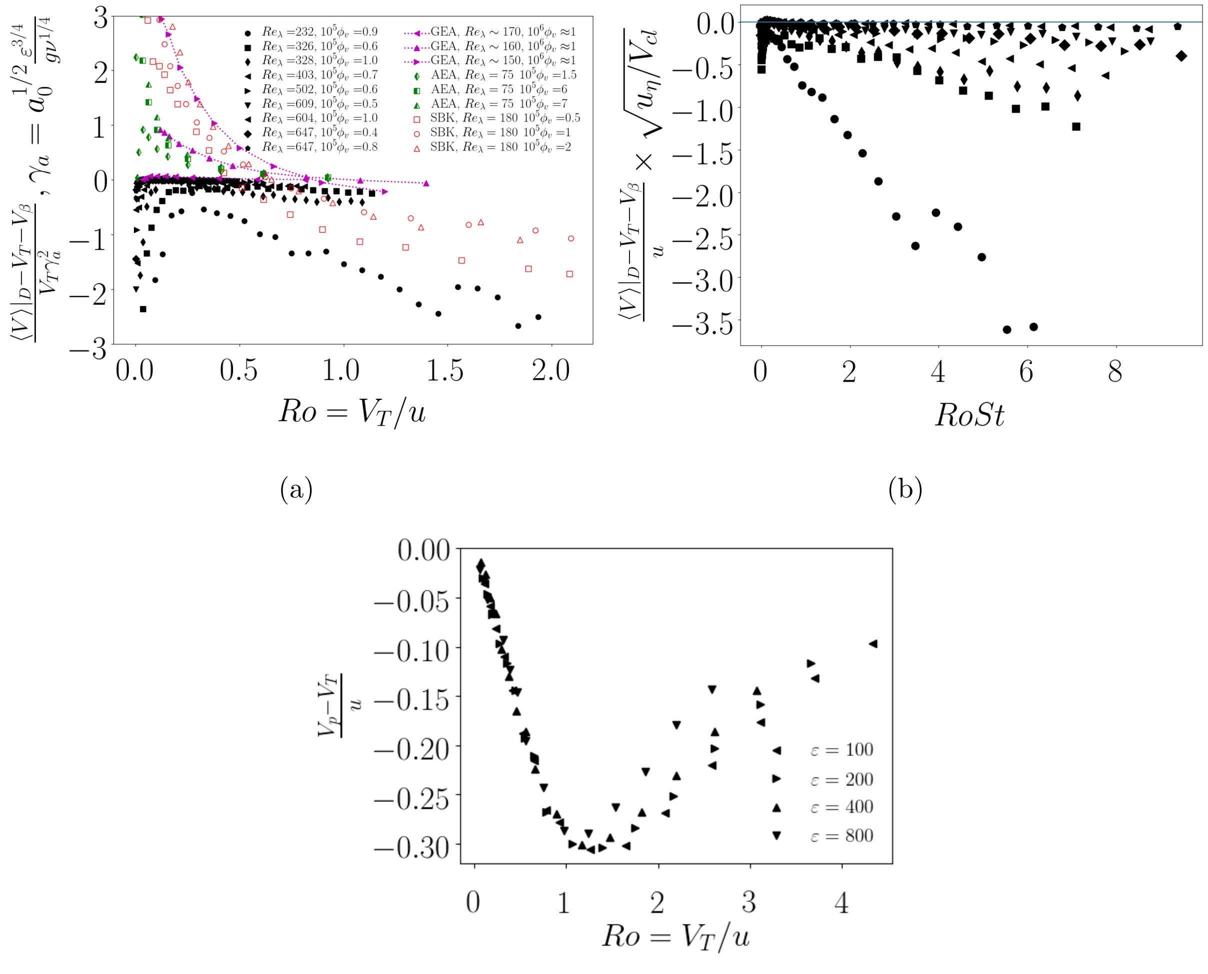

(a) (b)

(c)

FIG. 12: a) Sumbekova et al. scaling [16]. b) Combination of the velocity scales for the AG data. c) Data from fig 16 of Rosa et al. [29]. In the legends, GEA the data of Good et al.[24], AEA refers to the data of Aliseda et al. [22], and SBK refers to the data of Sumbekova [16].

fluid scales are are combined with the cluster falling velocity the curves come close together to some extent (figure 12b). This highlights again the including multiple scales may be necessary to understand the underlying physics of the particle settling modification by the turbulent carrier phase.

Rosa et al. [29] also found a linear hindering behavior, consistent with our findings of section IV A , with a slope close to -0.3, when the lateral movement of the particles was suppressed in direct numerical simulations (figure 12c).

---

[1] P. A. Vaillancourt and M. Yau, Review of particle-turbulence interactions and consequences for cloud physics, Bulletin of the American Meteorological Society **81**, 285 (2000).

[2] S. Sumbekova, A. Cartellier, A. Aliseda, and M. Bourgoin, Preferential concentration of inertial sub-Kolmogorov particles: The roles of mass loading of particles, Stokes numbers, and Reynolds numbers, Physical Review Fluids **2**, 24302 (2017).

[3] S. Balachandar and J. K. Eaton, Turbulent dispersed multiphase flow, Annual review of fluid mechanics **42**, 111 (2010).

[4] S. Elghobashi, Direct numerical simulation of turbulent flows laden with droplets or bubbles, Annual Review of Fluid Mechanics **51**, 217 (2019).

[5] M. Maxey, The gravitational settling of aerosol particles in homogeneous turbulence and random flow fields, Journal of Fluid Mechanics **174**, 441 (1987).

[6] A. D. Bragg, P. J. Ireland, and L. R. Collins, Mechanisms for the clustering of inertial particles in the inertial range of isotropic turbulence, Physical Review E **92**, 023029 (2015).

[7] S. Coleman and J. Vassilicos, A unified sweep-stick mechanism to explain particle clustering in two-and three-dimensional homogeneous, isotropic turbulence, Physics of Fluids **21**, 113301 (2009).

[8] M. Obligado, T. Teitelbaum, A. Cartellier, P. Mininni, and M. Bourgoin, Preferential concentration of heavy particles in turbulence, Journal of Turbulence **15**, 293 (2014).

[9] S. Goto and J. Vassilicos, Self-similar clustering of inertial particles and zero-acceleration points in fully developed two-dimensional turbulence, Physics of Fluids **18**, 115103 (2006).

[10] S. Ghosh, J. Davila, J. Hunt, A. Srdic, H. Fernando, and P. Jonas, How turbulence enhances coalescence of settling particles with applications to rain in clouds, Proceedings of the Royal Society A: Mathematical, Physical and Engineering Sciences **461**, 3059 (2005).

[11] L.-P. Wang and M. R. Maxey, Settling velocity and concentration distribution of heavy particles in homogeneous isotropic turbulence, Journal of fluid mechanics **256**, 27 (1993).

[12] J. Tom and A. D. Bragg, Multiscale preferential sweeping of particles settling in turbulence, Journal of Fluid Mechanics **871**, 244 (2019).

[13] P. Nielsen, Turbulence effects on the settling of suspended particles, Journal of Sedimentary Research **63**, 835 (1993).

[14] P. Nielsen, On the motion of suspended sand particles, Journal of Geophysical Research: Oceans **89**, 616 (1984).

[15] K. Kawanisi and R. Shiozaki, Turbulent effects on the settling velocity of suspended sediment, Journal of hydraulic engineering **134**, 261 (2008).

[16] S. Sumbekova, A. H. Cartellier, M. Bourgoin, and A. Aliseda, Enhancement versus hindering: impact of the turbulence characteristics on the settling behavior of heavy sub-Kolmogorov particles in a turbulent flow, in *10th International Conference on Multiphase Flow (ICMF 2019)* (Rio de Janeiro, Brazil, 2019).

[17] S. Sumbekova, A. Aliseda, A. Cartellier, and M. Bourgoin, Clustering and settling of inertial particles in turbulence, in *Proceedings of the 5th International Conference on Jets, Wakes and Separated Flows (ICJWSF2015)* (Springer, 2016) pp. 475–482.

[18] R. Monchaux and A. Dejoan, Settling velocity and preferential concentration of heavy particles under two-way coupling effects in homogeneous turbulence, Physical Review Fluids **2**, 104302 (2017).

[19] L. Baker, A. Frankel, A. Mani, and F. Coletti, Coherent clusters of inertial particles in homogeneous turbulence, Journal of Fluid Mechanics **833**, 364 (2017).

[20] P. Huck, C. Bateson, R. Volk, A. Cartellier, M. Bourgoin, and A. Aliseda, The role of collective effects on settling velocity enhancement for inertial particles in turbulence, Journal of Fluid Mechanics **846**, 1059 (2018).

[21] A. J. Petersen, L. Baker, and F. Coletti, Experimental study of inertial particles clustering and settling in homogeneous turbulence, Journal of Fluid Mechanics **864**, 925 (2019).

[22] A. Aliseda, A. Cartellier, F. Hainaux, and J. C. Lasheras, Effect of preferential concentration on the settling velocity of heavy particles in homogeneous isotropic turbulence, Journal of Fluid Mechanics **468**, 77 (2002).

[23] T. Bosse, L. Kleiser, and E. Meiburg, Small particles in homogeneous turbulence: settling velocity enhancement by two-way coupling, Physics of Fluids **18**, 027102 (2006).

[24] G. Good, P. Ireland, G. Bewley, E. Bodenschatz, L. Collins, and Z. Warhaft, Settling regimes of inertial particles in isotropic turbulence, Journal of Fluid Mechanics **759** (2014).

[25] J. Bec, H. Homann, and S. S. Ray, Gravity-driven enhancement of heavy particle clustering in turbulent flow, Physical review letters **112**, 184501 (2014).

[26] P. J. Ireland, A. D. Bragg, and L. R. Collins, The effect of reynolds number on inertial particle

dynamics in isotropic turbulence. part 1. simulations without gravitational effects, Journal of Fluid Mechanics **796**, 617 (2016).

[27] R. Dhariwal and A. D. Bragg, Small-scale dynamics of settling, bidisperse particles in turbulence, Journal of Fluid Mechanics **839**, 594 (2018).

[28] T. Wittemeier and J. S. Shrimpton, Explanation of differences in experimental and computational results for the preferential concentration of inertial particles, Computers & Fluids **173**, 37 (2018).

[29] B. Rosa, H. Parishani, O. Ayala, and L.-P. Wang, Settling velocity of small inertial particles in homogeneous isotropic turbulence from high-resolution dns, International Journal of Multiphase Flow **83**, 217 (2016).

[30] B. Rosa, J. Pozorski, and L.-P. Wang, Effects of turbulence modulation and gravity on particle collision statistics, International Journal of Multiphase Flow , 103334 (2020).

[31] R. Monchaux, M. Bourgoin, and A. Cartellier, Preferential concentration of heavy particles: A Voronoï analysis, Physics of Fluids **22**, 10.1063/1.3489987 (2010).

[32] M. Obligado, A. Cartellier, and M. Bourgoin, Experimental detection of superclusters of water droplets in homogeneous isotropic turbulence, EPL (Europhysics Letters) **112**, 54004 (2015).

[33] L. Mydlarski, A turbulent quarter century of active grids: from makita (1991) to the present, Fluid Dynamics Research **49**, 061401 (2017).

[34] D. O. Mora, E. Muñiz Pladellorens, P. Riera Turró, M. Lagauzere, and M. Obligado, Energy cascades in active-grid-generated turbulent flows, Phys. Rev. Fluids **4**, 104601 (2019).

[35] S. Sumbekova, *Concentration préférentielle de particules inertielles : la structure et la dynamique de clusters*, Ph.D. thesis, Universite Grenoble Alpes (2016).

[36] W. Bachalo and M. Houser, Phase/doppler spray analyzer for simultaneous measurements of drop size and velocity distributions, Optical Engineering **23**, 235583 (1984).

[37] J. D. Schwarzkopf, M. Sommerfeld, C. T. Crowe, and Y. Tsuji, *Multiphase flows with droplets and particles* (CRC press, 2011).

[38] A. J. Puga and J. C. LaRue, Normalized dissipation rate in a moderate taylor reynolds number flow, Journal of Fluid Mechanics **818**, 184 (2017).

[39] S. B. Pope, *Turbulent Flows* (Cambridge University Press, 2000).

[40] R. Clift, J. Grace, and M. Weber, *Bubbles, drops, and particles* (Dover Publ., 1978).

[41] H. Liepmann and M. Robinson, *Counting Methods and Equipment for Mean-Value Measure-*

ments in Turbulence Research. Washington, DC: National Advisory Committee for Aeronautics, Tech. Rep. (Technical Report, 1953).

[42] K. Sreenivasan, A. Prabhu, and R. Narasimha, Zero-crossings in turbulent signals, Journal of Fluid Mechanics **137**, 251 (1983).

[43] N. Mazellier and J. Vassilicos, The turbulence dissipation constant is not universal because of its universal dependence on large-scale flow topology, Physics of Fluids **20**, 015101 (2008).

[44] J. C. Vassilicos, Dissipation in turbulent flows, Annual Review of Fluid Mechanics **47**, 95 (2015).

[45] Y. Akutina, T. Revil-Baudard, J. Chauchat, and O. Eiff, Experimental evidence of settling retardation in a turbulence column, Physical Review Fluids **5**, 014303 (2020).

[46] C. N. Jacobs, W. Merchant, M. Jendrassak, V. Limpasuvan, R. Gurka, and E. E. Hackett, Flow scales of influence on the settling velocities of particles with varying characteristics, PloS one **11** (2016).

[47] G. Good, S. Gerashchenko, and Z. Warhaft, Intermittency and inertial particle entrainment at a turbulent interface: the effect of the large-scale eddies, Journal of Fluid Mechanics **694**, 371 (2012).

[48] B. Sawford, Reynolds number effects in lagrangian stochastic models of turbulent dispersion, Physics of Fluids A: Fluid Dynamics **3**, 1577 (1991).

[49] M. Obligado, A. Cartellier, A. Aliseda, T. Calmant, and N. de Palma, Study on preferential concentration of inertial particles in homogeneous isotropic turbulence via big-data techniques, Physical Review Fluids **5**, 024303 (2020).

[50] V. Boddapati, M. Manish, and S. Sahu, A novel approach for conditional measurement of droplet size distribution within droplet clusters in sprays, Experiments in Fluids **61**, 42 (2020).

[51] Y. Wang and K. Lam, Clustering behaviour and settling velocity of bidisperse inertial particles in turbulent open channel flow, International Journal of Multiphase Flow , 103303 (2020).

9.2 Work division

The work division was as follows:

Author	CR#1	CR#2	CR#3	CR#4	CR#5	CR#6	Score	Position
D.O. Mora	120	20	80	80	100	120	520	1
A. Cartellier	60	10	20	20	50	65	225	2
M. Obligado	30	35	-	-	30	35	130	3
A. Aliseda	40	35	-	-	20	30	125	4
Total	250	100	100	100	200	250	1000	-

The guidelines reflecting the scores and author ordering can be found in the appendix A. The thesis author (D.O. Mora) was engaged in the writing, revision, and and discussion of the paper (see also appendix B).

CHAPTER 10

Experimental campaign in wind tunnel with an active-grid-turbulence distributed by jets

10.1 Scientific justification

As stated in the introductory chapter (see chapter 1), the numerous gaps in our knowledge of particle laden flows require further experimental studies. Although some progress has been made [6, 10, 14], there is still a dire need of extending the available parameter space both in terms of the magnitudes of Re_λ, and the particles' concentration ϕ_v. Furthermore, some recent studies suggest that different turbulent generators [145] could affect the particle settling. For instance, at the University of Washington turbulence is induced by a jet grid (see section 2.1.3.1), while in Grenoble it is induced by means of an active grid. This prompts more questions regarding the influence of the facility (e.g. confinement effects, turbulence cascade) in the measured flow variables and flow physics. Thus, conducing experiments in both facilities offers a unique opportunity to explore the parameter space (different turbulence generators, and values of Re_λ), and to gauge the impact of the facility peculiarities (different wind tunnel cross sections, and droplet generators) on the data, for instance, when assessing the influence (existence) of $V_{physical}$ [2] on the particle settling velocity.

10.2 Facility status at the University of Washington

As described in section 3.2, in spring 2019 (6 months before the start of this work's author's stay), the wind tunnel facility was relocated from its old location to a new location. Hence, this thesis author was the main responsible –although I received in multiple occasions the kind help of the lab personnel– to rebuild the wind tunnel facility now known as *Chibchacum*, and the challenges it presented in its new location. For instance, this new building did not have the same utilities (e.g. water or pressure lines), as the old one. In addition, and due to the space restrictions a rack of PC fans was used to drive the free stream wind velocity (U_∞) instead of a compressor, and therefore, an analysis is to be conducted to check the turbulent conditions downstream of the grid (see section 10.2.3).

We strived to rebuild the experimental setup to a high fidelity so that ours and future experiments are run under similar conditions as those reported by the experiments of Bateson and Aliseda [62], and Huck et al. [14]. The rebuilding of the experimental facility, however, was not an easy task given that multiple situations including the COVID-19 pandemic affected the reassembly and fine tunning of the wind tunnel. We summarize the most important delays below, and the fixes required to put the wind tunnel back into functioning.

First, we had to refurbish the original grid, where the droplet injectors were affixed. The repair was needed due to the water leaks found in initial tests. Although some minor leaks are acceptable, the discrepancy between the different injector flow rates was as high as 20%. These moderate discrepancies would bias the experiment and could introduce non-negligible uncertainty in the conclusions drawn from experimental data. Thus, a major refurbishment of the grid was required. Second, it was found that the water manifold for droplet delivery had corrosion, and limestone deposits. The manifold was therefore disassembled machined, and anodized. Taking into account that these fixes were considerable, we will describe below the steps taken for future reference.

10.2.1 Grid refurbishment

The repairing procedure comprised the following steps:

1. The original grid (an excerpt from Bateson thesis [66]) was devised as a solid unit, and as such the injectors once built could not be easily removed. Thus, and after exploring several options, it was deemed necessary to cut the fore section (in the downstream direction) of the grid and extract the injectors. The fix could also only be conducted *in-situ*.
2. The latter entailed cutting the internal piping, and as a result, the injectors after being removed they had to be reattached and retested (see figure 10.2).
3. The barb-fittings where the water tubing were connected to, as well as the water manifold showed signs of limestone deposition. These deposition particulates led to continuous clogging of the fittings, rendering impossible to have a homogeneous droplet concentration. To cater for the latter, the internal section of the manifold was machined, and it was also bathed and scrubbed with white vinegar.
4. The water barb fittings were also remade, as the tiny diameters (0.3mm) for the droplet injectors constantly clogged, and were blocked by sediments on the manifolds.

Some relevant information parameters are summarized below for future repairs or adaptations if needed:

- The same plastic tubing reference was used for both air and water lines. The tubes had an internal diameter (ID) 1/8”, and outside diameter (OD) 3/16 inches.

- The tubing intended for the water was cut at 11 feet 3 inches and with an internal diameter of 1/8, and the tubing intended for the air was cut at 8 feet 1 inches.

- We employed ear clamps to connect the pipes to the droplet injectors. The clamp used was a *Vibration-Resistant Pinch Clamp* from McMaster (ref: **52545K13**), which is intended for 9/64" to 3/16" OD pipes. This kind of ear clam provided a better sealing (leak reduction) than other models including the original one.

10.2.2 Water manifolds refurbishment

Early tests with the refurbished grid revealed that the barbed fittings attached to the water manifold exhibited clogging. Although the clogging might be due to multiple reasons, aluminium corrosion was found inside the water manifold. Taking into account that this is a critical element of the droplet delivery system, it was decided to machine, and anodize the water manifold.

The anodizing process was conducted by the company Electro-Chem Metal Finishing Inc based in Portand, Oregon. The gold anodizing option was selected in order to reduce future corrosion (see figure 10.3(a)). We also rebuild some of the barbed fittings (see figure 10.3(b)) affixed to the manifold to control for the constant clogging seen in early tests. These barbed fitting specifications followed the experiments of Bateson [66]; a high pressure pipe (McMaster carr ref: **51755K19**) of length 35mm and internal diameter of 0.03mm glued, using marine epoxy, to a barbed fitting (from McMaster carr ref: **4406T16**).

10.2.3 Unladen phase, and droplet generation

A rack of 25 fans were affixed to the air conditioning section of the wind tunnel (see figure 10.4). The fans were connect in parallel, and were powered by a direct current (DC) power supply which provided 30 volts, and approximately 12 amps. Run at the maximum safest voltage, a downstream velocity profile was roughly 2 m/s (with the exception of the side walls). This velocity lies within the range of the original design limits (i.e. the particle residence time within the test section is 1-2 seconds, and therefore, the updated design was adequate for current and the future experiments.

The droplets were generated by the house-designed injectors (see figure 10.5). These injectors also allow to increase the turbulence levels (and thereby Re_λ) to the levels reported by Huck et al. [14]. Thus, we fed the air injectors with an air flux of 1100 LPM (liters per minute) so that the droplets diameters were on the same range as those reported by Bateson [66], and with a liquid water flux of 2LPM, the maximum attainable in the new building.

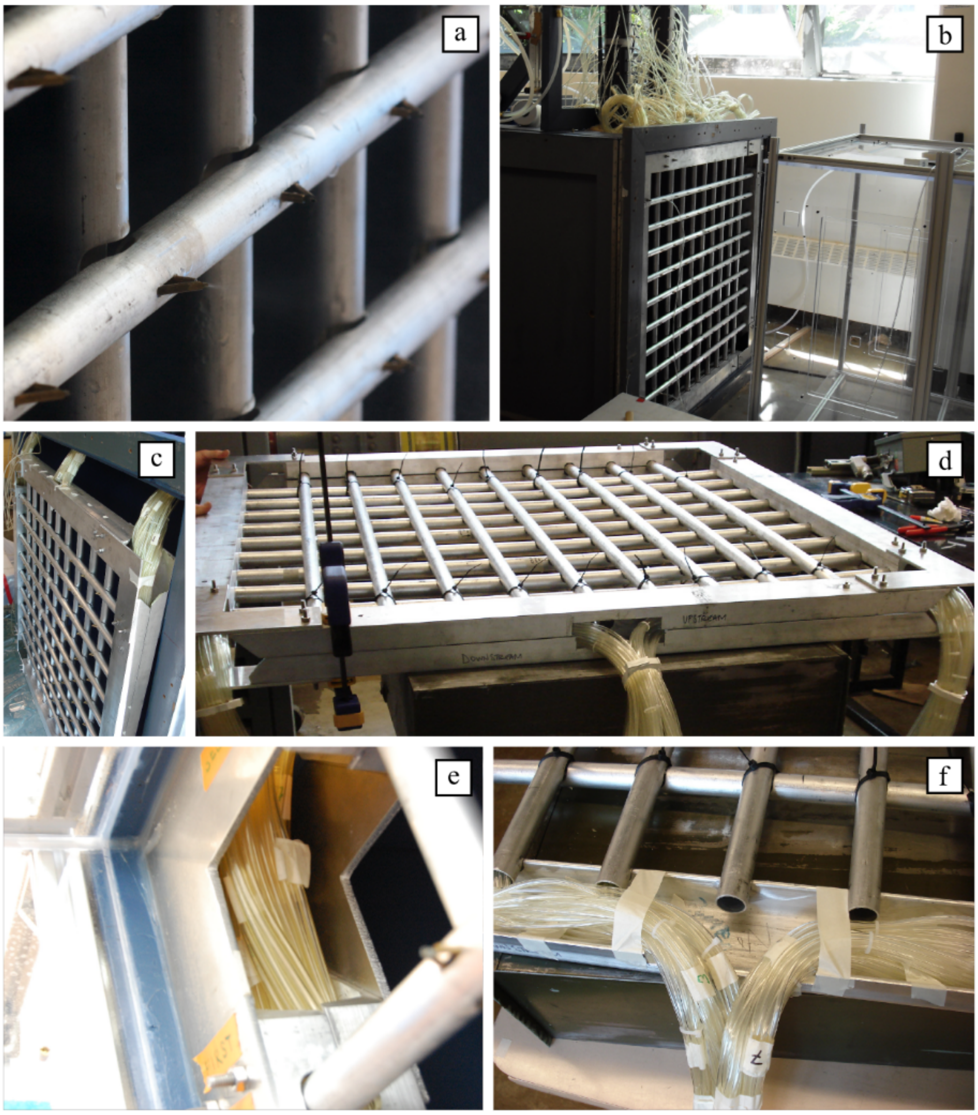

Figure 10.1 – Photos of the turbulence-inducing droplet injection grid. (a) The grid and the injectors in their final configuration. (b) The grid just after it was installed in the tunnel for the first time. (c) Feeding the injector supply lines through the wind tunnel wall. (d)The grid just after the supply line plumbing was finished. (e) The supply lines inside the grid frame. (f) The supply lines inside the grid frame with half of the frame removed for The supply line installation. The picture and its legend are taken from [66]

10.3 Wind tunnel reconstruction, and experimental setup

By the end of July 2020, we finished the reconstruction of the wind tunnel experiments (see figure 10.6). Due to the severe delays, and setbacks encountered, as previously described, and taking into account the tight time schedule to develop this thesis work, we report only details of the reconstruction of

(a) (b)

(c) (d)

Figure 10.2 – a-b) Illustration of the cuts required to access the injectors notice that the old piping was yellow, whereas the new piping is transparent.

(a) (b)

Figure 10.3 – . a) Anodized water manifold right golden vertical tube. b) Example of the barbed fittings rebuilt.


(a) (b)

Figure 10.4 – Illustration of PC fans employed. a) Rack of fans. b) Beginning of the conditioning section.

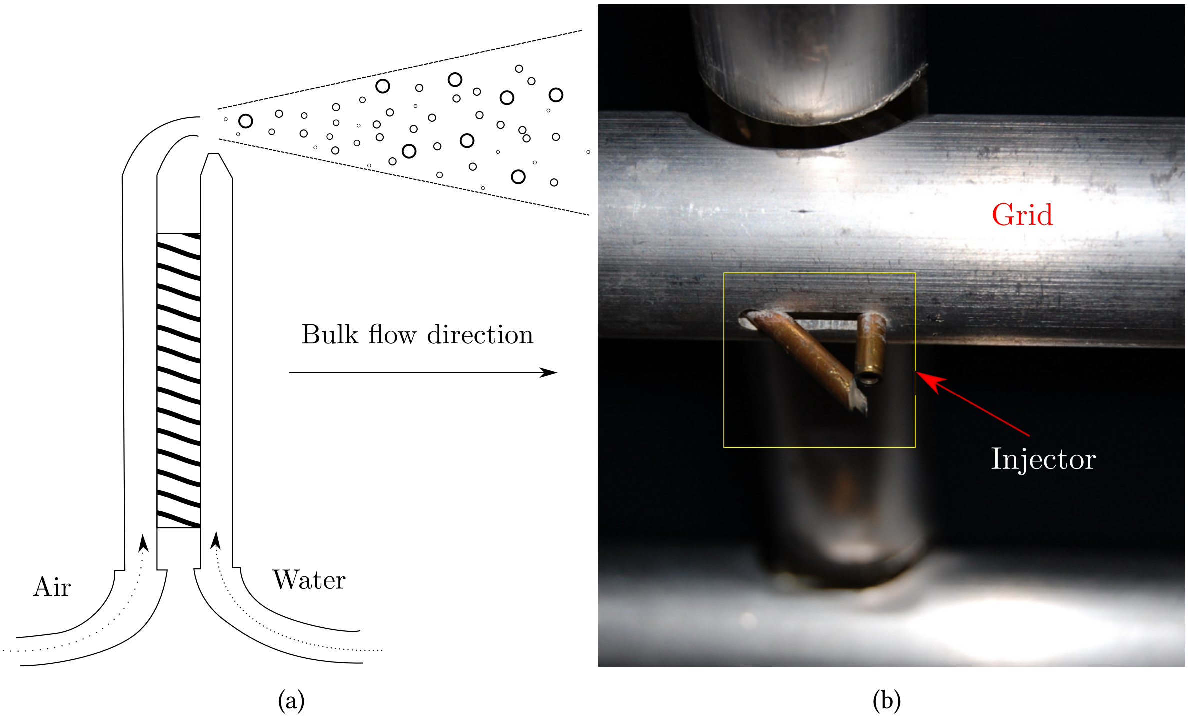

Figure 10.5 – a) Injector sketch. b) Injector sample outside used.

the wind tunnel experiments. We, however, briefly describe (see next section) the details of the experimental campaign conducted in Seattle in August 2020. Hence, experimental measurements, wind tunnel single phase characterization, and particles size characterization will be reported in coming publications elsewhere.

10.3.1 Experimental setup

At University of Washington; we aim at conducting stereo-PTV measurements (see figure 10.6) taking advantage of the previous experience and *know-how* from Aliseda's lab: a set of two state to the art high-speed cameras with a resolution of (2560x1600) pixels, and newly developed PTV-algorithm [149]. Based on the work of Huck et al. [14], we plan to track the injected water droplets, and measure their 3-velocity components and acceleration. Although most studies have focused on the vertical quantities (e.g., settling velocity), not so many studies have examined how this component (if at all) is affected by the background turbulence, increased local concentration (preferential concentration), or confinement effects. An experimental study of this kind is also necessary, as box-turbulence facilities [10] have shown that in the presence of gravity particle velocity fluctuations do not stay isotropic at increasing values of the Rouse number. Given that classical and modern approaches to explain preferential concentration do not consider the anisotropy of the particle fluctuations, one could speculate that the presence of such anisotropy may induce different mechanisms, yet to be examined, in real flows, e.g., cloud and rain formation.

Our experimental campaign is schedule to start in August 2020, and will be reported in future publications. The experimental setup will involve two high-speed cameras taking measurements at two positions 25M, and 35M downstream of the grid (see figure 10.7).

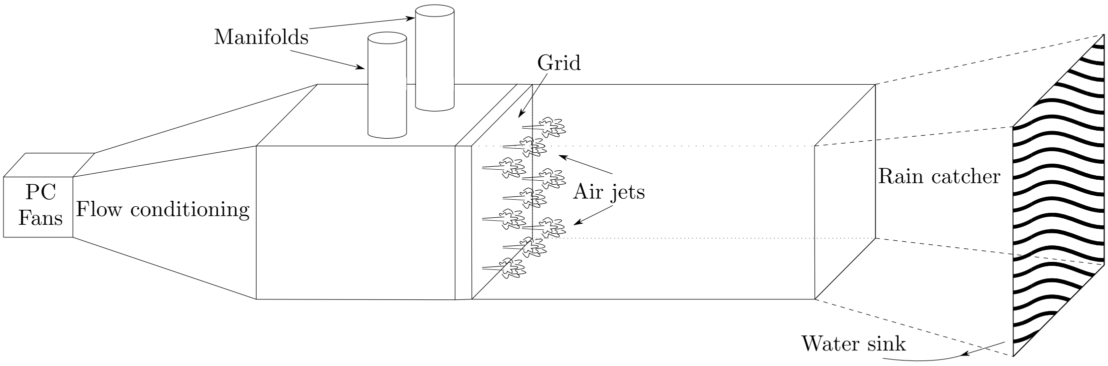

(a)

(b)

Figure 10.6 – a) Sketch of the experimental setup. b) Rebuilt wind tunnel setup. PTV cameras are shown in the red circle.

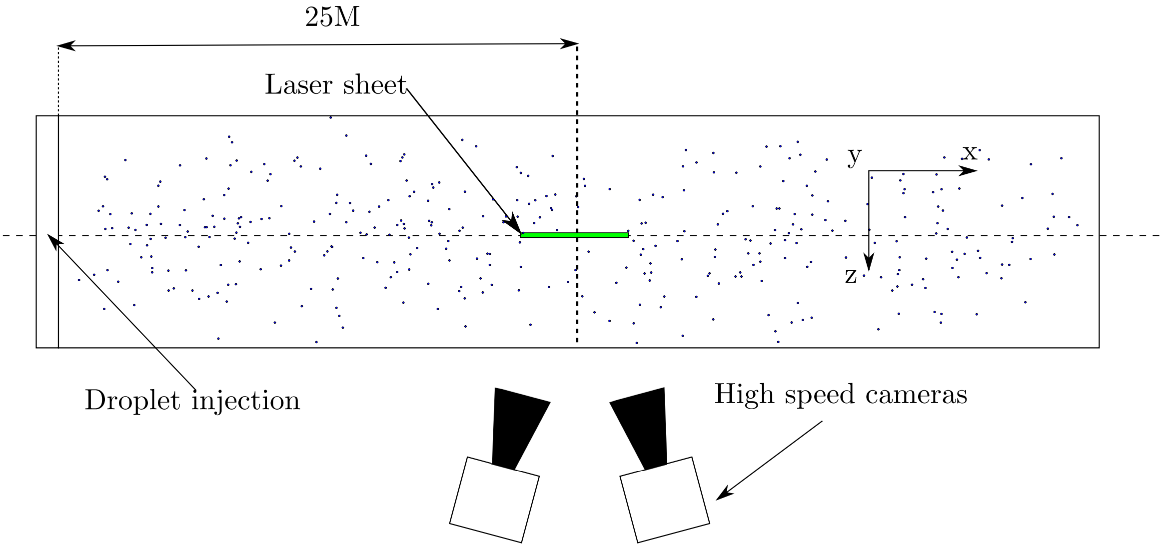

Figure 10.7 – Experimental setup sketch

Chapter 11

Contributions of this work

This work motivated from gaps in our knowledge of particle laden flows. Answering some of these open questions (see section 1.3), however, requires adequate experimental measurements and post-processing techniques. The latter two items also have technical difficulties and/or uncertainties that have not yet been completely explored, for instance, when particle laden flow experiments are conducted in wind tunnel facilities, and the recorded particle datasets are analyzed by means of Voronoï tessellations. We have explored some of these technical difficulties, and/or have proposed methods to overcome them. Given that the phenomena here studied revolve around the interaction between particles, and turbulence, we will start with the unladen phase results obtained in this work, and build upon them later including the discrete phase, and the coupling between both phases.

First, we have measured the unladen single phase turbulence downstream of an active grid [40] operated in two modes: triple random mode, and open mode (minimum blockage). Our results confirm that triple random mode does exhibit traditional Kolmogorov scalings $K41$ (i.e. $C_\varepsilon = constant$). On the other hand, our data shows that the open grid mode exhibits non-equilibrium scalings [35] similar to those found in fractal grids, i.e. $C_\varepsilon \sim Re_\lambda^{-1}$.

The implications of these results are two fold: one the one hand, the open grid behavior, not previously reported, has also peculiarities, for instance, the downstream location of the peak of turbulence intensity is a function of the inlet velocity; this observation could potentially aid to study the underlying principles of the transition between equilibrium and nonequilibrium scalings, which is an open problem in single phase turbulence. On the other hand, previous research reveals that in some particle laden flows preferential concentration depends on the type of turbulence generator [115, 145].

Our single phase work then suggests that care has to be taken when comparing experiments conducted with different turbulence generators, as the traditional picture of *memoryless* homogeneous isotropic turbulent flow interacting inertial particles may not be accurate, and/or should include these carrier phase phenomena. The latter may explain why the available particle laden flow experiments have no quantitative consensus on the trends exhibited.

Our work has also been able to provide two alternative solutions to common problem found when post-processing hot-wire records taken in active grid generated flows; the velocity autocorrelation function $\rho(r)$ does not in general cross zero [72], and thereby, it becomes difficult to estimate the integral length scale $\mathcal{L}$. This difficulty is not minor given the role that $\mathcal{L}$ has on numerical, and theoretical approaches of turbulence, e.g., $C_\varepsilon = \varepsilon\mathcal{L}/u^3$. For instance, using the method proposed by Puga and LaRue [72] we found that $\mathcal{L}$ could be underestimated by a factor of 2, as the their method is very sensitive on threshold δ needed to estimate $\mathcal{L}$. The solutions we proposed seem to be very robust, as tests with four different canonical flows show good agreement with traditional methods to estimate $\mathcal{L}$. More importantly, these new methods, can be extended to large scale experiments (e.g. Modane S3 wind tunnel) and/or field measurements, where having an adequate calibration could be difficult.

We now turn the attention into particle laden flow experiments. Accurate instruments to measure the discrete phase have been developed with the available technology: phase doppler interferometry in 1980s, and 2D or 3D imaging from the early 1980s and onwards. Although 2D/3D imaging techniques provide a more in depth insight of the particles spatial distribution, 1D phase doppler interferometry instruments are still in use because certain information of the particles behavior (e.g. the settling velocity) is not so easily accessible/feasible at large values of Re_λ via imaging techniques. Thus, developing post-processing tools from particle records coming from 1D/2D/3D measuring techniques is a necessary step to understand the complex particle laden flow underlying physics.

In this direction, Voronoï tessellations analysis applied to particle laden flows were introduced a decade ago. Contrary to other methods (e.g. radial distribution functions and pair distribution functions) to quantify preferential concentration, Voronoï diagrams provide easy access to the local concentration maps, and thereby allow a more direct computation of conditional statistics. These statistics are very much of interest, as they could extract key information of the underlying physics of the particle-turbulence interaction. Although this kind of analysis has become very popular in recent years, there has not been a comprehensive study of the biases found in the method.

In this work, we found that extending *rationale* that Monchaux et al. [8] proposed to analyze particle clustering coming from 2D imaging may not conclusive for particle records coming from 1D measuring techniques, for instance, phase Doppler interferometers or optical probes. More precisely, we found that under certain experimental conditions $Re_\lambda \in [30-250]$, and $\phi_v = O(10^{-5})$ where clustering has been found via 2D imaging, the criterion $\sigma_\mathcal{V}/\sigma_{RPP} > 1$, which gauges the presence of preferential concentration, might not hold (in 1D) if the probe measuring volume is very small, i.e., smaller than η (the Kolmogorov length scale). These observations are persistent in the parameter space explored and despite instrument retrieving the expected average values of the liquid fraction and/or particle velocity distribution.

This observed pitfall is not minor, as it affects the capacity of a 1D instrument to accurately characterize this phenomenon, an analogous, but distinct phenomenon has been reported for pair distribution functions [150]. To address this pitfall, we emulated an analogous eulerian measurement by means of orthogonally projecting 2D and 3D particle datasets. We show that in order to retrieve preferential concentration a reasonable rule of thumb would be to have a 1D instrument with a linear probe volume of order η. This recommendation, however, is very rough, and depends on the liquid concentration ϕ_v. Thus, a sensitive analysis should be conducted, and the instrument measurement volume varied in situations where particle clustering is certain, but is not recovered by 1D techniques.

Moreover, we have studied the origin of the power-law behavior widely reported in the clusters size PDF computed following the algorithm of Monchaux et al. [8], and widely reported in numerical simulations and experiments. We have proposed that a mixture PDF model could analytically describe this algorithm, and therefore, we were able to assess and identify possible biases. Several groups [13, 17, 26, 135] have proposed possible modifications to correct for these biases, which could undermine the main advantage of Voronoï tessellations over other methods to quantify preferential concentration: direct access of the local concentration maps and the possibility of identify individual clusters and their locations. Among the biases identified by these groups (that we avoided here by the use of a mixture PDF model) are that the random concentration fluctuations could be erroneously identified as clusters by the algorithm, leading to the computation of wrongly conditioned statistics, for instance, in 3D, the cluster volume PDF could have power-law tails even for a Poisson process, as noticed before by Uhlmann's group [26].

In this work, we have related the power law behavior in the particles cluster PDF to the carrier phase turbulence. We arrived at that conclusion by computing the histograms of the number of particles inside a cluster. These histograms exhibit a powerlaw behavior for turbulence driven records and 3D Poisson process (to an extent), while they exhibit an exponential behavior for Poisson processes in 1D and 2D. These results confirm the robustness of Voronoï tessellations in 2D as advanced by Monchaux [151], and provides an approach to disentangle turbulence driven clusters from those coming from random fluctuations in other dimensions by segregating clusters by their number of members (particles). Our approach seems to be more adequate than previous proposed amendments. First, it does not leave out compact clusters [152] , where *collective effects* may be dominant. Second, it is less sensitive to the presence of gravity [135].

Next, we focus on the particle measurements taken by phase doppler interferometry. The experimental campaign in LEGI wind tunnel provides further credence that studying the mechanical coupling of the turbulent carrier phase, and the discrete phase could be a key step to understand the particle laden flow physical mechanisms. Measuring both faces simultaneously is a very challenging task, and when feasible has been reported at very low values of $Re_\lambda \approx 30$ [24].

Taking into account the importance of study the dynamics of the turbulent carrier phase when the discrete phase is present, we have advanced a method to estimate the turbulent dissipation rate ε_p. This method is an extension of the zero-crossing method used in hot-wire anemometry [37]. Our results suggest that *sub-Kolmogorov* particles could enhance the carrier phase turbulence dissipation rate ε_p downstream of an active grid actuated in triple random mode. The carrier phase turbulence dissipation ε_p not only controls several turbulence parameters (e.g. Re_λ, Fr, η), but also it has been found that a larger value of ε_p further enhances particles settling velocity [21], an observation recovered in numerical studies including 'two-way' coupling [16, 18]. We also conjecture that the 4th root of ε in the computation of $\eta = \left(\nu^3/\varepsilon_p\right)^{1/4}$ could have masked in the past these coupling effects.

Our method despite being consistent with some numerical simulations [16] under the 'two-way' coupling regime, does not work in all experimental conditions, and it is rather limited to very strong turbulence $u/\overline{U} > 0.1$ conditions, and not so dilute concentrations $\phi_v \geq O(10^{-5})$. The latter imposes a limitation on its use to explore the boundary where the mechanical coupling between phases starts. The onset of this boundary is of much interest given that some theoretical and numerical approaches to preferential concentration invoke the negligible coupling between the carrier and discrete phases. Numerical simulations [1] set that boundary at volume concentrations close to 10^{-6}. This boundary has been scarcely validated in experiments given the mentioned difficulty of measuring both phases simultaneously [1, 17].

Finally, we comment on the work done on particle settling modification. We recover that for a fixed particle size distribution the particle settling is slower at increasing values of Re_λ in agreement with the study of Akutina et al. [148]. However, the experimental data, and the conclusions drawn, specially in the limit of very small Stokes numbers (i.e. $St \to 0$), were limited due to the several factors: optical alignment errors, instrument resolution, and the (possible) confinement effects.

First, the optical alignment errors are due to the projection of the horizontal component onto the vertical component in the phase doppler interferometry frame of reference. Given that former component is usually an order of magnitude larger than the vertical component, the smallest droplets in our experiments exhibited a larger degree of uncertainty, and dispersion. The instrument resolution $\pm 5mm/s$ also had impact on the velocities measured, and it sets a lower limit on the particle settling we could accurately measure. Our trends, however, are consistent with those of Sumbekova [2], who took measurements in the same facility with a resolution of $\pm 0.5mm/s$. The (potential) existence of confinement effects due to a weak mean flow could also have consequences for the particles with small Stokes number, which would follow the carrier phase more closely. The presence of such effects was also conjectured in the work of [2], and it could be inherent to wind tunnel experiments [10].

To circumvent these limitations, we focused on the moderate Rouse regime, i.e., $Ro \gg 0.1$. In this regime, we found that the particle settling velocity exhibits a quasilinear behavior consistent with previous experimental measurements. Furthermore, we recovered evidence that the cross-over point defining the boundary where the average particles settling is smaller than its respective stagnant fluid terminal velocity $\langle V_p^z \rangle / V_T < 1$ occurs at smaller Rouse ($Ro = V_T/u$) numbers with increasing values of Re_λ in agreement with the findings of Kawanisi and Shiozaki [113]. In addition, we plotted our data in a translating frame of reference moving at the average velocity of the particle distribution. By doing so, we aimed at bypassing the angle effects, and the weak mean flow effects that could present in our data records. Under this frame of reference, preliminary results show that the different experimental datasets collapse rather nicely, at the cost, however, of being unable to determine the origin of the weak mean flow, and of being limited to polydisperse distribution making impossible the comparison with numerical simulations.

In summary, this work has attempted to answer several open technical questions regarding the experimental measurement of particle laden flows. The solutions provided, to address the biases found in the post-processing methods, and to address the limitations found in the available measuring instruments, should aid to achieve a better understanding of underlying physics of particles turbulence interaction.

Chapter 12

Conclusion and perspectives

12.1 Conclusions

Although more detailed conclusions can be found in each of the articles chapters, we present below the most relevant global conclusions of this work:

- Taking into account the dominant influence the carrier phase turbulence has on the particle turbulence interaction [7, 115, 145], we have explored the turbulence cascade characteristics downstream of an active grid operated in triple random mode, and in open (passive) mode (minimum blockage). The results reveal that while the triple random mode follows standard K41 scalings, the open (passive) grid mode exhibits turbulence cascade scalings similar to those found in fractal grids, i.e., $C_\varepsilon \sim Re_\lambda^{-1}$. The results also reveal that the spatial extent of this regime increases with the inlet bulk velocity U_∞. This behavior could potentially aid to explore and explain the transition between K41, and non-equilibrium scalings.
- We have developed two new methods to estimate the integral length scale $\mathcal{L}$ for active grid generated flows under triple random mode. The need of this new development is the pathological behavior of the velocity autocorrelation function in those flows; it does not cross zero [72], which renders standard available methods ambiguous regarding the value of $\mathcal{L}$. These two new methods, however, have the potential of be extended to other types of flows where the instrument calibration is difficult, or unfeasible.
- Trying to circumvent the existing technological limits, for example, the small-scale resolution of the velocity fluctuations, we have proposed a method to estimate the carrier phase dissipation rate in the presence of inertial particles. Our results are consistent with numerical simulations, and support the conjecture that including the mechanical coupling between the carrier and discrete phases [16, 18, 141, 144] is a necessary ingredient to model the behavior of turbulent particle laden flows even at low particle volume fractions.
- It has been shown that the analyses of particle-turbulence interaction by means of 1D Voronoï analysis are not reliable under common experimental conditions. Specifically, under certain conditions it could fail to retrieve the presence of preferential concentration, even when there is certainty of the phenomenon presence beforehand. Likewise, when preferential concentration is retrieved by this kind of analysis the clusters PDF does not provide error-free information. These

pitfalls strongly affect the conditional statistics, one of the advantages of the Voronoï methods against other methods to quantify preferential concentration, and particle settling modification. Thus, in light of these observations, we recommend to use 2D imagining methods to further explore the underlying physics of particle-turbulence interactions.

- After modeling the cluster computation algorithm of Monchaux et al. [8] by means of a PDF-mixture model in 1D, 2D and 3D, we were able to explain the widely observed power-law behavior in the clusters probability density function. We present strong evidence that this power law originates in the turbulence carrier phase. Using this finding, we proposed an amendment to their method in order to separate turbulence-driven clusters from spatial random fluctuations of the particle concentration. Hence, new studies (especially those in 2D and 3D) could correctly compute conditional statistics of particles in clusters and disentangle the relationship between preferential concentration, and enhanced /reduced particle settling.

- We report that at moderate to higher Reynolds numbers $Re_\lambda \in [200-600]$ the particle settling velocity, in wind tunnel experiments seeded with polydisperse droplets, is reduced for all particles measured. In the moderate Rouse regime (i.e. $Ro = V_T/u \gg 0.1$) the particle settling exhibits a quasi-linear behavior: This behavior further suggests that the cross-over between the regimes of settling hindering and settling enhancement shifts to smaller Ro number at increasing values of Re_λ. Remarkably, our experimental data suggests that the ratio between the particle and the fluid acceleration (γ) does NOT play an important role in the particle settling velocity.

12.2 Perspectives and future work

The results presented in this thesis have produced several (and interesting) new questions yet to be examined. We make a brief recount below of the possible follow up projects from the work presented:

- The work conducted on the origin of the power-law found in the cluster PDF prompts some questions: is the extent of the power-law a consequence of the turbulence, and if so, what its relationship with the turbulence intensity or dissipation rate? what is the empirical relation between the cluster linear size and the integral length scale, i.e., $L_C = O(0.1\mathcal{L})$ found in previous analyses by means of Voronoï tessellations? does this coefficient carry any physical meaning or does it depend on the cluster definition?

- The existence of non-equilibrium turbulence by the use of active grids in open mode. Our preliminary results suggest that the peak of intensity for this type of grid varies with the bulk velocity U_∞. Thus, the onset of non-equilibrium could be potentially further studied by means of this grid arrangement. Indeed, a complete explicit characterization of these kind of grids with very low blockage should be conducted, considering the following steps:
    - Varying the flaps shape, size, and downstream ‘depth’. Taking into account that manufacturing several active grids with these characteristics could be very expensive, this study

  could be conducted by building an equivalent static open grid, i.e., a frozen solid version of an active grid. This solution would reduce the cost of the experimental setup, and would allow to reach higher values of U_∞ (and Re_λ), which is limited by the static torque of the step-motors of the current active grid installed in LEGI's wind tunnel.
  - Taking a PIV measurements in the lee of the grid to examine the evolution of the flow, and the iteration between the flap wakes and boundary layers that could be the origin of the non-equilibrium observed.

- Our work on relating the integral length scale ($\mathcal{L}$) to the variance of the distance between successive zero crossings ($\langle \Delta Z^2 \rangle$) has also raised many interesting questions, e.g., what is the relationship between this variance, and the turbulence cascade evolution (equilibrium and non-equilibrium), could this method to estimate ($\mathcal{L}$) be extended to 2D/3D measurements. Moreover, the physical significance of the power-law exponent found for $\langle \Delta Z^2 \rangle$ is yet to be investigated. Is $\langle \Delta Z^2 \rangle$ related to the power-spectrum, is it universal?, what determines its extent? Some of these answers could be obtained by

  - Conducting well-resolved PIV measurements using a set of different grids (passive, active). The challenge is , however, having a very large field of view, which has to be at least an order of magnitude larger than the integral length scale, and at the same time be able to resolve the Taylor length scale. This stringent resolution requirements are in principle needed if the procedure of estimating λ and $\mathcal{L}$ from 1-D hot-wire measurements is to be extended to 2D PIV measurements.
  - Taking longer hot-wire records (in the order of 10^9 integral length scales) so that adequate statistics at the larger scales could be computed.

- Our work on turbulence modification due to the presence of particles and the other results presented in this thesis also raises several potential ramifications: how does the polydispersity affect the turbulence modification? does the type of turbulence cascade change the turbulence modulation by the particles, i.e., are there any changes between particles interacting with equilibrium-turbulence and non-equilibrium turbulence ? Is the threshold between one-way and two-way coupling independent of the previous elements? To answer these questions, the following could be envisioned:

  - To conduct similar experiments using a mono-disperse distribution of particles spanning a parameter space of *sub-Kolmogorov* sizes, and concentrations. The challenge here lies on the limited amount of droplets generated by commercially available injectors.
  - To measure the discrete and continuous phases via means of PIV using passive grids, and active grids when feasible.

- The results for the particle settling velocity reported in this thesis suggest again that the particle polydispersity may play a non-negligible role that could mask or lead to misleading conclusions regarding the physical phenomenon. A definite answer would require to conduct experimental campaigns using mono-disperse particle distributions under similar experimental conditions. Moreover, it is yet to be examined how the settling scalings, developed for one-way coupling flows, apply to flows under two-way coupling conditions.

Bibliography

1. Balachandar, S & Eaton, J. K. Turbulent dispersed multiphase flow. *Annual review of fluid mechanics* **42,** 111–133 (2010) (cit. on pp. 1–3, 14, 16, 19, 20, 27, 95, 183, 184).
2. Sumbekova, S. *Concentration préférentielle de particules inertielles : la structure et la dynamique de clusters* PhD thesis (Universite Grenoble Alpes, 2016) (cit. on pp. 1, 2, 19, 20, 24, 25, 31, 37, 141, 171, 184).
3. Pope, S. B. *Turbulent flows* (IOP Publishing, 2001) (cit. on pp. 2, 17, 18).
4. Nielsen, P. On the motion of suspended sand particles. *Journal of Geophysical Research: Oceans* **89,** 616–626 (1984) (cit. on pp. 2, 19).
5. Elghobashi, S. On predicting particle-laden turbulent flows. *Applied scientific research* **52,** 309–329 (1994) (cit. on pp. 2, 3, 16, 20, 26, 96).
6. Aliseda, A., Cartellier, A., Hainaux, F & Lasheras, J. C. Effect of preferential concentration on the settling velocity of heavy particles in homogeneous isotropic turbulence. *Journal of Fluid Mechanics* **468,** 77–105 (2002) (cit. on pp. 2, 3, 17, 19, 20, 22, 24, 26, 36, 47, 171).
7. Coleman, S. & Vassilicos, J. A unified sweep-stick mechanism to explain particle clustering in two-and three-dimensional homogeneous, isotropic turbulence. *Physics of Fluids* **21,** 113301 (2009) (cit. on pp. 2, 3, 16, 17, 109, 185).
8. Monchaux, R., Bourgoin, M. & Cartellier, A. Preferential concentration of heavy particles: A Voronoï analysis. *Physics of Fluids* **22** (2010) (cit. on pp. 2, 4, 31, 37, 39, 47, 182, 186).
9. Obligado, M. *Fluid-particle interactions: from the simple pendulum to collective effects in turbulence* PhD thesis (Universite de Grenoble Alpes, 2013) (cit. on pp. 2, 3).
10. Good, G. *et al.* Settling regimes of inertial particles in isotropic turbulence. *Journal of Fluid Mechanics* **759** (2014) (cit. on pp. 2, 3, 11, 19, 20, 22, 24, 25, 141, 171, 178, 184).
11. Bec, J., Homann, H. & Ray, S. S. Gravity-driven enhancement of heavy particle clustering in turbulent flow. *Physical review letters* **112,** 184501 (2014) (cit. on pp. 2, 19–21, 25).
12. Bragg, A. D., Ireland, P. J. & Collins, L. R. Mechanisms for the clustering of inertial particles in the inertial range of isotropic turbulence. *Physical Review E* **92,** 023029 (2015) (cit. on pp. 2, 3, 16, 18, 23).
13. Baker, L., Frankel, A., Mani, A. & Coletti, F. Coherent clusters of inertial particles in homogeneous turbulence. *Journal of Fluid Mechanics* **833,** 364–398 (2017) (cit. on pp. 2, 4, 17, 19, 20, 26, 37, 47, 48, 182).
14. Huck, P. *et al.* The role of collective effects on settling velocity enhancement for inertial particles in turbulence. *Journal of Fluid Mechanics* **846,** 1059–1075 (2018) (cit. on pp. 2, 13, 19, 26, 32, 171–173, 178).

15. Elghobashi, S. Direct numerical simulation of turbulent flows laden with droplets or bubbles. *Annual Review of Fluid Mechanics* **51,** 217–244 (2019) (cit. on pp. 2, 3, 20).
16. Monchaux, R & Dejoan, A. Settling velocity and preferential concentration of heavy particles under two-way coupling effects in homogeneous turbulence. *Physical Review Fluids* **2,** 104302 (2017) (cit. on pp. 2, 3, 19, 20, 25, 95, 183, 185).
17. Petersen, A. J., Baker, L. & Coletti, F. Experimental study of inertial particles clustering and settling in homogeneous turbulence. *Journal of Fluid Mechanics* **864,** 925–970 (2019) (cit. on pp. 2, 3, 11, 19, 20, 22, 24, 26, 37, 47, 96, 182, 184).
18. Bosse, T., Kleiser, L. & Meiburg, E. Small particles in homogeneous turbulence: settling velocity enhancement by two-way coupling. *Physics of Fluids* **18,** 027102 (2006) (cit. on pp. 3, 19, 20, 95, 183, 185).
19. Mallouppas, G, George, W. & van Wachem, B. Dissipation and inter-scale transfer in fully coupled particle and fluid motions in homogeneous isotropic forced turbulence. *International Journal of Heat and Fluid Flow* **67,** 74–85 (2017) (cit. on pp. 3, 20).
20. Abdelsamie, A. H. & Lee, C. Decaying versus stationary turbulence in particle-laden isotropic turbulence: Turbulence modulation mechanism. *Physics of Fluids* **24,** 015106 (2012) (cit. on pp. 3, 20, 27, 97).
21. Rosa, B., Parishani, H., Ayala, O. & Wang, L.-P. Settling velocity of small inertial particles in homogeneous isotropic turbulence from high-resolution DNS. *International Journal of Multiphase Flow* **83,** 217–231 (2016) (cit. on pp. 3, 19, 20, 22, 24, 25, 183).
22. Tom, J. & Bragg, A. D. Multiscale preferential sweeping of particles settling in turbulence. *Journal of Fluid Mechanics* **871,** 244–270 (2019) (cit. on pp. 3, 20, 21, 23, 24, 26, 109).
23. Sumbekova, S., Cartellier, A., Aliseda, A. & Bourgoin, M. Preferential concentration of inertial sub-Kolmogorov particles: The roles of mass loading of particles, Stokes numbers, and Reynolds numbers. *Physical Review Fluids* **2,** 24302 (2017) (cit. on pp. 3, 17–19, 37, 47).
24. Poelma, C, Westerweel, J & Ooms, G. Particle–fluid interactions in grid-generated turbulence. *Journal of Fluid Mechanics* **589,** 315–351 (2007) (cit. on pp. 3, 20, 183).
25. Tanaka, T. & Eaton, J. K. Classification of turbulence modification by dispersed spheres using a novel dimensionless number. *Physical Review Letters* **101,** 114502 (2008) (cit. on p. 3).
26. Uhlmann, M. & Chouippe, A. Clustering and preferential concentration of finite-size particles in forced homogeneous-isotropic turbulence. *Journal of Fluid Mechanics* **812,** 991–1023 (2017) (cit. on pp. 4, 17–19, 27, 37, 47, 48, 183).
27. Goto, S. & Vassilicos, J. Local equilibrium hypothesis and Taylor's dissipation law. *Fluid Dynamics Research* **48,** 021402 (2016) (cit. on p. 10).
28. Pope, S. B. *Turbulent Flows* (Cambridge University Press, 2000) (cit. on pp. 9–11).

29. Tennekes, H. & Lumley, J. L. *A first course in turbulence* (MIT press, 1972) (cit. on pp. 9, 10).
30. Obligado, M., Dairay, T & Vassilicos, J. C. Nonequilibrium scalings of turbulent wakes. *Physical Review Fluids* **1,** 044409 (2016) (cit. on p. 10).
31. Valente, P. C. & Vassilicos, J. C. Universal dissipation scaling for nonequilibrium turbulence. *Physical review letters* **108,** 214503 (2012) (cit. on pp. 10, 109).
32. Goto, S. & Vassilicos, J. Unsteady turbulence cascades. *Physical Review E* **94,** 053108 (2016) (cit. on p. 10).
33. Bos, W. J. & Rubinstein, R. Dissipation in unsteady turbulence. *Physical Review Fluids* **2,** 022601 (2017) (cit. on p. 10).
34. Portela, F. A., Papadakis, G & Vassilicos, J. Turbulence dissipation and the role of coherent structures in the near wake of a square prism. *Physical Review Fluids* **3,** 124609 (2018) (cit. on p. 10).
35. Vassilicos, J. C. Dissipation in turbulent flows. *Annual Review of Fluid Mechanics* **47,** 95–114 (2015) (cit. on pp. 10, 22, 27, 109, 181).
36. George, W. K. The decay of homogeneous isotropic turbulence. *Physics of Fluids A: Fluid Dynamics* **4,** 1492–1509 (1992) (cit. on pp. 10, 11).
37. Mazellier, N. & Vassilicos, J. The turbulence dissipation constant is not universal because of its universal dependence on large-scale flow topology. *Physics of Fluids* **20,** 015101 (2008) (cit. on pp. 10, 20, 22, 38, 95, 109, 127, 183).
38. Davila, J. & Vassilicos, J. Richardson's pair diffusion and the stagnation point structure of turbulence. *Physical review letters* **91,** 144501 (2003) (cit. on pp. 10, 38).
39. Obligado, M, Aliseda, A, Calmant, T, de Palma, N & Cartellier, A. Study on preferential concentration of inertial particles in homogeneous isotropic turbulence via Big-Data techniques. *arXiv preprint arXiv:1907.07607* (2019) (cit. on p. 10).
40. Mydlarski, L. A turbulent quarter century of active grids: from Makita (1991) to the present. *Fluid Dynamics Research* **49,** 061401 (2017) (cit. on pp. 11, 181).
41. Mcdougall, T. J. Measurements of turbulence in a zero-mean-shear mixed layer. *Journal of Fluid Mechanics* **94,** 409–431 (1979) (cit. on p. 11).
42. Cheng, N.-S. & Law, A. W.-K. Measurements of turbulence generated by oscillating grid. *Journal of Hydraulic Engineering* **127,** 201–208 (2001) (cit. on p. 11).
43. McKenna, S. P. & McGillis, W. R. Observations of flow repeatability and secondary circulation in an oscillating grid-stirred tank. *Physics of Fluids* **16,** 3499–3502 (2004) (cit. on p. 11).
44. Marié, L & Daviaud, F. Experimental measurement of the scale-by-scale momentum transport budget in a turbulent shear flow. *Physics of Fluids* **16,** 457–461 (2004) (cit. on p. 11).

45. Volk, R., Odier, P. & Pinton, J.-F. Fluctuation of magnetic induction in von Kármán swirling flows. *Physics of Fluids* **18,** 085105 (2006) (cit. on p. 11).
46. Blum, D. B. *et al.* Signatures of non-universal large scales in conditional structure functions from various turbulent flows. *New Journal of Physics* **13,** 113020 (2011) (cit. on p. 11).
47. Hwang, W & Eaton, J. Creating homogeneous and isotropic turbulence without a mean flow. *Experiments in Fluids* **36,** 444–454 (2004) (cit. on p. 11).
48. Chang, K., Bewley, G. P. & Bodenschatz, E. Experimental study of the influence of anisotropy on the inertial scales of turbulence. *Journal of fluid mechanics* **692,** 464–481 (2012) (cit. on p. 11).
49. Bellani, G. & Variano, E. A. Homogeneity and isotropy in a laboratory turbulent flow. *Experiments in fluids* **55,** 1646 (2014) (cit. on p. 11).
50. Carter, D., Petersen, A., Amili, O. & Coletti, F. Generating and controlling homogeneous air turbulence using random jet arrays. *Experiments in Fluids* **57,** 189 (2016) (cit. on p. 11).
51. De Souza, D., Monchaux, R. & Dejoan, A. *SETTLING DYNAMICS OF INERTIAL PARTICLE* in *17th European Turbulence Conference* (Turin, Italy, Sept. 2019) (cit. on p. 11).
52. Simmons, L. & Salter, C. Experimental investigation and analysis of the velocity variations in turbulent flow. *Proceedings of the Royal Society of London. Series A, Containing Papers of a Mathematical and Physical Character* **145,** 212–234 (1934) (cit. on p. 11).
53. Corrsin, S. Turbulence: experimental methods. *Handbuch der Physik* **3,** 524–590 (1963) (cit. on pp. 11, 12).
54. Gamard, S. & George, W. K. Reynolds number dependence of energy spectra in the overlap region of isotropic turbulence. *Flow, turbulence and combustion* **63,** 443–477 (2000) (cit. on p. 11).
55. Comte-Bellot, G. & Corrsin, S. Simple Eulerian time correlation of full-and narrow-band velocity signals in grid-generated,'isotropic'turbulence. *Journal of Fluid Mechanics* **48,** 273–337 (1971) (cit. on p. 11).
56. Hurst, D & Vassilicos, J. Scalings and decay of fractal-generated turbulence. *Physics of Fluids* **19,** 035103 (2007) (cit. on p. 11).
57. Nagata, K. *et al.* Turbulence structure and turbulence kinetic energy transport in multiscale/fractal-generated turbulence. *Physics of Fluids* **25,** 065102 (2013) (cit. on p. 11).
58. Seoud, R. & Vassilicos, J. Dissipation and decay of fractal-generated turbulence. *Physics of Fluids* **19,** 105108 (2007) (cit. on p. 11).
59. Hearst, R. J. & Lavoie, P. Decay of turbulence generated by a square-fractal-element grid. *Journal of Fluid Mechanics* **741,** 567–584 (2014) (cit. on pp. 11, 13).
60. Gad-el Hak, M. & Corrsin, S. Measurements of the nearly isotropic turbulence behind a uniform jet grid. *Journal of Fluid Mechanics* **62,** 115–143 (1974) (cit. on pp. 11, 13).

61. Tassa, Y & Kamotani, Y. Experiments on turbulence behind a grid with jet injection in downstream and upstream direction. *the Physics of Fluids* **18,** 411–414 (1975) (cit. on pp. 11, 13).

62. Bateson, C. P. & Aliseda, A. Wind tunnel measurements of the preferential concentration of inertial droplets in homogeneous isotropic turbulence. *Experiments in fluids* **52,** 1373–1387 (2012) (cit. on pp. 11, 32, 172).

63. Hideharu, M. Realization of a large-scale turbulence field in a small wind tunnel. *Fluid Dynamics Research* **8,** 53 (1991) (cit. on pp. 11, 13, 14).

64. Mydlarski, L. & Warhaft, Z. On the onset of high-Reynolds-number grid-generated wind tunnel turbulence. *Journal of Fluid Mechanics* **320,** 331–368 (1996) (cit. on pp. 11, 13).

65. Mathieu, J & Alcaraz, E. Réalisation dune soufflerie à haut niveau de turbulence. *COMPTES RENDUS HEBDOMADAIRES DES SEANCES DE L ACADEMIE DES SCIENCES* **261,** 2435 (1965) (cit. on p. 13).

66. Bateson, C. P. *The radial distribution function as a quantification of the preferential concentration of cloud droplets in a turbulent flow* PhD thesis (University of Washington, 2010) (cit. on pp. 13, 32, 172–174).

67. Larssen, J. V. & Devenport, W. J. On the generation of large-scale homogeneous turbulence. *Experiments in fluids* **50,** 1207–1223 (2011) (cit. on p. 13).

68. Thormann, A. & Meneveau, C. Decay of homogeneous, nearly isotropic turbulence behind active fractal grids. *Physics of Fluids* **26,** 025112 (2014) (cit. on p. 13).

69. Griffin, K. P., Wei, N. J., Bodenschatz, E. & Bewley, G. P. Control of long-range correlations in turbulence. *Experiments in Fluids* **60,** 55 (2019) (cit. on p. 13).

70. Gramespacher, C., Albiez, H., Stripf, M. & Bauer, H.-J. The generation of grid turbulence with continuously adjustable intensity and length scales. *Experiments in Fluids* **60,** 85 (2019) (cit. on p. 13).

71. Küchler, C., Bewley, G. & Bodenschatz, E. Experimental study of the bottleneck in fully developed turbulence. *Journal of Statistical Physics* **175,** 617–639 (2019) (cit. on p. 13).

72. Puga, A. J. & LaRue, J. C. Normalized dissipation rate in a moderate Taylor Reynolds number flow. *Journal of Fluid Mechanics* **818,** 184–204 (2017) (cit. on pp. 13, 127, 181, 185).

73. O'Neill, P. L., Nicolaides, D., Honnery, D, Soria, J., *et al. Autocorrelation functions and the determination of integral length with reference to experimental and numerical data* in *15th Australasian fluid mechanics conference* **1** (2004), 1–4 (cit. on pp. 14, 127).

74. Gagne, Y., Castaing, B., Baudet, C. & Malécot, Y. Reynolds dependence of third-order velocity structure functions. *Physics of Fluids* **16,** 482–485 (2004) (cit. on p. 14).

75. Monchaux, R., Bourgoin, M. & Cartellier, A. Analyzing preferential concentration and clustering of inertial particles in turbulence. *International Journal of Multiphase Flow* **40,** 1–18 (2012) (cit. on pp. 15–18, 20, 28, 37).
76. Clift, R, Grace, J. & Weber, M. Bubbles, drops, and particles (1978) (cit. on p. 15).
77. Brennen, C. E. & Brennen, C. E. *Fundamentals of multiphase flow* (Cambridge university press, 2005) (cit. on p. 15).
78. Maxey, M. R. & Riley, J. J. Equation of motion for a small rigid sphere in a nonuniform flow. *The Physics of Fluids* **26,** 883–889 (1983) (cit. on pp. 15, 27).
79. Gatignol, R. *et al.* The Faxén formulae for a rigid particle in an unsteady non-uniform Stokes flow (1983) (cit. on p. 15).
80. Maxey, M. The gravitational settling of aerosol particles in homogeneous turbulence and random flow fields. *Journal of Fluid Mechanics* **174,** 441–465 (1987) (cit. on pp. 15, 16, 22–24, 26).
81. Wang, L.-P. & Maxey, M. R. Settling velocity and concentration distribution of heavy particles in homogeneous isotropic turbulence. *Journal of fluid mechanics* **256,** 27–68 (1993) (cit. on pp. 16, 17, 20–22, 24).
82. Chen, L, Goto, S & Vassilicos, J. Turbulent clustering of stagnation points and inertial particles. *Journal of Fluid Mechanics* **553,** 143–154 (2006) (cit. on pp. 16, 17).
83. Gustavsson, K & Mehlig, B. Statistical models for spatial patterns of heavy particles in turbulence. *Advances in Physics* **65,** 1–57 (2016) (cit. on p. 16).
84. Ferry, J. & Balachandar, S. A fast Eulerian method for disperse two-phase flow. *International journal of multiphase flow* **27,** 1199–1226 (2001) (cit. on p. 16).
85. Lazaro, B. & Lasheras, J. Particle dispersion in a turbulent, plane, free shear layer. *Physics of Fluids A: Fluid Dynamics* **1,** 1035–1044 (1989) (cit. on p. 17).
86. Squires, K. D. & Eaton, J. K. Preferential concentration of particles by turbulence. *Physics of Fluids A: Fluid Dynamics* **3,** 1169–1178 (1991) (cit. on pp. 17, 22).
87. Fessler, J. R., Kulick, J. D. & Eaton, J. K. Preferential concentration of heavy particles in a turbulent channel flow. *Physics of Fluids* **6,** 3742–3749 (1994) (cit. on p. 17).
88. Eaton, J. K. & Fessler, J. Preferential concentration of particles by turbulence. *International Journal of Multiphase Flow* **20,** 169–209 (1994) (cit. on p. 17).
89. Bec, J. *et al.* Acceleration statistics of heavy particles in turbulence. *Journal of Fluid Mechanics* **550,** 349–358 (2006) (cit. on pp. 17, 18).
90. Boffetta, G., De Lillo, F. & Gamba, A. Large scale inhomogeneity of inertial particles in turbulent flows. *Physics of Fluids* **16,** L20–L23 (2004) (cit. on p. 17).
91. Bec, J. *et al.* Heavy particle concentration in turbulence at dissipative and inertial scales. *Physical review letters* **98,** 084502 (2007) (cit. on p. 17).

92. Bragg, A. D. & Collins, L. R. New insights from comparing statistical theories for inertial particles in turbulence: I. Spatial distribution of particles. *New Journal of Physics* **16,** 055013 (2014) (cit. on pp. 17, 18).

93. Goto, S. & Vassilicos, J. Self-similar clustering of inertial particles and zero-acceleration points in fully developed two-dimensional turbulence. *Physics of Fluids* **18,** 115103 (2006) (cit. on pp. 17, 18, 37).

94. Tennekes, H. Eulerian and Lagrangian time microscales in isotropic turbulence. *Journal of Fluid Mechanics* **67,** 561–567 (1975) (cit. on p. 17).

95. Obligado, M., Teitelbaum, T., Cartellier, A., Mininni, P. & Bourgoin, M. Preferential concentration of heavy particles in turbulence. *Journal of Turbulence* **15,** 293–310 (2014) (cit. on pp. 17, 19, 47).

96. Ferenc, J.-S. & Néda, Z. On the size distribution of Poisson Voronoi cells. *Physica A: Statistical Mechanics and its Applications* **385,** 518–526 (2007) (cit. on pp. 18, 28, 37, 39).

97. Hascoët, E & Vassilicos, J. in *Advances in Turbulence XI* 482–484 (Springer, 2007) (cit. on pp. 18, 21).

98. Ireland, P. J., Bragg, A. D. & Collins, L. R. The effect of Reynolds number on inertial particle dynamics in isotropic turbulence. Part 1. Simulations without gravitational effects. *Journal of Fluid Mechanics* **796,** 617–658 (2016) (cit. on p. 18).

99. Bragg, A. D., Ireland, P. J. & Collins, L. R. On the relationship between the non-local clustering mechanism and preferential concentration. *Journal of Fluid Mechanics* **780,** 327–343 (2015) (cit. on p. 18).

100. Ireland, P. J., Bragg, A. D. & Collins, L. R. The effect of Reynolds number on inertial particle dynamics in isotropic turbulence. Part 2. Simulations with gravitational effects. *Journal of Fluid Mechanics* **796,** 659–711 (2016) (cit. on pp. 18, 26).

101. Dou, Z. *et al.* Effects of Reynolds number and Stokes number on particle-pair relative velocity in isotropic turbulence: a systematic experimental study. *Journal of Fluid Mechanics* **839,** 271–292 (2018) (cit. on p. 18).

102. Chouippe, A. & Uhlmann, M. On the influence of forced homogeneous-isotropic turbulence on the settling and clustering of finite-size particles. *Acta Mechanica* **230,** 387–412 (2019) (cit. on pp. 19, 27, 37).

103. Wood, A., Hwang, W & Eaton, J. Preferential concentration of particles in homogeneous and isotropic turbulence. *International journal of multiphase flow* **31,** 1220–1230 (2005) (cit. on p. 19).

104. Wittemeier, T. & Shrimpton, J. S. Explanation of differences in experimental and computational results for the preferential concentration of inertial particles. *Computers & Fluids* **173,** 37–41 (2018) (cit. on p. 19).

105. Mora, D. O., Cartellier, A. & Obligado, M. Experimental estimation of turbulence modification by inertial particles at moderate Re_λ. *Phys. Rev. Fluids* **4,** 074309 (7 2019) (cit. on pp. 19, 20, 22, 95, 96).

106. Yang, T. & Shy, S. Two-way interaction between solid particles and homogeneous air turbulence: particle settling rate and turbulence modification measurements. *Journal of fluid mechanics* **526,** 171–216 (2005) (cit. on pp. 19, 20).

107. Good, G., Gerashchenko, S & Warhaft, Z. Intermittency and inertial particle entrainment at a turbulent interface: the effect of the large-scale eddies. *Journal of Fluid Mechanics* **694,** 371–398 (2012) (cit. on pp. 19, 22, 24, 141).

108. Nielsen, P. Turbulence effects on the settling of suspended particles. *Journal of Sedimentary Research* **63,** 835–838 (1993) (cit. on pp. 19, 24, 25).

109. Sreenivasan, K., Prabhu, A & Narasimha, R. Zero-crossings in turbulent signals. *Journal of Fluid Mechanics* **137,** 251–272 (1983) (cit. on pp. 20, 38, 95, 127).

110. Ghosh, S *et al.* How turbulence enhances coalescence of settling particles with applications to rain in clouds. *Proceedings of the Royal Society A: Mathematical, Physical and Engineering Sciences* **461,** 3059–3088 (2005) (cit. on p. 21).

111. Yang, C. & Lei, U. The role of the turbulent scales in the settling velocity of heavy particles in homogeneous isotropic turbulence. *Journal of Fluid Mechanics* **371,** 179–205 (1998) (cit. on p. 21).

112. Rosa, B. & Pozorski, J. Impact of subgrid fluid turbulence on inertial particles subject to gravity. *Journal of Turbulence* **18,** 634–652 (2017) (cit. on pp. 21, 22, 24, 26, 27).

113. Kawanisi, K. & Shiozaki, R. Turbulent effects on the settling velocity of suspended sediment. *Journal of hydraulic engineering* **134,** 261–266 (2008) (cit. on pp. 22, 24, 25, 184).

114. Jacobs, C. N. *et al.* Flow scales of influence on the settling velocities of particles with varying characteristics. *PloS one* **11** (2016) (cit. on p. 22).

115. Goto, S. & Vassilicos, J. The dissipation rate coefficient of turbulence is not universal and depends on the internal stagnation point structure. *Physics of Fluids* **21,** 035104 (2009) (cit. on pp. 22, 109, 181, 185).

116. Mora, D. O., Muñiz Pladellorens, E., Riera Turró, P., Lagauzere, M. & Obligado, M. Energy cascades in active-grid-generated turbulent flows. *Phys. Rev. Fluids* **4,** 104601 (10 2019) (cit. on pp. 22, 31, 109).

117. Yang, T. & Shy, S. The settling velocity of heavy particles in an aqueous near-isotropic turbulence. *Physics of fluids* **15,** 868–880 (2003) (cit. on p. 24).

118. Maxey, M. t. & Corrsin, S. Gravitational settling of aerosol particles in randomly oriented cellular flow fields. *Journal of the atmospheric sciences* **43,** 1112–1134 (1986) (cit. on p. 24).

119. Uhlmann, M. An immersed boundary method with direct forcing for the simulation of particulate flows. *Journal of Computational Physics* **209,** 448–476 (2005) (cit. on p. 27).

120. Fiabane, L., Zimmermann, R., Volk, R., Pinton, J.-F. & Bourgoin, M. Clustering of finite-size particles in turbulence. *Physical Review E* **86,** 035301 (2012) (cit. on p. 27).

121. Fornari, W., Picano, F. & Brandt, L. Sedimentation of finite-size spheres in quiescent and turbulent environments. *Journal of Fluid Mechanics* **788,** 640–669 (2016) (cit. on p. 28).

122. Fornari, W., Zade, S., Brandt, L. & Picano, F. Settling of finite-size particles in turbulence at different volume fractions. *Acta Mechanica* **230,** 413–430 (2019) (cit. on p. 28).

123. Mazellier, N. *Dynamique spatio-temporelle du champ de vorticité en turbulence: mesures par corrélation acoustique dynamique.* PhD thesis (2005) (cit. on p. 31).

124. Obligado, M. *Fluid-particle interactions: from the simple pendulum to collective effects in turbulence* PhD thesis (Grenoble, 2013) (cit. on p. 31).

125. Obligado, M, Cartellier, A, Aliseda, A, Calmant, T & de Palma, N. Study on preferential concentration of inertial particles in homogeneous isotropic turbulence via big-data techniques. *Physical Review Fluids* **5,** 024303 (2020) (cit. on p. 33).

126. Benzi, R *et al. TurBase: a software platform for research in experimental and numerical fluid dynamics* in *2017 International Conference on High Performance Computing & Simulation (HPCS)* (2017), 51–57 (cit. on p. 33).

127. Bec, J, Biferale, L, Lanotte, A., Scagliarini, A. & Toschi, F. Turbulent pair dispersion of inertial particles. *Journal of Fluid Mechanics* **645,** 497–528 (2010) (cit. on p. 33).

128. Bec, J, Biferale, L, Cencini, M, Lanotte, A. & Toschi, F. Intermittency in the velocity distribution of heavy particles in turbulence. *Journal of Fluid Mechanics* **646,** 527–536 (2010) (cit. on p. 33).

129. Bruun, H. H. *Hot-wire anemometry: principles and signal analysis* 1996 (cit. on p. 33).

130. Hong, M., Cartellier, A. & Hopfinger, E. J. Characterization of phase detection optical probes for the measurement of the dispersed phase parameters in sprays. *International Journal of multiphase flow* **30,** 615–648 (2004) (cit. on p. 34).

131. Raimundo, P. M. *Analysis and modelization of local hydrodynamics in bubble columns* PhD thesis (2015) (cit. on p. 34).

132. Bachalo, W. & Houser, M. Phase/Doppler spray analyzer for simultaneous measurements of drop size and velocity distributions. *Optical Engineering* **23,** 235583 (1984) (cit. on p. 35).

133. Schwarzkopf, J. D., Sommerfeld, M., Crowe, C. T. & Tsuji, Y. *Multiphase flows with droplets and particles* (CRC press, 2011) (cit. on p. 35).

134. Obligado, M., Cartellier, A. & Bourgoin, M. Experimental detection of superclusters of water droplets in homogeneous isotropic turbulence. *EPL (Europhysics Letters)* **112,** 54004 (2015) (cit. on p. 37).

135. Uhlmann, M. & Doychev, T. Sedimentation of a dilute suspension of rigid spheres at intermediate Galileo numbers: the effect of clustering upon the particle motion. *Journal of fluid mechanics* **752,** 310–348 (2014) (cit. on pp. 37, 47, 183).

136. Antonia, R. On estimating mean and instantaneous turbulent energy dissipation rates with hot wires. *Experimental thermal and fluid science* **27,** 151–157 (2003) (cit. on p. 38).

137. Liepmann, H. & Robinson, M. Counting methods and equipment for mean-value measurements in turbulence research (1953) (cit. on pp. 38, 127).

138. Mora, D. O., Aliseda, A, Cartellier, A. & Obligado, M. *Pitfalls Measuring 1D Inertial Particle Clustering* in *iTi Conference on Turbulence* (2018), 221–226 (cit. on p. 39).

139. Mora, D. O., Aliseda, A., Cartellier, A. & Obligado, M. Characterizing 1D Inertial Particle Clustering, Submitted (2020) (cit. on p. 47).

140. Frühwirth-Schnatter, S. *Finite mixture and Markov switching models* (Springer Science & Business Media, 2006) (cit. on p. 47).

141. Rosa, B., Pozorski, J. & Wang, L.-P. Effects of turbulence modulation and gravity on particle collision statistics. *International Journal of Multiphase Flow,* 103334 (2020) (cit. on pp. 95, 185).

142. Rice, S. O. Mathematical analysis of random noise. *Bell System Technical Journal* **24,** 46–156 (1945) (cit. on p. 95).

143. Vessaire, J. *Couplages particules/turbulence dans un écoulement tourbillonnaire et fortement ensemencé* PhD thesis (Lyon, 2019) (cit. on p. 96).

144. Saito, I., Watanabe, T. & Gotoh, T. A new time scale for turbulence modulation by particles. *Journal of Fluid Mechanics* **880** (2019) (cit. on pp. 96, 185).

145. Weiss, P., Oberle, D., Meyer, D. W. & Jenny, P. Impact of turbulence forcing schemes on particle clustering. *Physics of Fluids* **31,** 061703 (2019) (cit. on pp. 109, 171, 181, 185).

146. Mora, D. O. & Obligado, M. Estimating the integral length scale on turbulent flows from the zero crossings of the longitudinal velocity fluctuation. *Experiments in Fluids* **61** (2020) (cit. on p. 127).

147. Mora, D. O., Obligado, M., Aliseda, A. & Cartellier, A. Polydisperse particle settling velocity in decaying homogeneous isotropic turbulence, To be submitted (2020) (cit. on p. 141).

148. Akutina, Y., Revil-Baudard, T., Chauchat, J. & Eiff, O. Experimental evidence of settling retardation in a turbulence column. *Physical Review Fluids* **5,** 014303 (2020) (cit. on pp. 141, 184).

149. Clark, A., Machicoane, N. & Aliseda, A. A quantitative study of track initialization of the four-frame best estimate algorithm for three-dimensional Lagrangian particle tracking. *Measurement Science and Technology* **30,** 045302 (2019) (cit. on p. 178).

150. Kostinski, A. B. & Shaw, R. A. Scale-dependent droplet clustering in turbulent clouds. *Journal of fluid mechanics* **434,** 389–398 (2001) (cit. on p. 182).

151. Monchaux, R. Measuring concentration with Voronoï diagrams: the study of possible biases. *New Journal of Physics* **14,** 095013 (2012) (cit. on p. 183).

152. Zamansky, R., Coletti, F., Massot, M. & Mani, A. Turbulent thermal convection driven by heated inertial particles. *Journal of Fluid Mechanics* **809,** 390–437 (2016) (cit. on p. 183).

153. Albert, T. & Wager, E. How to handle authorship disputes: a guide for new researchers (2010) (cit. on p. 202).

154. McNutt, M. K. *et al.* Transparency in authors' contributions and responsibilities to promote integrity in scientific publication. *Proceedings of the National Academy of Sciences* **115,** 2557–2560 (2018) (cit. on p. 202).

155. Wager, E. Recognition, reward, and responsibility: Why the authorship of scientific papers matters. *A Guide to the Scientific Career: Virtues, Communication, Research and Academic Writing,* 361–368 (2019) (cit. on p. 202).

156. Pignatelli, B, Maisonneuve, H. & Chapuis, F. Authorship ignorance: views of researchers in French clinical settings. *Journal of Medical Ethics* **31,** 578–581 (2005) (cit. on p. 202).

APPENDIX A

Authorship guidelines

Before introducing the articles written during this thesis, and considering the regulations that rule this type of work (see end of section 1.4), we briefly summarize the guidelines learnt societies, and academic bodies have developed to determine authorship in scientific publications. Here below, we quote some relevant texts:

- Authorship should be limited to those who have made a significant contribution to the concept, design, execution or interpretation of the research study. All those who have made significant contributions should be offered the opportunity to be listed as authors. Other individuals who have contributed to the study should be acknowledged, but not identified as authors. (The Americal Physics society available at 15/03/2020 in `https://www.aps.org/policy/statements/02_2.cfm`)

- What qualifies for authorship? In general, authorship for ECDC outputs with scientific content and intended for use outside of the Centre, and based on work performed on behalf of ECDC, whether by ECDC staff during their official duties or by commissioned externals within a service contract with the Centre, should be based on the principles set out in the ICMJE recommendations (also known as Vancouver guidelines).

  This means that to be listed as author one needs to fulfil criteria 1-4 below:

  - **CRITERION 1**: Everyone finally listed as an author should have made a substantial, direct and active intellectual contribution to essential parts of the work leading to a publication like conception/ design of the work and elaboration of the methods; collection, analysis and interpretation of the data and results.
  - **CRITERION 2**: Everyone that made a substantial, direct and active intellectual contribution to the work should be given the opportunity to and actively contribute to the writing, critical review and revision of the final output regardless of whether the person has left the position held at the time of contribution.
  - **CRITERION 3**: All listed authors have fulfilled criteria 1 and 2 and have given their final approval of the version to be published.
  - **CRITERION 4**: All listed authors have agreed to be accountable for all aspects of the work, and ensure that questions related to accuracy or integrity of any part of the work are appropriately investigated and resolved.

  What does not qualify for authorship? Honorary authorship is not allowed nor is ghost authorship. As for scientific journals, review alone does not constitute authorship. he

> sole contribution of data does not qualify for authorship. Contributors of data and other relevant information should be named in the acknowledgments.
>
> (The European center for disease prevention and control (ECDC) directive **ECDC/IP/104**)

- Authorship credit should be based only on:
  1. Substantial contributions to conception and design, or acquisition of data, or analysis and interpretation of data.
  2. Drafting the article or revising it critically for important intellectual content.
  3. Final approval of the version to be published

  Conditions (1), (2), and (3) must all be met. Acquisition of funding, the collection of data, or general supervision of the research group, by themselves, do not justify authorship. (Committee on Publication Ethics [153])

In theory, most of the journals adhere to best practices of the International Committee of Medical Journal Editors (ICMJE) [153, 154], but it is hard to quantify whether the ICMJE criteria is universally respected [155]. Thus, the issue of authorship is still not settled, and several studies have point out that due to the current 'publish or perish' scientific culture that has taken off in the last decades most of these directives are not followed in several scientific studies [153, 155] compromising scientific integrity and leading to authorship problems (e.g. listing as an author someone that should be listed in the acknowledgement section). In France, these authorships problems are common [156].

On the author order (who comes first, second, and third), there are not universal metrics, or system that could justify this order. Moreover,

> although it is generally assumed that individuals are listed in decreasing order of their contribution, this convention is virtually never explained, and importance is sometimes also attached to being the last or corresponding author. (Wager [155])

Perhaps, the absence of such general 'hard' system to quantify authorship order is due to the subjectivity of the criteria proposed; some even have proposed to list the authors in alphabetic order, or to discuss andto agree on the order before drafting the manuscript [153].

A.1 Authorship point system for this work

Given that the nature of this work aims at obtaining a Doctoral degree, it is required to that the author of this work has made an original contribution to the field of study. **To justify this is the case, and that is warranted that the author of this manuscript deserves to be the first author on all the articles published**, we adopted a quantitative approach based on a points system similar to the one developed by Professor Stephen Kosslyn:

The point totals of each phase should be agreed upon in advance; some projects, for example, use standard designs (e.g., "Stroop") or analyses (e.g., correlations),in which case the number of points for that phase should be reduced. The following are "default" point values, with a total of 1000. The total points for each phase is divided among authors in proportion to their contribution in that phase of the project. *In my lab, if someone contributed more than 0 but less than 10% of the total number of points, they are acknowledged in the footnote.* If they contributed at least 10%, they are an author, and the ordering of authorship is determined by the relative number of points.

1. The idea (250 points): Without the idea, nothing else happens. If the idea grew out of a discussion, all who contributed get 'credit'–but perhaps not equally so, if one or more people were primarily responsible for the insights leading to the best way to pose the question to be answered by the research and the logic of the design.
2. The design (100 points): The details of the design include counterbalancing issues, control conditions, whether a within-subjects or between-subjects design is used, and so on. A bad design later will render the results useless, so this is a critical step.
3. The implementation (100 points): Someone must implement the design into actual materials, devise instructions, and so on. To the extent this is simple boilerplate (a variation on well-developed methods using available materials),this step may be given much less weight (perhaps only 5 points).Typically 2 of 2person doing the implementation is supervised closely, so some of the point smay go to the supervisor.
4. Conducting the experiment (100 points): The person who tests subjects *can*earn up to 100 points, but may earn merely 5 points if all they do is mindlessly test subjects. Authorship is awarded only to those who contribute substantially and creatively to a project; if someone is receiving class credit or payment and all they do is follow instructions and test subjects, this is worthy of an acknowledgement in the paper, but not authorship. On the other hand, if they notice what subjects are actually doing and make constructive suggestions for how to improve the experiment, this qualifies them to be included as an author.Specifically, if one notices problems in the method or procedure, and makes constructive suggestions about how to repair them, observes interesting hints about what's really going on in the debriefings, and so on, this counts as a substantial creative contribution at this stage.
5. Data analysis (200 points): Simply running the data through an ANOVA program is not enough to earn authorship at this phase. However, devising some new way to look at the data (e.g., as difference scores or ratios of somekind), or otherwise contributing a novel insight into the best way to reveal the underlying patterns in the data, may be sufficient. Particularly labor-intensive or creative data analysis, such as involved in PET and fMRI, can "earn" the full number of points. Depending on the project, the maximum of 200 points may or may not be allocated.
6. Writing (250 points). Nothing happens if the results are not reported. Writingis usually shared by several people. Credit is allocated primarily to the one who shapes the conceptual content, although a good and insightful literature review also counts

> heavily. If someone writes a first draft that is not used at all, this does not contribute towards points: good intentions are not enough; the question is who has contributed how much to the final product. Similarly, the sheer amount of time one has spent on the project is not relevant; competent people who work more efficiently should competent people who work more efficiently should not be penalized.

(Available at `https://kosslynlab.fas.harvard.edu/files/kosslynlab/files/authorship_criteria_nov02.pdf`)

The authorship order in the respective manuscripts goes as a pascal triangle (see figure A.1) with the top two scores on the outsides (*first, and last*), and the remaining ones in the middle, for example for 3 people, the authorship order will be shown as:

Top score,	**Last score**,	**Runner up**

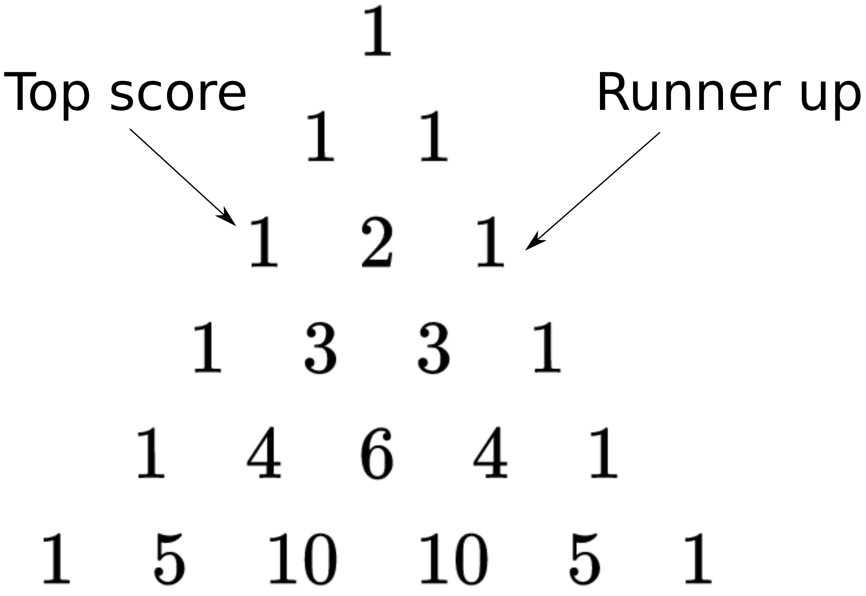

Figure A.1 – Authorship order in articles based on the points system that looks like a Pascal triangle, for instance, for 3 people involved: the top score goes to the left, the second largest score goes to the right, and the lowest score goes in the middle.

APPENDIX B

Declaration of honor

Daniel Andrés Odens Mora Paiba (**the candidate**); and Alain Cartellier, Martin Obligado, and Alberto Aliseda (**the supervisors**), collectively referred as the undersigned

hereby certify

that (subject to the additional declarations below):

1. The information here provided is correct and complete.
2. The work contained in this doctoral thesis, and the articles sent to publication were original works developed by the candidate.
3. The candidate was the main responsible of articles the publication cycle: writing of the articles content, their formatting, and preparing the response to the respective reviews.
4. The candidate was the first author in the works sent to publication given his leading contribution pursuant the guidelines found in the appendix A.

Signature for the candidate:

Daniel Andrés Odens Mora
Candidate

Signature for the supervisors:

Alain Cartellier
Supervisor

Martin Obligado
Supervisor

Alberto Aliseda
Supervisor